Strathclyde institute of Pharmacy and Biomedical Sciences (SIPBS)

EXPLOITING SURFACE FUNCTIONALISATION AND MICROPATTERNING FOR LIVE CELL IMAGING OF MITOCHONDRIAL TRAFFICKING IN HIPPOCAMPAL NEURONAL CULTURES

SO JEONG KIM

A thesis submitted in fulfilment of the requirements for the degree of Doctor of Philosophy

2025.03.31

This thesis is the result of the author's original research. It has been composed by the author and has not been previously submitted for examination which has led to the award of a degree.

Signed: 

Date: 31-03-2025

I. Acknowledgements

First and foremost, I would like to express my deepest gratitude to my supervisors, Dr. Susan Chalmers and Dr. Mairi Sandison, for their unwavering support, patience, and guidance throughout this long journey. This thesis has faced numerous delays for various circumstances, including the impact of COVID-19 and challenges of starting a job in Korea, which often left me with little time to focus on research. Despite these obstacles, my supervisors never ceased to encourage me, provide invaluable insights, and never gave up on me. Their belief in my work and in my ability to see this through has been truly invaluable.

I would also like to extend my heartfelt thanks to my family for their unconditional love and encouragement, and to Simba, my feline companion, for providing me with comfort and company during countless late nights. This journey has been long and challenging but knowing that I had the unwavering support of those around me gave me the strength to persevere.

I am also grateful to the Engineering and Physical Sciences Research Council (EPSRC) for funding this research, without which this work would not have been possible.

Finally, I would like to express my deepest gratitude to God, whose guidance and strength have sustained me throughout this journey. Through every challenge and moment of doubt, I found the resilience to continue, and for that, I am profoundly thankful.

This thesis is a testament to the patience, faith, and support of those who stood by me, and I dedicate it to all who never stopped believing in me.

II. Abstract

Mitochondrial motility is essential for neuronal function, ensuring proper ATP distribution, calcium buffering, and synaptic maintenance. However, tracking mitochondrial transport in neurons remains challenging due to their highly branched and overlapping processes. The conditions used to grow neurons *in vitro*, including the substrate on which the cells are grown, impact morphology, branching, extent of neurite growth, and potentially intracellular transport, including mitochondrial transport and dynamics, yet the specific effects on mitochondrial motility remain unclear. This thesis investigates mitochondrial motility in primary hippocampal neurons cultured on traditionally used substrates - poly-D-lysine (PDL), laminin and dual PDL/laminin – and on chemically charged substrates: carboxyethylsilanetriol (CES) and aminopropyltriethoxysilane (APTES). Additionally, microcontact printing was employed to create micropatterned substrates to restrict neurite outgrowth and enable structured mitochondrial tracking.

To optimise micropatterning for neuronal cultures, key parameters—including stamp wettability, bio-ink composition and substrate blocking—were adjusted to enhance pattern fidelity and reduce off-pattern adhesion. Live-cell imaging and kymograph analyses were used to quantify mitochondrial motility within neurons grown on different substrate conditions. Compared to traditional coatings, CES-coated substrates significantly reduced the fraction of motile mitochondria, segmental velocities, and run lengths, while increasing pause duration and frequency. APTES substrates supported moderately higher motility than CES, indicating that surface charge influences cytoskeletal interactions and organelle transport. Additionally, neuron-to-astrocyte ratios were higher on CES and APTES surfaces, suggesting substrate chemistry impacts cell composition.

Micropatterned substrates induced further reductions in motile fractions and travel distances across all conditions, with a significant shift in mitochondrial pausing behaviour. These findings suggest that both biochemical and spatial constraints influence neurons to affect intracellular organelle transport, providing a controlled framework for studying neuronal trafficking mechanisms.

This study establishes a reproducible platform for quantifying mitochondrial motility under defined spatial constraints and highlights how substrate composition and patterning can modulate intracellular transport. These insights offer a foundation for future studies investigating transport deficits in neurodegenerative diseases and axonal injury.

III. Table of Contents

IV. List of Figures

V. List of Tables

VI. Abbreviations

AD	Alzheimer's Disease
Aβ	Amyloid-β
ALS	Amyotrophic Lateral Sclerosis
AMPA	α-amino-3-hydroxy-5-methylisoxazole-4-propionate acid
ANOVA	Analysis of Variance
APP	Amyloid Precursor Protein
APTES	Aminopropyl-triethoxysilane
APTMS	Aminopropyl-trimethoxysilane
ATP	Adenosine Triphosphate
CES	Carboxyethylsilanetriol Di-sodium Salt
CNS	Central Nervous System
DAPI	4',6-Diamidino-2-phenylindole
DCDMS	Dichlorodimethylsilane
DEP	Dielectrophoresis
DIV	Days In Vitro
D1R	D1-like Dopamine Receptor
D2R	D2-like Dopamine Receptor
ECM	Extracellular Matrix
ER	Endoplasmic Reticulum
ESC	Embryonic Stem Cells
ETC	Electron Transport Chain
FITC	Fluorescein Isothiocyanate
FOTCS	Tridecafluoro-1,1,2,2-tetrahydrooctyl trichlorosilane
GFAP	Glial Fibrillary Acidic Protein
IMM	Inner Mitochondrial Membrane
IQR	Interquartile Range
KHC	Kinesin Heavy Chains
KIF5	Kinesin-1

KLC	Kinesin Light Chains
InsP3R	Inositol 1,4,5-triphosphate Receptor
iPSC	Induced Pluripotent Stem Cell
IP_3	Inositol 1,4,5-triphosphate
LGI1	Leucine-Rich Glioma-Inactivated 1
MAP2	Microtubule-Associated Protein 2
MAPT/tau	Microtubule-Associated Protein Tau
MCU	Mitochondrial Ca^{2+} Uniporter
MEA	Microelectrode Arrays
MFN1	Mitofusion-1
MFN2	Mitofusion-2
Mito-GFP	Green Fluorescent Protein
Mito-RFP	Red Fluorescent Protein
MPTP	1-methyl-4-phenyl-1,2,3,6-tetrahydrophyridine
NCLX	Na^+/Ca^{2+} exchanger
NFA	Network Formation Assay
NMDA	*N*-methyl-D-aspartate
OMM	Outer Mitochondrial Membrane
OPA1	Optic Atrophy 1
OXHOS	Oxidative Phosphorylation
PD	Parkinson's Disease
PDL	Poly-D-lysine
PDMS	Polydimethylsiloxane
PEG	Polyethylene Glycol
PFS	Trichloro(1H,1H,2H,2H-perfluorooctyl)silane
PLL	Poly-L-lysine
PLL-g-PEG	Poly(L-lysine)-graft-poly(ethylene glycol)
P+L	Polylysine and Laminin (dual coating)
ROI	Region of Interest
ROS	Reactive Oxygen Species

RyR	Ryanodine Receptors
SAMs	Self-Assembled Monolayers
SDS	Sodium Dodecyl Sulphate
SH-SY5Y	Human Neuroblastoma Cell Line
SNCA	α-synuclein
TMRE	Tetramethyl Rhodamine Ethyl Ester
VDAC	Voltage-Dependent Anion Channel
VGCC	Voltage-Gated Ca2+ Channel
6-OHDA	6-hydroxydopamine
µCP	Microcontact Printing

CHAPTER ONE:

General Introduction

1.1 The Role and Structure of Mitochondria

1.1.1 Mitochondrial Structure

Mitochondria are cytoplasmic organelles which play a critical role in regulating cellular life and death. In neurons, mitochondria are essential for generating adenosine triphosphate (ATP), the primary energy currency required to sustain synaptic function (Reddy, 2009; Mattson *et al*., 2008). Beyond energy production, mitochondria contribute to reactive oxygen species (ROS) generation, intracellular calcium buffering and cellular signalling modulation (Reddy, 2009; Mattson *et al*., 2008).

Mitochondria possess a double-membrane structure, consisting of an outer mitochondrial membrane (OMM) and an inner mitochondrial membrane (IMM). The intermembrane space, located between the OMM and IMM, contains proteins such as cytochrome c, which are involved in mitochondrial energetics and apoptosis. The innermost compartment, enclosed by the IMM, is the mitochondrial matrix where the IMM's curvature forms cristae (Fig 1A).

The OMM contains various pore-forming membrane proteins, including the voltage-dependent anion channel (VDAC), which allows the passage of ions and small uncharged molecules between the OMM and IMM (Bayrhuber, *et al*., 2008; McCarron, *et al*., 2013). Larger molecules, such as proteins, require specialised translocases for import. Due to its permeability, the OMM lacks membrane potential, whereas the IMM is impermeable to most ions and molecules.

The electron transport chain (ETC) embedded in the IMM plays a critical role in oxidative phosphorylation (OXHOS) by pumping protons to establish an electrochemical gradient (Fig 1B). This gradient consists of (1) a charge difference, or membrane potential, and (2) a proton concentration difference, or pH gradient. The ETC comprises five distinct complexes (I-V): Complex I receive electrons from NADH, while Complex II accepts electrons from $FADH_2$. These electrons are transferred through the lipid-soluble coenzyme ubiquinone (Q) to Complex III, and subsequently to cytochrome c located on the outer face of the IMM. At Complex IV, molecular oxygen (O_2) is reduced to water (H_2O) in the presence of protons (H^+).

During this process, Complexes I, III and IV actively pump H^+ into the intermembrane space, generating an electrochemical gradient across the IMM. Protons then flow back into the mitochondrial matrix through Complex V (ATP synthase), driving the synthesis of ATP from ADP and inorganic phosphate (Mitchell, 1966). Additionally, ROS may be generated when electrons escape to oxygen at Complexes I and III (Skulachev, 1996).

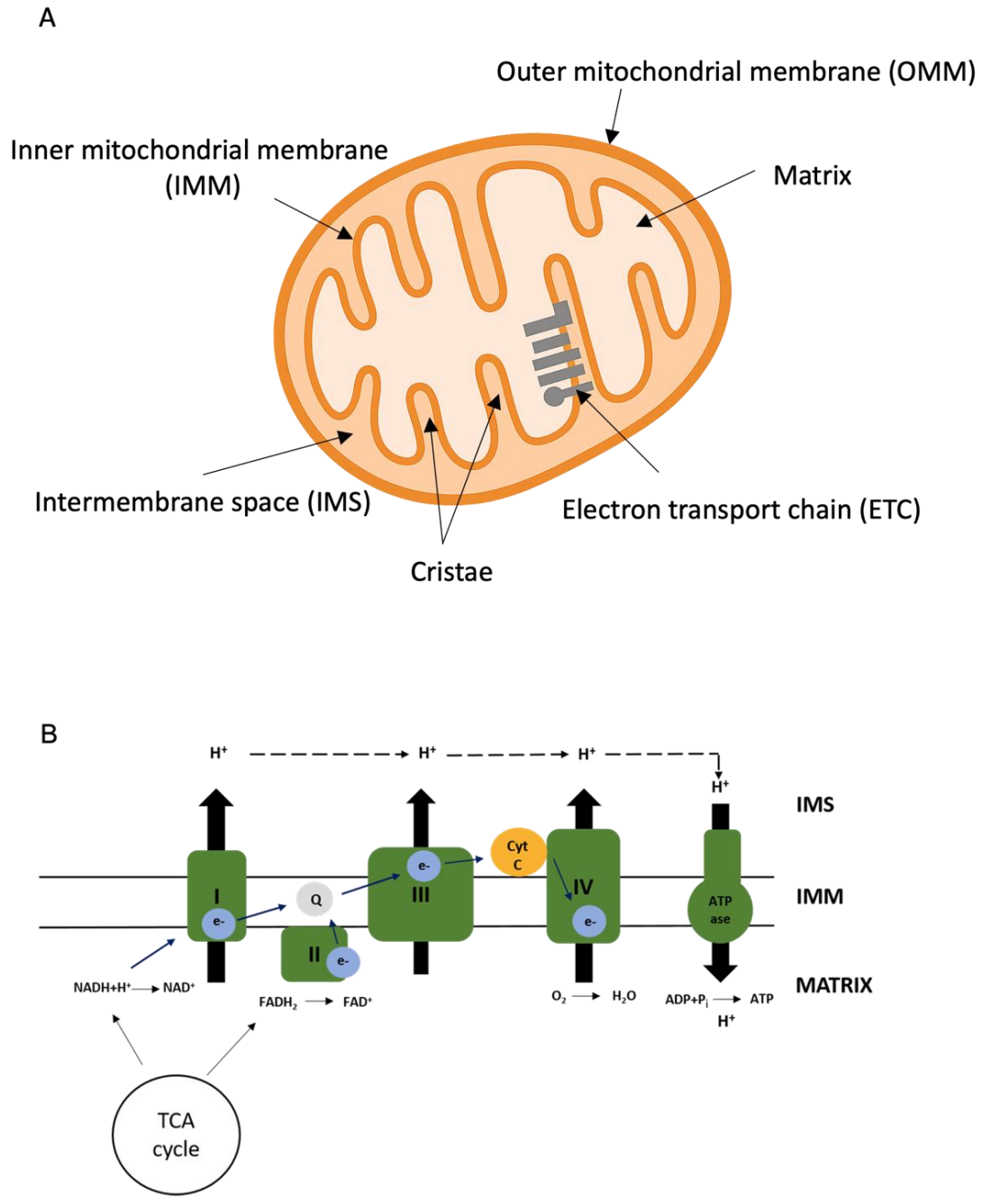

Figure 1. Schematic diagram of mitochondrial structure.

(A) The mitochondrial outer and inner membranes form distinct compartments within mitochondria. (B) The electron transport chain. Electrons from the TCA cycle pass through four complexes (I-IV), generating an electrochemical gradient across the inner mitochondrial membrane (IMM). Proton (H+) transport into the intermembrane space (IMS) is facilitated by Complexes I, III, and IV, and mitochondrial ATP is synthesized by ATP synthase (Complex V). Generated in BioRender.

1.1.2 Mitochondrial in Neuronal Calcium Homeostasis

Mitochondria play a pivotal role in ATP production and calcium (Ca^{2+}) buffering, supporting neurotransmitter release, synaptic vesicle recycling, and maintenance of the electrochemical gradient - all of which require precise Ca^{2+} regulation (Devine and Kittler, 2018). Mitochondrial Ca^{2+} handling occurs through two primary pathways. The mitochondrial Ca^{2+} uniporter (MCU), a highly selective, Ca^{2+}-permeable channel, facilitates the accumulation of Ca^{2+} into the mitochondrial matrix when cytosolic Ca^{2+} concentration $[Ca^{2+}]_c$ exceeds basal levels (Kirichok, 2004) (Fig. 2A). In contrast, two antiporters- the Na^+/Ca^{2+} exchanger (NCLX) and the H^+/Ca^{2+} exchanger - export Ca^{2+} out of the matrix at a slower rate than its uptake via the uniporter, thereby maintaining intra mitochondrial Ca^{2+} homeostasis after cell stimulation (Drago *et al*., 2011). Ca^{2+} accumulation within mitochondria is membrane potential-dependent, allowing for rapid Ca^{2+} influx through the MCU upon neuronal stimulation when cytosolic Ca^{2+} levels are elevated.

In neurons, Ca^{2+} serves as a major intracellular second messenger, linking plasma membrane depolarisation to synaptic activity. The influx of Ca^{2+} through presynaptic voltage-gated Ca^{2+} channels (VGCC) is crucial for neurotransmitter release, which can result in an elevation of post synaptic $[Ca^{2+}]$ (Yuste *et al*., 2000, Burnished and Rozov, 2005, Hartmann and Konnerth, 2005) (Fig 2B). Post-synaptic cytoplasmic Ca^{2+} levels ($[Ca^{2+}]_c$) increase via direct activation of ionotropic glutamate receptors, including α-amino-3-hydroxy-5-methylisoxazole-4-propionate acid (AMPA)- and *N*-methyl-D-aspartate (NMDA)-receptors (AMPARs and NMDARs), as well as through indirect activation of VGCC. Additionally, intracellular Ca^{2+} is

released from post-synaptic endoplasmic reticulum (ER) stores via inositol 1,4,5 trisphosphate (IP_3) or ryanodine receptors (RyR) (Berridge, 2009).

Figure 2. Mitochondrial Ca^{2+} dynamics can regulate synaptic activity.

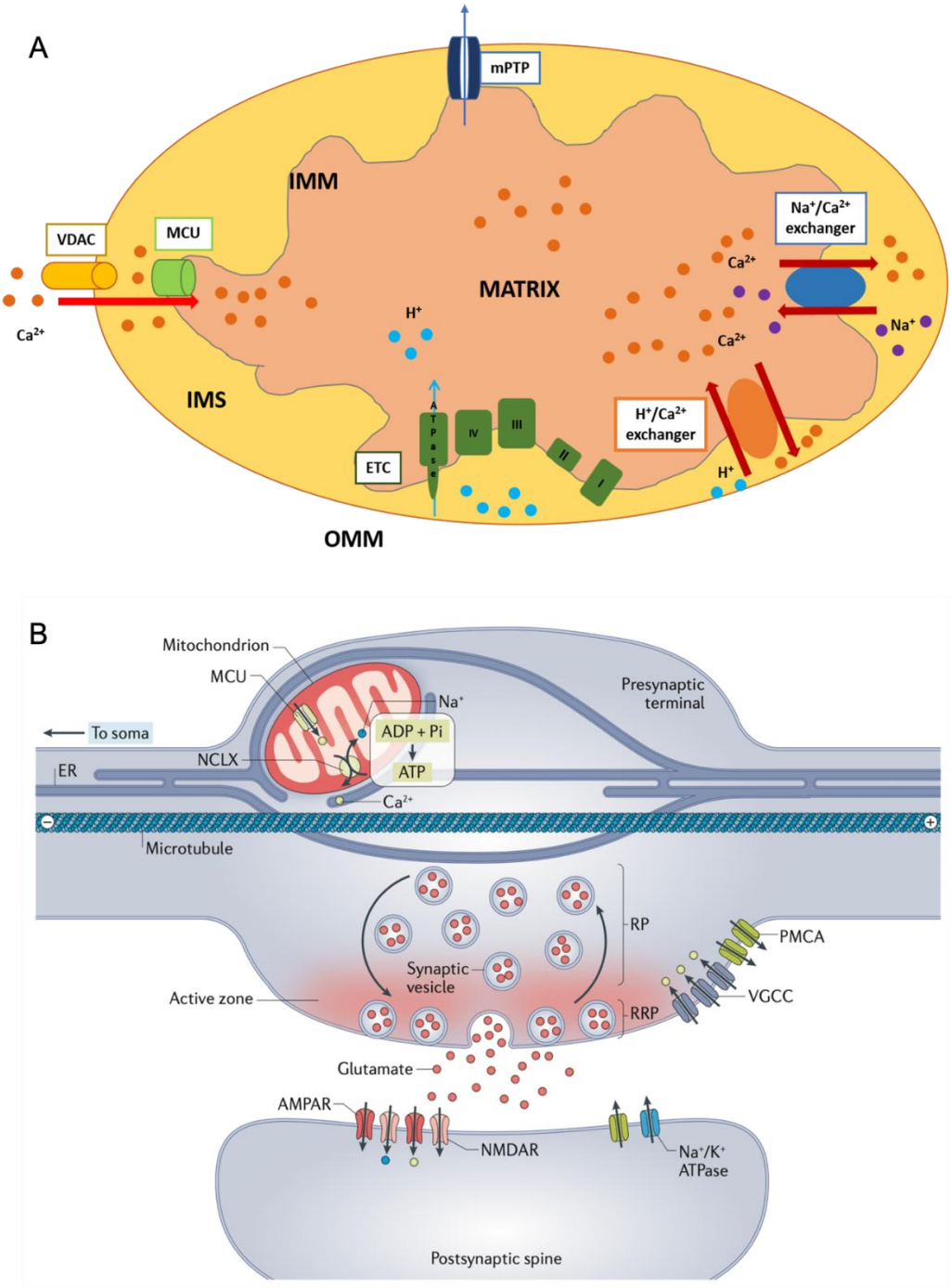

(A) Schematic of mitochondrial Ca^{2+} transport. Ca^{2+} enters via VDAC in the outer membrane and MCU in the inner membrane, while NCLX and H^+/Ca^{2+} exchangers mediate efflux. The ETC generates the electrochemical gradient for Ca^{2+} uptake. (B) Presynaptic mitochondrial Ca^{2+} buffering regulates Ca^{2+} influx via VGCC, affecting

synaptic vesicle release. Released glutamate activates postsynaptic AMPARs and NMDARs, while Na^+/K^+ ATPase and PMCA restore ionic balance. Adapted from (Devine and Kittler, 2018).

1.1.3 Mitochondrial fusion and fission

Mitochondria undergo dynamic cycles of fission and fusion to regulate their size, shape and intracellular distribution (Chen *et al*., 2020). Fission results in fragmented mitochondria by dividing a single organelle, while fusion enables the merging of two adjacent mitochondria into an elongated structure (Sebastian and Zorzano, 2018). These morphological adaptations allow mitochondria to meet cellular metabolic demands and respond to external stressors or pathological conditions. For instance, damaged mitochondria exposed to UV irradiation or oxygen deprivation can be selectively removed through fission-mediated processes. Conversely, fusion permits healthy mitochondria to compensate for impaired ones by facilitating component exchange and functional complementation (Chen *et al*., 2020).

In neurons, mitochondrial distribution is crucial for cellular function. Disruption in fusion can result in the clustering of small, fragmented mitochondria within the soma and proximal axons, impairing mitochondrial transport and contributing to neurodegenerative diseases (Baloh *et al*., 2007). In hippocampal cells, excessive mitochondrial fission has been shown to increase dendritic mitochondrial populations and dendritic spine densities, leading to altered synaptic function (Li *et al*., 2004). Therefore, a well-regulated balance between fusion and fission is essential for maintaining mitochondrial distribution and neuronal function (Chen *et al*., 2020).

Mitochondrial fusion is mediated by dynamin-family GTPases, primarily mitofusin-1 and -2 (MFN1 and MFN2) on the OMM and optic atrophy 1 (OPA1) on the inner mitochondrial membrane (IMM). MFN1 and MFN2 facilitate the tethering and fusion of adjacent mitochondria by interacting through their catalytic N-terminal GTP-binding domains, while OPA1, anchored to the IMM, is responsible for mediating inner membrane fusion (Wai and Langer, 2016; Delettre *et al*., 2000).

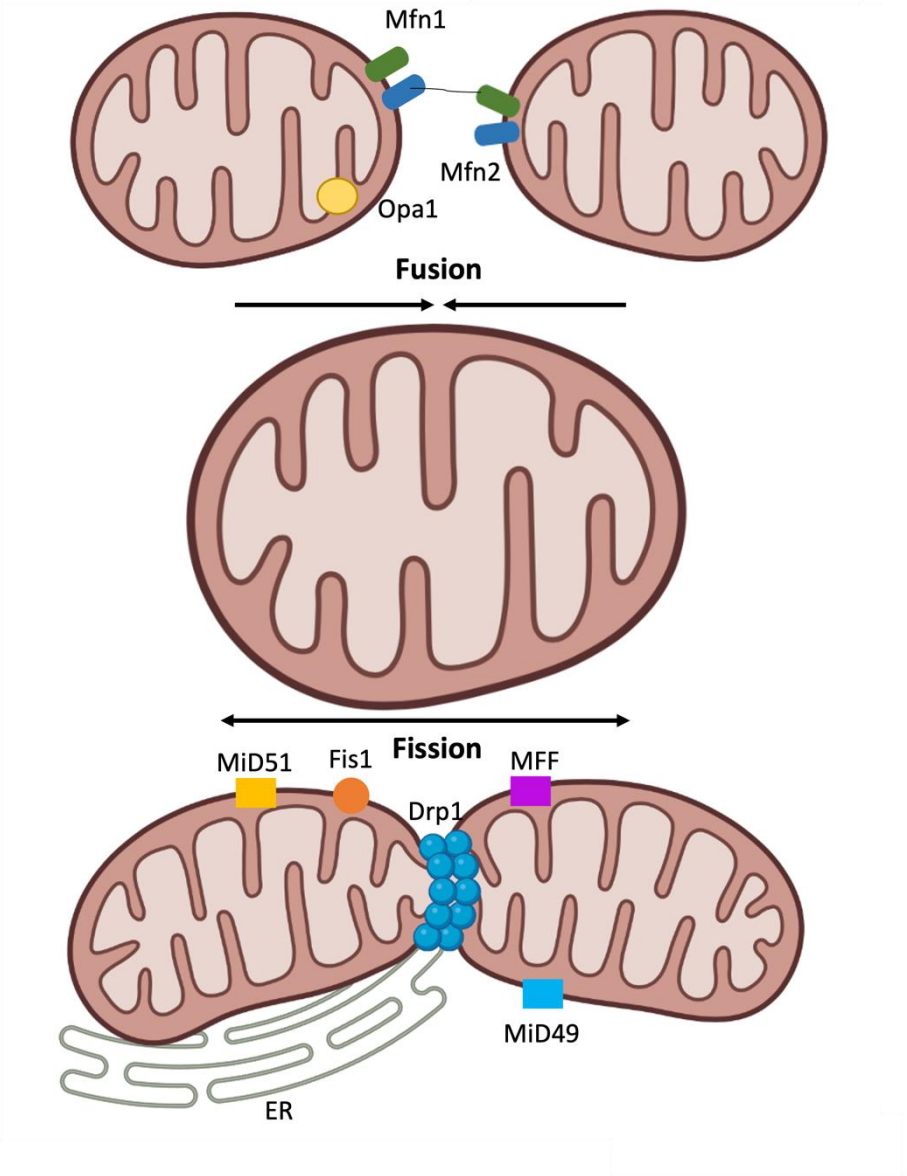

Figure 3. Mitochondrial fusion and fission in mammalian cells.

Mitochondrial fusion is regulated by MFN1 and 2 on the OMM which draw two mitochondria together. Fission occurs as the ER is recruited to the site where constriction takes place. Drp1 is then recruited to the surface of mitochondria by multiple OMM-bound proteins such as Fis1, Mff, MiD49 and 51, inducing splitting of the OMM. Figure adapted from Liu et al., (2020), generated in BioRender.

1.2 Mitochondrial Movements in Neurons

Mitochondria are highly dynamic organelles that undergo continuous transport and redistribution within neurons. They localize to subcellular regions with high metabolic demands, such as growth cones, pre- and post-synaptic terminals, and nodes of Ranvier, and disperse when growth activity ceases (Morris and Hollenbeck, 1993). The asymmetric distribution of mitochondria is crucial for maintaining neuronal energy homeostasis, and impaired mitochondrial motility is linked to neurodegenerative disorders, including Amyotrophic Lateral Sclerosis (ALS) (De Vos *et al*., 2007), Alzheimer's disease (AD) (Pigino *et al*., 2003; Edda and Eva-Maria, 2007; Yanfang *et al*., 2006) and Parkinson's disease (PD) (Wang *et al*., 2011).

Mitochondria exhibit bidirectional movement along neuronal processes, undergoing anterograde transport toward synaptic regions and retrograde transport back to the soma for recycling (Goldstein et al., 2008; Smith and Gallo, 2018). These movements vary in direction, speed, and duration, with mitochondria alternating between continuous motion and transient pausing (Barnhart, 2016; Ligon and Steward, 2000; Sheng, 2014).

Mitochondrial transport is primarily mediated by microtubule-based motor proteins that utilize ATP hydrolysis (Sheng and Cai, 2014). Axonal microtubules exhibit uniform polarity with plus-ends oriented distally, whereas dendritic microtubules have mixed polarity (Sheng and Cai, 2014; Mandal and Drerup, 2019). Long-range transport is facilitated by kinesin motor proteins for anterograde movement and cytoplasmic dynein for retrograde transport (Pilling *et al*., 2006). Additionally, mitochondria can also move along actin filaments via myosin motors, although this transport is transient and localised (Morris and Hollenbeck, 1995; Hollenbeck and Saxton, 2005). Actin-based mitochondrial movement is particularly important in dendritic spines, growth cones, and synaptic boutons where the actin cytoskeleton is highly enriched (Lovas and Wang, 2013). Actin-based transport is significantly slower (~0.02–0.04 µm/s) compared to microtubule-based transport (~0.1–0.7 µm/s) (Ligon and Steward 2000; Pilling *et al*., 2006).

1.2.1 Anterograde Mitochondrial Motor Proteins, KIFs

KIFs The kinesin superfamily consists of 45 genes across 14 families involved in intracellular transport, with kinesin-1 (KIF5) primarily responsible for mitochondrial transport (Hurd and Saxton, 1996; Lovas and Wang, 2013; Tanaka *et al.*, 1998). KIF5 comprises two identical kinesin heavy chains (KHCs) and kinesin light chains (KLCs). The heavy chains contain an N-terminal motor domain that binds microtubules and hydrolyses ATP, while the light chains interact with mitochondrial adaptor proteins (Tanaka *et al.*, 1998). Among the KIF5 isoforms, KIF5A and KIF5C are neuron-specific, whereas KIF5B is ubiquitously expressed (Tanaka *et al.*, 1998; Kanai *et al.*, 2000).

KIF5B -/- mice exhibited embryonic lethality. To investigate mitochondrial distribution, primary cultures were derived from extra-embryonic yolk sac cells of KIF5B knockout embryos. These cells displayed abnormally clustered mitochondria in the perinuclear region, supporting the essential role of KIF5B in anterograde mitochondrial transport (Tanaka *et al*., 1998). In *Drosophila*, KIF5 mutations reduce both anterograde and retrograde mitochondrial transport in larval motor axons (Pilling *et al*., 2006).

1.2.2 Mitochondrial Motor Adaptors

Kinesins/KIFs are commonly attached to their targets via adaptor proteins, with Miro and Milton playing key roles in mitochondrial transport. The Milton/Miro complex binds to KIFs, allowing mitochondria to associate with microtubules and facilitating their movement within neurons (Fig 4) (Glater *et al*., 2006; van Spronsen *et al*., 2013).

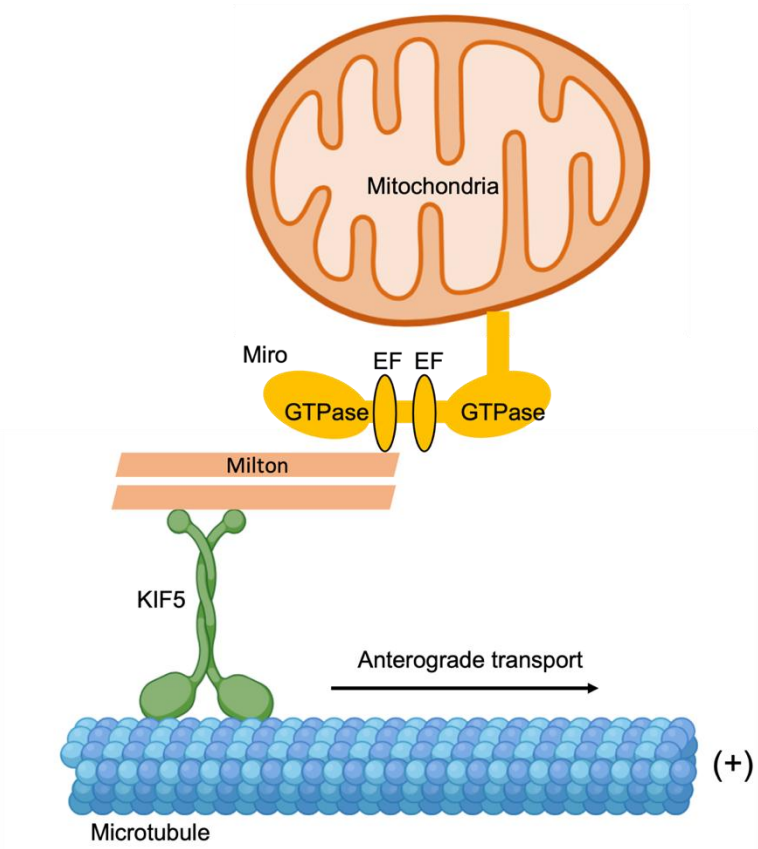

Figure 4. The Miro-Milton-kinesin complex.

Miro contains two GTPase domains and two Ca^{2+} binding EF hand motifs. The C-terminal transmembrane domain of Miro anchors it in the OMM. Milton interacts with both Miro and KIF5, forming the Miro-Milton-kinesin complex, which enables anterograde mitochondrial transport.

Miro proteins are OMM-anchored Rho GTPases that regulate mitochondrial transport and positioning within neurons. Each Miro isoform (Miro1 and Miro2) contains two GTPase domains, two Ca^{2+}-binding EF-hand motifs, and a transmembrane domain anchoring them to the OMM. Miro interacts with TRAK1 and TRAK – the mammalian homologues of Drosophila Milton – to form a transport complex that links mitochondria to kinesin and dynein motor proteins (Glater *et al.*, 2006; van Spronsen *et al.*, 2013).

Beyond its transport function, Miro plays a key role in regulating mitochondria – ER contact sites, thereby influencing mitochondrial Ca^{2+} uptake,

cristae organization, and cellular energy distribution (Modi *et al.*, 2019). Recent studies suggest that Miro not only serves as a motor adaptor but also modulates TRAK function and mitochondrial arrest in response to Ca^{2+} signalling (Devine and Kittler, 2018). Additionally, Miro is involved in regulating mitophagy by mediating PINK1/Parkin-dependent mitochondrial quality control, ensuring the removal of damaged mitochondria (Nemani *et al.*, 2018). Disruptions in Miro function impair both kinesin- and dynein-mediated transport, reduce mitochondrial localisation to synapses, and disrupt ER-mitochondrial interactions, potentially contributing to neurodegenerative pathologies (Guo *et al.*, 2005; Russo *et al.*, 2009).

Milton was discovered through genetic studies in *Drosophila* aimed at identifying mutants that disrupt photoreceptor synaptic transmission (Stowers *et al.*, 2002). It's functions by recruiting kinesin heavy chain (KHC) to mitochondria, and its loss results in a lack of mitochondria in synaptic terminals and axons despite their presence in cell bodies (Stowers *et al.*, 2002; Glater *et al.*, 2006).

TRAK1 and TRAK2 share approximately 30% sequence identity with Milton and are also required for the movement of mitochondria in axons and dendrites through different transport machineries. They interact with KHC/KIF5; TRAK1 binds to both KIF and dynein and is mostly present in axons, whereas TRAK2 preferentially interacts with dynein and is more abundant in dendrites (van Spronsen *et al.*, 2013). Knockout of TRAK1, but not TRAK2, in cultured neurons impaired mitochondrial motility, which could be rescued when either TRAK1 or TRAK2 was expressed (Brickley and Stephenson, 2011). This demonstrates the pivotal role of TRAK as a KHC adaptor in mediating mitochondrial trafficking. In addition, TRAK1 and TRAK2 are required for normal axonal outgrowth and dendritic development (van Spronsen *et al.*, 2013).

Studies with rat hippocampal neuronal cultures show that Miro1 acts as a major mitochondrial acceptor site for TRAK2 and forms a complex that plays a key role in the regulation of mammalian mitochondrial transport (MacAskill *et al.*, 2009a). Increased expression of Miro increased TRAK2 recruitment to mitochondria and promoted anterograde mitochondrial movement, whereas deletion of the

kinesin-binding domain in TRAK2 and uncoupling of the complex with Miro1 dramatically reduced the transport of mitochondria into distal ends of neuronal processes (MacAskill *et al.*, 2009a).

Recent evidence suggests that actin-dependent mitochondrial movement also involves a regulatory role of Miro via its activity in recruiting mitochondrial myosin 19 (Myo19) to the OMM (Lopez-Domenech *et al.*, 2018; Oeding *et al.*, 2018). This highlights the multifaceted role of Miro in coordinating mitochondrial transport across different cytoskeletal networks.

1.2.3 Mitochondrial Docking Mediated by Microtubules

Efficient control of the mitochondrial docking system is necessary at particular sites of axons, to maintain the cellular processes and synaptic signalling that are required for appropriate neuronal development and synaptic function. Once mitochondria are transported along developing axons, mitochondria can be immobilised on microtubules, such stalling is mediated by the mitochondrial anchoring protein syntaphilin. Syntaphilin is neuron-specific and functions to immobilise axonal mitochondria by interacting with microtubules (Kang *et al*., 2008), and it also links KHC directly to the OMM via its C-terminal tail (Cai *et al*., 2005). Syntaphilin-mediated immobilisation of mitochondria was found to reduce synaptic plasticity (Kang *et al*., 2008) and inhibit axon regeneration after injury by preventing mitochondria travelling towards the distal axon (Zhou *et al*., 2016). Deletion of the syntaphilin gene in mice caused a substantial increase of motile axonal mitochondria and a decrease in the overall density of mitochondria (Kang *et al*., 2008). Conversely, overexpression of syntaphilin abolished mitochondrial movement (Chen *et al*., 2009).

1.2.4 Retrograde Movements of Mitochondria - Dynein Motors

Dynein is the primary motor protein responsible for retrograde mitochondrial transport toward the cell body within axonal processes. Dynein consists of two heavy motor chains that directly interact with microtubules, along with multiple

intermediate chains, light-intermediate chains, and light chains which contribute to cargo attachment and regulatory functions (Lovas and Wang, 2013).

Dynein interacts with dynactin, a multiprotein complex composed of 11 subunits that enhances dynein's binding to microtubules and facilitates its interaction with mitochondria (King and Schroer, 2000). Dynactin acts as a crucial cofactor for dynein function, allowing the retrograde transport of mitochondria along microtubules.

The Miro-TRAK complex not only facilitates kinesin-driven anterograde transport but also participates in dynein-mediated retrograde movement (Russo *et al*., 2009). Miro thus serves as a bidirectional regulator that links mitochondria to both kinesin and dynein motors, ensuring proper intracellular distribution and trafficking to distal synaptic regions (Russo *et al*., 2009).

1.2.5 The Role of Calcium in the Regulation of the KIF-Miro-Milton Complex

Cytosolic calcium signals play a crucial role in regulating mitochondrial motility, particularly in active synapses (MacAskill *et al.*, 2009b; Wang and Schwarz, 2009). In both neuronal and non-neuronal cells, elevated intracellular Ca^{2+} concentration halts both anterograde and retrograde mitochondrial movement, whereas resting levels of Ca^{2+} permit motility (Fig. 5B). The regulation of mitochondrial motility by Ca^{2+} is essential for determining the localisation of mitochondria to regions with high metabolic demand, such as synaptic terminals where extensive ion fluxes occur.

Several studies indicate that local increases in Ca^{2+} concentrations at synaptic regions halt mitochondrial motility (MacAskill *et al.*, 2009b; Saotome *et al.*, 2008; Wang and Schwarz, 2009). Miro-mediated mitochondrial arrest is triggered by these local Ca^{2+} signals, acting through Ca^{2+} binding to the EF-hand motifs on Miro. This binding inactivates the Miro-TRAK-Kinesin complex, induces a conformational change in Miro, and leads to cessation of mitochondrial transport. The dynein transport machinery does not compensate when the KIF5 transport system is

disrupted, suggesting that the Miro-Ca^{2+} pathway primarily functions through an anchoring mechanism rather than through a direct shift to retrograde transport.

Evidence suggests that the activation of the Miro-Ca^{2+} pathway, in the absence of syntaphilin, does not halt axonal mitochondrial motility but still arrests dendritic mitochondria (Chen and Sheng, 2013). This indicates that Ca^{2+}-dependent mitochondrial stalling in neurons is jointly mediated by Miro and syntaphilin, and that their interplay is crucial for the compartment-specific localisation of mitochondria in axons versus dendrites.

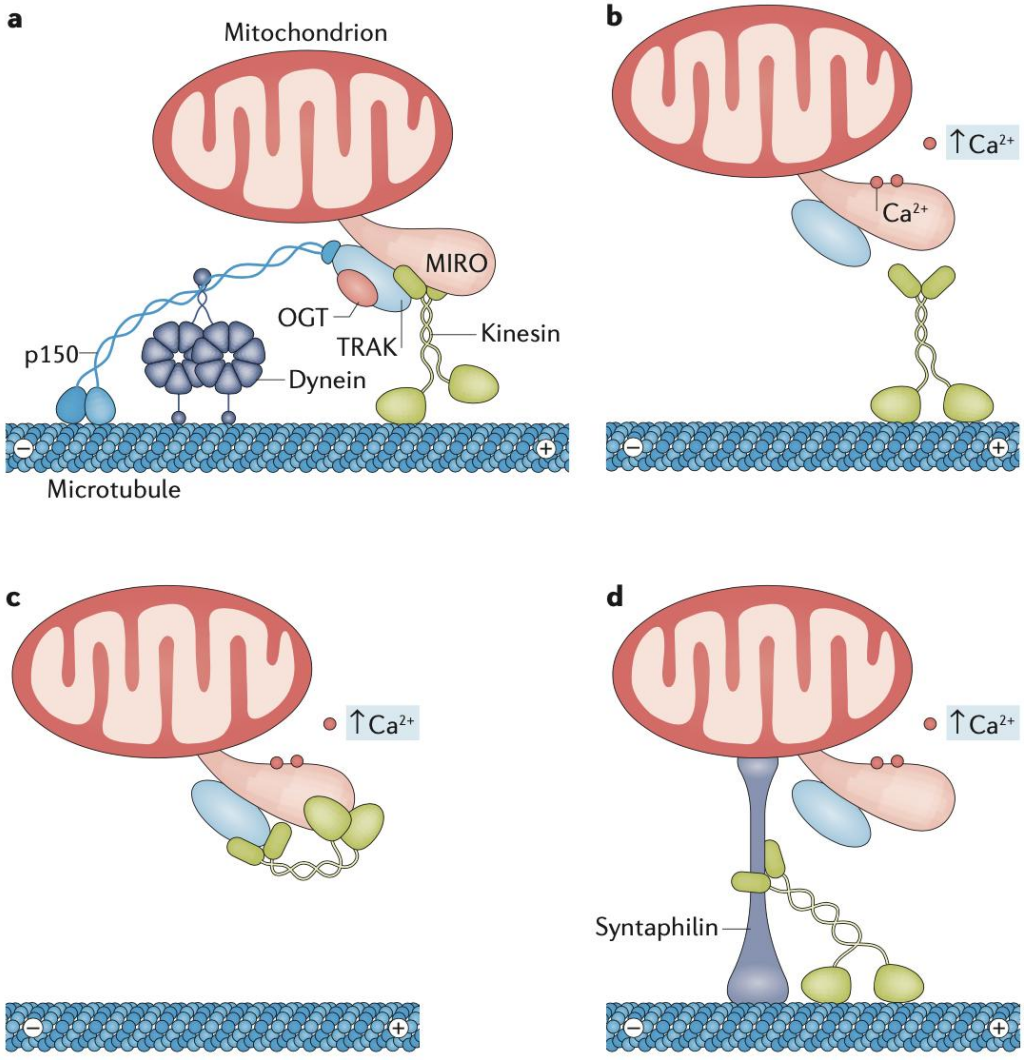

Figure 5. Regulation of mitochondrial transport by Miro and Ca^{2+} signalling.
(A) Microtubule-driven mitochondrial transport is mediated by Miro, which directly interacts with KIF5 or directly links to dynein via TRAK and p150. (B) Elevated Ca^{2+} concentrations disrupt the interaction between Miro and KIF5, uncoupling

mitochondria from anterograde transport. (C) Alternatively, Miro, TRAK and KIF5 may remain together but detach as from microtubules in response to increased [Ca^{2+}]. (D) A third possibility is that Ca^{2+} binding to Miro causes its disassociation from KIF5, which then binds to syntaphilin, anchoring mitochondria to microtubule (Devine and Kittler, 2018).

1.3 Dysfunction of Mitochondria Leading to Neurodegenerative Diseases

Neuronal cell death and neurodegenerative diseases can arise, either wholly or in part, from various mitochondrial dysfunctions, including impaired transport, quality control, turnover, and calcium signalling (Chaturvedi and Flint Beal, 2013; Yin *et al.*, 2014). Neurons have a limited capacity to upregulate glycolysis or counteract oxidative damage, making them highly vulnerable to mitochondrial failure. Disruptions in energy supply lead to increased reactive oxygen species (ROS) production, contributing to neuronal degeneration in multiple brain disorders (Fernandez-Fernandez *et al.*, 2012).

1.3.1 Calcium homeostasis dysfunction

Aging and pathological states impair neuronal Ca^{2+} regulation, leading to dysregulated Ca^{2+} flux and accumulation. Oxidative stress, exacerbated by free radicals generated during OXPHOS, is a major factor contributing to Ca^{2+} dishonesties and neuronal loss. Oxidative damage affects ion-motive ATPases, including Na^+/K^+-ATPases and Ca^{2+}-ATPases, as well as glutamate and glucose transporters, leading to enhanced membrane depolarisation, increased Ca^{2+} influx via NMDARs and VGCC, and ultimately Ca^{2+} overload (Mattson, 1998). Ca^{2+} overload is particularly relevant in stroke pathology, as antagonists of glutamate receptors and VGCC provide neuroprotection (Weiss *et al.*, 1990).

Dysfunctional mitochondrial Ca^{2+} regulation can result from excessive Ca^{2+} release from the ER, increased Ca^{2+} influx from extracellular space, impaired extrusion via the mitochondrial NCLX, and reduced buffering capacity, all of which promote Ca^{2+} overload and neuronal death (Calì *et al.*, 2012). Genetic and

pharmacological modulation of mitochondrial Ca^{2+} sequestration has been shown to prevent excitotoxicity-induced neuronal death (Duchen, 2000; Keller *et al.*, 1998). Several mitochondrial and ER-associated proteins, including Mn-superoxide dismutase (Mn-SOD), Bcl-2, and Herp (homocysteine-inducible ER stress protein), provide neuroprotection against Ca^{2+} overload-induced cell death (Guo *et al.*, 1997; Keller *et al.*, 1998; Chan *et al.*, 2004).

Pro-apoptotic proteins (Bax and Bad) and anti-apoptotic proteins (Bcl-2 and Bcl-xL) regulate mitochondrial permeability transition and apoptosis (Beal, 1998; Springer *et al.*, 2000; Camandola *et al.*, 2005). Mitochondrial depolarisation, Ca^{2+} overload, oxidative stress, ATP depletion, and apoptotic protein release contribute to multiple neurodegenerative conditions. Age-related changes in Ca^{2+} signalling include increased Ca^{2+} release via inositol 1,4,5-trisphosphate receptors (InsP3R) and RyR, enhanced Ca^{2+} influx through L-type VGCC, and alterations in synaptic plasticity, such as increased susceptibility to long-term depression and reduced long-term potentiation (Foster, 2007; Zhou *et al.*, 2004; Shinoda *et al.*, 2005). These changes underlie age-related cognitive decline and memory impairment.

1.3.2 Alzheimer's disease and Calcium-derived mitochondrial dysfunction

Alzheimer's disease (AD) is the most common neurodegenerative disorder, affecting 10–20% of individuals over 65 years old (Talmelli *et al.*, 2010). AD is characterized by progressive cognitive decline, memory loss, and behavioural impairments, significantly affecting daily life (Goedert and Spillanian, 2006). The two pathological hallmarks of AD are extracellular amyloid-β (Aβ) plaques and intracellular neurofibrillary tangles composed of hyperphosphorylated tau proteins (Selkoe, 2003; Dickson, 1997). Aβ peptides result from proteolytic cleavage of amyloid precursor protein (APP) and aggregate into plaques, triggering inflammation, synaptic loss, and neurodegeneration, especially in the cortex and hippocampus—regions highly vulnerable in early AD (Hardy and Selkoe, 2002; Henke *et al.*, 1999).

Ca^{2+} dysregulation has long been implicated in AD pathogenesis. As early as 1989, Khatchaturian proposed that aging neurons exhibit impaired ATP production

and Ca^{2+} handling, leading to increased free Ca^{2+}, mitochondrial Ca^{2+} overload, oxidative stress, and apoptosis or necrosis (Khachaturian, 1989). This dysregulation is observed in both sporadic, late-onset AD (Tolar *et al.*, 1999; Boada *et al.*, 2010) and familial, early-onset AD (Zatti *et al.*, 2004).

Mitochondrial abnormalities in AD include altered morphology and distribution (Hirai *et al.*, 2001). Aβ oligomers enhance ER-mitochondrial Ca^{2+} transfer, promoting mitochondrial Ca^{2+} overload and dysfunction (Ferreiro *et al.*, 2008; Sanz-Blasco *et al.*, 2008). Aβ accumulation also impairs mitochondrial transport and AMPAR trafficking, disrupting synaptic function (Rui *et al.*, 2006; Rui, 2010). Additionally, Aβ interaction with glutamate receptors increases intracellular Ca^{2+}, sensitizing neurons to excitotoxicity and apoptosis (Mark *et al.*, 1995; Keller *et al.*, 1998; Mattson *et al.*, 1997). Elevated Ca^{2+} levels and activation of Ca^{2+}-dependent proteases, such as calpain, are linked to neurofibrillary tangles and neurodegeneration in AD (Murray *et al.*, 1992; Nixon, 2003).

1.3.3 Parkinson's disease and Calcium-derived mitochondrial dysfunction

Parkinson's disease (PD) is the second most common progressive neurodegenerative disorder, characterised by resting tremor, bradykinesia, and rigidity due to dopaminergic neuron loss in the substantia nigra (Johri and Beal, 2012; Calì *et al.*, 2012). Mitochondrial dysfunction and oxidative stress are key contributors to PD. In 1983, drug users exposed to 1-methyl-4-phenyl-1,2,3,6-tetrahydropyridine (MPTP) developed PD-like symptoms (Langston, 1983). The active metabolite of MPTP inhibits mitochondrial complex I, leading to dopaminergic neuron toxicity (Fig 6A). Complex I inhibitors such as rotenone, paraquat, and 6-hydroxydopamine (6-OHDA) also induce mitochondrial dysfunction, oxidative stress, and neuronal degeneration in PD models (Cicchetti *et al.*, 2005).

Several PD-associated genes, including SNCA (α-synuclein), LRRK2, Parkin, PINK1, VPS35, and CHCHD2, are involved in mitochondrial metabolic dysfunction, impaired quality control mechanisms, and disrupted Ca^{2+} homeostasis (DiMauro

and Schon, 2008; Park *et al.*, 2018) (Fig 6B). Mutant SNCA affects Ca^{2+} influx, either through direct pore formation (Lashuel *et al.*, 2002) or by modulating plasma membrane Ca^{2+} channels (Furukawa *et al.*, 2006). Its accumulation at mitochondria leads to mitochondrial Ca^{2+}overload, nitric oxide production, oxidative damage, and cytochrome c release (Parihar *et al.*, 2009).

PINK1 is a mitochondrial kinase that initiates the removal of depolarised mitochondria through mitophagy, thereby preventing apoptosis. Loss-of-function mutations in PINK1 impair this quality control mechanism and exacerbate SNCA-induced mitochondrial Ca^{2+} dysfunction (Marongiu *et al.*, 2009). LRRK2 mutations activate apoptotic pathways by increasing cytochrome c release and caspase-3 activation (Iaccarino *et al.*, 2007). DJ-1, an antioxidant protein, regulates cytosolic Ca^{2+} levels and mitochondrial ROS production, protecting against oxidative stress (Taira *et al.*, 2004; Guzman *et al.*, 2010).

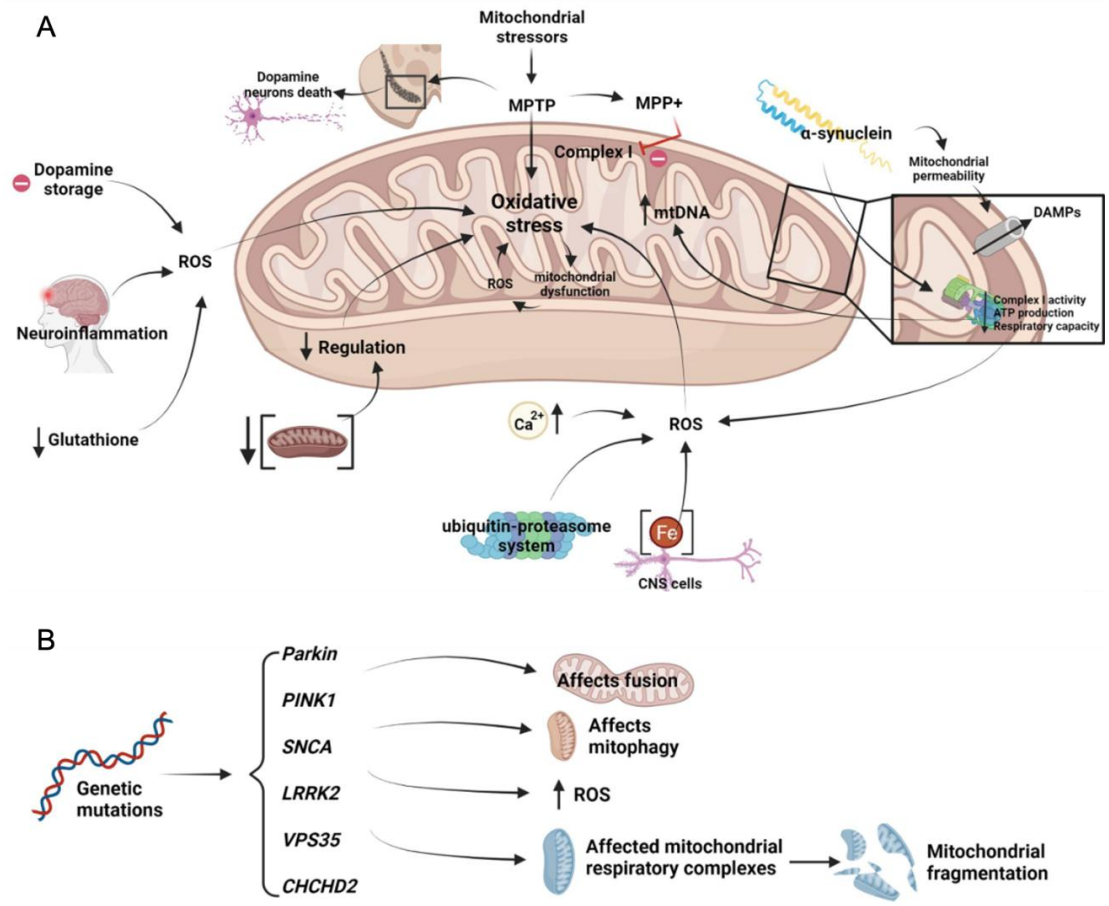

Figure 6.Mitochondrial involvement in Parkinson's disease.

(A) Mitochondrial dysfunction plays a central role in the pathogenesis of PD, primarily through increased oxidative stress. Reduced mitochondrial content and impaired function lead to elevated ROS production, which, in turn, triggers a feedback loop involving nuclear and mitochondrial DNA damage, neuroinflammation, and further mitochondrial dysfunction. Additional factors such as dysregulated calcium homeostasis, dysfunction of the ubiquitin-proteasome system, neuroinflammation, impaired dopamine storage, and decreased glutathione levels contribute to neuronal damage. SNCA species can interact with OMM proteins, promoting MPTP opening and damage-associated molecular pattern (DAMP) release. SNCA also affects the ETC, reducing complex I activity, ATP production, and respiratory capacity while increasing ROS levels and mitochondrial DNA damage. (B) Genetic mutations in key PD-associated genes, including Parkin, PINK1, SNCA, LRRK2, VPS35, and CHCHD2, contribute to mitochondrial dysfunction.

These mutations impair mitochondrial fusion and mitophagy, increase ROS production, and promote mitochondrial fragmentation by disrupting mitochondrial respiratory complexes. (Adapted from Zambrano et al., 2022).

1.4 Quantitative Methods of Mitochondrial Motility-Based Analysis and Limitations and *In Vitro* Neural Models

There are challenges in tracking and quantifying mitochondria as it is difficult to identify mitochondria from the image in every frame and to analyse and generate connections between each frame. To resolve these challenges, fluorescence labelling approach is used in imaging to distinguish mitochondria such as MitoTracker dye or transfection of fluorescence-fused mitochondrial targeting proteins, such as red fluorescent protein (Mito-RFP) or green fluorescent protein (Mito-GFP) (Chazotte, 2009; Course *et al*., 2017). Moreover, to track associations between frames, various software tools and strategies have been employed (Kandel *et al*., 2015) (Table 1).

Table 1. Quantitative methods of mitochondrial motility-based analysis

Imaging Methods	Working Principle	Softwares	Applications	Pros	Cons	References
Overall measurement of motility of mitochondria	• Subtraction of every frame from the previous frame • Pixels left that only change position on the resulting frame	• Image J (Macro)	-	• Fast	• Highly variable • Dependent on factors not related to mitochondrial motion • Inaccurate detection at low signal-to-noise	Rintoul *et al*., 2003
Kymograph (semi-automatic)	• Manual tracking moving mitochondria on live images with manual tracing trajectories on kymographs • Automatic calculation of extracted data from kymographs	• ImageJ (Macro)	• KymoAnalyzer • Kymolyzer	• Precise • less prone to false-positive trajectories	Tracing kymographs are: • Tedious • Time consuming • Prone to user bias	Jakobs *et al*., 2019 Neumann *et al*., 2017 Basu *et al*., 2020
Kymograph (automatic)	• Automatic drawing on the kymographs and calculation of data	• ImageJ • Matlab	• KymoButler • KymographClear& KymographDirect	• Less susceptible to bias • Time efficient • (Mathis, 2018)	• Often broken segments at long-range bidirectional movements • Faint tracks not detectable • Incorrect assigned crossed over tracks	Jakobs *et al*., 2019 Mangeol *et al*., 2016 Basu *et al*., 2020 Neumann *et al*., 2017
Commercial software	• Conversion of images to a surface and mitochondria is tracked using 3D tracking option. • Subtraction of the 1st time point from the next time point until the end • Calculation of average speed, acceleration etc.	-	• Imaris • Volocity • MetaMorph	• Provides solution to all standard image analysis strategies • Mostly compatible with user system's configuration • Supports 3D projections • Large data sets • Less labour intensive	• Often under- or over-estimates some motion parameters • Cannot extend any of software packages • Cannot make custom hardware changes to imaging system	Eliceiri *et al*., 2012 Bros *et al*., 2015

1.4.1 Total Mitochondrial Motility Analysis

A general way to evaluate the overall movement of mitochondria is to calculate the percentage of mitochondrial area that mitochondria travelled between two sequential frames (De Vos and Sheetz, 2007). This is achieved by subtracting pixel intensity values of consecutive frames, so that only pixels that correspond to mitochondria with changed position would appear on the resulting frame (Fig 7A-D). Mitochondria that stayed stationary are removed, whereas moving mitochondria remain visible. A macro was created using the software ImageJ (FIJI, NIH) (Schindelin *et al*., 2012) for this analysis. An in-house generated ImageJ macro was used initially in this study to automatically measure global measurement of mitochondrial motility. The analysis was fast and less labour intensive, however, sometimes it caused anomalies when flashes or flickering of mitochondrial fluorophores occured while imaging and happened to produce higher percentage of total mitochondrial movements compared to manual tracking. Rintoul *et al* also performed a similar approach to estimate mitochondrial movement in primary cortical neurons (between DIV 12 – 19) by measuring changes in fluorescence intensity of individual pixels (Rintoul *et al*., 2003). A 255 x 255 pixel subregion that shows neuronal processes was selected from the full-frame image field and individual pixel fluorescence values were subtracted from successive images to visualise motion (Fig 7D).

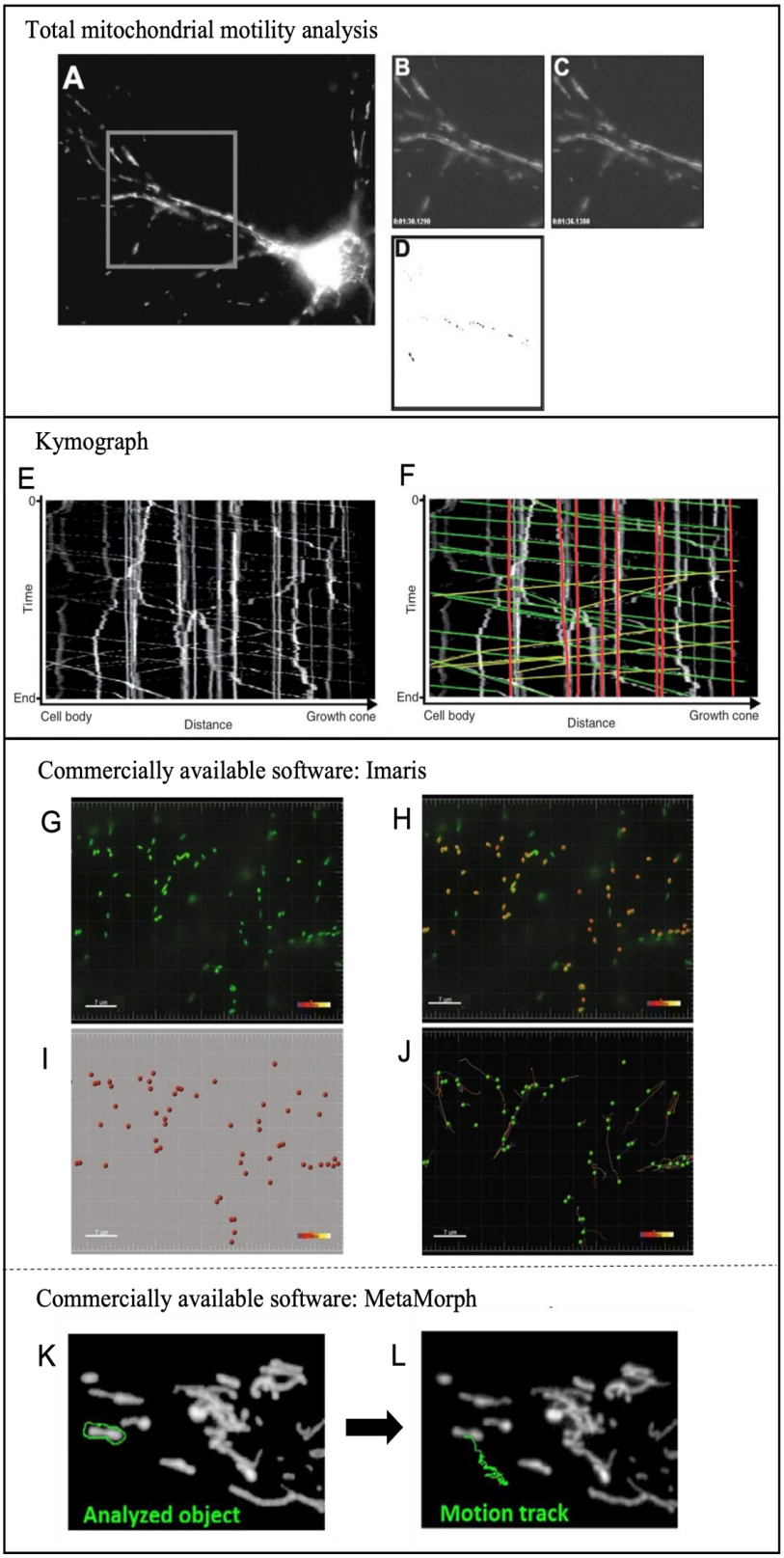

Figure 7. Representative examples of imaging analysis tools used to track mitochondrial movement.

(A-D) A time-lapse image series is collected and a 255 x 255 pixel subregion is selected in (A). Fluorescence intensity differences between successive images are subtracted in (B-C), highlighting changes in mitochondrial position. Moving mitochondria appear as dark pixels in (D) (Rintoul et al., 2003).
(E-F) A kymograph is generated from time series images of cortical neurons transfected with pDsRed1-mito. Individual mitochondrial movements are represented as diagonal lines in (E). Automated tools quantify movement trajectories (yellow: retrograde, green: anterograde, red: stationary) (De Vos and Sheetz, 2007).
(G-J) Time-lapse images of mitochondria expressing mito-GFP in (G). Mitochondria are detected using a "spot" detection tool (red dots) in (H). Non-mitochondrial structures are removed, leaving only mitochondria represented by red spots in (I). Mitochondrial movements are tracked, with colour-coded markers indicating time points (blue: 0 s, white: 30 s) (Scale bar = 7 µm) (Senanayake et al., 2015).
(K-L) Mitochondria are outlined by a green contour in (K), and their trajectories are tracked using the "Track object" plugin in MetaMorph in (L) (Drabik et al., 2020).

1.4.2 Kymograph Analysis

Another widely used method for quantifying mitochondrial motility is kymograph analysis, which extracts motion-based parameters from time-lapse images (Fig 7E-F). A kymograph is a two-dimensional representation of moving particles along a predefined path, where time is displayed along the y-axis and distance along the x-axis (Jakobs *et al*., 2019; Basu *et al*., 2020). Linear traces indicate constant-speed mitochondrial movement, with the slope representing velocity (De Vos and Sheetz, 2007; Mangeol *et al*., 2016). The direction of movement—anterograde or retrograde—can be determined based on the orientation of the slope (De Vos and Sheetz, 2007). Compared to total mitochondrial motility analysis, kymographs provide more detailed motion parameters, including velocity, directionality, and distances travelled (De Vos and Sheetz, 2007).

Several tools facilitate kymograph-based mitochondrial motion analysis, ranging from semi-automated to fully automated approaches. Semi-automated tools require manual input, such as drawing trajectories on kymographs, which increases accuracy but is labour-intensive (Zara *et al*., 2013; Neumann *et al*., 2017; Basu *et al*., 2020). Manual tracking avoids the need for contrast adjustments or thresholding filters, reducing false-positive trajectory identification (Mangeol *et al*., 2016; Neumann *et al*., 2017; Jakobs *et al*., 2019). KymoAnalyzer, a set of six ImageJ macros, allows manual tracing of tracks and particle trajectory assignment, followed by automatic motion parameter extraction. This tool has been validated for various fluorescently tagged moving cargoes in mammalian neurons (PrPC-EGFP, mito-EGFP) and mechanosensory neurons in *C. elegans* (Neumann *et al*., 2017). Another semi-automated tool, Kymolyzer, provides motion parameters such as pause/reversal rates, distances, and velocities but also requires user input to identify moving and stationary mitochondria (Basu *et al.*, 2020). However, manual kymograph tracing is time-consuming and susceptible to researcher bias in trajectory selection, leading to variability in measured parameters (Mangeol *et al*., 2016; Neumann *et al*., 2017).

To address the limitations of manual analysis, fully automated tools have been developed. Mangeol *et al* introduced KymographClear and KymographDirect, which automate kymograph generation and trajectory analysis (Mangeol *et al*., 2016). KymographClear applies Fourier filtering to distinguish forward-, backward-moving, and stationary mitochondria, while KymographDirect, developed in LabVIEW, enables trajectory extraction from low-signal-to-noise ratio (SNR) images. These tools allow accurate tracking even in dense cellular environments, with reliable performance at SNR <1.

Another AI-based tool, KymoButler, employs deep learning to automatically trace kymograph lines and extract motility data (Jakobs *et al*., 2019). Comparative analysis using synthetic and biological datasets demonstrated that KymoButler outperforms traditional manual and automated methods in speed and accuracy. It achieved a precision mean of 92% for unidirectional tracks and 78% for complex

bidirectional tracks. However, the accuracy depends on threshold settings, with lower thresholds increasing ambiguous detections and higher thresholds discarding valid tracks (recommended threshold: 0.1–0.3). Recently, Franze's group used KymoButler for live imaging of primary *Drosophila melanogaster* neurons to analyse microtubule behaviour (Jakobs *et al*., 2022).

Hybrid approaches combining manual and automated tools have also been explored. For example, Minckley *et al* used Kymolyzer for manual background noise removal and subsequently applied KymoButler for automated data extraction. This approach enabled the investigation of Zn^{2+} effects on microtubule-based cargo transport in hippocampal neurons and HeLa cells (Minckley *et al*., 2023)

1.4.3 Commercially Available Software

Several commercial software packages provide automated mitochondrial tracking (Bros *et al*., 2015), including Imaris (Bitplane) (Ekanayake *et al*., 2015), Volocity (Perkin-Elmer) (Higuchi-Sanabria *et al*., 2016; Lee *et al*., 2014; Drabik *et al*., 2020) and MetaMorph (Molecular Devices) (Drabik *et al*., 2020) (Fig 7G-J and K-L). These tools integrate standard image processing workflows such as live-cell imaging acquisition, multi-dimensional tracking, and statistical analysis (Eliceiri *et al*., 2012).

Drabik *et al* demonstrated the utility of Imaris and MetaMorph for quantifying mitochondrial motility in fibroblasts from Alzheimer's disease patients. In their study, mitochondrial dynamics were analysed in Imaris by converting time-lapse images into surface-rendered 3D reconstructions. Mitochondrial motility was quantified using an automated tracking module, which measured movement dynamics by comparing the number of disconnected components across successive frames. MetaMorph was used to quantify mitochondrial velocity by tracking individual mitochondria until they underwent fission or fusion events. Their findings showed decreased mitochondrial velocity and fusion-fission event frequency in fibroblasts from Alzheimer's patients.

Similarly, Ekanayake *et al*. used Imaris to study plant mitochondrial dynamics and quantify mitochondrial movement (Ekanayake *et al*., 2015).

Commercial software packages offer advantages such as robust compatibility with various imaging systems and standardized analytical workflows. However, automated tracking tools require frequent validation and correction, as they may overestimate mitochondrial velocity and underestimate movement track duration compared to manual tracking (Bros *et al*., 2015).

1.5 *In Vitro* Neural Models

In vitro neural models have become an important tool for investigating the cellular and molecular mechanisms underlying neurodegenerative diseases, including Alzheimer's disease, Parkinson's disease and Huntington's disease. Various cerebral models, ranging from traditional 2D cell cultures to high-throughput 3D systems have been developed, each with distinct advantages and limitations. These models provide valuable platforms for studying mitochondrial function and dysfunction.

1.5.1 Types of In Vitro Neural Models

A variety of *in vitro* models have been developed to study neurodegenerative disease pathogenesis, spanning from simple single-cell cultures to complex organotypic brain slices (Polikov *et al.*, 2008). Increased model complexity enhances physiological relevance but may compromise experimental control and reproducibility. The choice of model depends on the study's objectives and each system's inherent limitations.

1.5.2 Advantages & Disadvantages of in vitro models and Mitochondrial Analysis Applications

1.5.2.1 Cell lines

Immortalised cell lines are the simplest *in vitro* models, derived from a single cell type, which minimises contamination from other cell types. They are easy to culture, highly proliferative, and cost-effective compared to primary neurons, making them widely used for large-scale protein and mRNA extraction (Gordon *et*

al., 2013; Polikov *et al.*, 2008). However, since these lines originate from tumours or genetically modified cells, they may exhibit genomic instability and lose biological relevance over multiple passages (Zhang *et al.*, 2022).

A widely used neuronal cell line is the human neuroblastoma SH-SY5Y, which can differentiate into neuron-like cells and is particularly valuable for PD research (Xicoy *et al.*, 2017). This model has been used to study various aspects of PD, including mitochondrial dysfunction, oxidative stress, protein misfolding, and neuroinflammation. For example, Taylor-Whiteley's group demonstrated that differentiated SH-SY5Y cells developed Lewy body-like inclusions upon exposure to exogenous α-synuclein, mimicking PD pathology (Taylor-Whiteley, *et al*., 2019).

Regarding mitochondrial analysis, Simoes's group used differentiated SH-SY5Y cells to study mitochondrial trafficking, reporting a mitochondrial velocity of 0.1–0.6 μm/s (Simoes *et al*., 2021). The cells were treated with mitochondrial toxicants such as 6-OHDA and rotenone, leading to significant reductions in mitochondrial motility. Mitochondrial trajectories were quantitatively analysed using parameters such as straightness, efficiency, anisotropy, and kurtosis. This highlights the utility of SH-SY5Y cells for mitochondrial motility studies, though their lack of standardised differentiation protocols remains a limitation (Xicoy *et al.*, 2017).

1.5.2.2 Primary Cell Cultures

Primary neuronal cultures more closely replicate *in vivo* neuronal environments than cell lines, maintaining physiological characteristics of human neurons (Slanzi *et al.*, 2020). They also include supporting glial cells, such as astrocytes and microglia, which enhance neuronal function. However, primary cultures are more expensive and raise ethical concerns due to animal requirements and involve complex isolation protocols (Polikov *et al.*, 2008). Unlike cell lines, they cannot be passaged, as their phenotype changes upon prolonged culture (Zhang *et al.*, 2022).

For example, Dobbertin *et al.* used primary cortical neurons from embryonic day 17 (E17) Sprague-Dawley rats to study neurite development in response to

RPTPβ/phosphacan, a chondroitin sulfate proteoglycan upregulated after CNS injury (Dobbertin *et al.*, 2003). The hippocampus and striatum were removed before enzymatic digestion of the cortical neurons.

In mitochondrial studies, Chen *et al.* (2008) investigated the effects of dopamine on mitochondrial transport in primary rat hippocampal neurons. They found that dopamine inhibits mitochondrial motility via the D2-like dopamine receptor (D2R), while the D1-like dopamine receptor (D1R) promotes mitochondrial movement. Selective D2R agonists (e.g., bromocriptine) replicated dopamine's inhibitory effects, whereas D1R agonists (e.g., SKF38393) enhanced mitochondrial transport. The hippocampal culture provided an optimal model due to its co-expression of both receptor subtypes.

1.5.2.3. Stem Cells-Derived Neurons

Stem cell-derived neurons, particularly from human embryonic stem cells (ESCs) and induced pluripotent stem cells (iPSCs), are valuable for neuroscience research. These cells can differentiate into multiple neuronal subtypes, enabling disease modelling, drug screening, and regenerative therapies (Shi *et al.*, 2016; Slanzi *et al.*, 2020). iPSCs offer advantages such as accessibility, personalised medicine potential, and genetic manipulation via CRISPR-Cas9 (Shi *et al.*, 2016). However, differentiation and maturation require extensive optimisation and typically take 4–6 weeks, with full functional maturation taking several months (Mahmoud *et al.,* 2025).

In mitochondrial research, Mou's group used iPSCs differentiated into telencephalic glutamatergic neurons to investigate mitochondrial transport defects in hereditary spastic paraplegia (Mou *et al*., 2020). Several other studies have explored mitochondrial dysfunction in iPSC-derived neurons from PD patients carrying different mutations, examining ROS production, mitochondrial respiration, proton leakage, and intracellular mitochondrial movement (Cooper *et al.*, 2012; Little *et al.*, 2018). These studies highlight iPSC-derived neurons as powerful tools for mitochondrial analysis in disease contexts.

1.5.2.4 Brain Slices

Brain slice cultures, including organotypic cultures and 3D organoids, can offer *in vivo*-like environments for studying neural networks and mitochondrial dynamics (Polikov *et al.*, 2008). These models preserve cell-to-cell interactions, making them suitable for long-term studies of synaptic plasticity and disease mechanisms. Compared to primary cultures, brain slices can be maintained for months, reducing animal use and potentially improving experimental reproducibility (Koeneman *et al.*, 2004; Zhang *et al.*, 2022).

For instance, Lugara*'s group* used hippocampal slices to investigate the role of leucine-rich glioma-inactivated 1 (LGI1) in synaptic excitability (Lugara *et al*., 2020). They demonstrated that LGI1 downregulation increased excitability in dentate granule cells and facilitated low-frequency transmission from mossy fibres to CA3 pyramidal cells, suggesting applications for studying limbic encephalitis and temporal lobe epilepsy.

Brain slices have also been applied to mitochondrial research. Kann and Kovács used hippocampal slice preparations to study mitochondrial aspects during neuronal activity (Kann and Kovács, 2007). They demonstrated that mitochondrial ATP synthesis is tightly coupled to neuronal firing rates, providing insights into how mitochondrial dysfunction contributes to epilepsy. However, despite advances in perfusion systems and culture chambers, maintaining long-term viability in *ex vivo* brain slices remain a challenge (Zhang *et al.*, 2022).

Thus, studies of mitochondrial dynamics - including several mitochondrial responses and movements - using various *in vitro* neural models provide insights into convergence of cellular disease mechanisms and help to understand the importance of mitochondrial dysfunction in neurodegenerative diseases.

However, traditional *in vitro* models often lack the spatial organisation, cellular diversity, and mechanical cues found *in vivo*, limiting their ability to accurately replicate physiological neuronal environments. Additionally, *in vivo*-like models such as brain organoids can be highly variable, embryonic in nature and

limited in ability to model neurodegenerative diseases, These limitations have driven the emergence of microengineering approaches—such as micropatterning, microfluidics, and dielectric guidance—which aim to enhance the physiological relevance of *in vitro* systems for studying subcellular dynamics like mitochondrial motility.

1.6 Microengineering Approaches for *In Vitro* Models

Since the 1990s, microengineering techniques have rapidly advanced, enabling precise control over cellular microenvironments for biomedical applications. These approaches help mimic the complex architectures and properties of *in vivo* tissues and cells. Various 3D microengineering methods, including microfluidics, organ-on-a-chip models, and micropatterned surfaces, have significantly impacted studies in neuroscience, oncology, dermatology, and tissue engineering (Martinez-Rivas *et al*., 2017). These techniques allow the fabrication of cell-sized features on biocompatible substrates, facilitating a wide range of applications in *in vitro* cell models and improving our understanding of cellular behaviour.

A key focus in neuronal research is the ability to pattern biomolecular cues to control neuronal adhesion, morphology, and connectivity. This has led to the development of advanced micropatterning approaches, including soft lithography-based techniques, which offer high precision, reproducibility, and compatibility with a range of biomaterials.

1.6.1 Soft Lithography for Micropatterning

To enable micropatterning in biological applications, soft lithography has emerged as a powerful and versatile technique. Originally developed to overcome the limitations of traditional microfabrication methods (Xia and Whitesides, 1998), soft lithography involves replicating micro- or nano-scale features from a master template onto elastomeric materials such as poly(dimethylsiloxane) (PDMS) (Qin *et al*., 2010). The process involves casting uncured PDMS over a master, allowing it to

cure, and then peeling off the polymerized elastomer to obtain a negative replica of the original pattern.

Unlike conventional photolithographic methods, which require expensive cleanroom facilities and rigid substrates, soft lithography is cost-effective, rapid, and applicable to both planar and flexible surfaces (McDonald and Whitesides, 2002). This makes it particularly suitable for cell culture applications, where controlling cellular microenvironments is critical.

Among the many soft lithography techniques, microcontact printing (μCP) is one of the most widely used for micropatterning biomolecules. μCP utilizes PDMS stamps coated with biomolecules (such as extracellular matrix proteins) to selectively pattern substrates, guiding cell adhesion and axonal outgrowth (Offenhäusser *et al*., 2007). These engineered substrates allow neurons to grow in predefined patterns, enabling precise control over network formation and facilitating studies on neuronal development, axonal transport, and synaptic connectivity.

1.6.2 PDMS

PDMS elastomer is the most widely used material as an elastomeric stamp or mold for soft lithography techniques. It provides multiple attractive properties and is, particularly suitable for biomedical applications (Qin *et al*., 2010, McDonald and Whitesides, 2002). PDMS is non-toxic to mammalian cells, which can be directly cultured on PDMS. It also shows good permeability to oxygen and carbon dioxide, but low permeability to water (Lee *et al*., 2004). PDMS is maintained in liquid form at room temperature and can be converted into solid when heated at high temperatures. It is available in two different components which are liquid prepolymer, also called as base and liquid curing agent. Mixing appropriate ratio (w/w) of these two components with heat produce cross-linked elastic solid PDMS which stiffness can be controlled by different ratio. As the proportion of curing agent increases, the cross-linked structure of the material also increases which decreases PDMS elasticity and makes it more rigid. Applying higher temperature

also enhances the cross-linking reaction (Liu *et al*., 2009). The moderately stiff elastomer of PDMS can be relatively easily deformative, which allows it to conform to surfaces and release easily from a mold without damage to the patterns. The proportion of 10:1 mixing ratio of 10 Sylgard 184 silicone elastomer base and 1 Sylgard 184 silicone elastomer curing agent of PDMS is the most widely used recently (Dai and Xie, 2017) which provides moderately stiff status of PDMS.

PDMS is hydrophobic and has an inorganic siloxane backbone (-O-Si(CH_3)$_2$-chains) and organic methyl groups (Si-CH_3) attached to its silicone molecules. The hydrophobic nature of PDMS results in poor wettability which limits cell adhesion on its surface. Wettability is the ability of water to maintain contact with a solid surface. The wettability can be quantified by measuring the water contact angle, which is the measurement of angle between a liquid drop and the surface where the drop sits. A contact angle below 90° is regarded as hydrophilic and between 90°- 150° as hydrophobic, and over 150°, as super hydrophobic (Pelayo *et al*., 2015; AlZahid *et al.*, 2018). PDMS has approximately $108^{\circ} \pm 7^{\circ}$ water contact angle (Gokaltun *et al*., 2017) which makes it challenging for cells to adhere on its surface. However, surface modification of PDMS by plasma treatment can increase hydrophilicity when exposed to an oxygen plasma, as the hydrophobic methyl groups are replaced by hydrophilic silanol (Si-OH) groups which decreases water contact angle to as low as ~ 10° (Mata *et al*., 2005, Ng *et al*., 2002) (Fig 8). Plasma-treated PDMS keeps its hydrophilicity when the surface is in contact with water or polar organic solvents, as this inhibits hydrophobic recovery (Guckenberger *et al.,* 2012; McDonald and Whitesides, 2002). Culturing neuronal cells on hydrophilic materials promotes cell attachment and growth, whereas hydrophobic materials do not (Kleinfeld *et al*., 1988). Thus, keeping PDMS hydrophilic for cell culture studies is crucial, both for cell attachment and because the protein transfer may be hampered if the substrates are too hydrophobic (Tan *et al*., 2002).

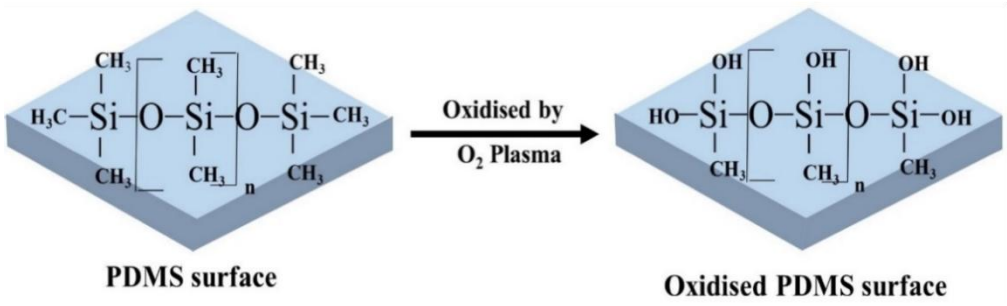

Figure 8. Surface modification of PDMS by oxygen plasma treatment.

The hydrophobic methyl groups (-CH_3) are converted into the hydrophilic silanol groups (SiOH) upon oxygen plasma exposure, reducing the water contact angle and improving cell adhesion (Akther et al., 2020).

1.6.3 Silanes

Important surface functionalisation reagents often used in microfabrication processes, silane coupling agents are silicon compounds that contain at least a silicon-carbon bond, (Si-CH_3), which is referred as an organosilane (Zhu *et al*., 2020). They normally consist of two types of reactive groups with different functionalities which attach to the silicon atom. The molecular structure of silane coupling agents include reactive groups, which are organofunctional group (R) such as epoxy, amino, methacryloxy or sulphide and a hydrolysable group (X) such as alkoxy, acyloxy, halogen or amine, which can form silanol groups (Si-OH) (Fig 9A) (Zhu *et al*., 2020; Gelest). A reactive group is formed after a hydrolysis process in the presence of water or moisture in the atmosphere which can condense with other silanol groups, forming a siloxane structure (Si-O-Si) (Fig 9B). They then react and couple to an inorganic surface such as ceramics and oxide layers on metals and covalently attach to substrate by condensation process with hydroxyl groups. Therefore, silane coupling agents play a role in bridging between inorganic substrates (e.g. glass or silicon substrates) and polymers and promote adhesion (Zhu *et al*., 2020).

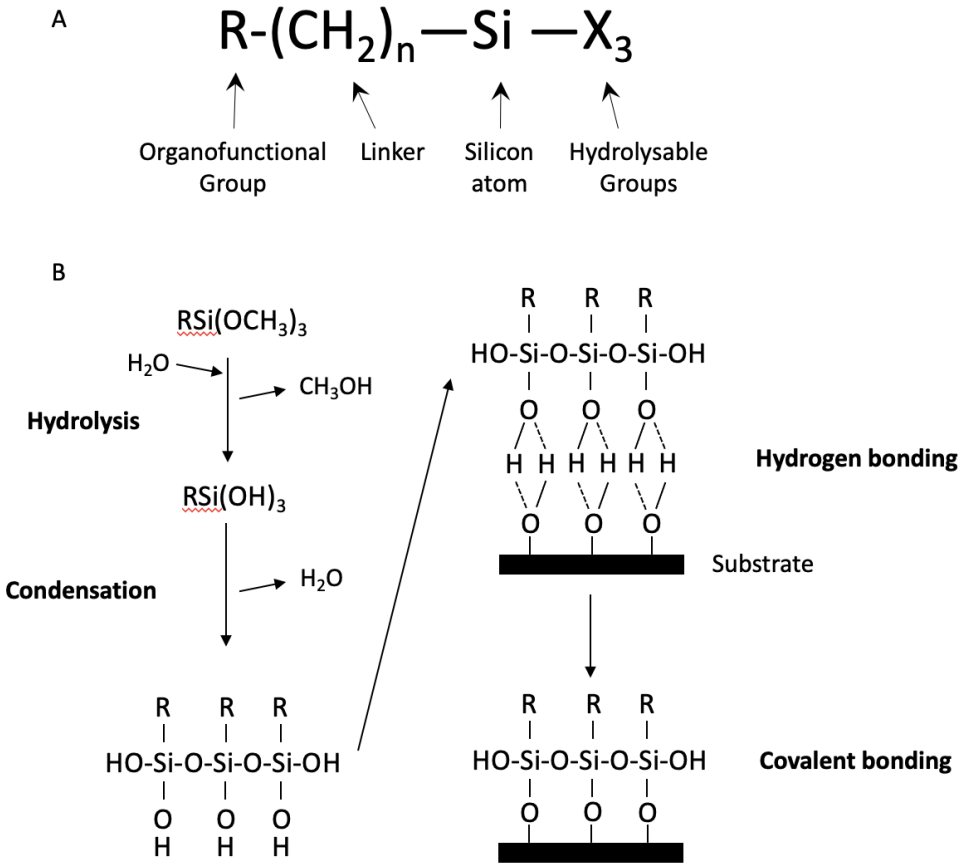

Figure 9. Molecular structure and reaction mechanism of silane coupling agents for surface modification.

(A) General molecular structure of silane coupling agent and (B) the process of silane surface modification through hydrolysis, condensation and covalent bonding to an inorganic substrate (Figure adapted from Zhu et al., 2020).

In micropatterning engineering studies, PDMS substrates with silanol groups (i.e., after O_2-plasma treatment) can be additionally surface coated to ensure long-term stability, (Chuah *et al*., 2015, Kuddannaya *et al*., 2015) (Fig 10). Surface-coating can introduce a wide range of functionalities by generating a range of desired important functional groups on the PDMS surface, either to be hydrophobic or hydrophilic, or to present other reactive groups (Ng *et al*. 2002). This covalent attachment is generally stable under chemical or physical stress, such as electrolyte attack or temperature gradients or flow shear-stress conditions (Offenhäusser *et al*. 2007). For example, introducing a poly(ethylene glycol)di-(triethoxy)silane to oxidised PDMS may generate a permanent hydrophilic PDMS surface and decrease the chance of non-specific protein absorption (Ng *et al*. 2002). Alternatively, the oxidised surface of PDMS can be silanised with an amino-terminated silane, such as aminopropyltriethoxysilane (APTES) and aminopropyltrimethoxysilane (APTMS), which produce an amino-terminated surface layer to support adhesion of biomolecule (Fig. 10A) (Hardelauf *et al*., 2014, Sandison et al., 2010). Often, a cross-linker (e.g. glutaraldehyde) is used to crosslink a biomolecule (e.g. a protein) to a functionalised surface (e.g. an amino-functionalised surface) to improve PDMS surface modification and provide better biocompatible platform for a biomolecule of interest (Fig 10B).

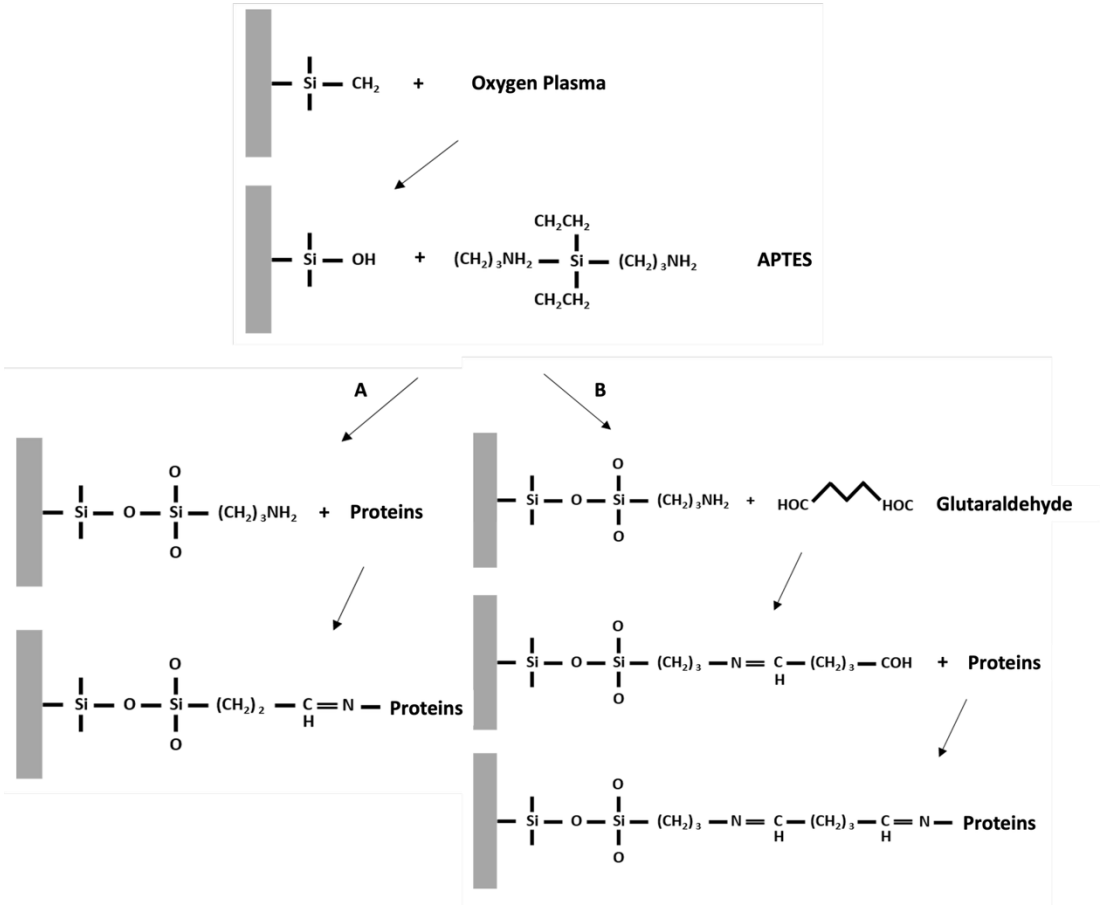

Figure 10. Stepwise surface modification of PDMS.

The highly hydrophobic nature of PDMS can be converted into hydrophilic substrate by oxygen plasma treatment. (A) The oxidised PDMS surface can maintain its hydrophilicity for longer term and keep its reactivity by silanisation with an amino-terminated silane, APTES which provides biomolecule adhesion (B) A cross-linker, such as glutaraldehyde, can be applied to crosslink a biomolecule to an amino-functionalised surface to support more efficient adhesion of biomolecule.

1.7 Microengineering Techniques for Guiding Neuronal Cultures

Quantifying intracellular dynamics such as mitochondrial movement within neuronal cells presents significant challenges due to the complex and disorganised outgrowth of neuronal processes in conventional cultures. Traditional methods often struggle to accurately monitor organelle transport in dense neurite networks, particularly in distinguishing directionality within axons (Kim *et al*., 2012). To overcome these limitations, recent advancements in microengineering approaches have enabled novel methods for studying neuronal cultures, providing insights into neuronal function and dysfunction by examining the relationship between circuit architecture and function in *in vitro* neural networks (Hasan and Berdichevsky, 2016). Various microengineering techniques have been developed using microfabrication technologies, particularly photolithographic patterning methods, including microcontact printing, microfluidics, dielectrophoresis, optical tweezers, and microwell arrays.

1.7.1 Microcontact Printing

μCP is an advanced lithographic technique that enables the selective deposition of biomolecules onto various substrates, forming micropatterns that guide cellular adhesion and network formation (Offenhäusser *et al.*, 2007). Initially developed to transfer alkanethiols for self-assembled monolayers (SAMs) on gold (Kumar & Whitesides, 1993), μCP has since evolved to accommodate biomolecules such as extracellular matrix (ECM) proteins and polyamine anchors like poly-L-lysine (PLL), facilitating neuronal patterning for high-resolution imaging and neurobiological studies (Hardelauf *et al.*, 2014).

The μCP process involves the fabrication of an elastomeric PDMS stamp from a silicon master, which is subsequently coated with a biomolecular ink and used to transfer defined molecular patterns onto a substrate (Ruiz & Chen, 2007) (Fig 11A-B). This technique has been widely employed for neuronal micropatterning, where printed PLL or ECM proteins selectively promote neuronal attachment and alignment. To ensure long-term pattern stability, cytophobic

backfilling strategies, such as poly(L-lysine)-graft-poly(ethylene glycol) (PLL-g-PEG) coatings, have been employed, enhancing substrate durability and preventing non-specific cell adhesion (Hardelauf *et al*., 2014).

Using μCP on PLL-g-PEG-modified substrates, neurons were successfully confined to adhesion nodes, forming structured, high-occupancy networks (Fig. 11C-E). These micropatterned neuronal cultures demonstrated >95% node occupancy over 9 days *in vitro* (DIV), maintaining stable connectivity throughout long-term cultures up to 33 DIV. Additionally, μCP-based neuronal cultures exhibited high fidelity to the underlying patterns, with robust neurite outgrowth and network connectivity reaching near-maximal levels (~2.5 connections per node) by 7 DIV. In contrast, silane-PEG coatings exhibited limited pattern stability, with degradation observed beyond 25 DIV (Hardelauf *et al*., 2014).

This evidence supports the utility of μCP for guiding neuronal growth in structured networks, providing a powerful platform for neurobiological assays, synaptic activity studies, and neurodegenerative disease modelling. The high-resolution patterning allows for quantitative analysis of neurite dynamics, network plasticity, and axonal transport in a reproducible and scalable manner.

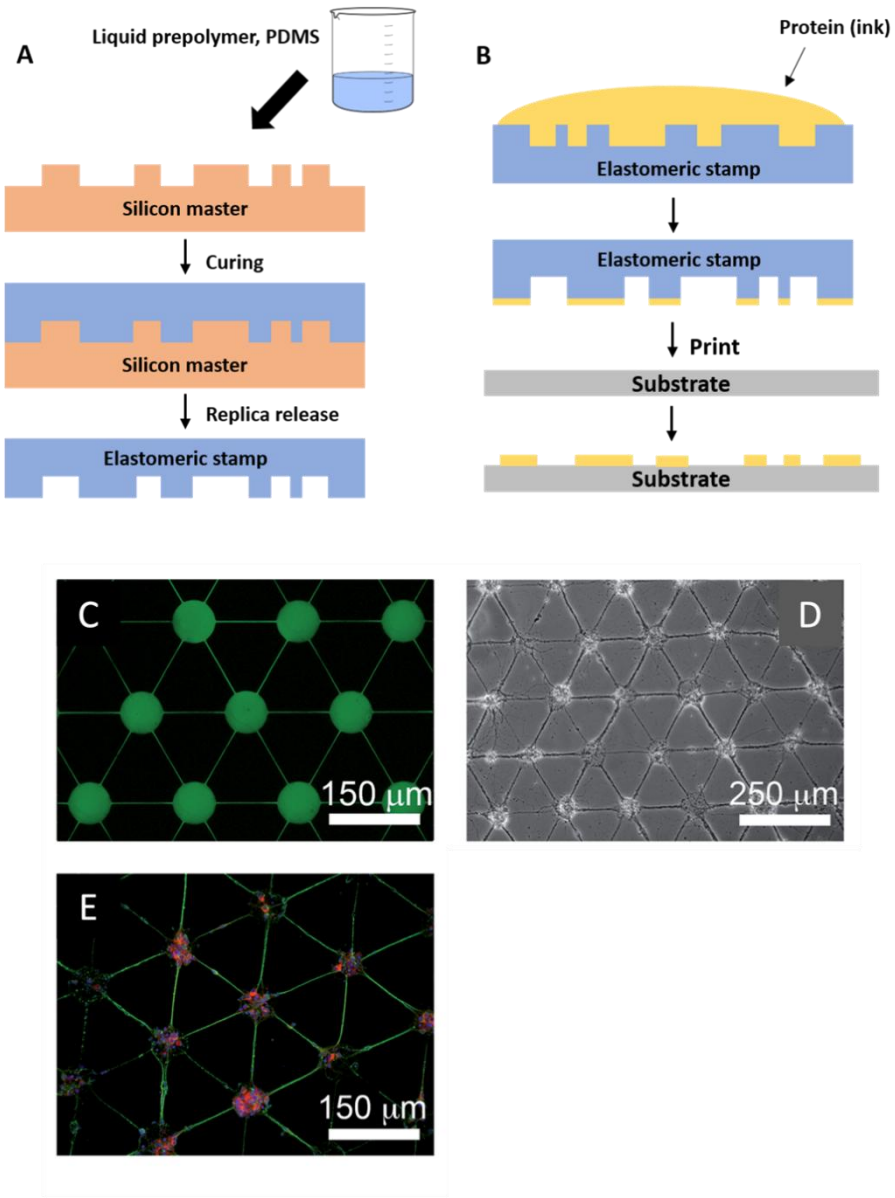

Figure 11. Microcontact printing for neuronal micropatterning and network formation.

(A-B) µCP process. (A) Fabrication of a PDMS elastomeric stamp using a microfabricated silicon master. The liquid PDMS prepolymer is poured over the silicon mold, cured, and peeled off to generate a reusable micropatterned stamp. (B) Schematic of the µCP process. The PDMS stamp is inked with a protein solution, dried, and pressed onto a substrate, transferring biomolecular patterns that facilitate selective neuronal adhesion.

(C-E) Neuronal patterning and network formation using µCP (Hardelauf et al., 2014). (C) Fluorescence imaging of fluorescein isothiocyanate (FITC)-PLL micropatterned

substrates demonstrating high signal-to-noise patterning. (D) Brightfield image showing primary neurons adhering to the adhesion nodes and extending neurites to form structured internodal connections. (E) Immunofluorescence of neuronal cultures on micropatterned substrates. Neurons were stained with β-III-tubulin (green), MAP-2 (red), and nuclei with DAPI (blue), showing high-fidelity neuronal networks aligned to the patterned substrate.

1.7.1.1 Experimental Considerations and Limitations

Despite its advantages, μCP has several limitations that can hinder the reproducible creation of submicrometre features. Due to the softness of elastomeric PDMS stamps, deformation can occur both during stamp removal from the template and upon contact with the substrate, significantly reducing the resolution of the printed patterns (Xia & Whitesides, 1998; Perl *et al.*, 2009). To minimise the risk of stamp deformation, the aspect ratio—defined as the height (*h*) of the features divided by their lateral dimensions (*d*)—should be maintained between approximately 0.2 and 2 (Delamarche *et al.*, 1997). Aspect ratios that are too high can cause buckling and lateral collapse of PDMS features, whereas excessively low aspect ratios can lead to roof collapse (Xia & Whitesides, 1998) (Fig 12).

Various strategies have been proposed to address the deformability of PDMS stamps. One approach involves washing the substrates with ~1% aqueous sodium dodecyl sulphate (SDS) solution followed by rinsing with heptane to restore the original shape of the PDMS features (Delamarche *et al.*, 1997). Using rigid substrates, such as glass, instead of flexible surfaces can further reduce distortions during the soft lithography process.

PDMS also exhibits dimensional instability due to its inherent material properties. During curing, PDMS can shrink by approximately 1%, leading to deviations in pattern dimensions. Additionally, exposure to nonpolar organic solvents such as toluene and hexane can cause PDMS swelling, altering the intended shape of micropatterned features (Lee *et al.*, 2003). Consequently, μCP is generally limited to apolar inks that are ethanol-soluble, as ethanol minimally

affects PDMS swelling. Furthermore, the elasticity and thermal expansion of PDMS impose constraints on multilayer fabrication and nanofabrication, where high precision is required.

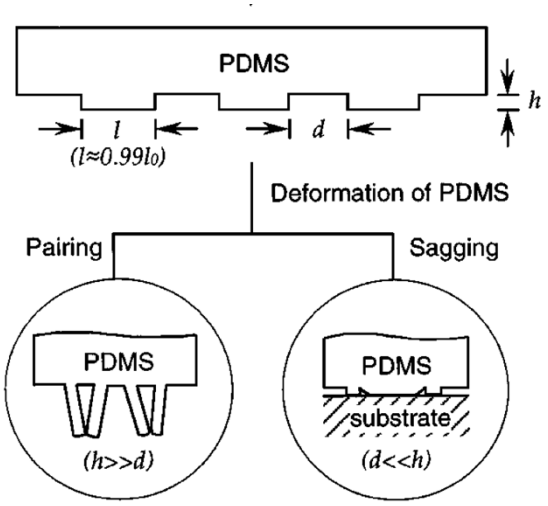

Figure 12. Deformative events in PDMS stamps due to high or low aspect ratios. *Illustration of possible PDMS stamp deformations caused by inappropriate aspect ratios. High aspect ratios can result in buckling or lateral collapse, whereas low aspect ratios may lead to roof collapse. Maintaining an optimal aspect ratio can reduce these defects and improve pattern fidelity (Xia & Whitesides, 1998).*

1.7.2 Microfluidics

Microfluidic devices have been extensively utilised to establish compartmentalised environments for neurons, allowing for the isolation of axons and soma within a controlled setting. These platforms facilitate directed axonal growth, fluidic isolation of neuronal compartments, and targeted biochemical or electrophysiological stimulations. For example, Lu's group developed a microfluidic device with two large open compartments connected by a parallel array of microchannels, enabling the unidirectional extension of dopaminergic axons while maintaining fluidic separation between neuronal soma and axons (Lu *et al*., 2012). This design allows for the spatiotemporal control of biochemical gradients, making it ideal for studying axon guidance and mitochondrial transport.

Another significant advancement is the integration of multielectrode arrays (MEA) with microfluidics for real-time electrophysiological recordings of neuronal activity. By guiding neuronal processes through microchannels, these hybrid systems improve signal-to-noise ratios in action potential recordings and enable the isolation of axonal signals from somal activity (Dworak and Wheeler, 2009). This approach has been utilised to monitor axon regeneration, synaptic communication, and signal propagation along neuronal networks, providing insights into functional connectivity *in vitro*.

One notable example is the multidomain microfluidic device developed by Taylor *et al.* which consists of two interconnected channels and a network of parallel tubes. This system was specifically designed to isolate central nervous system (CNS) axons and direct their growth without requiring neurotrophins, which play a crucial role in neuronal development, maintenance, and function (Taylor *et al*., 2005). This approach enables the study of axonal injury, regeneration, and transport mechanisms, allowing researchers to isolate axonal mRNA from primary rat cortical and hippocampal neurons without somal or dendritic contamination.

1.7.3 Dielectrophoresis (DEP)

Dielectrophoresis (DEP) is an electric field-based technique used to manipulate and position cells within a microfluidic environment. This approach has been widely employed to create well-defined neuronal patterns and direct axon and dendrite growth. By applying non-uniform electric fields, DEP allows neuronal positioning without physical contact, making it an attractive method for neural circuit construction and neurodegenerative disease modelling (Gupta *et al*., 2022).

Furthermore, DEP-based microfluidic platforms have been applied to study axon growth in response to external stimuli, including electric fields and chemical gradients. These systems provide a label-free approach for positioning neurons, making them particularly valuable for constructing neural circuits and investigating axon regeneration in neurodegenerative disease models (Kim *et al*., 2018).

1.7.4 Microwell Arrays for Single-Cell Neuronal Cultures

Microwell arrays offer a high-throughput approach to confining and organising neurons into predefined microenvironments. These microfabricated platforms consist of arrays of small wells that trap individual neurons or small clusters, enabling precise control over neuronal density and connectivity. Lin' *et al.* developed a dual-well microfabricated system to capture single neural progenitor cells and guide their differentiation into functional neurons (Lin *et al*., 2015). This platform facilitated controlled neurite outgrowth, allowing for systematic investigations into neurodevelopment and synaptogenesis.

The advantage of microwell arrays lies in their ability to preserve the physiological microenvironment of neurons while enabling single-cell resolution studies. By integrating biochemical gradients, extracellular matrix coatings, and patterned adhesion molecules, these systems allow researchers to explore how microenvironmental cues influence neuronal differentiation and connectivity (Tseng *et al*., 2016).

1.7.5 Microengineered Devices Developed for the Analysis of Mitochondrial Dynamics

Among various microengineering strategies, microengineered approaches provide structured environments that enable precise tracking of mitochondrial movement. Although micropatterned substrates have been employed for neuronal cultures, their application specifically for mitochondrial studies remains limited. Burbulla's group utilised microcontact printing to generate 10 µm-wide line patterns, which supported long-term studies of mitochondrial dynamics in iPSC-derived neurons (Burbulla *et al*., 2016) (Fig. 13A-B). Their analysis demonstrated that mitochondrial morphology evolved over time, transitioning from a punctate state at early differentiation stages (Day 40) to an elongated and interconnected network at later stages (Day 100), indicative of increased mitochondrial fusion. Additionally, kymograph-based quantification revealed a decrease in mitochondrial motility over time, with reduced anterograde transport and increased stationary mitochondria at Day 100. These findings underscore the importance of micropatterned neuronal cultures in providing structured environments for tracking mitochondrial transport and morphological adaptations over extended periods.

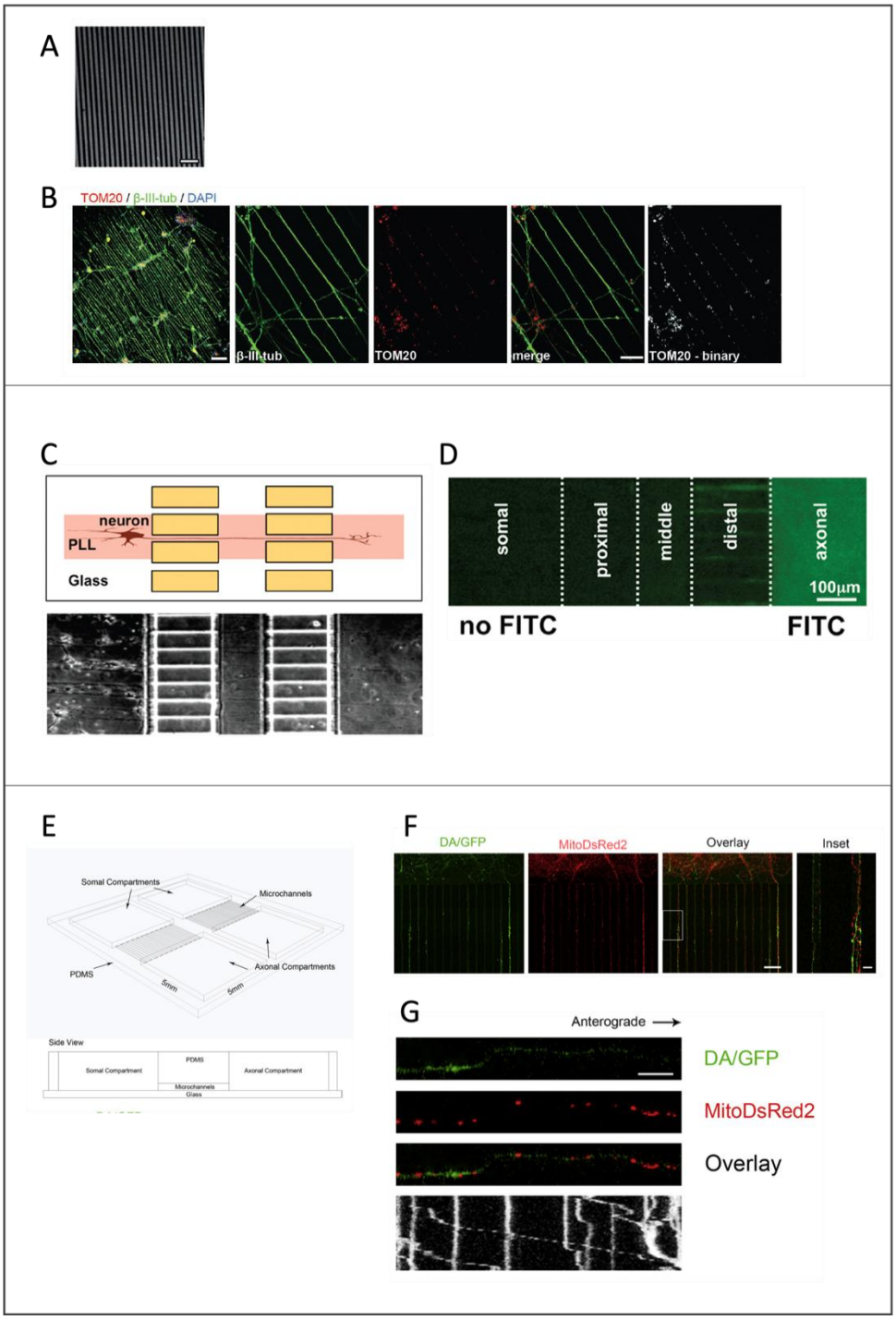

Figure 13. Microengineered platforms for analysing mitochondrial dynamics in neurons.

(A-B) Micropatterned substrates for structured neuronal growth and mitochondrial analysis (Burbulla et al., 2016). (A) SEM image of 10 µm-wide micropatterned lines facilitating structured neurite outgrowth. (B) Immunofluorescence of iPSC-derived neurons cultured on micropatterned substrates, showing β-III-tubulin (green),

TOM20-labeled mitochondria (red), and DAPI-stained nuclei (blue). Binary transformation of TOM20 signals for quantitative analysis of mitochondrial morphology and motility. (C-D) Micropatterned substrates in a compartmentalized microfluidic device (Kim et al., 2012). (C) Schematic of a PDMS-based microfluidic device integrating poly-L-lysine (PLL) micropatterns for controlled axonal outgrowth. (D) Fluidic isolation demonstrated using FITC-dextran (10 kDa), confirming selective compartmentalization between somal and axonal regions. (E-G) Open compartment microfluidic system for dopaminergic neuron culture (Lu et al., 2012) (E) Open compartment microfluidic system for dopaminergic neuron cultures (Lu et al., 2012). (F) DA/GFP-expressing dopaminergic neurons (green) extend axons through microchannels (10 µm width, 900 µm length), with mitochondria labelled using MitoDsRed2 (red). (G) Kymographs depicting anterograde (axon terminal-directed) and retrograde (soma-directed) mitochondrial transport within microchannels.

Other micropatterning strategies have incorporated microfluidic devices with structured substrates to further enhance the control of neuronal outgrowth and mitochondrial transport analysis (Kim *et al*., 2012; Lu *et al*., 2012). Kim *et al*. utilized a ladder-like micropatterning of PLL strips within a compartmentalized microfluidic system to investigate mitochondrial trafficking in axons (Fig. 13C-D). This system enabled precise neuronal alignment and automated mitochondrial movement tracking using image processing techniques. Their study revealed that the effect of Aβ on mitochondrial motility is highly localised, with Aβ application to the axonal compartment nearly halting mitochondrial transport in distal axons, demonstrating the potential of compartmentalized micropatterning platforms for studying neurodegenerative disease mechanisms and localised mitochondrial dysfunction.

Similarly, Lu's group developed an open compartment microfluidic device specifically designed for visualising mitochondrial transport in aligned dopaminergic axons. The device comprises two culture chambers connected by parallel microchannels, enabling fluidic isolation between the soma and axonal

compartments and allowing for precise tracking of mitochondrial movement (Lu *et al*., 2012) (Fig. 13E-G). Traditional compartmentalised culture systems such as Campenot chambers, which use Teflon barriers to isolate axons from soma, have long been used for axonal studies but present challenges in axonal alignment and sealing reliability. Microfluidic devices overcome these limitations by providing structured guidance of axons, improved compartmentalisation, and enhanced compatibility with high-resolution live-cell imaging. Using this platform, Lu's group cultured dopaminergic neurons for up to 4 weeks, with axons extending into the microchannels by DIV 14, enabling the analysis of mitochondrial movement along clearly aligned axonal segments.

Within these microchannels, mitochondria exhibited distinct anterograde and retrograde transport, with anterograde velocities averaging 0.39 ± 0.03 μm/s and retrograde velocities 0.34 ± 0.03 μm/s. These findings highlight the capability of microfluidic platforms to support sustained culture and dynamic analysis of axonal transport in a structured environment

Together, these studies highlight the versatility of microengineered platforms in investigating mitochondrial dynamics in neurons. The integration of micropatterned substrates and microfluidic devices provides a structured environment for tracking mitochondrial movement, analysing transport defects, and studying their implications in neurodegenerative disorders. These approaches collectively offer a powerful toolset for advancing our understanding of mitochondrial transport in health and disease.

1.8 Research Objectives

1.8.1 Motivation

Mitochondria are essential organelles that play a critical role in energy metabolism and cellular homeostasis in neurons. Dysfunctional mitochondria and abnormal movements have been associated in numerous neurodegenerative disorders, including AD and PD. Understanding mitochondrial movements in neurons is critical for developing effective therapeutic strategies for these conditions.

However, studying mitochondrial motility in conventional neuronal cultures presents significant challenges. Neurons form highly complex and unorganised networks, with dendrites and axons extending in multiple directions and overlapping with neighbouring cells. This complexity makes it difficult to isolate individual mitochondria and accurately track their movements. Differing culture conditions, including culture surface properties, will also have an impact on neuronal morphologies and network geometries. To address these limitations, this study both investigates the effect of differing surface coatings on neuronal adhesion, morphology and mitochondrial motility and employs microcontact printing to create controlled cellular environments. This technique enables the precise patterning of neuronal cultures, facilitating systematic and reproducible quantification of mitochondrial dynamics.

1.8.2 Novelty

This study presents several novel aspects that contribute to advancing the understanding of mitochondrial dynamics in neurons.

First, while previous studies have examined how different coating materials influence neuronal adhesion and morphology, the effect of substrate coatings on mitochondrial motility remains largely unexplored. Investigating how various substrate coatings impact mitochondrial movements in primary hippocampal neurons offers new insights into the relationship between extracellular

environments and intracellular mitochondrial dynamics, an area that has been largely overlooked in past research.

Second, this study is among the first to investigate mitochondrial motility in primary hippocampal neurons using microcontact printing. Burbulla *et al*. employed microcontact printing and mitochondrial imaging of axonal transport in their work (Burbulla *et al*., 2017). However, they focused upon long-term phenotypic outcomes in iPSC-derived human neurons, demonstrating how micropatterning improves network formation and quantifying changes in mitochondrial dynamics over time. In contrast this study, which employs primary hippocampal neurons and a different micropatterned architecture, focuses upon extensive characterisation of mitochondrial motility by live-cell imaging across a range of different substrates, enabling comparisons between micropatterned and unpatterned primary neuronal cultures, as well as between different adhesive biomolecular cues.

Third, this study leverages KymoAnalyzer, an advanced motion-tracking tool capable of extracting over 20 parameters related to mitochondrial motility. Compared to conventional tracking methods, which often focus on a limited set of transport parameters, this approach enables a more comprehensive and quantitative assessment of mitochondrial behaviour. The integration of high-resolution motility analysis with micropatterned neuronal cultures provides a unique methodology for studying mitochondrial transport in a more physiologically relevant and reproducible setting.

By integrating microcontact printing with high-resolution motility analysis, this research provides a novel and systematic approach to studying mitochondrial transport in neurons, with potential implications for neurodegenerative disease research.

1.8.3 Research Objectives

This thesis has two primary research objectives:

1. Investigating the effects of different coating materials on hippocampal cell cultures and mitochondrial motility

- Conventional and charged coatings were compared to evaluate their impact on neuronal adhesion, network formation, and mitochondrial motility.

- Neuronal morphology and cell-type composition were characterised across different substrates.

- Mitochondrial dynamics were quantitatively assessed using KymoAnalyzer at different maturation stages of the cultures.

2. Developing a microcontact printing approach to study mitochondrial motility in structured neuronal networks

    - Optimisation of microcontact printing techniques to create patterned substrates suitable for hippocampal neuron growth.

    - Evaluation of how different coating materials influence mitochondrial motility in patterned versus unpatterned cultures.

    - Establishing standardised protocols for µCP-based neuronal culture systems to facilitate quantitative mitochondrial motility analysis.

1.8.4 Organisation of Thesis

This thesis is organised into six chapters, each building upon previous findings to systematically explore mitochondrial motility in hippocampal neurons.

Chapter 1 provides an overview of mitochondrial structure and dynamics, particularly in neurons, and their implications in neurodegenerative diseases. It also reviews current quantitative methods for analysing mitochondrial motility. The second part of this chapter introduces microcontact printing, detailing its application in neuronal patterning and mitochondrial research.

Chapter 2 outlines the materials and methods used throughout the study, describing experimental procedures in detail.

Chapter 3 focuses on selecting and validating an appropriate tool for mitochondrial motility analysis. KymoAnalyzer was chosen for its ability to quantify

various motion parameters, and its performance was assessed using hippocampal neurons treated with pharmacological agents. Additionally, mitochondrial motility changes during neuronal maturation in vitro were investigated.

Chapter 4 examines the impact of different coating materials on neuronal adhesion, morphology, and mitochondrial dynamics. The influence of substrate properties on mitochondrial motility was analysed at different stages of neuronal maturation.

Chapter 5 details the optimisation of microcontact printing for guiding neuronal growth along defined patterns, facilitating systematic mitochondrial motility analysis. This chapter also explores how different coating materials affect mitochondrial movement in patterned neuronal cultures.

Chapter 6 presents the overall conclusions of the study and discusses potential future directions. This includes further optimising microcontact printing for studying mitochondrial dynamics and exploring its application in disease modelling and therapeutic screening.

CHAPTER TWO:
Materials and Methods

2.1 Hippocampal cell isolation, cultures, and imaging

2.1.1 Substrate preparation - washing

To prepare clean surfaces for cell adhesion, 19 mm coverslips were immersed in 10% Decon 90 in deionised water and cleaned in an ultrasonic bath (FB15051, Fisher Scientific, Loughborough, UK) for 15 min. Coverslips were rinsed three times in deionised water and sonicated for an additional 5 min in deionised water. Inside a fume hood, the coverslips were soaked sequentially for 5 min each in acetone and methanol before being blow-dried with nitrogen gas (UN1066, BOC, UK). To ensure removal of organic residues and create hydroxyl-rich surfaces for silanisation, the coverslips were cleaned using piranha solution, a strong oxidising agent. A 7:3 mixture of sulfuric acid (H_2SO_4) and hydrogen peroxide (H_2O_2) was prepared by slowly adding H_2O_2 to H_2SO_4 to prevent overheating. The solution was cooled to below 60°C before immersing the coverslips for 15 min. Coverslips were then rinsed thoroughly with deionised water and dried with nitrogen gas. Due to the acidic nature of piranha solution, small volumes were prepared and waste solution was diluted extensively with water before disposal.

For additional cleaning, coverslips were treated with an oxygen plasma asher (Pico, Diener, Hillingdon, UK) at 100 W for 1 min, followed by sterilisation under UV light (DaRo UV, Sudbury, UK) for 15 min.

2.1.2 Bulk surface coating

Cleaned glass coverslips were coated within 24 h prior to cell isolation using one of the following solutions: 0.1 mg/ml poly-D-lysine (PDL; Sigma Aldrich, P0899, Poole, UK) (Gibco, Fisher scientific), 0.1 mg/ml laminin (Sigma), or a combination of 0.05 mg/ml laminin and 0.05 mg/ml PDL. A 250 µl aliquot of the selected coating solution was applied to each coverslip and incubated at room temperature in a laminar flow hood for 1 h or overnight at 37°C in a culture incubator. PDL-coated and PDL-laminin-coated coverslips were washed three times with sterile water and allowed to air-dry, while laminin-coated coverslips were washed and stored in sterile water until use. For dual coating, coverslips were first coated with 0.1 mg/ml

PDL for 1 h, rinsed with sterile water, and then coated with 0.1 mg/ml laminin for an additional hour. After washing, dual-coated coverslips were stored in sterile water until use.

Silanisation of substrates was performed using two types of silanes to create functionalised surfaces: carboxyethylsilanetriol di-sodium salt (CES, 23-27% in water, Fluorochem, Derbyshire, UK) or aminopropyl-trimethoxysilane (APTES, Fluorochem). For COOH-functionalised surface, coverslips were immersed in 2% CES in methanol for 20 min, rinsed three times with methanol and cured at 80°C for 30 min. For amino-functionalised surfaces, coverslips were immersed in 2% (v/v) of APTES in 95% ethanol/5% deionised water for 20 min, rinsed three times with ethanol and cured at 80°C for 30 min. Both types of functionalised coverslips were stored in sterile water at 4°C for up to one week.

2.1.3 Cell culture

Hippocampi were isolated from postnatal day 0-2 (p0-2) rat pups euthanised by cervical dislocation, in accordance with the Animals (Scientific Procedures) Act 1986 (revised under European Directive 2010/63/EU). The tissue was dissected in Hibernate media (Life Technologies, Paisley, UK) under sterile conditions. For enzyme dissociation, hippocampi were digested in 2 mg/ml papain (Worthington, Lakewood, USA) prepared in Hibernate media supplemented with 0.1 M EGTA and 1 M NaOH to chelate calcium ions. The tissue was incubated at 30 °C for 30 min, followed by dilution with 1.5x volume of Hibernate media and centrifugation at 120 x g for 4 min.

To obtain a single-cell suspension, the digested tissue was gently triturated using a fire-polished glass Pasteur pipette. Debris was allowed to settle, and the supernatant was transferred to a fresh tube, centrifuged at 120 x g for 4 min and resuspended in Neurobasal A medium (Life Technologies) supplemented with 2% B27, 2 mM GlutaMax and 10 μg/ml gentamicin. Cells were counted using Trypan Blue (Sigma, Poole, UK) exclusion to ensure viability and plated on prepared substrates at a density of 300 cells/mm² in 12-well plates or gridded 35 mm dishes

(30 µ-Dish $^{35mm, high}$ Grid-500 ibidi Glass Bottom; Thistle Scientific, Uddingston, UK). Cultures were maintained at 37°C in a humidified atmosphere with 5% CO_2, with half the medium exchanged every 3-4 days.

2.1.4 Labelling of mitochondria

Mitochondria were labelled using 100 nM MitoTracker Green-FM (Life Technologies), a green-fluorescent dye that labels mitochondria regardless of membrane potential. Substrates with hippocampal cells were incubated with MitoTracker Green (with or without tetramethylrhodamine ethyl ester, TMRE) for 30 min at 37°C in Neurobasal A *without* B27, followed by an additional 30 min incubation in Neurobasal A *with* B27 (no MitoTracker Green, TMRE if using) to allow dye de-esterification prior to imaging.

TMRE was used in a subset of experiments to qualitatively assess mitochondrial membrane potential. Although routinely performed in the lab by myself and others, TMRE_based live-cell imaging was not included in this thesis due to fluorescence instability and excessive signal flickering, likely caused by phototoxicity under standard illumination conditions. Additionally, TMRE could not be used in combination with mito-RFP due to overlapping excitation/emission spectra. Despirte these limitations, TMRE staining provided qualitative reassurance that mitochondrial membrane potential remained largely intact across conditions.

2.1.5 Imaging cells and mitochondria

Brightfield images of hippocampal cells were acquired using a 20x air 0.25 NA objective (Nikon, Surrey, UK) on a Nikon ECLIPSE Ti inverted epifluorescence microscope. Fluorescence images of FITC-PLL were captured using a 20x air 0.75 NA objective (Nikon) with 480 nm excitation light provided by a CoolLED pE300 lamp (Andover, UK).

Fluorescent mitochondria were visualised with a 100 x oil immersion objective (S-Fluor 0.5-1.3 NA set to 1.3 NA; Nikon). Fluorescence excitation was performed at 470 nm for MitoTracker Green and 550 nm for TMRE using a pE-4000

multi-LED light source (CoolLED). Images were recorded with an Orca Flash 4.0 CMOS camera (Hamamatsu, Welwyn Garden City, UK), controlled via WinFluor software (v3.7.2; John Dempster, University of Strathclyde). Each image was acquired for 600 ms per frame, with dual-wavelength recordings alternated, generating 300-frame image stacks over a total duration of 3 min.

For multi-day time-lapse mitochondrial imaging, 0.05% v/v mitochondrial-red fluorescent protein (CellLight mitochondria-RFP BacMam 2.0, Life Technologies) was added into hippocampal cell cultures in 35 mm gridded dishes when the cells were 2 days *in vitro* (DIV). Imaging was conducted at 7, 10, 15 and 21 DIV, targeting the same regions of interest. The excitation wavelength was set to 550 nm, and imaging was performed with the 100x oil objective under the same conditions as described above. Cells were maintained at 37°C in humidified air containing 5% CO_2 using a stage-top chamber (H301 mini, OKOlabs, Naples, Italy).

2.1.6 Drug treatments: Nocodazole or latrunculin B

Cells labelled with MitoTracker Green were imaged as described above. Following baseline imaging, cells were treated *in situ* with either 10 µM nocodazole (Sigma), an inhibitor of microtubule polymerisation, or 10 µM latrunculin B (Sigma), an inhibitor of actin polymerisation. The same regions were re-imaged 30 min post-treatment to assess changes in mitochondrial dynamics.

2.1.7 Immunocytochemistry

After live-cell imaging, cells were fixed with 10% neutral buffered formalin solution (HT5012, Sigma) for 10 min, followed by ice-cold methanol for 10 min. Permeabilisation was performed using 0.01% Triton X-100 (Fisher Scientific) in phosphate-buffered saline (PBS; Fisher Scientific) for 10 min. Blocking was carried out with 1% bovine serum albumin (BSA; Sigma) plus 5% fetal bovine serum (FBS, Sigma) in PBS for 30 min.

Coverslips were stored in 0.02% sodium azide (Sigma) at 4°C or immediately processed for antibody staining after 3 washes with PBS. Primary antibodies were

applied for 1h at room temperature or overnight at 4°C in 1% BSA and 5% FBS blocking buffer: anti-GFAP antibody (1:1000; rabbit, ab7260, Abcam), anti-MAP2 antibody (1:5000; chicken, NB300-213, Novus), anti-tau antibody (1:100; TAU-5, mouse, ab80579, Abcam). Following two washes with PBS, coverslips were incubated for 1 h at room temperature with secondary antibodies: Alexa 488-conjugated anti-rabbit IgG (1:500; ab150077, Abcam), Alexa 555-conjugated anti-chicken IgY (1:500; ab150170, Abcam) and Cy5-conjugated anti-mouse IgG (1:1000; ab6563, Abcam). Nuclei were counterstained with 0.1 µg/ml DAPI. Cells were washed twice in PBS and imaged on the Nikon ECLIPSE Ti microscope using a 40 x oil 1.3 NA objective (1.3 NA, Nikon).

2.2 Mitochondrial Motility Quantification: KymoAnalyzer

KymoAnalyzer (Neumann et al 2017), an ImageJ plugin, was used to quantitatively analyse mitochondrial motility in live-cell videos. The plugin contains six macros executed sequentially in which the user manually assigns particle tracks and then automatically calculates transport parameters of particles visible within individual tracks.

BatchKymographGeneration

Kymographs were generated by manually drawing a polyline along axonal processes from the soma to the periphery. Live-cell movies were loaded, and each neuronal process was traced with a polyline tool to assign mitochondrial directionality accurately.

Tracks

Mitochondrial trajectories were manually assigned on kymographs (plots of distance moved over time). Stationary mitochondria appeared as horizontal lines, while motile mitochondria appeared as horizontal lines, while motile mitochondria were represented by diagonal lines. In cases where the neuronal soma was visible at the edge of the field of view and the direction of neurite extension could be confidently identified, directional labels were applied: anterograde: (movement away from soma; line sloping rightward) and retrograde (towards soma; lines

sloping leftward). Only neurites with clearly identifiable polarity and unambiguous soma orientation were included in this direction-based classification.

In contrast, in Chapter 3 experiments, where the soma was not visible or where neurite origins were unclear, directionality could not be confidently assigned. In these cases, mitochondrial movements were instead classified as either unidirectional or bidirectional, without assigning anterograde or retrograde labels. All track lines were recorded in the ROI manager in Image J.

CargoPopulation

The macro calculated mitochondrial parameters, including density, flux and switch frequency.

NetCargoPopulation

Net mitochondrial movement parameters, including net velocity and overall directionality were computed automatically.

Segments

Track segments were analysed to identify changes in velocity, run length, pause duration and frequency. This macro recorded the detailed dynamics of individual mitochondrial movements.

PoolData

Final data were compiled and exported as text files, with each parameter analysed across datasets.

The workflow is illustrated in Fig 14, showing kymograph generation and segment analysis. Table 2 provides detailed definitions of the quantified parameters, such as mitochondrial velocity, run length and pause frequency.

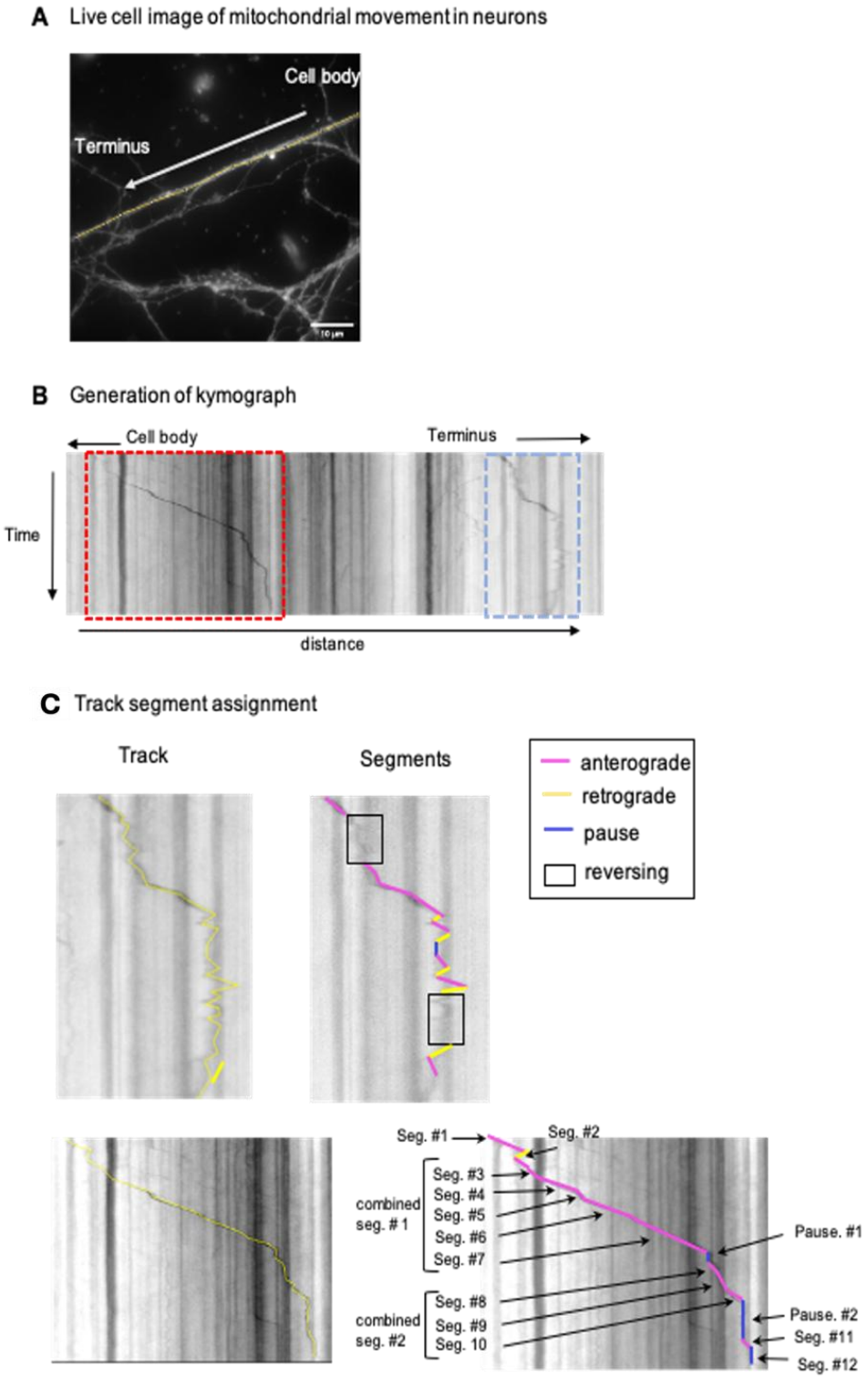

Figure 14. Generation of kymographs manual assignment of mitochondrial tracks.

(A) Axonal processes were manually traced using the 'BatchKymographGeneration' macro, with directionality assigned from the soma to the periphery. (B) Kymographs were generated using the 'Tracks' macro, with the cell body positioned on the left and the axonal terminus on the right. (C) Enlarged views of the regions indicated by red and blue boxes in (B) show segment assignments and pauses within tracks. Each track's velocity changes were represented as segments and combined segments reflect movement in the same direction.

Table 2. Description of transport-related parameters quantified by KymoAnalyzer

KymoAnalyzer parameters	Unit	Definition
Mitochondrial Fraction	-	Fraction of mitochondria that are moving either anterograde, retrograde, reversing or stationary.
Net Mitochondrial Fraction	-	Fraction of mitochondria that are moving either net anterograde, net retrograde or net stationary. Reversing mitochondria are either net anterograde or net retrograde.
Percent Time Motion	%	Percentage of total time that mitochondria spent on moving either anterograde or retrograde direction.
Net Velocity	µm/s	Net velocities of all mitochondria moving both net anterograde and net retrograde.
Segmental Velocity	µm/s	Average velocities of mitochondria travel within a single segment - a portion of a motion track with a constant velocity.
Combined Segmental Velocity	µm/s	Average velocity of mitochondria traveling within a combined segment - a period of movement in the same direction within a track, delimited by pauses or reversals.
Run Length	µm	Length of combined segmental runs regardless of direction.

Pause Duration	-	Total duration of pauses of all mitochondria (mitochondria moving ≥0.1 μm/s).
Pause Frequency	pauses/s	Frequency of pauses per moving mitochondria per second with either direction.

2.3 Micropatterning and surface functionalisation

2.3.1 Microcontact printing

Poly(dimethylsiloxane) (PDMS; Sylgard 184, DowSil, UK) stamps were fabricated for μCP. A 10:1 ratio of polymer base to curing agent was mixed, degassed in a vacuum desiccator for 30 min, and cast onto a silicon master patterned with SU-8 photoresist (SU8 3010). The PDMS was cured at 50°C overnight or at 80°C for 2 h before peeling off the master. The micropatterned SU-8 master was provided by Dr Michele Zagnoni (University of Strathclyde) and contained a range of designs with nodes (5μm and 10 μm) and interconnecting lines (10 μm). PDMS stamps were cut and optionally treated with oxygen plasma (18 s, 50W) to enhance hydrophilicity. The stamps were sterilised under UV light for 15 min. Inks, including 100 μg/ml PDL, 100 μg/ml Laminin, a 1:1 mixture of laminin-PDL (50 μg/ml each) or 100 μg/ml FITC-PLL (P3069, Sigma) were prepared using the same protocols described in section 2.1.2 and adsorbed onto the stamps for 30 min. Stamps were rinsed with sterile water three times, blow-dried with nitrogen gun and gently tapped onto coverslips for 15 min. Once the stamps were removed carefully from the surface, coverslips were washed with sterile water twice and stored either in dried condition (PDL) or in sterile water (laminin or laminin-PDL) until use.

2.3.2 Micropattern Image Stitching

To generate a continuous representation of micropatterned substrates, individual high-resolution images were acquired and stitched together using Image J's Grid/Collection Stitching plugin. Images were captured sequentially along the patterned substrates, ensuring sufficient overlap between adjacent images to facilitate accurate alignment. The grid size was defined based on the number of

images acquired per row and column, with an average of five to eight images successfully stitched together per sample.

2.3.3 Blocking surface to prevent off-pattern cell adhesion

To backfill micropatterned substrates, silanes such as 1% (v/v) of Trichloro(1H,1H,2H,2H-perfluorooctyl)silane (PFS; Sigma) (Fig 15A) in ethanol or 5% (v/v) of dichlorodimethylsilane (DCDMS; Fluka) (Fig 15B) in toluene were applied for 30 min at room temperature. Coverslips treated were rinsed three times with ethanol, air-dried and baked at 80°C for 30 min. Alternatively, 0.5% (w/v) of Lipidure®-CM (CN5206, AMSBIO, Abingdon) in ethanol was applied for 1 min, rinsed with ethanol three times and dried at room temperature until use.

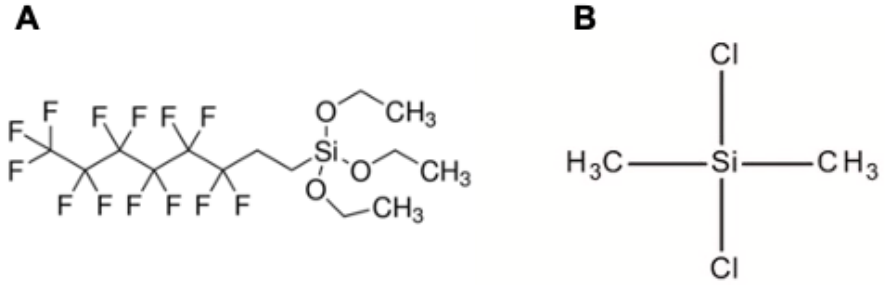

Figure 15. Chemical structure of (A) PFS and (B) DCDMS.

2.4 Statistical analyses

Statistical analyses were conducted using GraphPad Prism. For mitochondrial motility analysis, Kolmogorov-Smirnov non-parametric unpaired t-tests were applied to assess differences between two independent groups, while Kruskal-Wallis non-parametric ANOVA followed by Dunn's post-hoc test was used for multiple group comparisons. Data were presented as mean ± standard deviation (SD). For micropattern analysis, one-way ANOVA was performed to quantify the proportion of cells adhering to patterns, and paired t-tests (Wilcoxon test) were used to compare cell type distributions between different substrates paired in immunocytochemistry analysis of micropatterned cultures. A significance threshold of $p < 0.05$ was used for all statistical analyses.

CHAPTER THREE:
Quantification of Mitochondrial Motility in "Standard" Primary Hippocampal Cells

3.1 Introduction

The goal of this chapter was to identify a satisfactory method for quantifying key parameters of mitochondrial motility, that could subsequently be applied to evaluate mitochondrial dynamics in neurons cultured on surface-modified substrates throughout the project. Live-cell imaging enables the visualisation of neuronal networks and is essential for tracking mitochondrial movement. Mitochondria display diverse and complex motion patterns. A single mitochondrion may undergo a burst of directed motion of tens of µm, pause, switch direction, exhibit jittery back-and-forth movement or remain stationary, appearing tethered to a specific location. Quantifying these intricate motility patterns presents significant technical challenges due to the small size of mitochondria and the variability of their movements.

Initially, an in-house generated ImageJ macro was employed, which utilised sequential image subtraction to calculate the overall area that mitochondria moved into (normalised to total mitochondrial area). However, the resultant measurements were highly variable and influenced by factors unrelated to mitochondrial motility, such as cell density and background fluorescence intensity. To address these limitations, the published analysis tool KymoAnalyzer was adopted (Neumann *et al*., 2017). KymoAnalyzer offers robust quantification of motility-related parameters, including the fraction of motile mitochondria, velocities, run lengths and frequencies of pausing or direction-switching. Unlike simpler analysis tools, KymoAnalyzer provides a comprehensive assessment of mitochondrial dynamics and demonstrates resilience to challenges such as low signal-to-noise ratios or high mitochondrial density (Neumann *et al*., 2017). However, the analysis process is labour-intensive, requiring manual tracing of mitochondrial tracks, which introduces the potential for user bias when selecting neurite trajectories for analysis (Neuman *et al*., 2017; Jakobs *et al*., 2019; Shahen *et al*., 2018). Mitochondrial movement in neurons is predominantly microtubule-dependent, with some involvement of actin filaments (Morris and Hollenbeck, 1995; Ligon and Steward, 2000). To evaluate the suitability of KymoAnalyzer for mitochondrial

motility studies, hippocampal neurons were treated with nocodazole, a microtubule polymerisation inhibitor, and latrunculin B, an actin polymerisation inhibitor that is not expected to significantly affect mitochondrial transport.

To further validate KymoAnalyzer and investigate mitochondrial motility in relation to neuronal development, additional experiments assessed motility changes at different stages of neuronal maturation (7 to 21 days *in vitro*, DIV). These time points were chosen to represent different stages of maturation as synapse formation and spontaneous calcium oscillations, which typically occur around DIV 12-14 (Basarsky *et al*., 1994). Mitochondrial motility has been shown to decline significantly during neuronal maturation, both *in vitro* and *in vivo* (Lewis *et al*., 2016; Smit-Rigter *et al*., 2016). This study aims to leverage the detailed motion-related parameters provided by KymoAnalyzer to offer novel insights into mitochondrial dynamics across neuronal maturation, extending beyond the scope of existing literature. By incorporating these comprehensive analyses, this chapter not only highlights the utility of KymoAnalyzer as a quantitative tool but also contributes to a deeper understanding of how mitochondrial motility evolves during neuronal development.

3.2 Results

3.2.1 Mitochondrial Motility Following Pharmacological Disruption of Microtubules or Actin Cytoskeleton

To determine the dependence of mitochondrial motility on the cytoskeletal network, hippocampal cells cultured on PDL-substrates was monitored at DIV 7 before and after treatment *in situ* with either the microtubule-depolymerising drug nocodazole (10 µM) or the actin-destabilising drug latrunculinB (10 µM). Cells were loaded with MitoTracker Green (100 nM) for 30 min and imaged for 3 min. Following a 60-min *in situ* drug treatment, the same cells were re-imaged for another 3 min. Using KymoAnalyzer, individual neurites were manually traced to generate kymographs and mitochondrial movement was tracked over time to extract motility-associated parameters.

Representative still frames from single cell region imaged before and after incubation with nocodazole are shown in Fig 16. Prior to drug exposure, mitochondria appeared to actively move along neurites (Fig 16A, two example mitochondria are highlighted in blue and pink moving >25 µm in the upper image panels) which motions were visible as non-vertical lines on the corresponding kymograph. Following nocodazole treatment, mitochondrial motility was significantly reduced, with most mitochondria remaining stationary or displaying minimal displacement (Fig 16B, examples highlighted in orange and green). This reduction in movement is evident in the corresponding kymograph, where fewer diagonal trajectories and an increase in vertical stationary lines indicate a substantial decline in active transport.

In contrast, latrunculin B treatment did not appear to significantly alter mitochondrial transport. Prior to treatment, mitochondria exhibited active movement along neurites, which was captured as diagonal trajectories in the kymograph (Fig 17A, examples highlighted in orange and red). After latrunculin B treatment, mitochondrial motility remained largely unaffected, with moving mitochondria still visible (Fig 17B, highlighted in green and blue). The corresponding kymograph continued to display diagonal trajectories, suggesting that actin cytoskeleton disruption does not significantly impair mitochondrial movement in hippocampal neurons.

These findings indicate that mitochondrial motility in hippocampal cells is primarily microtubule-dependent, as nocodazole-mediated microtubule depolymerisation led to a marked reduction in transport. In contrast, actin filament disruption with latrunculin B had little effect on mitochondrial motility, suggesting a more limited role of the actin cytoskeleton in long-range mitochondrial transport.

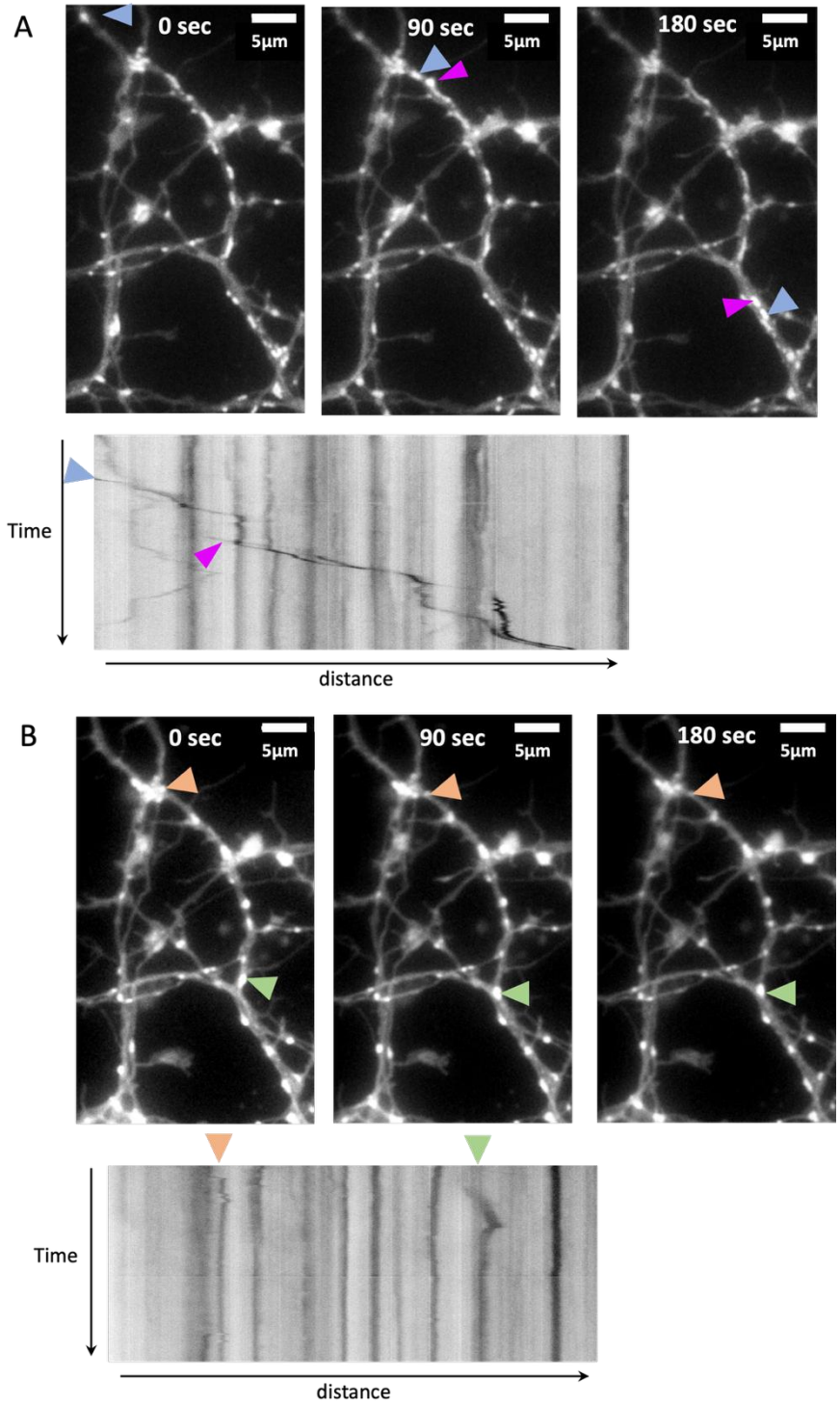

Figure 16. Mitochondrial motility in hippocampal cells before and after nocodazole treatment.

Hippocampal cell cultures loaded with 100 nM MitoTracker Green were imaged for 180 s then treated with 10 µM nocodazole. (A) Mitochondria in neurites at 0, 90 and 190 s. Two motile mitochondria (blue and purple arrows) exhibit active

transport before treatment. The corresponding kymograph displays these mitochondria as diagonal trajectories, while stationary mitochondria appear as vertical lines. (B) The same region after nocodazole treatment. Two mitochondria (orange and green arrows) show minimal displacement. The kymograph reflects the reduction in motility. Scale bars = 5 µm.

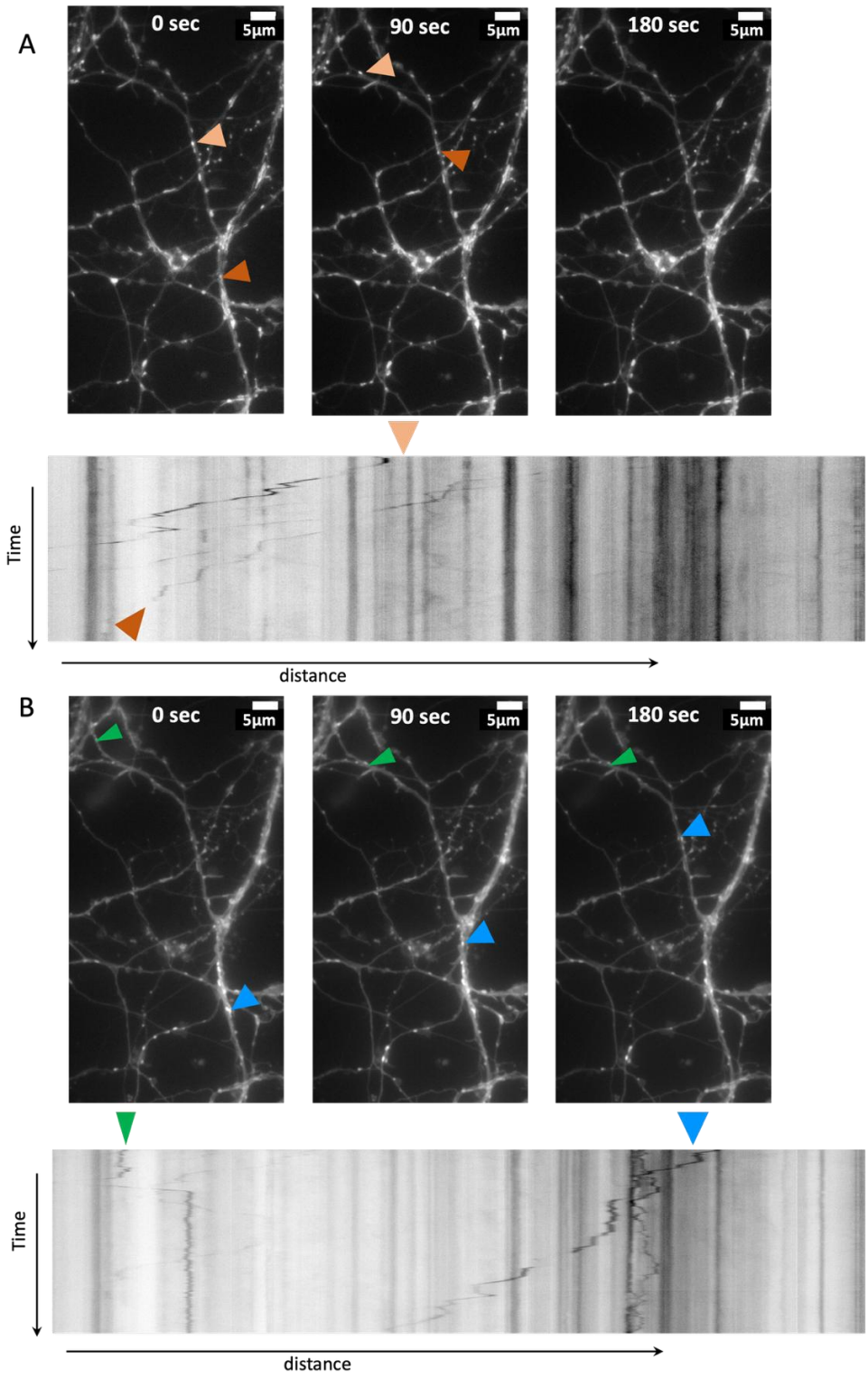

Figure 17. Mitochondrial motility in hippocampal cells before and after latrunculin B treatment.

Cells were imaged for 180 s before and after treatment with 10 µM latrunculinB. (A)

Before treatment, moving mitochondria (orange and red arrows) exhibit long-range

transport represented as diagonal trajectories in the kymograph. (B) After latrunculin B treatment, mitochondrial movement remains largely unaffected, with moving mitochondria (blue and green arrows) continuing to exhibit directed motion in the kymograph. Scale bar = 5 µm.

3.2.2 KymoAnalyzer Quantification of Mitochondrial Motion-Related Parameters

Once the kymographs were generated for each manually traced neurite from the live-cell imaged regions, individual mitochondrial trajectories were manually annotated on kymographs (representative examples in Fig 18, showing motion of mitochondria for untreated, nocodazole-treated and latrunculin B-treated cells). Various transport parameters were extracted by KymoAnalyzer. One of the primary parameters analysed was the fraction of motile (regardless of directionality: including anterograde, retrograde and reversing) or stationary (Fig 18A-B).

In untreated cells, 44.7% of mitochondria were motile (median, interquartile range [IQR] = 28.6 – 61.0). However, after nocodazole treatment, this proportion significantly decreased to 21.8% (IQR = 10.0 – 38.3; $p>0.001$), with a corresponding increase in stationary mitochondria (Fig 18A). Similarly, latrunculin B treatment also resulted in a lower fraction of motile mitochondria, decreasing from 44.5% in untreated cells (IQR = 29.7 – 55.6) to 20.7% after treatment (IQR = 14.3 – 40.1; $p<0.01$; Fig 18B).

As mitochondria are not constantly motile, it is also informative to consider what fraction of time do those mitochondria that are motile spend in motion, thus KymoAnalyzer also calculates the percent time in motion. When the percentage of the time that mitochondria spent either moving or paused was calculated, there was a considerable decrease in moving time after nocodazole treatment, from 51.0% in untreated cells (IQR = 19.5 – 89.3) to 32.3% after treatment (IQR = 13.2 – 65.8; $p<0.001$; Fig 18C). In contrast, latrunculin B treatment did not cause a significant change in this parameter, as motile mitochondria in untreated cells spent 42.0% of their time moving (IQR = 15.3 – 86.2), compared to 48.0% in latrunculin B-treated cells (IQR = 17.5 – 96.8; $p>0.05$; Fig 18D). Representative kymographs further illustrate these trends (Fig 18E). In control cells, kymographs contained a

higher density of non-vertical tracks, indicating greater mitochondrial movement. Following nocodazole treatment, kymographs showed fewer diagonal tracks, reflecting a reduction in motility. The kymographs for latrunculin B-treated cells, however, still contained several motile mitochondria with unidirectional (green and red) and reversal (yellow) tracks, similar to untreated conditions. These results support the quantitative analysis, further demonstrating that microtubule disruption significantly impairs mitochondrial motility, whereas actin disruption results in a more variable response, with some impairment observed but less consistently than with nocodazole treatment.

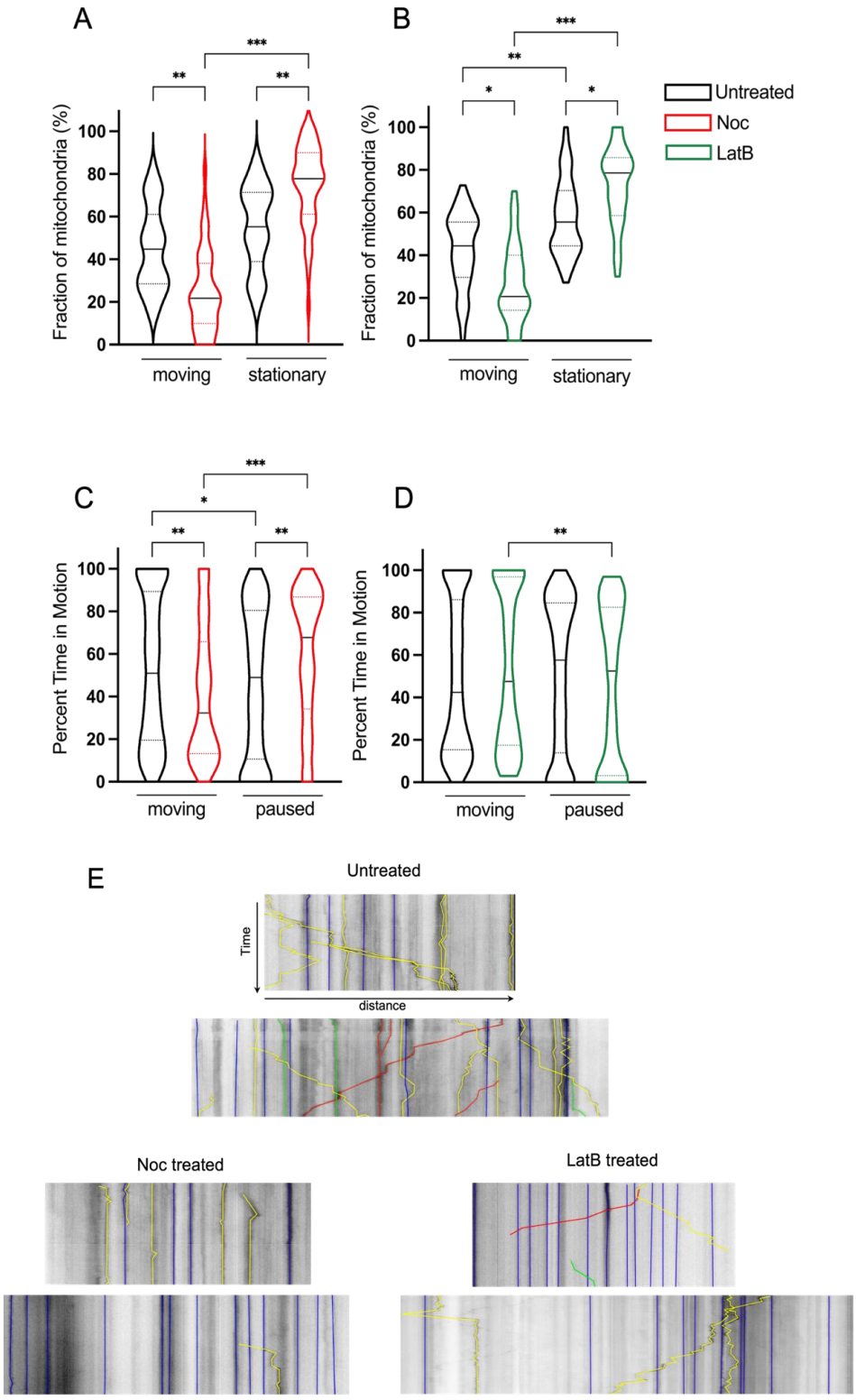

Figure 18. Quantification of mitochondrial motility in hippocampal cells before and after nocodazole or latrunculin B treatment.

(A) Fraction of mitochondria before and after nocodazole or (B) latrunculin B treatment. (C) Percentage of time of motile mitochondria before and after

*nocodazole or (D) latrunculin B treatment. *P<0.01, **P<0.001 and ***P<0.0001. Violin plots show the distribution of all data points, with median values (solid black lines) and 1.5 x interquartile range (dotted line). Statistical analyses were performed using Kruskal-Wallis non-parametric tests followed by Dunn's post-hoc analysis. (E) Representative kymographs showing mitochondrial transport before and after nocodazole or latrunculin B treatment. Manually traced mitochondrial trajectories are colour-coded: unidirectional (green and red), reversal (yellow) and stationary mitochondria (blue). Data were collected from 3 independent cultures, with 5 regions/images per culture and per drug treatment condition. For each image, 5-10 neurites were manually traced to generate kymographs for analysis*

To further investigate the transport properties of motile mitochondria, velocity-related parameters were quantified, including net velocity, segmental velocity and run length (Fig 19). Net velocity represents the overall displacement per unit time, while segmental velocity measures movement within a single burst without changes in speed or direction. Run length refers to the total distance travelled across multiple movement bursts (see Table 1 in Chapter 2).

Following nocodazole treatment, mitochondria exhibited a significant reduction in motility across all velocity parameters. The median net velocity decreased from 229 nm/s in untreated cells to 48 nm/s after nocodazole treatment ($p<0.0001$), and segmental velocity decreased from 339 to 225 nm/s ($p<0.0001$) (Fig 19A-B).

Similarly, the median run length was reduced from 7.93 µm in untreated cells to 4.49 µm after nocodazole treatment ($p<0.0001$) (Fig 19C). These findings are consistent with the role of microtubules as essential tracks for mitochondrial transport, with nocodazole-induced microtubule depolymerisation severely impairing mitochondrial movement. In contrast, latrunculin B treatment did not significantly affect mitochondrial velocity or run length (Fig 19A-C), indicating that while actin filaments may regulate the transport dynamics of motile mitochondria, although their disruption decreases the proportion of mitochondria that are motile.

Representative kymographs illustrate these differences (Fig 19D-E). In untreated cells, kymographs show a high proportion of moving mitochondria, displaying long unidirectional (green and red) and reversing (yellow) trajectories. Following nocodazole treatment, the kymographs predominantly consist of vertical stationary mitochondria (blue). Figure 19E further highlights individual mitochondria tracks with velocity and pausing characteristics. In untreated cells, numerous non-vertical tracks are present, reflecting frequent changes in speed and direction within a given trajectory. In contrast, after nocodazole treatment, fewer motile mitochondria are observed with significantly shorter run lengths and more frequent pauses.

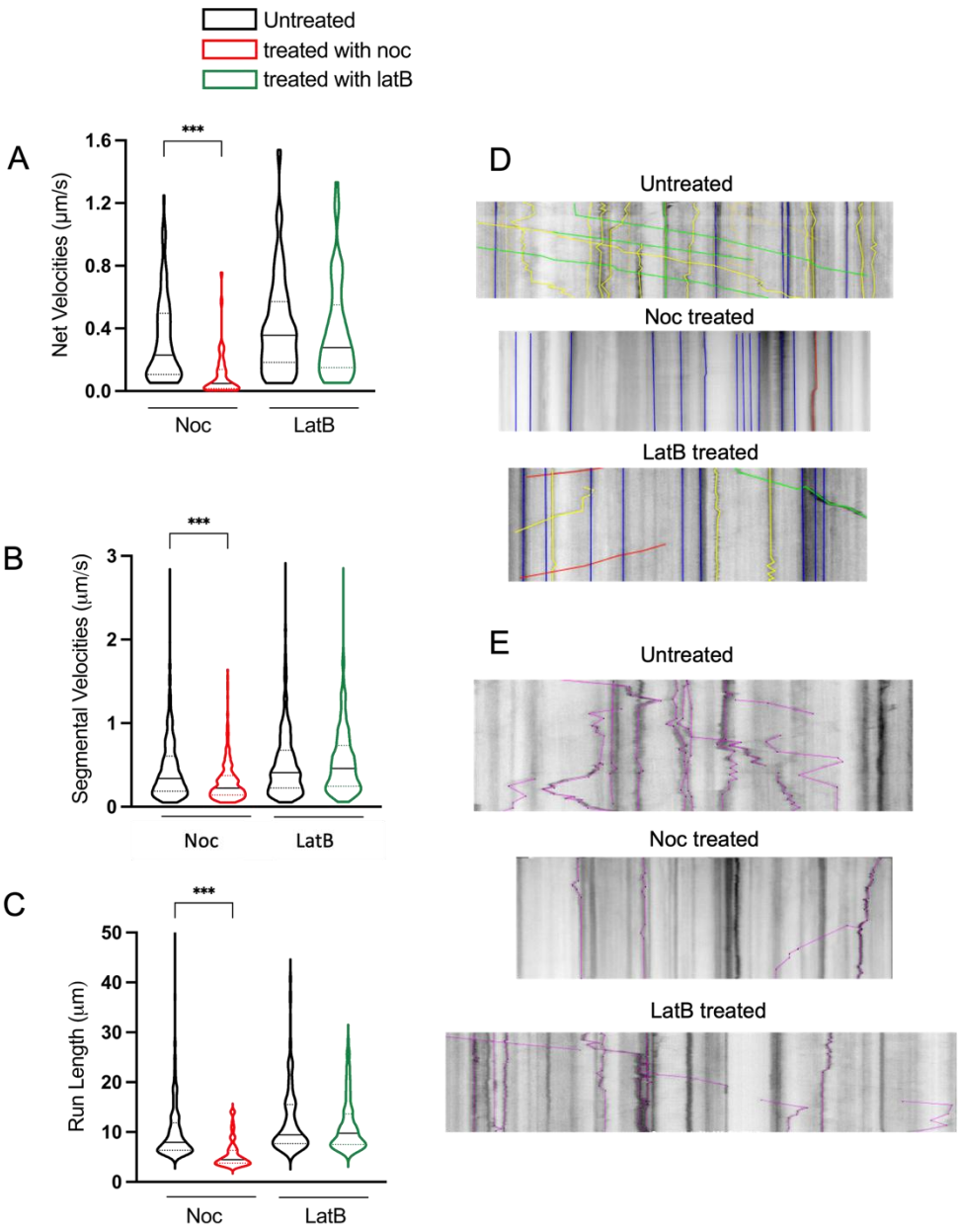

Figure 19. Mitochondrial velocity and run lengths analysis before and after treatment with nocodazole or latrunculin B.

(A) Net velocities of mitochondria before and after treatment, representing the overall displacement per unit time. (B) Segmental velocities, measured within single segment bursts of motion without changes in speed or direction. (C) Run length, defined as the cumulative distance travelled across multiple movement segments. (D) Representative kymographs showing mitochondrial movement under control conditions and after nocodazole or latrunculin B. Unidirectional movement is

*indicated in green and red, reversal in yellow and stationary mitochondria in blue. (E) Representative kymographs illustrating track segment assignment. Only motile mitochondria are displayed in purple, showing variations in velocity and pausing behaviour. Statistical comparisons were conducted using Kolmogorov-Smirnov non-parametric unpaired t-tests, with statistical analysis between pairs of treatment groups, p<0.05 considered significant, *** = p<0.0001.*

The efficiency of mitochondrial transport can also be assessed by measuring how much the organelles pause or change direction. To quantify these parameters, the number of pauses and switches (direction reversals) that mitochondria made while travelling per track per unit of time were calculated (Fig 20). Following nocodazole treatment, mitochondria showed a significant increase in pause frequency, with the median frequency increasing from 0.0116 s^{-1} (IQR = 0.011 – 0.018) in control cells to 0.0118 s^{-1} (IQR – 0.011 – 0.018) after nocodazole treatment ($p < 0.01$) (Fig 20A). Similarly, the frequency of directional switches also increased significantly, rising from 0.0117 s^{-1} (IQR – 0.006 – 0.018) in control cells to 0.0168 s^{-1} (IQR = 0.006 – 0.039) after nocodazole treatment ($p <0.0001$) (Fig 20B). These results indicate that microtubule depolymerisation leads to a disruption in mitochondrial transport, increasing stochastic pausing and direction switching. In contrast, latrunculin B treatment did not significantly alter either parameter, suggesting that actin filaments play a minimal role in regulating mitochondrial pausing and directional control.

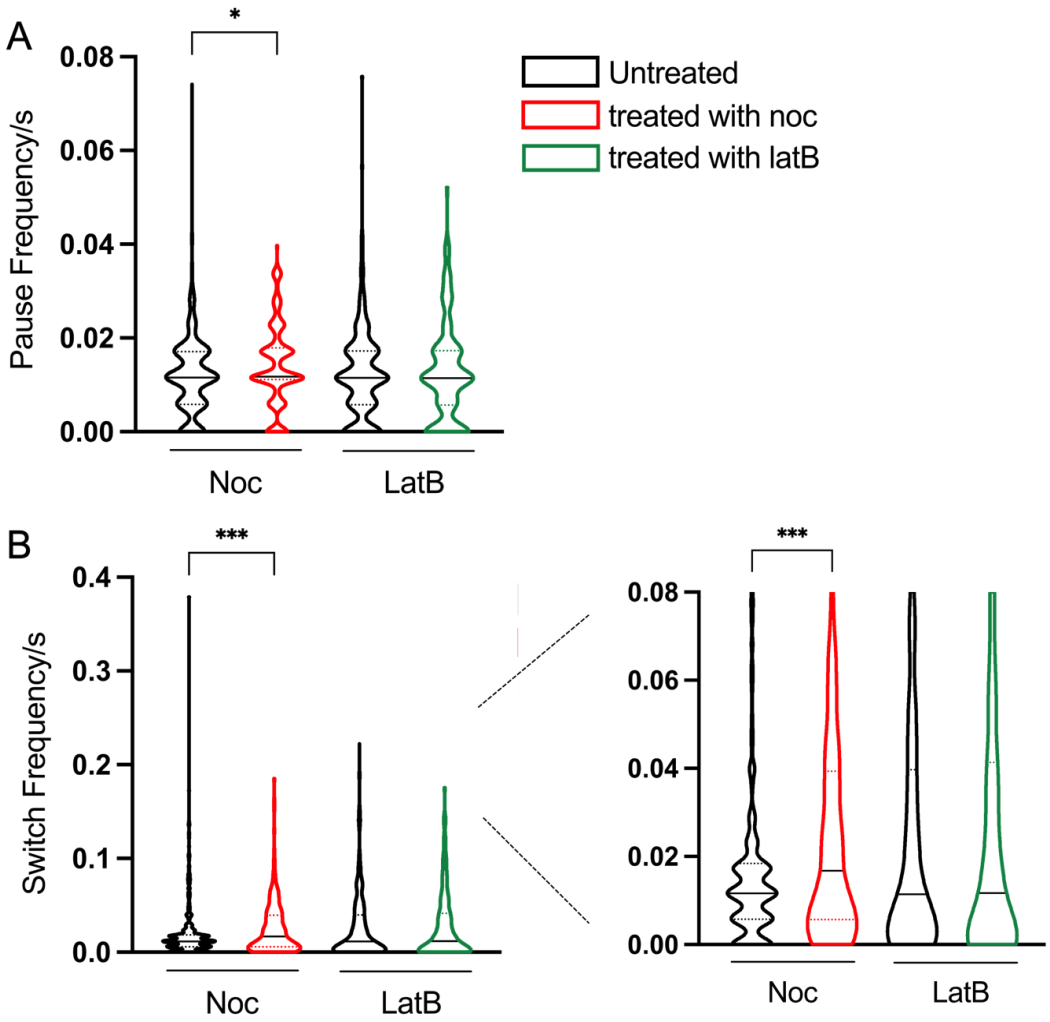

Figure 20. Quantification of mitochondrial pausing and directional switching before and after nocodazole or latrunculin B treatment.

*(A) Pause frequency, defined as the number of pauses per track, where segmental velocity ≤ 0.1 µm/s. (B) Switch frequency, representing the number of directional reversals per track during the imaging period. The panel on the right displays a zoomed-in view of the data to highlight median values and interquartile ranges. Statistical significance was determined using the Kolmogorov-Smirnov non-parametric unpaired t-test following normality testing. *= p<0.01, *** = p<0.0001.*

3.2.3 Changes in Mitochondrial Motility with Neuronal Maturation In Vitro

Following the validation of mitochondrial movement analysis with and without cytoskeletal disruption, the same methodology was applied to examine changes in mitochondrial motility during neuronal maturation *in vitro*. Hippocampal cells were cultured on PDL-coated substrates and mitochondrial movement was analysed at different time points; DIV 7, 10, 14-15 and 19-21.

Mitochondria were visualised using two different labelling methods: MitoTracker Green (100 nM) staining or expression of MitoRFP through BacMam transduction. The BacMam construct (CellLights BacMam 2.0 Life Technologies) was introduced into cell cultures at DIV 1 at a concentration of 200,000 particles per dish (0.95 particles per cell), ensuring a low transfection rate. At these two methods differ in their mechanisms for visualising mitochondria, potential differences in mitochondrial motility between labelling strategies were examined and quantified using KymoAnalyzer.

Mitochondrial motility was first examined in MitoRFP-expressing neurons, with representative images shown in Figure 21. Fig 21A displays still frames of mitochondria at different time points (DIV 7, 10, 15, and 21), with tracked neurite trajectories overlaid in red. At DIV 7, mitochondria exhibited short-distance, slow movements, whereas at DIV 10 and 15, mitochondria displayed more frequent and longer-range transport, with overlapping trajectories. By DIV 21, mitochondrial movement was largely absent, though occasional motile mitochondria were observed in other neurite regions, suggesting that the cells remained viable. The corresponding kymographs (Fig 21B) depict mitochondrial movement over time along the tracked neurite paths, confirming these observed changes in motility.

A similar trend was observed in neurons labelled with MitoTracker Green, as shown in Figure 22. Figure 22A presents still frames of mitochondrial movement at DIV 7, 10, and 15, with manually drawn mitochondrial tracks (red lines) overlaid on the images. Unlike the MitoRFP dataset, cells were recorded from different regions for each time point, as MitoTracker staining requires separate labelling for each session. The resulting kymographs (Fig 22B) confirm that mitochondrial motility was

present at DIV 7, 10, and 15, with movement along neurites visible at all recorded time points. However, cells did not survive at DIV 21, preventing further imaging at this stage. Despite the differences in labelling strategies, both MitoRFP and MitoTracker Green datasets demonstrated a progressive decline in mitochondrial motility with neuronal maturation, with the most active transport observed at DIV 7 and 10.

While these observations suggest a correlation between neuronal maturation and mitochondrial transport dynamics, a quantitative analysis of motility parameters is necessary to confirm these trends. In the following section, KymoAnalyzer was used to extract detailed transport parameters, allowing a direct comparison across developmental stages, similar to the analyses performed for nocodazole- and latrunculin B-treated cells.

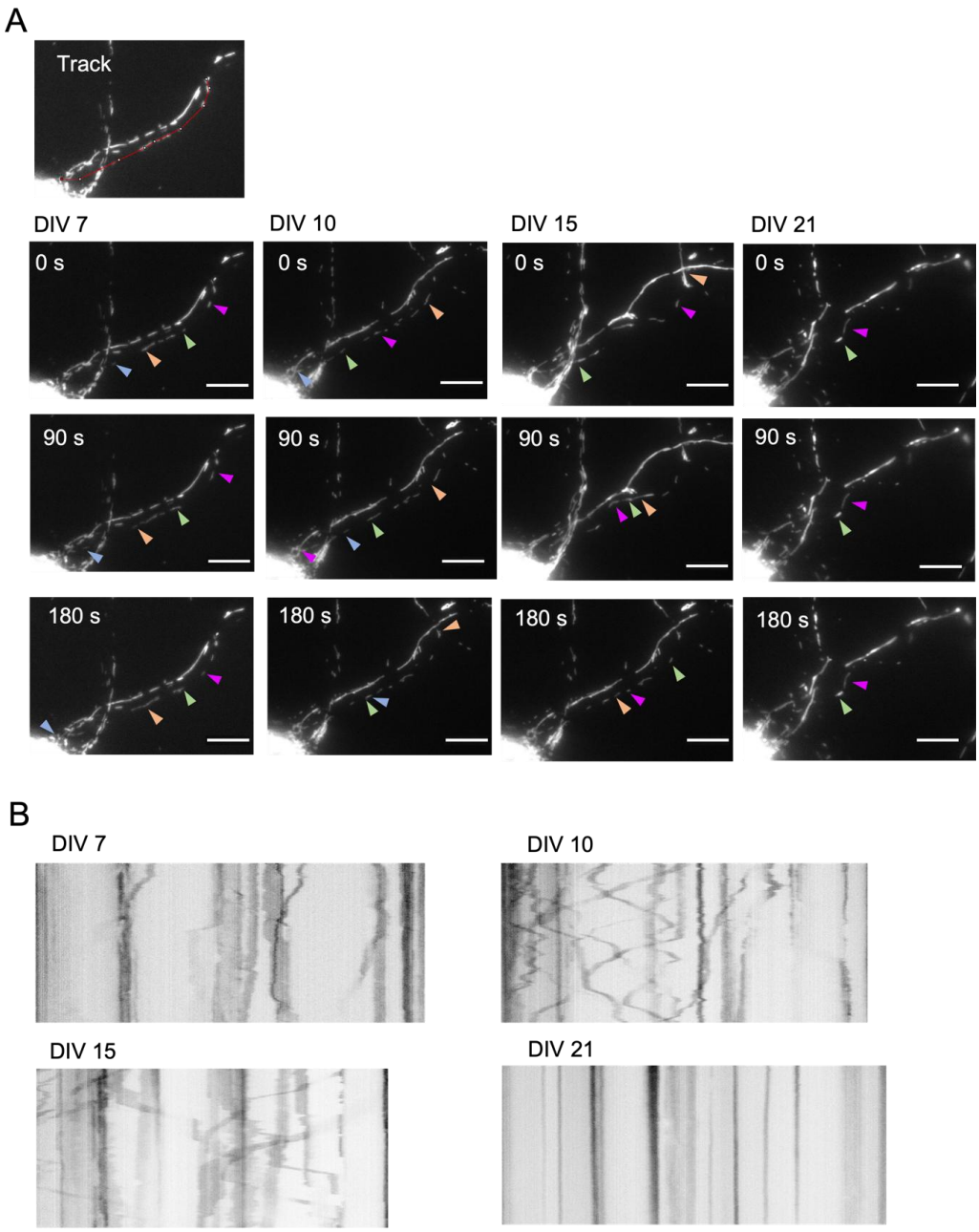

Figure 21. Mitochondrial movement in the same hippocampal cells tracked over 3 weeks using MitoRFP labelling.

(A) Still frames of mitochondrial movement in a single neuron imaged at DIV 7, 10, 15 and 21. The same cell was identified and tracked at each time point using a gridded chamber system, allowing precise relocation of the imaging region across multiple sessions. Representative neurites trajectories are shown in red (upper panels). Scale bar = 10 µm. (B) Corresponding kymographs depicting mitochondrial movement along the tracked neurites at each time point.

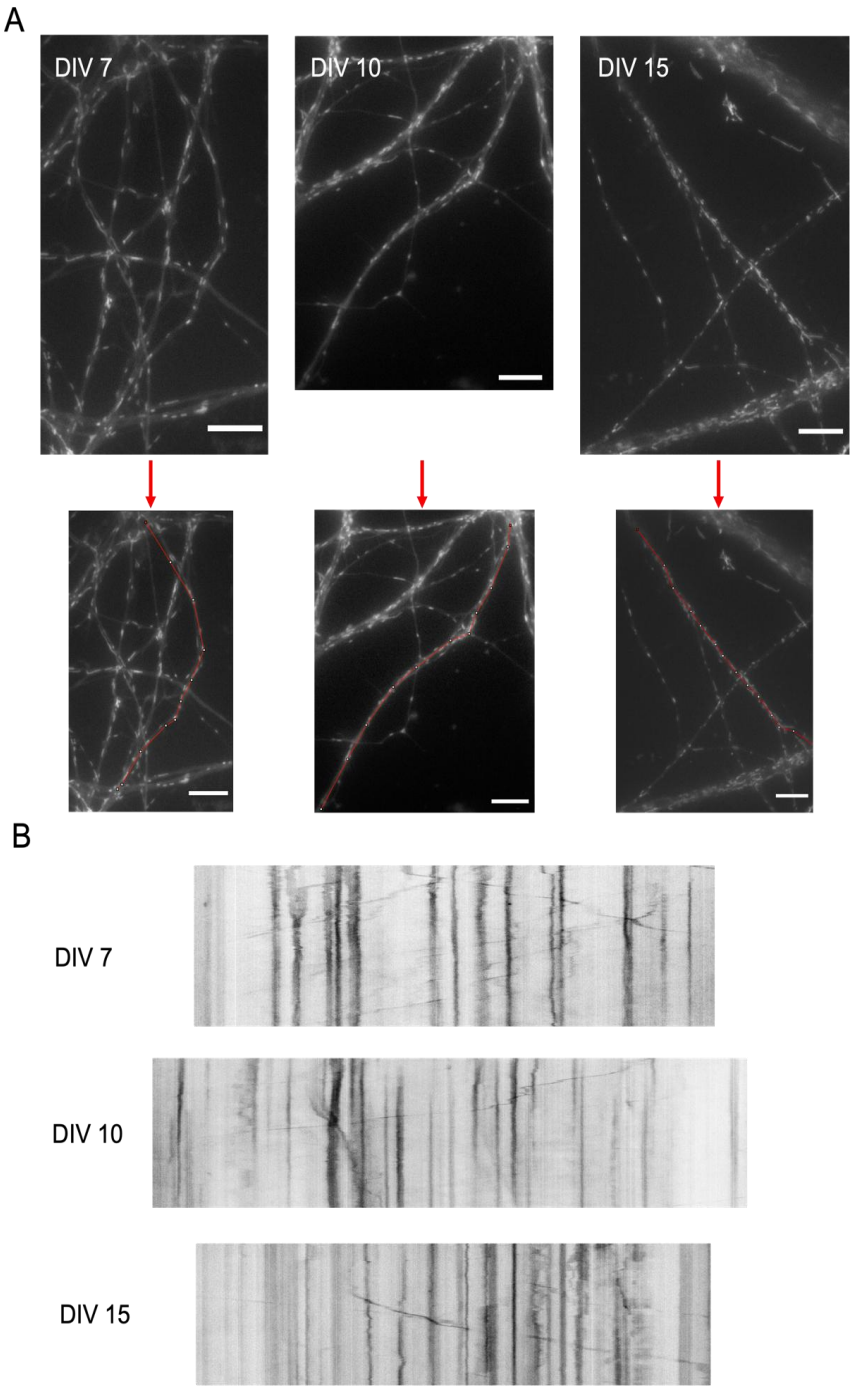

Figure 22. Mitochondrial movement in hippocampal cells during in vitro maturation (MitoTracker labelling).

(A) Still frames of mitochondrial movement in neurons stained with MitoTracker Green at DIV 7, 10 and 15. Manually drawn mitochondrial tracks are shown in red (lower panels). Cells did not survive at DIV 21. Scale bar = 10 µm. (B) Corresponding kymographs illustrating mitochondrial motility at each time point.

3.2.4 KymoAnalyzer Quantification of Motion Within Neuronal Processes – MitoRFP and MitoTracker Green

To quantitatively assess mitochondrial motility changes during neuronal maturation, KymoAnalyzer was used to analyse mitochondria in hippocampal neurons at different time points (DIV7, 10, 14-15 and 19-21). Mitochondrial motilities were measured in both MitoRFP-expressing cells and MitoTracker Green-labelled cells, allowing for a direct comparison of mitochondrial movement trends using two distinct labelling methods. The fraction of motile mitochondria, regardless of directionality (combining purely anterograde, retrograde and reversing movements), was calculated (Fig 23A). In both MitoRFP and MitoTracker Green datasets, mitochondrial motility progressively declined with increasing neuronal age. In MitoRFP-expressing cells, the fraction of motile mitochondria decreased from a median of 38.5% at DIV 7 (IQR = 19.1 – 60.8) to 13.7% at DIV 10 (IQR = 0.0 – 33.3), 25% at DIV 14-15 (IQR = 0.0 – 44.7) and finally 0% at DIV 19-21 (IQR = 0.0 – 0.0) (Fig 23A, left panel). A similar pattern was observed in MitoTracker Green-labelled cells, with motile mitochondria decreasing from 50% at DIV 7 (IQR = 41.7 – 60.0) to 30% at DIV 10 (IQR = 14.3 – 42.9) and 26.9% at DIV 14-15 (IQR = 11.1 – 41.2) (Fig 23A, right panel). However, imaging could not be performed at DIV 19-21 for MitoTracker Green-labelled cells as cells did not survive at this stage.

To further classify mitochondrial movement patterns, mitochondria were categorised into unidirectional (anterograde or retrograde), reversing, or stationary populations (Figure 23B). At DIV 7, when mitochondrial motility was highest, the majority of motile mitochondria exhibited reversing movements rather than purely unidirectional transport. In MitoRFP-expressing cells, reversing mitochondria accounted for 25% (IQR = 10.6 – 47.5), while unidirectional mitochondria were 7.69% (IQR = 0.0 – 18.8) (Figure 23B, upper panel). Similarly, in MitoTracker Green-labelled cells, reversing mitochondria were 36.36% (IQR = 26.7 – 50.0), whereas unidirectional mitochondria accounted for 12.5% (IQR = 5.6 – 20.0) (Fig 23B, lower panel). At later time points (DIV 10, 14–15 and 19–21), the fraction of motile mitochondria decreased, with an increasing proportion of stationary mitochondria.

By DIV 19–21, nearly all mitochondria remained stationary in MitoRFP-expressing cells.

Representative kymographs illustrate mitochondrial movement patterns at each time point (Fig 23C). The kymographs confirm the progressive reduction in motility across neuronal maturation, with frequent reversing trajectories observed at DIV 7, which are represented as yellow lines. As neuronal maturation progressed, these reversing movements became less frequent, and an increasing proportion of mitochondria remained stationary, which are represented as blue lines. Both labelling methods revealed a similar trend of declining mitochondrial motility with increasing neuronal age, supporting the hypothesis that mitochondrial transport is dynamically regulated during neuronal maturation.

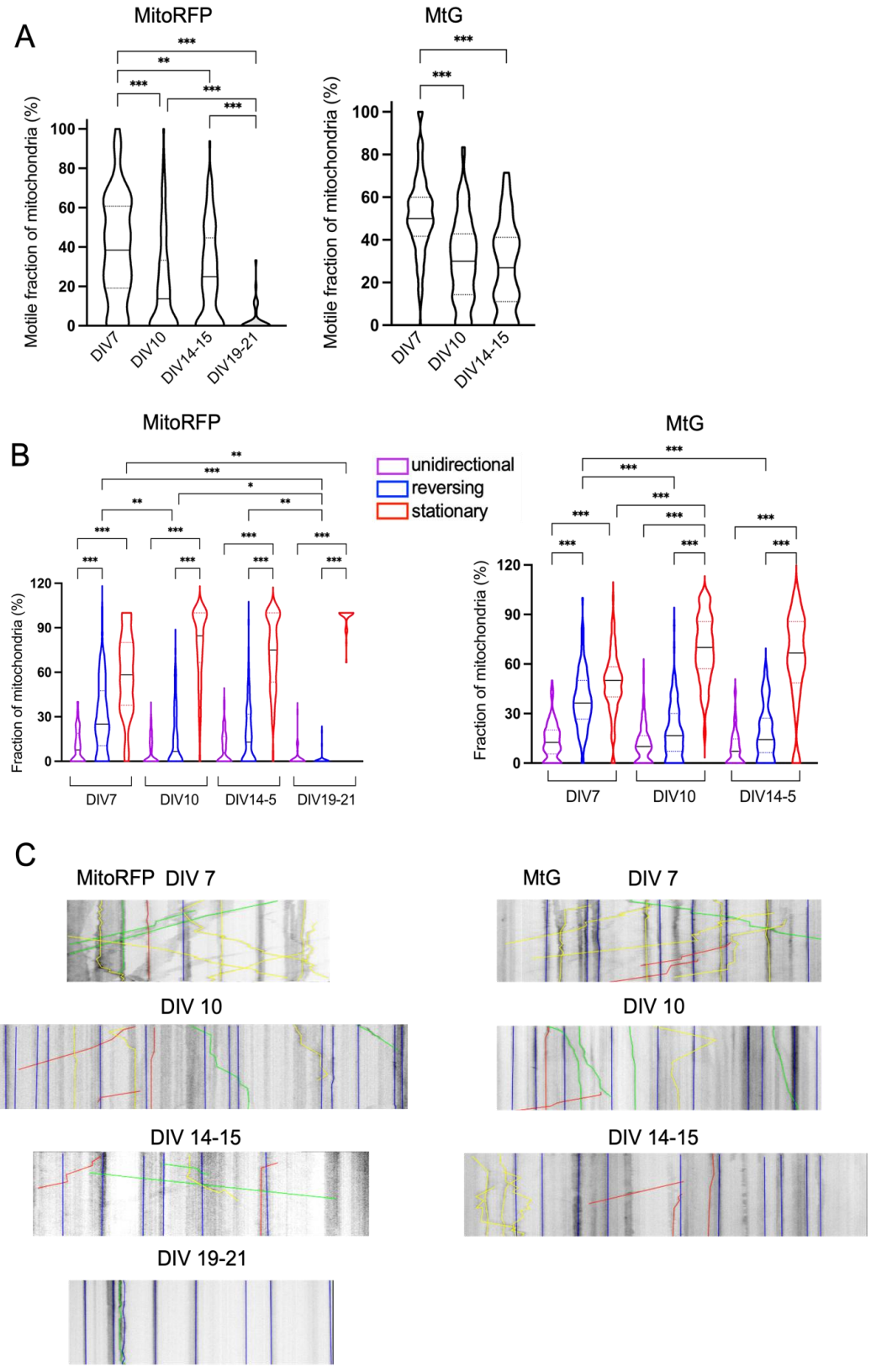

Figure 23. Quantification of mitochondrial motility across neuronal maturation in hippocampal cell cultures (DIV 7, 10, 14-15 and 19-21).

*(A) Fraction of all motile mitochondria, measured in neurons expressing MitoRFP (left) and neurons labelled with MitoTracker Green (right). No data were available for MitoTracker Green at DIV 19-21 due to cell death. (B) Classification of mitochondrial movement directionality (unidirectional, reversing or stationary) at different time points. MitoRFP-labelled mitochondria are shown in the left panel and MitoTracker Green-labelled mitochondria are shown in the right panel. (C) Representative kymographs illustrating mitochondrial movement at each time point. Colour-coded tracks denote different movement types: unidirectional (red, green), reversing (yellow) and stationary (blue) for each time point is shown that supports quantitative data. *= p<0.05, ** p<0.005 and *** = p<0.0001.*

To further explore mitochondrial motility dynamics during neuronal maturation, velocity-related parameters were analysed at different time points (DIV 7, 10, 14–15, and 19–21) using KymoAnalyzer. Mitochondrial velocity and travelled distance were compared between MitoRFP-expressing cells and MitoTracker Green-labelled cells (Fig 24).

When net velocity was calculated, no significant differences were observed across different time points (Fig 24A). However, it is important to note that fewer mitochondria were analysed at DIV 19–21 (Fig 24A, left panel with MitoRFP), as the overall fraction of motile mitochondria was the lowest at this stage (see Fig 23A). In contrast, segmental velocity analysis revealed a significant difference in mitochondrial movement among MitoRFP-expressing cells, while no notable changes were observed in MitoTracker Green-labelled cells (Fig 24B). The median segmental velocity in MitoRFP-expressing cells increased from 0.22 µm/s at DIV 7 (IQR = 0.13 – 0.39) to 0.25 µm/s at DIV 10 (IQR = 0.15 – 0.42) and 0.26 µm/s at DIV 14–15 (IQR = 0.15 – 0.46). However, at DIV 19–21, mitochondrial movement was significantly slower, with a median velocity of 0.14 µm/s (IQR = 0.10 – 0.20).

A similar trend was observed for combined segmental velocities, where the median velocity in MitoRFP-expressing cells increased from 0.20 µm/s at DIV 7 (IQR = 0.13 – 0.33) to 0.24 µm/s at DIV 10 (IQR = 0.15 – 0.38) and 0.25 µm/s at DIV 14–15

(IQR = 0.15 – 0.45). However, at DIV 19–21, mitochondrial movement slowed down considerably (Fig 24C, left panel). In contrast, mitochondria labelled with MitoTracker Green exhibited no significant changes in velocities across different time points (Fig 24C, right panel).

When the total distance travelled by mitochondria was analysed, mitochondria at DIV 19–21 displayed the shortest movement distances, with a median of 3.06 µm (IQR = 2.00 – 4.70) compared to 9.52 µm at DIV 7 (IQR = 7.80 – 16.2), 8.58 µm at DIV 10 (IQR = 6.37 – 13.2), and 8.55 µm at DIV 14–15 (IQR = 5.61 – 12.2) (Fig 24D).

Additionally, there were no significant differences in pause duration or the frequency of direction switches (reversals) between time points, regardless of labelling method (data not shown). Representative kymographs supporting these quantitative findings are presented in Fig 24E, where the progressive reduction in mitochondrial motility over time is visually apparent.

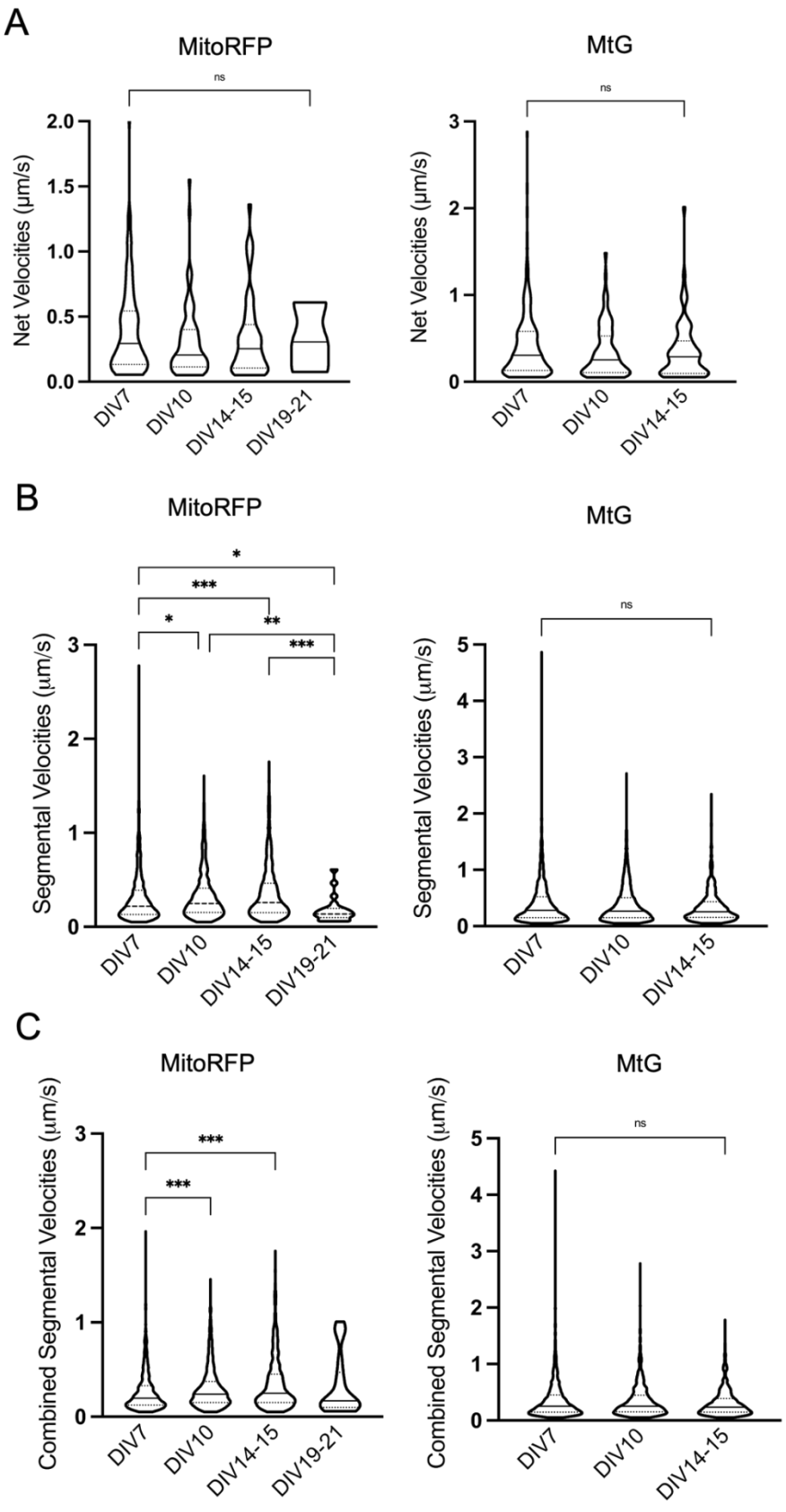
A
MitoRFP
MtG
Net Velocities (μm/s)
ns
DIV7
DIV10
DIV14-15
DIV19-21
B
MitoRFP
MtG
Segmental Velocities (μm/s)
*
***
**
C
MitoRFP
MtG
Combined Segmental Velocities (μm/s)

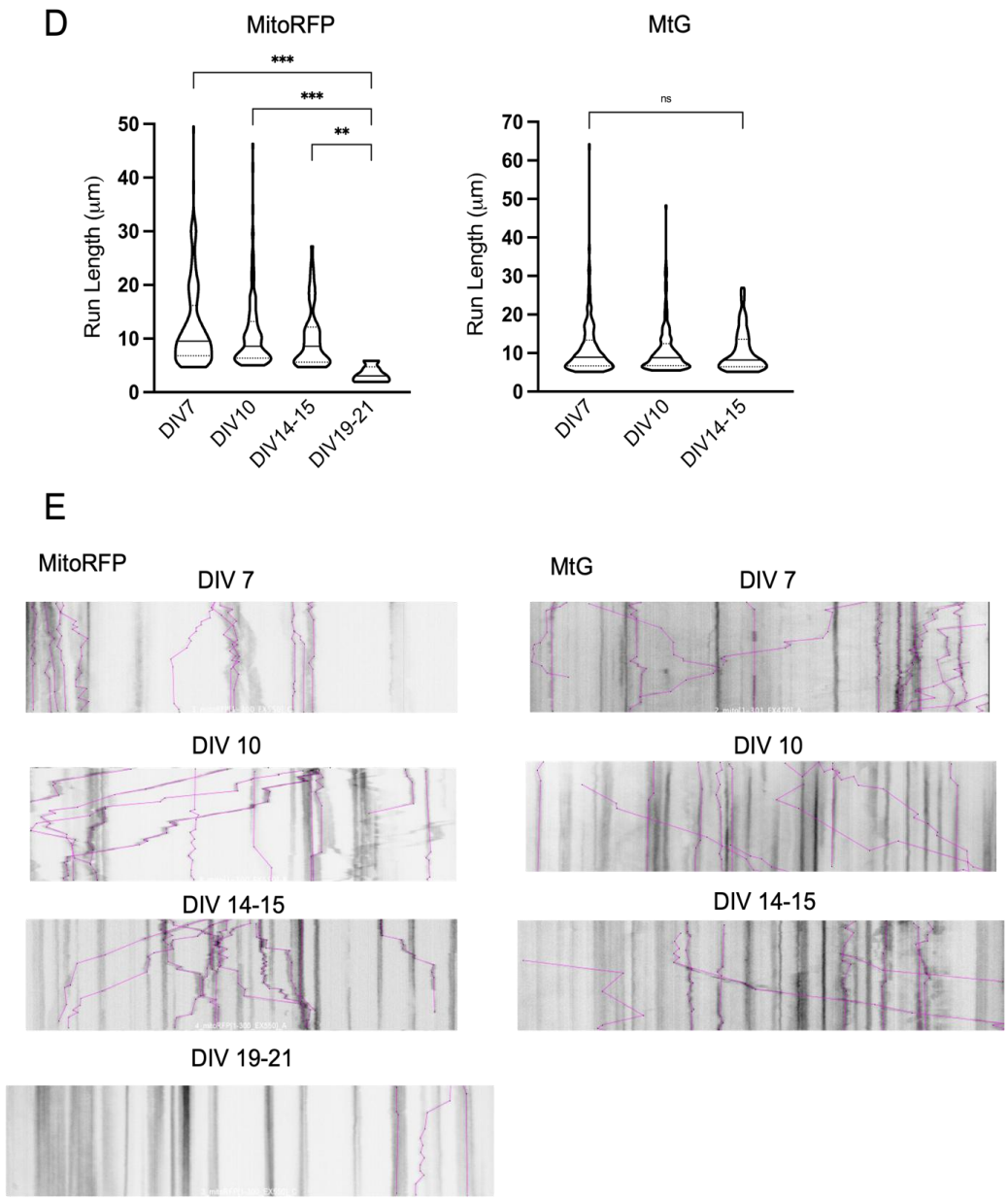

Figure 24. Velocity-related quantification of mitochondrial movements during neuronal maturation (DIV7, 10, 14-15 and 19-21) in neurons expressing MitoRFP (left panels) or labelled with MitoTracker Green (right panels).

(A) Net velocities of mitochondria moving net anterograde or net retrograde. (B) Segmental velocity measurements of mitochondrial movement within individual trajectory segments at different time points. (C) Combined segmental velocities, representing uninterrupted mitochondrial movement along a trajectory (D) Total distance travelled by mitochondria during the imaging period, regardless of movement direction (E) Representative kymographs at each time point for neurons

*expressing MitoRFP or labelled with MitoTracker Green. *= p<0.05, ** p<0.005 and *** = p<0.0001.*

3.3 Discussion

This study aimed to validate KymoAnalyzer as an effective tool for quantifying mitochondrial motility in hippocampal neurons by assessing its ability to detect changes in mitochondrial transport under different experimental conditions. The results demonstrate that KymoAnalyzer successfully captured biologically relevant variations in mitochondrial movement following pharmacological disruption of cytoskeletal components and during neuronal maturation, supporting its reliability for mitochondrial transport analysis.

Like other kymograph-based analysis methods, KymoAnalyzer requires manual tracing of neurite trajectories, making it a labour-intensive process. However, this manual approach allows for greater accuracy in identifying moving mitochondria, particularly in conditions where automated tracking algorithms may fail due to low signal-to-noise ratios or high mitochondrial density (Neumann *et al.*, 2017; Jakobs *et al*., 2019). A potential limitation of KymoAnalyzer is the risk of user bias in selecting neurite tracks, which could affect data reproducibility. To minimise this issue, neurites were randomly chosen (5–8 per image) to prevent over-representation of specific tracks, ensuring a more unbiased evaluation of mitochondrial motility.

To validate KymoAnalyzer's ability to capture expected biological changes, mitochondrial motility was analysed following treatment with nocodazole or latrunculin B, which disrupt microtubules and actin filaments, respectively. Because mitochondrial transport is primarily microtubule-dependent, nocodazole treatment significantly reduced motility, whereas latrunculin B had minimal impact. Live-cell imaging and kymographs (Fig 16 and 17) confirmed that nocodazole-treated mitochondria exhibited reduced movement and increased stationary behaviour, while mitochondria in latrunculin B-treated cells remained motile at similar levels to controls. Quantification of these effects further revealed that nocodazole treatment

significantly decreased the fraction of motile mitochondria, the percentage of time spent in motion, and mitochondrial velocities (Figs 18–20).

These findings are consistent with previous reports demonstrating that microtubule depolymerisation impairs mitochondrial transport (Morris and Hollenbeck, 1995; Ligon and Steward, 2000; Woods *et al*., 2016). For example, Ligon and Steward observed a rapid decline in mitochondrial motility within 12 minutes of nocodazole treatment, but a subset of mitochondria remained motile. This suggests that some mitochondria may move along microtubules that were not fully disrupted or may rely on alternative transport mechanisms such as actin-based movement. Further analysis of velocity-related parameters (Fig 19A–C) demonstrated that nocodazole treatment significantly reduced net velocity, segmental velocity, and total distances travelled, supporting the conclusion that mitochondrial transport is highly microtubule-dependent. In contrast, latrunculin B treatment did not significantly alter mitochondrial movement, reinforcing the idea that actin filaments play a minimal role in long-distance mitochondrial transport under normal conditions.

To further validate KymoAnalyzer, mitochondrial motility was examined during neuronal maturation in vitro (DIV 7–21) using two distinct labelling methods: MitoRFP expression and MitoTracker Green staining. In both conditions, the fraction of motile mitochondria was highest at DIV 7 and progressively declined with neuronal age (Fig 23A). Interestingly, young neurons exhibited a higher proportion of mitochondria undergoing reversing movements, whereas older neurons had more stationary mitochondria (Fig 23B). These findings are consistent with previous studies showing a progressive reduction in mitochondrial motility during neuronal differentiation (Chang and Reynolds, 2006; Loss and Stephenson, 2017). Loss and Stephenson reported that hippocampal and cortical neurons exhibited a significant decrease in motile mitochondria between DIV 6 and 14, particularly in axons. This decline is believed to be linked to neuronal development and synaptogenesis, which requires localised ATP production, potentially leading to mitochondrial anchoring at synaptic sites rather than continuous transport. While this anchoring is considered physiological rather than pathological, there remains

the possibility that dysfunctional mitochondria could remain present within these cells, however in parallel observations hippocampal cells were co-stained with MitoTracker Green and TMRE (the latter loading into mitochondria dependent upon their membrane potential). Although TMRE-based imaging was not included in the main motility analysis due to fluorescence instability during extended imaging, these sessions showed no obvious signs of widespread mitochondrial depolarisation or, for example of mitochondrial depolarisation in only certain motility classes of mitochondria. Across all TMRE-stained samples, fluorescence intensity remained consistent across various ages of cell cultures, suggesting that the decline in motility was not due to mitochondrial dysfunction but rather reflects physiological adaption.

Although overall mitochondrial motility decreased with maturation, segmental and combined segmental velocities increased in MitoRFP-expressing neurons between DIV 7 and 14–15, while net velocity remained unchanged (Fig 24B-C).

Interestingly, previous studies have reported that while the fraction of motile mitochondria decreases, mitochondrial velocities increase (Loss and Stephenson, 2017; Shahen *et al*., 2018). This may be due to upregulation of mitochondrial transport regulators such as Miro and TRAK, which promote efficient mitochondrial transport in mature neurons (Loss and Stephenson, 2017). However, despite these increases in velocity, the total distance travelled by mitochondria remained similar between DIV 7 and 14–15, only declining significantly at DIV 19–21 (Fig 24D). Few studies have examined mitochondrial transport in neurons beyond three weeks in vitro, but it has been proposed that mature neurons reduce mitochondrial motility to stabilise synaptic structures (Chang and Reynolds, 2006). Alternatively, mitochondria in older neurons may travel faster but pause more frequently, localising at synaptic sites where they provide energy for sustained neuronal activity (Shahen *et al*., 2018).

Overall, this study confirms that KymoAnalyzer is a powerful tool for quantifying mitochondrial motility, effectively capturing biologically relevant changes associated with cytoskeletal perturbation and neuronal maturation. The

results highlight the critical role of microtubules in mitochondrial transport, while actin filaments appear to have minimal impact under baseline conditions. Additionally, neuronal maturation leads to reduced mitochondrial motility, likely due to increased energy demands at synaptic sites, with younger neurons exhibiting higher motile fractions and frequent reversing movements.

Given the complexity of mitochondrial transport, future studies could explore how synaptic activity influences mitochondrial motility, particularly in mature neurons. Moreover, employing micro-patterned substrates to guide neurite outgrowth could enhance the precision of mitochondrial tracking, reducing variability in neurite trajectory selection. These advancements will further improve our ability to analyse mitochondrial transport in both developmental and disease contexts.

CHAPTER FOUR:
A Comparison of Mitochondrial Motility in Neurons Grown on Conventional and Novel Charged Surfaces

4.1 Introduction

One of the key factors that influences survival and growth of long-term neuronal cultures *in vitro* is the substrates onto which the cells adhere (Widge *et al*., 2007). Neurons have highly polarised morphology with a few anchoring points for adhesion compared to most mammalian cells (Sun *et al*., 2012). Since neurons cannot adhere to solid surfaces such as bare glass, various coating materials have been used to enable neuronal cells to anchor and improve their initial adhesion (Sun *et al*., 2012, Taylor *et al*., 2020).

One commonly used coating material is poly-lysine, a polypeptide comprised of lysine sequences. It is a non-native protein containing cationic groups that combine with anionic groups on the cell surface, facilitating cell adhesion and enhancing neurite extension and proliferation (Mazia *et al*., 1975). Poly-lysine exists in two forms (i.e. *d* and *l*). Both are known to mediates neuronal cell adhesion, but the *d*-form is preferred over the *l*-form. Poly-*d*-lysine (PDL) is resistant to proteases such as trypsin, which enhances the stability of surface coatings in long term cultures (Li and Yeung, 2008; Rao and Winter, 2009). However, poly-lysine has a disadvantage that coated substrates can be degraded by proteolysis (Clement *et al*., 2021). PDL was used as the major surface coating material for hippocampal cell cultures in my previous studies (Chapter 3).

ECM proteins, such as laminin, collagen and fibronectin, offer another widely used alternative. These proteins more closely mimic the natural cellular environment, supporting neuronal outgrowth, differentiation and proliferation by providing biochemical cues essential for adhesion (Akeson *et al*., 1986 and Freire *et al*., 2002). Unlike poly-lysine which is non-receptor mediated polymers, neuronal cultures bind to ECM proteins via transmembrane molecules like integrins, which promotes adhesion stability of cells.

Interestingly, research has demonstrated that applying ECM proteins as a secondary layer over an initial poly-lysine coating can further improve neuronal adhesion (Clark *et al*., 1993; Ma *et al*., 2008; Orlowska *et al*., 2017; Wysotzki and Gimsa, 2019). The negatively charged ECM proteins electrostatically bind to the positively

charged poly-lysine, after which ECM proteins interact directly with neuronal surface receptors through integrin binding. This dual-coating strategy creates a more conductive surface for neuronal growth and adhesion compared to single-material coatings. Indeed, several studies have shown that the combination of poly-lysine with ECM proteins such as laminin or fibronectin, promotes stronger adhesion and enhanced neurite outgrowth in PC12 cells when compared to using either material (Orlowska *et al*., 2017). Based on these findings, the study investigates the use of three widely known coating methods – PDL, laminin, and a dual-coating of PDL/laminin – to explore their effects on mitochondrial motility in neuronal cultures.

In addition to these traditional coating agents, producing biomaterial surfaces with specific chemical functional groups has also been explored as a method to enhance neuronal cultures. While many studies have demonstrated that positively charged surfaces promote strong electrostatic interactions with negatively charged neuronal membranes (Kleinfedl *et al*., 1988 and Stenger *et al*., 1992), this view is not comprehensive. Other research suggests that the variety of functional groups and local present in *in vivo* environment can significantly modulate neuronal behaviour (Tessier-Lavigne et al., 1996). This highlights the importance of investigating how different chemical identities affect neuronal adhesion and growth *in vitro*, as it may provide insights into creating environment that better mimic *in vivo* conditions. For example, Kim's group demonstrated that chemically charged surfaces influence neuronal adhesion and maturation. Their study showed that primary neurons cultured on negatively charged surfaces, such as carboxylate (COO-) or sulfonate (SO^3-), exhibited accelerated neurite outgrowth, faster maturation and higher adhesion and survival rates compared to neurons grown on positively charged surfaces like PDL (Kim *et al*., 2017). These findings suggest that negatively charged surfaces might better support neuronal health and development.

Based on these findings, primary hippocampal cell cultures were tested on two types of chemically charged substrates. To create a negatively charged surface with

carboxyl (COO)-functional groups, carboxyethylsilanetriol di-sodium salt (CES) was used as a coating material. Alternatively, aminopropyltriethoxysilane (APTES) was used to create a positively charged amine-functionalised surface to study the effects of amine groups on neuronal cultures.

This chapter investigates the effects of these various coating materials on hippocampal cell cultures by examining qualitative changes in cell morphology and the proportion of different cell types, including neurons and astrocytes. Additionally, mitochondrial motility within cultures grown on the different substrates was analysed to assess the impact of surface charges on motion-related mitochondrial dynamics. As in Chapter 3, the tool KymoAnalyzer was used to quantitatively assess mitochondrial movement.

4.2 Results

4.2.1 Whole Field-of-View Global Quantification of Mitochondria Motion on PDL-, Laminin-, Dual-, CES- or APTES- coated substrates

Robust adhesion of neuronal cultures to substrates is critical for cell survival and growth *in vitro*. Therefore, the morphologies of hippocampal cells and cell adherence and neurite growth across different substrate types were examined. To evaluate the effects of substrate types on neuronal adhesion and growth, brightfield images of primary hippocampal cell cultures were captured on DIV 7 and DIV 14. The cultures were maintained on substrates coated with PDL, laminin or dual; coated with PDL and then laminin on top. Additionally, silane-based coatings such as CES and APTES were applied to provide negatively and positively charged functional groups, respectively.

Brightfield images taken on DIV 7 (Fig 25A) show that hippocampal cultures on PDL substrates exhibited well-dispersed soma, with long, thin neurites forming a network between individual cells. In contrast, cultures on laminin or dual-coated substrates had fewer individual somas, with a higher tendency for soma clustering and thicker neurites. By DIV 14 (Fig 25B), cultures on PDL substrates began to

exhibit signs of soma clustering and partial detachment, a pattern commonly observed in long-term hippocampal culture. Laminin-coated cultures maintained continuous thick neurite processes and aggregated cell clusters, while dual-coated cultures displayed a mix of healthy, long neurite outgrowths in some regions. While the DIV 14 PDL condition does not represent the most optimal cellular health, this was not indicative of the neurons used for mitochondrial motility quantification. Brightfield images were not routinely acquired alongside live-cell imaging; instead, only fields with intact neuronal morphology and active processes were selected for analysis.

On CES- and APTES-coated substrates, neuronal adherence and neurite growth were observed, but the rate of neurite extension and cell maturation appeared slower compared to the traditionally coated substrates. Notably, there were no signs of thickened neurite processes on these substrates at DIV 7 (Fig 26A). By DIV 14, cultures on CES substrates demonstrated longer neurite extensions, and cultures on APTES showed accelerated maturation, with pronounced elongation of neurite growths (Fig 26B).

Quantitative analysis was not performed for these brightfield images due to the qualitative nature of the data and the inherent limitations in accurately measuring neurite outgrowth without additional florescence markers or more detailed imaging techniques.

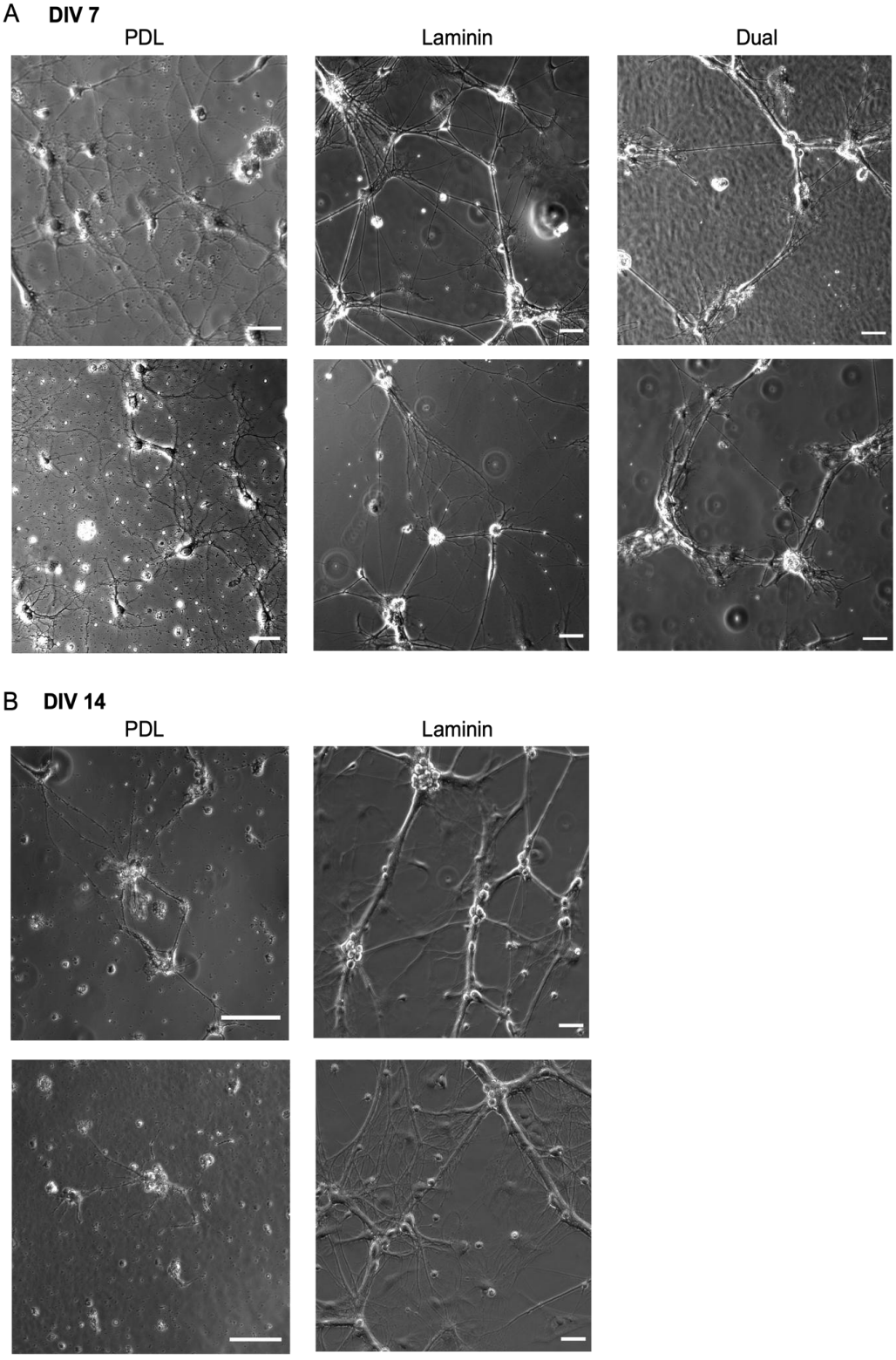

Figure 25. Brightfield images of hippocampal cells grown on traditionally coated substrates (PDL, laminin or dual) substrates.

(A)DIV 7 and (B) DIV 14. Scale bar = 50 µm

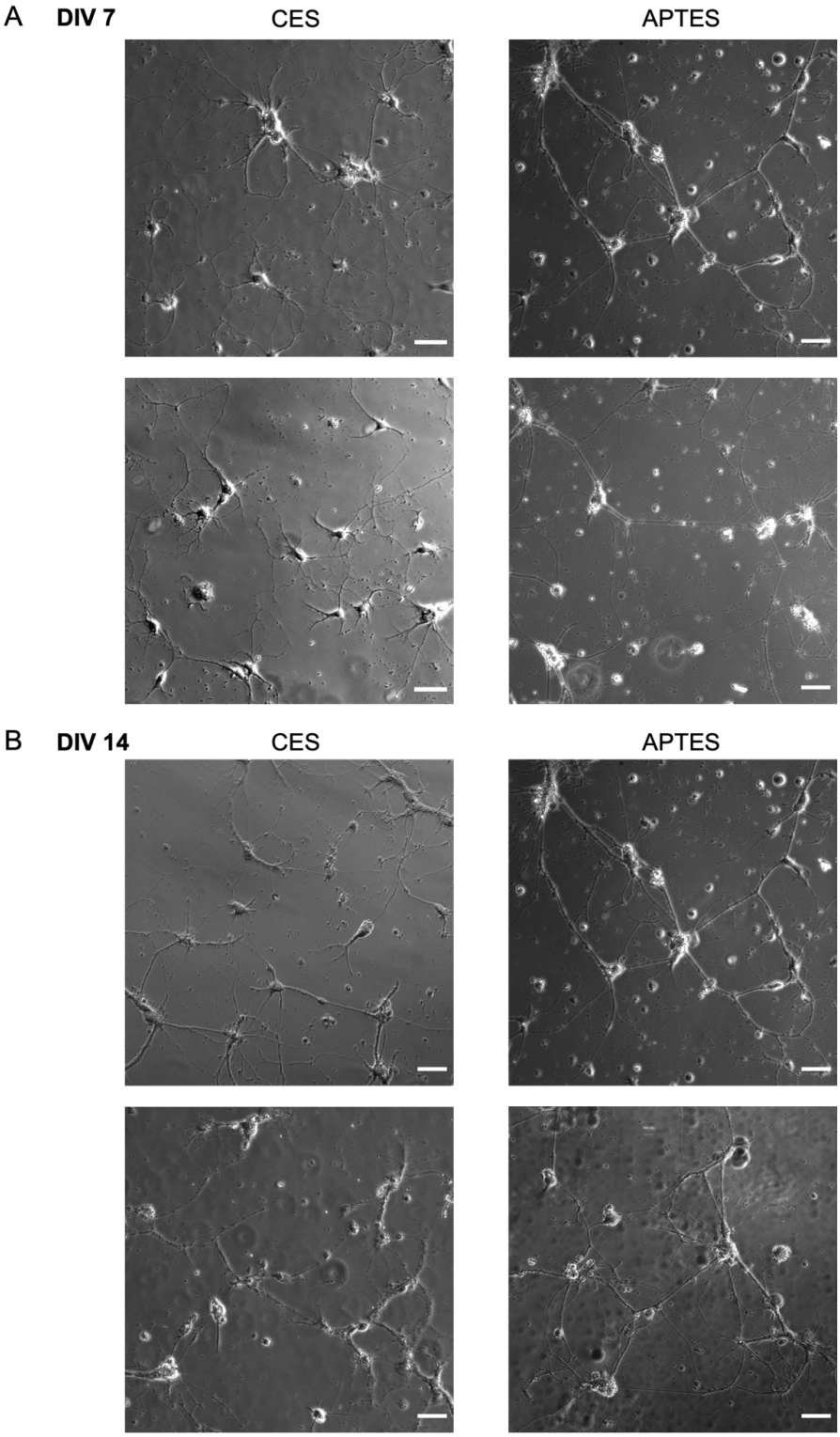

Figure 26. Brightfield images of hippocampal cells grown on charged substrates (CES or APTES).

(A) DIV 7 and (B) DIV 14. Scale bar = 50 µm.

4.2.2 Immunocytochemical Analysis of Cell Types Present

Hippocampal cell cultures consist of various cell types, including neurons, astrocytes and other non-neuronal, non-astrocytic cells. To distinguish between these cell types, the cultures grown on different substrates, which were previously analysed through brightfield imaging, were subjected to immunocytochemical staining using specific markers. Neuronal cells were labelled for MAPT/tau, while astrocytes were stained for GFAP (Fig 27). Nuclei were counterstained with DAPI, allowing for a more accurate comparison of the relative proportions of neurons and astrocytes.

Representative images from DIV 7 (Fig. 27A) revealed neuronal adhesion across all substrates. Quantitative analysis of the stained cultures (Fig. 27B) demonstrated that the proportion of astrocytes were consistently lower than that of neurons across all substrates. This difference was most pronounced on CES- and APTES-coated substrates, where the ratio of neurons was significantly higher. Specifically, neuronal populations accounted for 74.3±12.9% on CES substrates and 67.9±8.90% on APTES substrates, while astrocytes made up only 13.1±5.54% on CES and 9.71±5.29% on APTES. No significant difference in the proportion of astrocytes was observed across the five different substrate types.

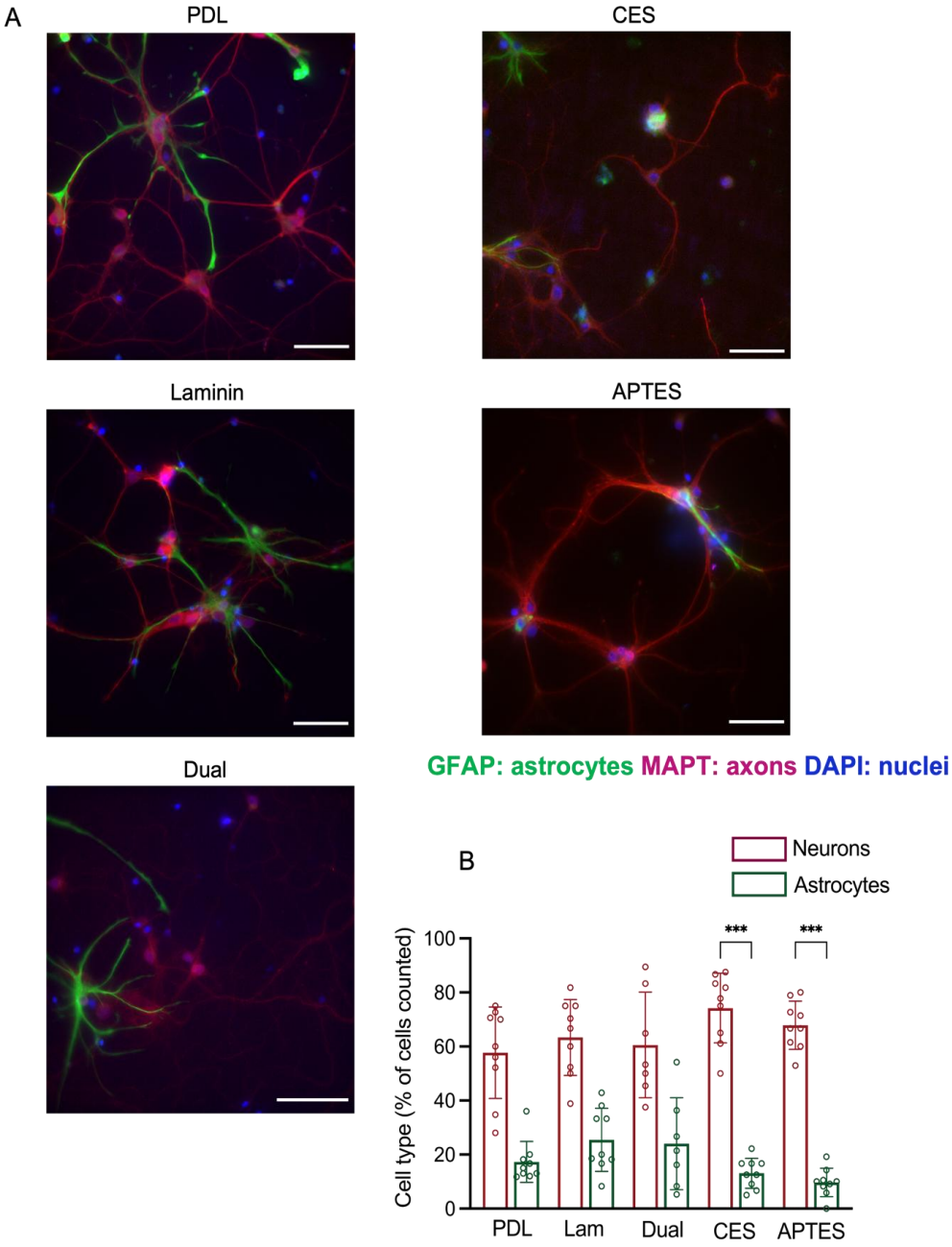

Figure 27. Immunocytochemistry of hippocampal cells cultured on PDL-, laminin-, dual-, CES- or APTES-coated substrates at DIV 7.

(A) Cells were stained with astrocytic (GFAP) and neuronal (MAPT/tau) markers, while nuclei were stained with DAPI. (B) Quantitative analysis of the percentage of neurons and astrocytes on different substrates. The remaining cells were categorised as "other" cell types. Cell counting was performed manually using ImageJ on five randomly selected images per coverslip (x20 objective), based on three independent cultures per condition. Neurons were identified as DAPI+/MAPT+

*and astrocytes as DAPI+/GFAP+. Kruskal-Wallis non-parametric test was used for statistical analysis (Mean ± S.D, ***P< 0.001, Scale bar = 30 µm).*

At DIV 14, cells were stained to assess the relative proportions of neurons and astrocytes (Fig. 28). The results revealed that cells grown on APTES substrates still exhibited a significantly higher number of neurons (71.7±9.69%) compared to astrocytes (16.6±8.87%). In contrast, cultures grown on other substrates (PDL, laminin and CES) also showed a trend toward a higher number of neurons compared to astrocytes, with this trend being particularly noticeable on CES substrates.

When comparing the numbers of neurons and astrocytes between DIV7 and DIV 14, no significant differences were observed across the substrates, indicating that all substrate types, indicating that all conditions generally supported cell adhesion and survival over the two-week culture period. However, it is important to note that some neuronal cultures, particularly those maintained on PDL substrates at DIV 14, occasionally displayed signs of neurite degeneration of compromised morphology. As such, while the overall neuron-to-astrocyte ratios remained stable, caution is warranted when interpreting late-stage neuronal health solely based on population proportions. These results suggest that the initial surface characteristics of the substrates influenced early neuronal development but had little effect on the overall cell population ratios as the cultures matured.

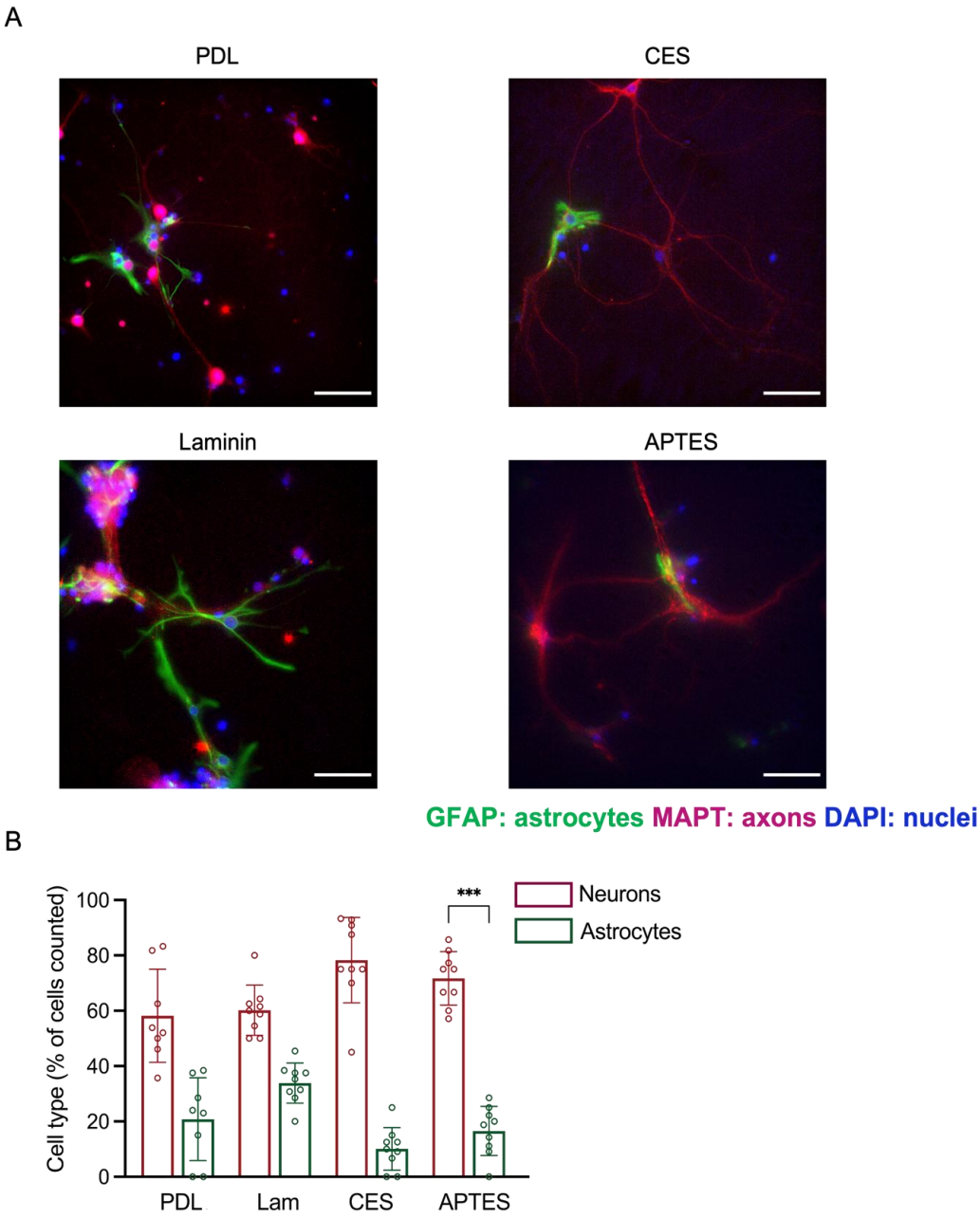

Figure 28. Immunocytochemistry of hippocampal cells on PDL-, laminin-, dual-, CES- or APTES-coated substrates at DIV 14.

*(A) Cells were stained with GFAP (for astrocytes) and MAPT/tau (for neurons), and nuclei were stained with DAPI. (B) Ratio of neurons to astrocytes across the different substrates. The rest of the cells were categorised as "other" cell types. N=9 regions from 3 independent experiments for laminin-, CES-, or APTES-substrates, and N=8 regions from 3 sets for PDL-substrates. Dual-coated substrates were not included in this analysis (Mean ± S.D, ***P< 0.001, Scale bar = 30 µm).*

4.2.3 KymoAnalyzer Quantification of Mitochondrial Motion Within Neuronal Processes on Traditionally Coated Substrates

To investigate whether substrate coating materials affect mitochondrial dynamics within neuronal processes, mitochondrial movements were observed in hippocampal neurons cultured on traditionally coated substrates (PDL, laminin, and dual coatings) at DIV 7 and DIV 14. The relative fraction of motile mitochondria, including all forms of movement, is shown in Fig 29A. Although no significant differences were observed between the three substrates, there was a significant decrease in the fraction of motile mitochondria at DIV 14 compared to DIV 7 across all substrate types. The median fractions of motile mitochondria at DIV 7 were 36.6% (IQR = 25.0–47.1) for PDL, 33.3% (IQR = 12.5–33.3) for laminin and 41.3% (IQR = 0.00–33.8) for dual coatings. This decreased significantly at DIV 14 to 21.1% (IQR = 12.5–33.3) for PDL, 0.00% (IQR = 0.00–36.4) for laminin, and 16.7% (IQR = 0.0–33.8) for dual coatings ($p<0.001$).

To further explore the directionality of mitochondrial movements, motile mitochondria were classified into anterograde (away from the soma), retrograde (towards the soma) and reversing movements (Fig 29B-C). In all analysed neurites, soma positions were clearly identifiable within the field of view, allowing confident assignment of movement direction. At DIV 7, no significant differences were detected in the fractions of each movement type between the substrates (Fig 29B). However, at DIV 14, dual-coated substrates exhibited a significantly lower fraction of reversing mitochondria (median = 10%, IQR = 0.00–25.8) compared to PDL (14.3%, IQR = 6.70–25.9, $p<0.05$) and laminin (25.4%, IQR = 11.8–45.2, $p<0.001$) (Fig 29C).

Comparing the movement types between DIV 7 and DIV 14 within each substrate revealed further insights (Fig 29D-F). At DIV 7, a greater fraction of mitochondria displayed anterograde movement across all substrates (Fig 29D). The median fractions were 6.25% (IQR = 0.00–12.6) for PDL, 5.8% (IQR = 0.00–11.8) for laminin, and 7.42% (IQR = 0.00–14.1) for dual coatings. By DIV 14, this fraction decreased to 0% across all substrates ($p<0.05$ – 0.001).

For retrograde movement, mitochondria on PDL substrates showed a higher fraction at DIV 7 (3.7%, IQR = 0.00–7.14) compared to DIV 14 (0%, IQR = 0.00–5.26, $p<0.05$) (Fig 29E). Reversing movement also showed significant reductions, particularly on PDL and dual-coated substrates (Fig 29F). At DIV 7, reversing mitochondria accounted for 25% (IQR = 17.2–35.4) on PDL and 37% (IQR = 19.2–50.0) on dual coatings, which decreased to 14.3% (IQR = 6.67–25.0) on PDL and 10% (IQR = 0.00–25.8) on dual coatings by DIV 14 ($p<0.001$).

These results suggest that mitochondrial motility decreases significantly with neuronal maturation, particularly in the fraction of anterograde and reversing movements. The influence of substrate type on mitochondrial movement becomes more pronounced at later stages (DIV 14), with dual-coated substrates showing the most significant reduction in reversing mitochondria.

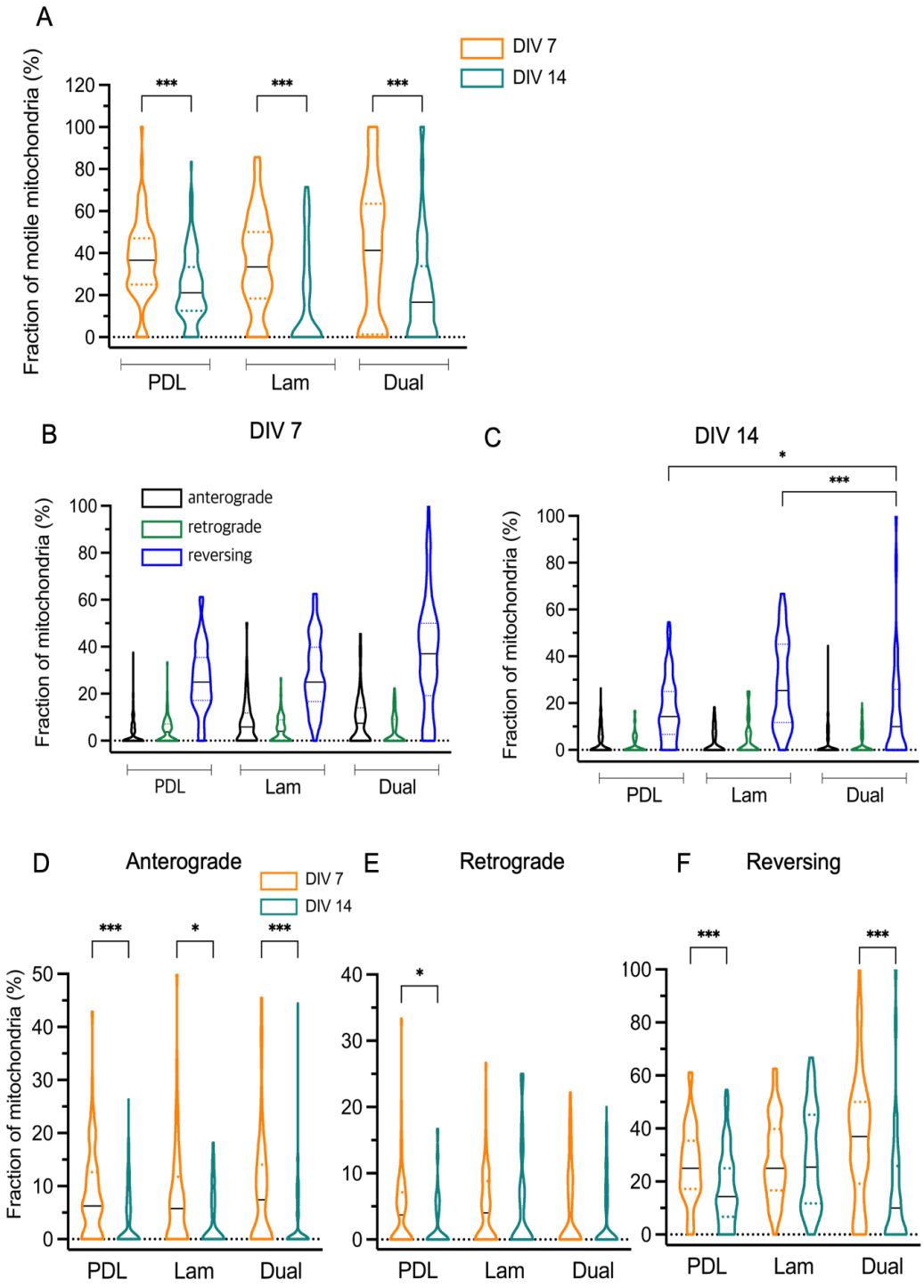

Figure 29. Quantitative analysis of the fraction of motile mitochondria in hippocampal cell cultures on PDL-, laminin- and dual-coated substrates.

Cells were labelled with 100 nM MitoTracker Green and imaged at DIV 7 and 14. (A) The fraction of all motile mitochondria, combining anterograde, retrograde and reversing movements, on each substrate at DIV 7 and DIV 14 (B-C) The fraction of

*mitochondria showing anterograde, retrograde or reversing movement was compared between substrates at (B) DIV 7 and (C) DIV 14. (D-F) The fraction of each type of movement (anterograde, retrograde or reversing) was compared within each substrate between DIV 7 and DIV 14. Data are presented as violin plots showing median values (solid line) and interquartile ranges (dotted line). Statistical significance: *p<0.05, ***p<0.001; Kruskal-Wallis non-parametric ANOVA with Dunn's post-hoc test; n=3 experiments.*

The percentage of time that mitochondria spent travelling in different forms of motion; anterograde, retrograde or remained paused were analysed (Fig 30). When cells within each substrate was compared at DIV 7 (Fig 30A), mitochondria spent significantly lesser time moving retrograde on PDL – median of 10.9% (IQR = 1.74–29.0) than on laminin-substrates – 16.0% (IQR = 3.77–37.8, $p<0.05$). In addition, the time mitochondria spent being paused on laminin substrate – 56.3% (IQR = 12.7–84.9) was smaller than on dual substrates – 64.4% (IQR = 28.0–87.0, $p<0.05$). At DIV 14, no significant differences were observed across the three substrates (Fig 30B). When each motion of mitochondria within each substrate between DIV 7 and 14 was compared (Fig 30C-E), some significant difference was found on retrograde and paused motion of mitochondria on some substrates. I found that mitochondria spent lesser time on PDL- or dual-substrates at DIV 7 compared to mitochondria at DIV 14 whereas mitochondria on laminin substrates did not show major differences (Fig 30D) (10.9% of retrograde mitochondria on PDL substrate at DIV 7; IQR = 1.72–29.0 compared to 16% at DIV 14; IQR = 6.70–30.1, $p<0.001$) and (12.4% retrograde mitochondria on dual at DIV 7; IQR = 4.08–26.3 compared to 17.2% at DIV 14; IQR = 6.36–33.7, $p<0.01$). In addition, mitochondria on dual substrate also showed higher time remained paused at DIV 7 (64.4%; IQR = 28.0–87.0) than at DIV 14 (55.4%; IQR = 21.3–81.0, $p<0.05$) (Fig 30E).

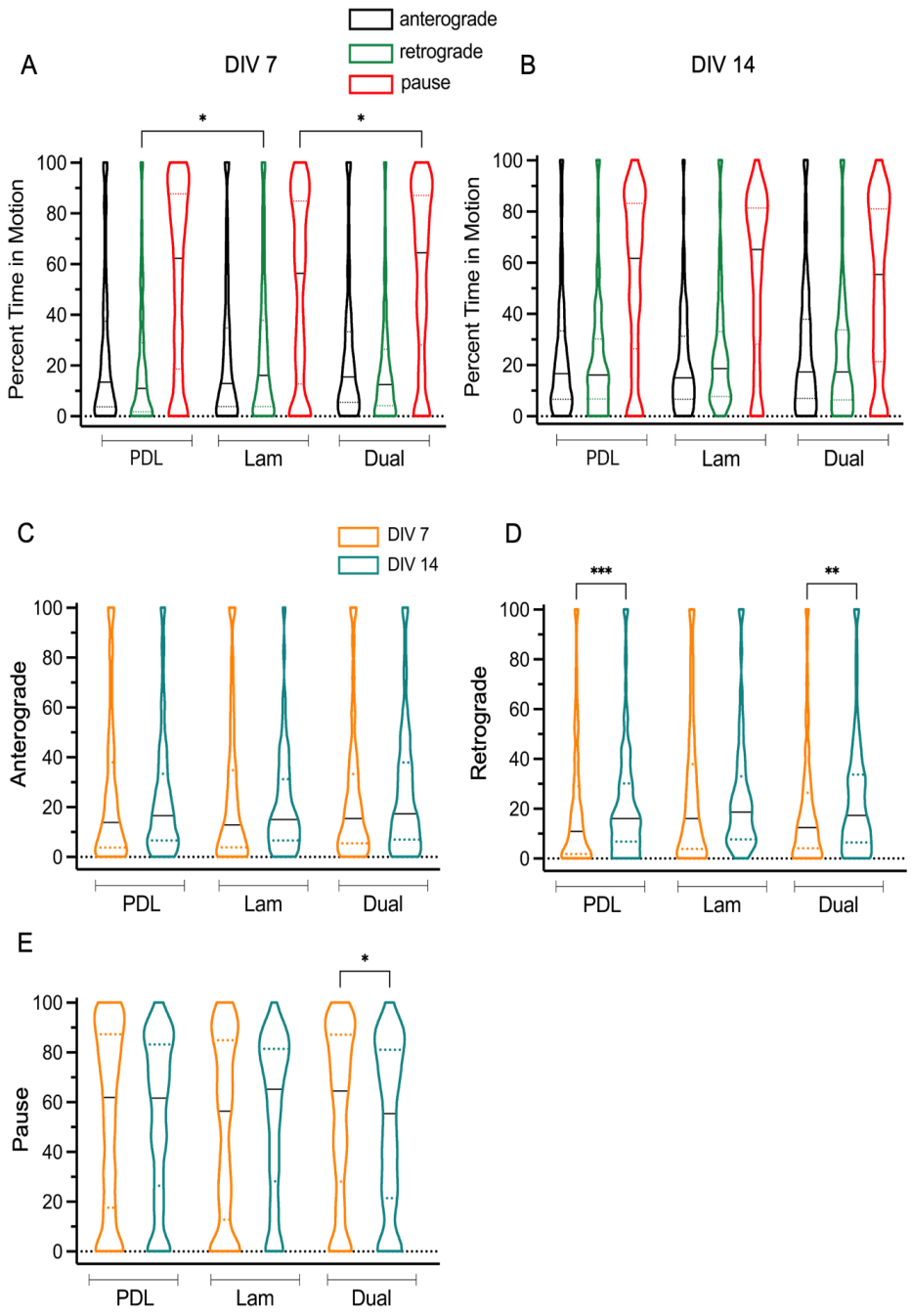

Figure 30. Quantitative graphs of percentage of time mitochondria moving either unidirectionally anterograde or retrograde, or paused between substrates at DIV 7 and 14.

(A-B) Comparison of each mitochondrial motion between across PDL-, laminin- and dual-coated substrates at (A) DIV 7 and (B) at DIV 14. (C-E) Comparison of the percentage of time spent in each motion state between DIV 7 and 14 of each motion of mitochondria on each substrate. Data are shown as violin plots with median

*values (solid lines) and interquartile ranges (dotted lines). Statistical comparisons for (A-B) were performed using Kruskal-Wallis non-parametric ANOVA followed by Dunn's post-hoc test; for (C-E), Kolmogorov-Smirnov non-parametric unpaired t-tests were used. *p<0.05, **p<0.01, ***p<0.001. n=3 independent experiments.*

Transport dynamics of mitochondria in hippocampal cell cultures were further investigated by studying various aspects of mitochondrial velocities. Measuring the overall mean velocities of anterograde or retrograde over the full imaging period indicates that no major changes were found across substrates at both timeframes; DIV 7 and DIV14 (Fig 31A-B). Similarly, no major differences were found when anterograde or retrograde motion of mitochondria within each substrate between DIV 7 (Fig 31C) and DIV 14 (Fig 31D) was explored.

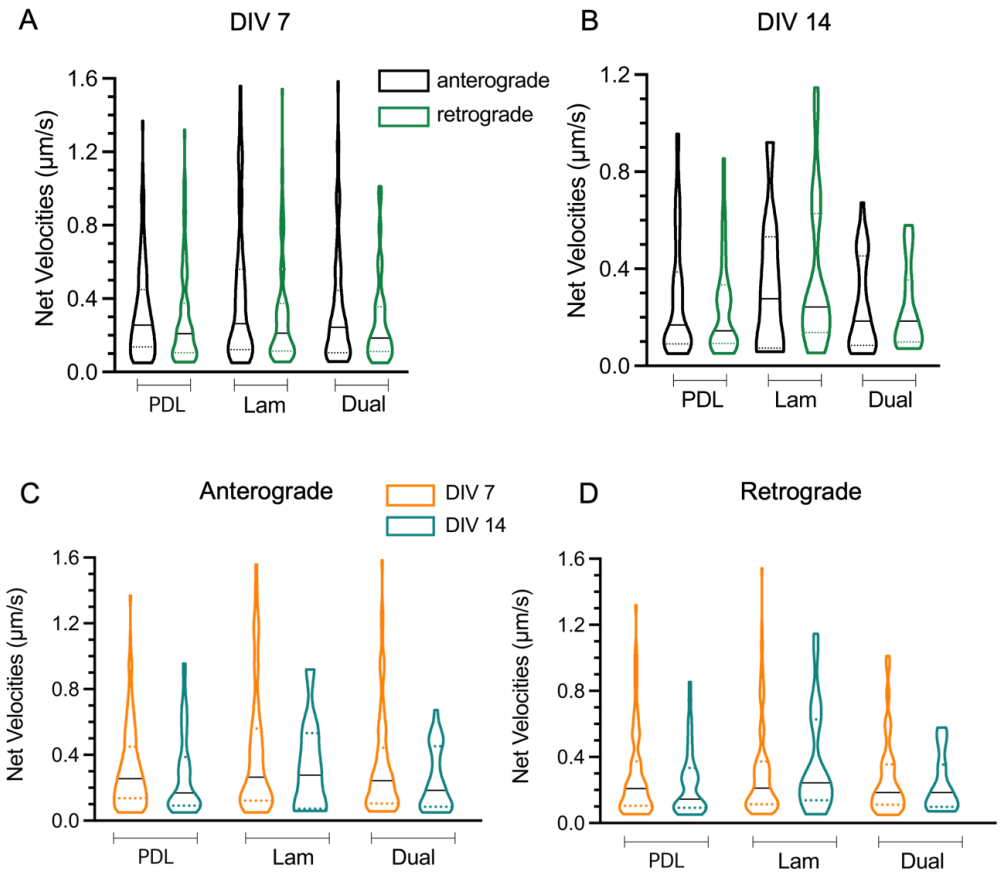

Figure 31. Overall net velocities of mitochondria in cell cultures travelling either net anterograde or net retrograde on PDL-, laminin- or dual-substrates.

(A-B) Velocities of anterograde or retrograde motion of mitochondria between three substrates was compared at (A) DIV 7 and (B) at DIV 14. (C-D) Overall comparisons of each motion of mitochondria; (C) anterograde or (D) retrograde within each substrate between DIV 7 and 14 was observed. Data are presented as violin plots with median values (solid lines) and interquartile ranges (dotted lines). Statistical comparisons for (A-B) were performed using Kruskal-Wallis non-parametric ANOVA followed by Dunn's post-hoc test; comparisons for (C-D) between DIV 7 and DIV 14 were analysed using Kolmogorov-Smirnov non-parametric unpaired t-tests. n=3 independent experiments.

However, some significant differences were observed when the velocities of mitochondria travelling within a single segment (a burst of mitochondrial movement with a constant velocity) were measured (Fig 32). The results in Figure 32A show that mitochondria on dual substrates showed significant differences in their segmental velocities than mitochondria on other substrates when each anterograde and retrograde motion at DIV 7. Anterograde mitochondria of cells within dual substrates were much slower (0.19 µm/s; IQR = 0.10–0.33) than on PDL (0.27 µm/s; IQR = 0.144–0.48, $p<0.001$ and on laminin (0.29 µm/s; IQR = 0.05–0.53), $p<0.001$. Moreover, retrograde motion of mitochondria on dual substrates also showed lower segmental velocities (0.18 µm/s; IQR = 0.10–0.33) than on PDL (0.26 µm/s; IQR = 0.14–0.48) and on laminin substrates (0.28 µm/s; IQR = 0.15–0.48), $p<0.001$). At DIV 14, however, only a slight change of anterograde mitochondria between PDL- and laminin-substrates was found (Fig 32B), that slower anterograde mitochondria on laminin-substrates (0.10 µm/s; IQR = 0.07–0.17) was observed than on PDL-substrates (0.11 µm/s; IQR = 0.07–0.20, $p<0.05$).

Then, measurements of segmental velocities of each motion of mitochondria within each substrate between DIV 7 (Fig 32C) and 14 (Fig 32D) were shown. The results show that mitochondria displaying either form of motion regardless of types of substrates all showed major reduction of segmental velocities as cells aged at DIV 14. For anterograde motion of mitochondria in Fig 32C,

velocities of mitochondria on PDL- (median of 0.27µm/s; IQR = 0.14–0.48), on laminin- (0.29 µm/s; IQR = 0.15–0.53) and on dual-substrates (0.19 µm/s; IQR = 0.11–0.37) significantly decreased at DIV 14, followed by mitochondria on PDL- (median of 0.11 µm/s; IQR = 0.07–0.20, $p<0.001$), on laminin- (0.10 µm/s; IQR = 0.07–0.17, $p<0.001$) and on dual-substrates (0.11 µm/s; IQR = 0.10–0.19), $p<0.001$. Similarly, for retrograde motion of mitochondria shown in Figure 32D, velocities of mitochondria on each PDL- (0.26 µm/s; IQR = 0.14–0.48), laminin- (0.28 µm/s; IQR = 0.16-0.48) and dual- (0.18 µm/s; IQR = 0.10–0.33) at DIV 7 was slowed at DIV 14 (0.10 µm/s on PDL; IQR = 0.07–0.17, 0.10 µm/s on laminin; IQR = 0.07–0.19 and 0.11 µm/s on dual; IQR = 0.07–0.19), $p<0.001$.

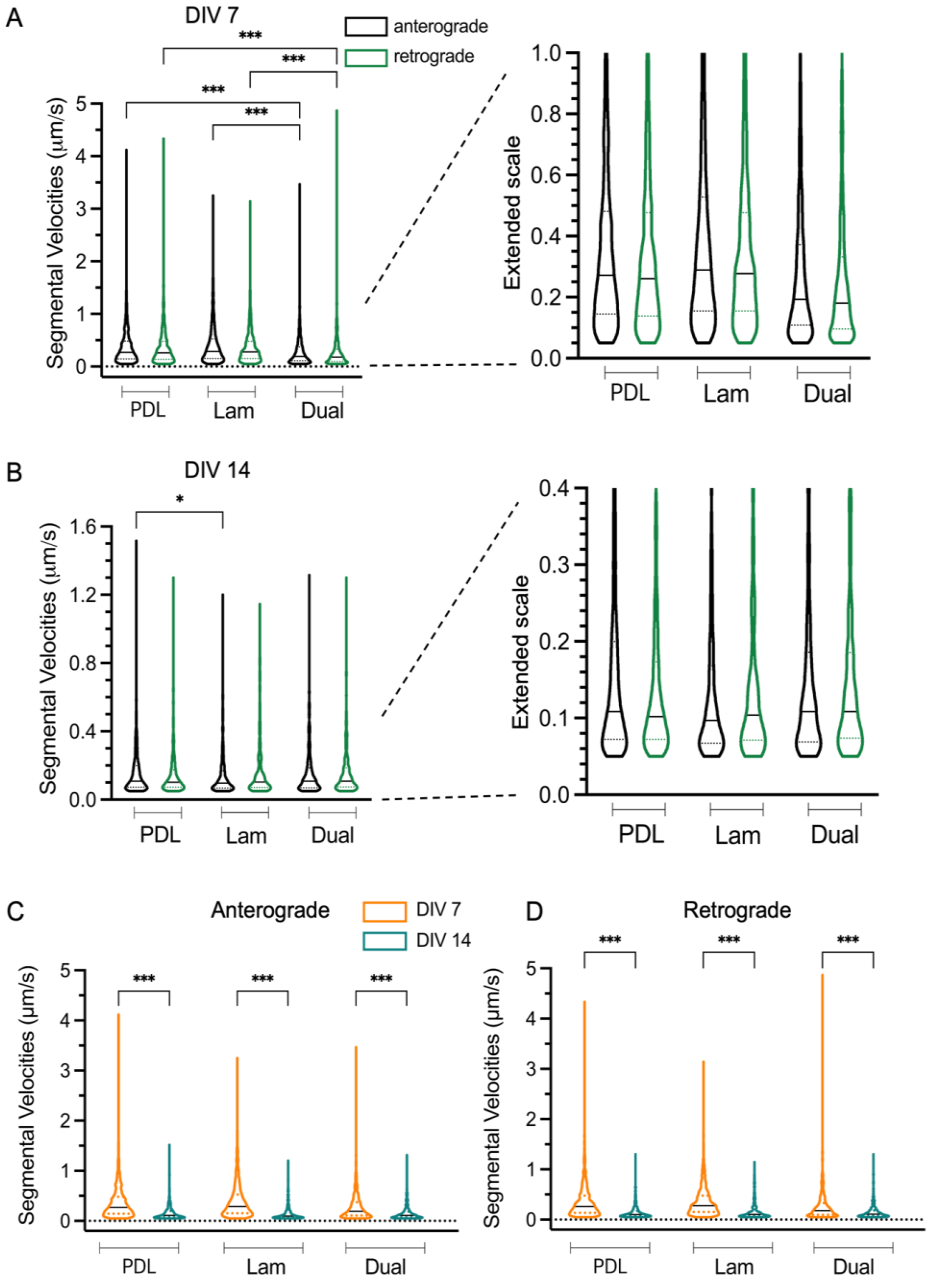

Figure 32. Quantitative graphs of segmental velocities of unidirectional mitochondrial transport within hippocampal cell cultures.

(A) shows unidirectional motion of mitochondria on PDL-, laminin-, or dual-substrates at DIV 7 and (B) at DIV 14. The right panels on (A) and (B) show an enlarged scale of the graph to show clear medians and interquartile ranges. (C-D) comparisons of each motion; (C) anterograde or (D) retrograde of mitochondria within each substrate between DIV7 and 14. Note that A/B and C/D represent the same dataset but analysed under different comparative conditions (substrate

*coating vs. neuronal age). Violin plots show all data points with solid lines indicating medians and dotted lines indicating 1.5x interquartile ranges. Kruskal-Wallis non-parametric ANOVA with Dunn's post-hoc test was used for comparisons across substrates in (A-B), and Kolmogorov-Smirnov non-parametric t-tests were used for DIV 7 vs DIV 14 comparisons in (C-D). *p<0.05, ***p<0.001.*

Mitochondrial velocities during uninterrupted periods of mitochondrial movements (with no pauses or reversals but allowing changes of speed) were also calculated. Similar results were found to segmental velocities (Fig 32), that much slower mitochondria travelling either direction on dual substrates were found compared to mitochondria on PDL- or laminin- substrates at DIV 7. However, no major changes were found across the substrates at DIV 14. When mitochondria within cells between DIV 7 and 14 was analysed, major decreases in velocities were found in any unidirectional form of motion of mitochondria from all substrates at DIV 14.

To understand how far mitochondria travelled within neurite processes, the mean distance that mitochondria moved within combined segments was also quantified in Fig 33. Similar to segmental velocities (Fig 32), there were major differences found between PDL- or laminin-substrates with dual-substrates. Each anterograde or retrograde motion of mitochondria on PDL- or laminin-substrates travelled further than on dual substrates at DIV 7 (Fig 33A) – median of 6.37 /5.46 µm for anterograde and retrograde on PDL (IQR = 4.81–9.88/ 4.29–8.32) and 5.98/ 6.11 µm on laminin (IQR = 4.29–9.75/ 4.55–9.23), respectively, travelled longer than median of 4.16/ 3.51 µm on dual substrates (IQR = 2.86–6.50/ 2.47–5.72, p<0.001).

At DIV 14, anterograde motion of mitochondria on laminin substrate travelled shorter distances (1.95 µm; IQR – 1.30–2.99) than on PDL (3.00 µm; IQR = 2.21–4.94) or dual-substrates (2.73 µm; IQR = 1.89–4.97, p<0.001) (Fig 33B). Moreover, each motion of mitochondria between DIV7 and 14 was compared within each substrate. Fig. 33C displayed distances of mitochondria moving anterograde – median of 6.37/5.98/4.16 µm on PDL-, laminin- or dual-substrates at

DIV 7, respectively, (IQR = 4.81–9.88/ 4.29–9.75/ 2.86–6.50), showing longer movements of mitochondria than 3.0/1.95/2.73 µm at DIV 14, (IQR = 2.21–4.94/ 1.30–2.99/ 1.89–4.97) respectively, $p<0.001$. Retrograde motion of mitochondria in Fig. 33D also showed that distances of mitochondria at DIV 7 – 5.46/6.11/3.51 µm on PDL-, laminin-, or dual-substrates (IQR = 4.29–8.32/ 4.55–9.23/ 2.47–5.72) travelling further than 2.47/2.73/2.37 µm (IQR = 1.76–4.18/ 1.66–4.62/ 1.74–4.01) at DIV 14, respectively; $p<0.001$.

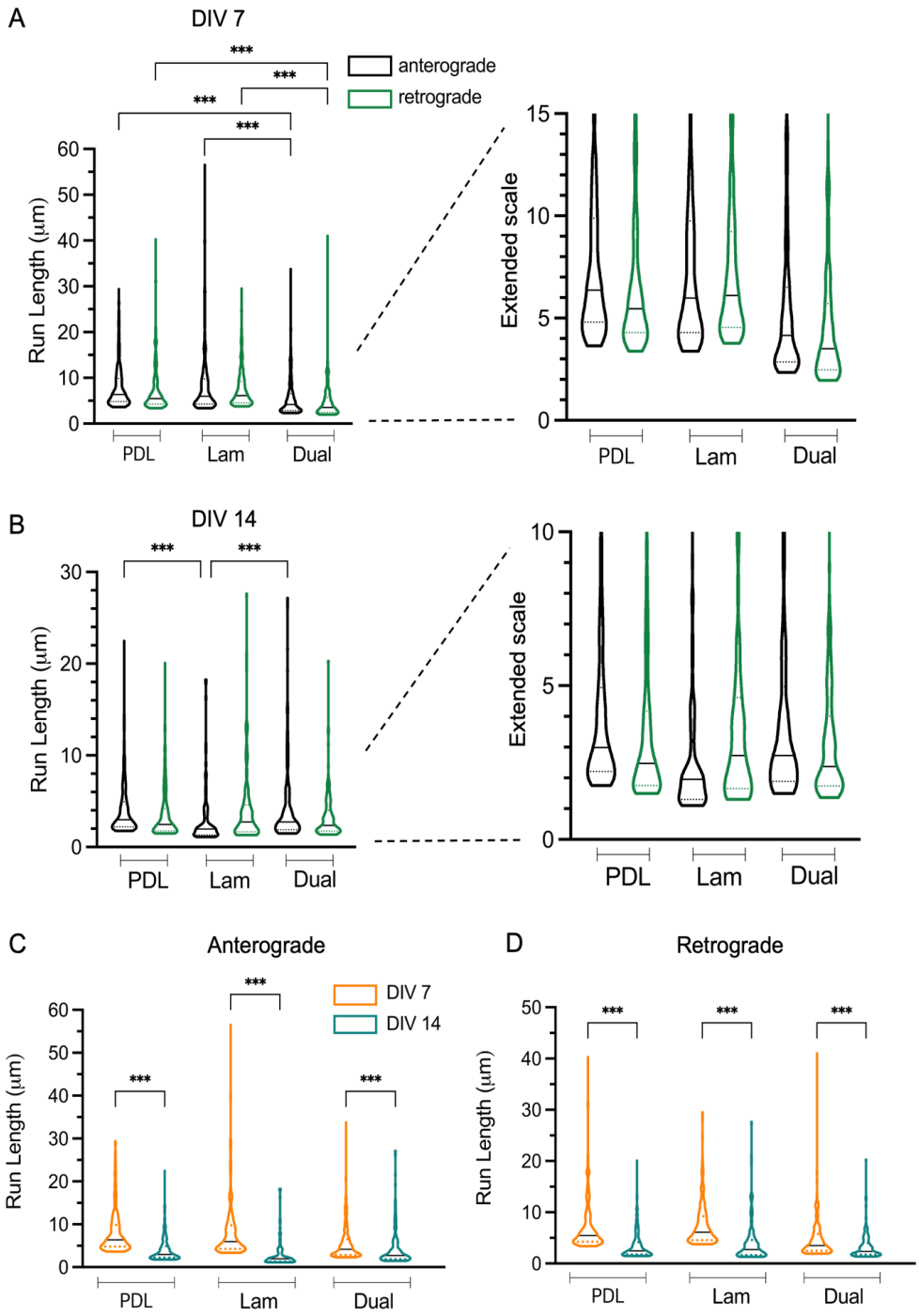

Figure 33. Quantitative graphs of the travelled distances of mitochondria within combined segments.

(A) shows measurements of distances of movements moving either anterograde or retrograde between substrates at DIV 7 and (B) at DIV 14. The extended scale of graphs shown on the right panels on (A) and (B) show clear medians and interquartile ranges. (C-D) run length of mitochondria within each substrate moving

*(C) anterograde or (D) retrograde between DIV7 and 14. Note that A/B and C/D represent the same dataset but analysed under different comparative conditions (substrate coating vs. neuronal age).Violin plots display all data points, with solid lines indicating medians and dotted lines representing 1.5x interquartile ranges. Kruskal-Wallis non-parametric ANOVA with Dunn's post-hoc test was used for comparisons across substrates in (A-B) and Kolmogorov-Smirnov non-parametric unpaired t-tests were used for DIV 7 vs DIV 14 comparisons in (C-D). ***p<0.001.*

Finally, to further evaluate the efficiency of mitochondrial motion dynamics, the duration of pauses was calculated from the duration of segments with a velocity < 0.1 μm/s. At DIV 7 in Fig 34A, pauses were slightly longer on PDL, median 32.4 s (IQR = 14.4–77.1) compared to those in cells on dual coatings – 28.2 s (IQR = 12.6–64.8, $p<0.05$). Mitochondria in DIV 14 cells on dual coated-substrates paused for shorter durations compared to mitochondria on PDL- or laminin-substrates (Fig 34B) – median of 25.2 s on dual-substrates was found (IQR = 13.2–52.2) which were lower than 33.0 s on PDL- (IQR = 16.8–73.8) and 31.2 s on laminin-substrates (IQR = 16.2–74.7, $p<0.01$ and $p<0.001$).

The frequency of pauses on dual was slightly greater than on laminin – median 0.012 s^{-1} on dual- (IQR = 0.006–0.017) compared to 0.011 s^{-1} on laminin-substrates (IQR = 0.006–0.017), $p<0.01$ (Fig 34C). There was no difference in the frequency of pauses across substrates between DIV 7 and 14 (Fig 34D).

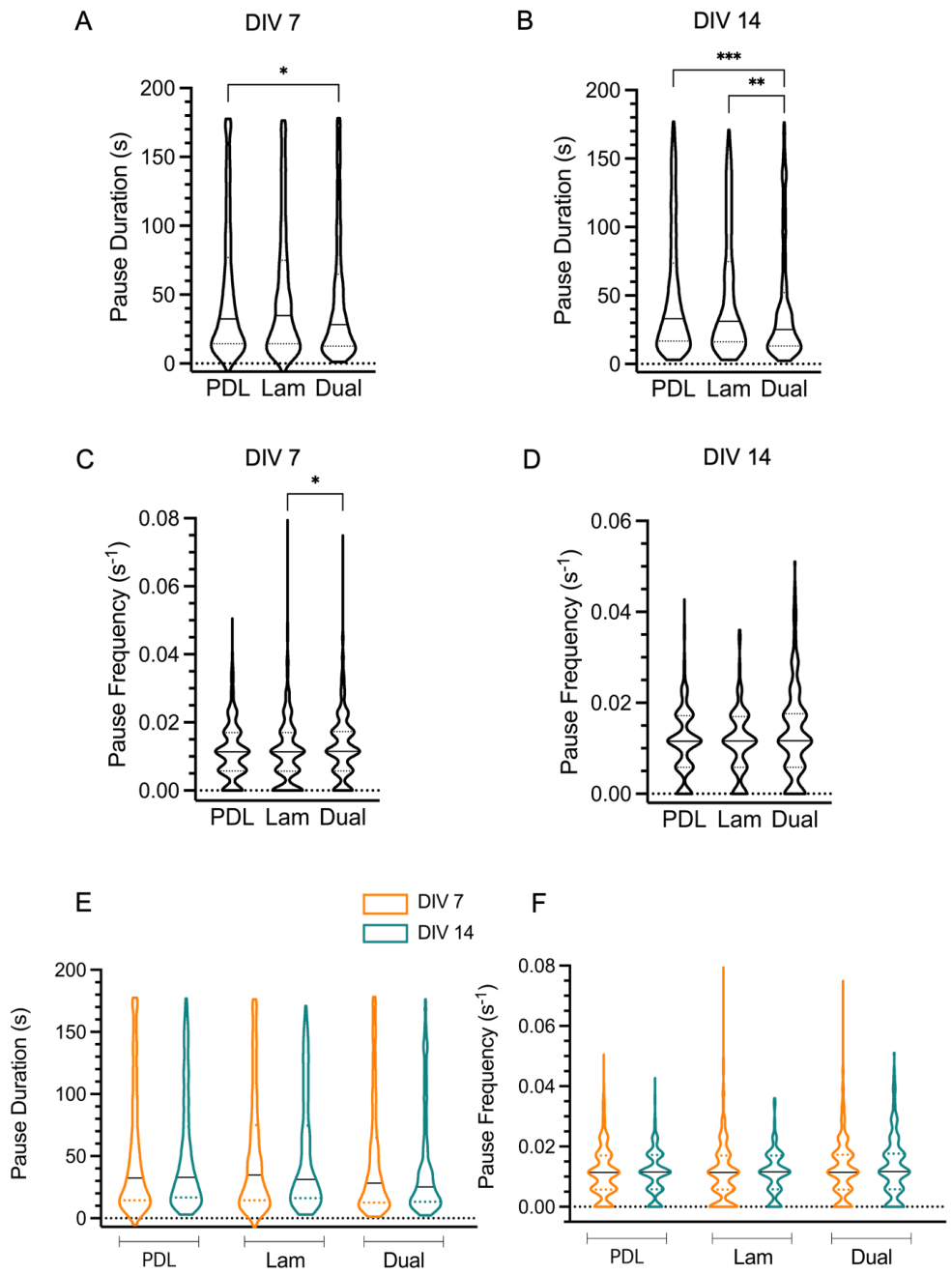

Figure 34. Pause-related parameters of mitochondrial movements within hippocampal cells.

(A) Segments with a velocity less than 0.1 µm/s were considered as pauses. The duration of pauses (with segments with a velocity less than 0.1 µm/s) between substrates at DIV 7 and (B) at DIV 14 were shown. (C) shows measurements of the number of pauses mitochondria performed during the imaging period between substrates at DIV 7 and (D) at DIV 14. (E) comparisons of pause duration of motile

*mitochondria within each substrate between DIV 7 and 14. (F) Frequency of pauses of mitochondria within each substrate between DIV 7 and 14. Violin plots represent the distribution of all data points; solid lines indicate medians and dotted lines indicate 1.5x interquartile ranges. Kruskal-Wallis non-parametric ANOVA with Dunn's post-hoc test was used for comparisons across substrates in (A-D), and Kolmogorov-Smirnov non-parametric unpaired t-tests were sued for DIV7 vs DIV 14 comparisons in (E-F). *p<0.05, **p<0.01, ***p<0.001. a*

4.2.4 KymoAnalyzer Quantification of Motion Within Neuronal Processes on Positively and Negatively Charged Substrates

To investigate how charged substrates influence mitochondrial motility *in vitro*, neuronal cultures were grown on CES-coated (negatively charged carboxyl-functionalised) and APTES-coated (positively charged amino-functionalised) substrates. Mitochondrial movements were visualised using MitoTracker Green at DIV 7 and DIV 14, and motility was quantified using the ImageJ KymoAnalyzer plugin.

The overall fraction of motile mitochondria within neuronal cultures on CES and APTES substrates was quantified (Fig. 35A). At DIV 7, the median fraction of motile mitochondria on CES was 21.4% (IQR = 9.10–37.5), which significantly decreased to 10% (IQR = 0.00–17.9, $p<0.001$) by DIV 14. Similarly, on APTES substrates, the fraction of motile mitochondria decreased from 30% (IQR = 15.4–40.0) at DIV 7 to 14.3% (IQR = 6.47–23.5, $p<0.001$) at DIV 14. APTES substrates consistently supported a higher fraction of motile mitochondria compared to CES at both time points. Although motile mitochondrial fractions were quantifiable on both CES and APTES, they appeared lower than those observed on bulk PDL/laminin-coated substrates, potentially reflecting reduced cell density or neuronal health on charged substrates.

Mitochondrial motility was further classified as anterograde, retrograde, or bidirectional (reversing). At DIV 7 (Fig 35B), cells on APTES substrates displayed a higher proportion of reversing mitochondria (18.18%, IQR = 10.0–29.0) compared to

CES (12.5%, IQR = 0.00–23.1, $p<0.05$). Similar trends were observed at DIV 14 (Fig 35C), with APTES showing 8.17% (IQR = 0.00–16.7) reversing mitochondria compared to 4.17% (IQR = 0.00–12.1) on CES ($p<0.01$). Across all directional categories, mitochondrial movement appeared generally reduced compared to that observed under conventional PDL/laminin conditions, further supporting the influence of substrate type on neuronal transport capacity.

The specific motility patterns (anterograde, retrograde, and reversing) were also compared between DIV 7 and DIV 14 (Fig. 35D-F). At DIV 7, CES substrates supported more anterograde mitochondria (median 0%, IQR = 0.00–7.69), but this decreased to 0% (IQR = 0.00–4.55) by DIV 14 (Fig 35D). Reversing motion was more prevalent on both substrates at DIV 7, with 12.5% (IQR = 0.00–23.1) of mitochondria on CES and 18.2 % (IQR = 10.0–29.0) on APTES, decreasing to 4.17% (IQR = 0.00–12.1) on CES and 8.17% (IQR = 0.00–17.7) on APTES by DIV 14 (Fig 35F).

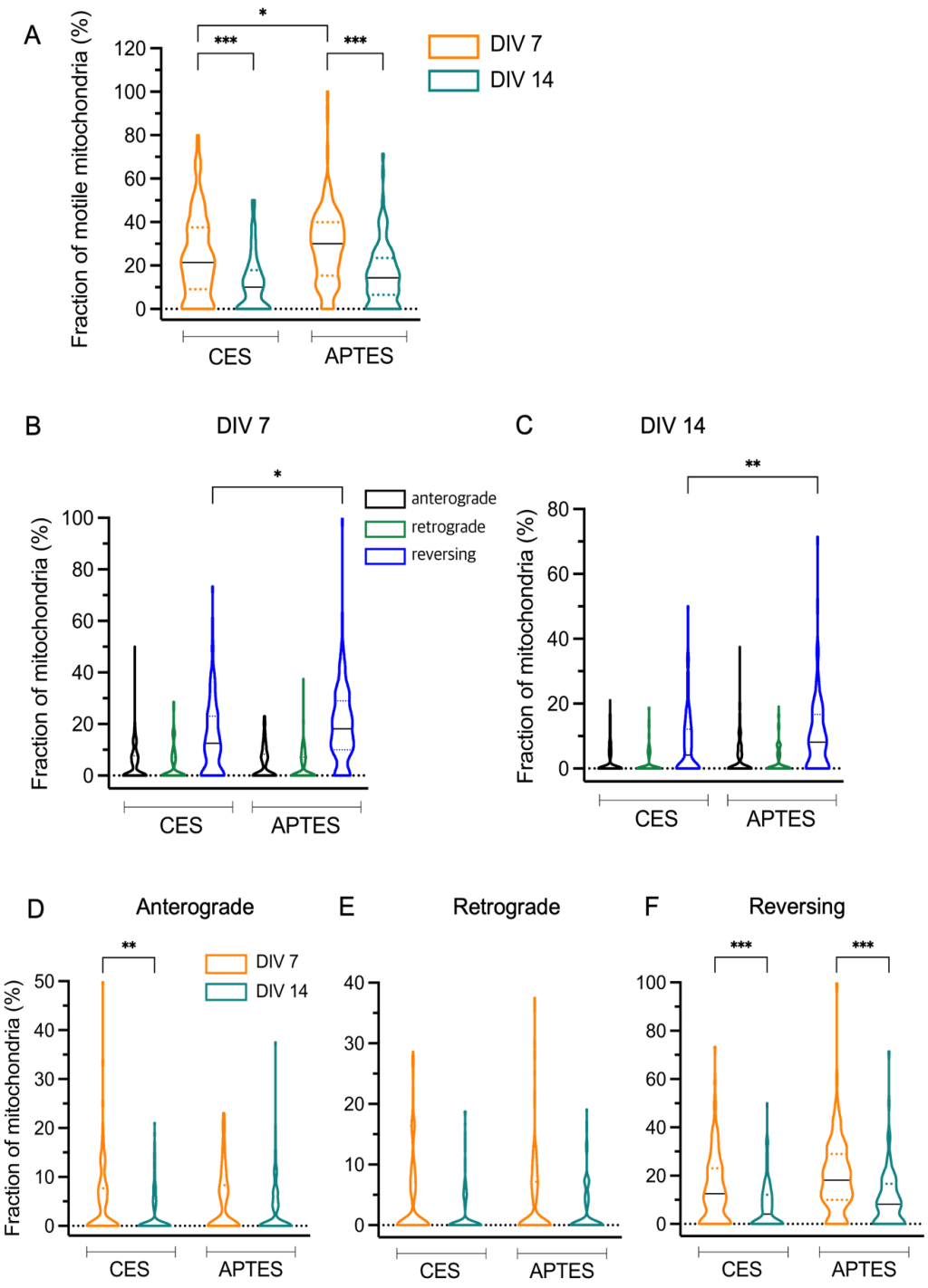

Figure 35. Quantification of mitochondrial motility within hippocampal cell cultures.

(A) Overall fraction of motile mitochondria (excluding stationary mitochondria) on CES- or APTES-coated substrates at DIV 7 and DIV 14. (B-C) Fraction of mitochondria showing unidirectional (anterograde or retrograde) or bidirectional (reversing)

motion between substrates at (B) DIV 7 and (C) DIV 14. (D-F) Comparison of each type of mitochondrial motion (D: anterograde, E: retrograde, F: reversing) between DIV7 and 14. n= 3 independent experiments, Kruskal-Wallis non-parametric ANOVA with Dunn's post-hoc test. Violin plots show data distribution with median values (solid line) and 1.5x interquartile range (dotted line).

The time spent by mitochondria in anterograde, retrograde, or reversing movements was quantified to assess motility behaviour on CES and APTES substrates (Fig 36). A mitochondrion was considered as moving in a particular direction even if it only travelled for a small percentage of the time (1%) and remained paused for the rest. When comparing the two substrates, no major differences in time spent moving anterograde, retrograde, or reversing were observed at both DIV 7 (Fig 36A) and DIV 14 (Fig 36B).

When comparing mitochondrial motility within each substrate between DIV 7 and DIV 14 (Fig 36C-E), there were no significant changes in the percentage of time spent in purely anterograde or retrograde motion. However, for both substrates, mitochondria spent a greater proportion of time paused at DIV 7 (CES: 38.0%, IQR = 16.7–68.6; APTES: 38.8%, IQR = 14.5–69.4) compared to DIV 14 (CES: 30.2%, IQR = 9.60–70.7; APTES: 28.9%, IQR = 10.2–64.3, $p<0.01$), indicating reduced motility over time as cultures aged.

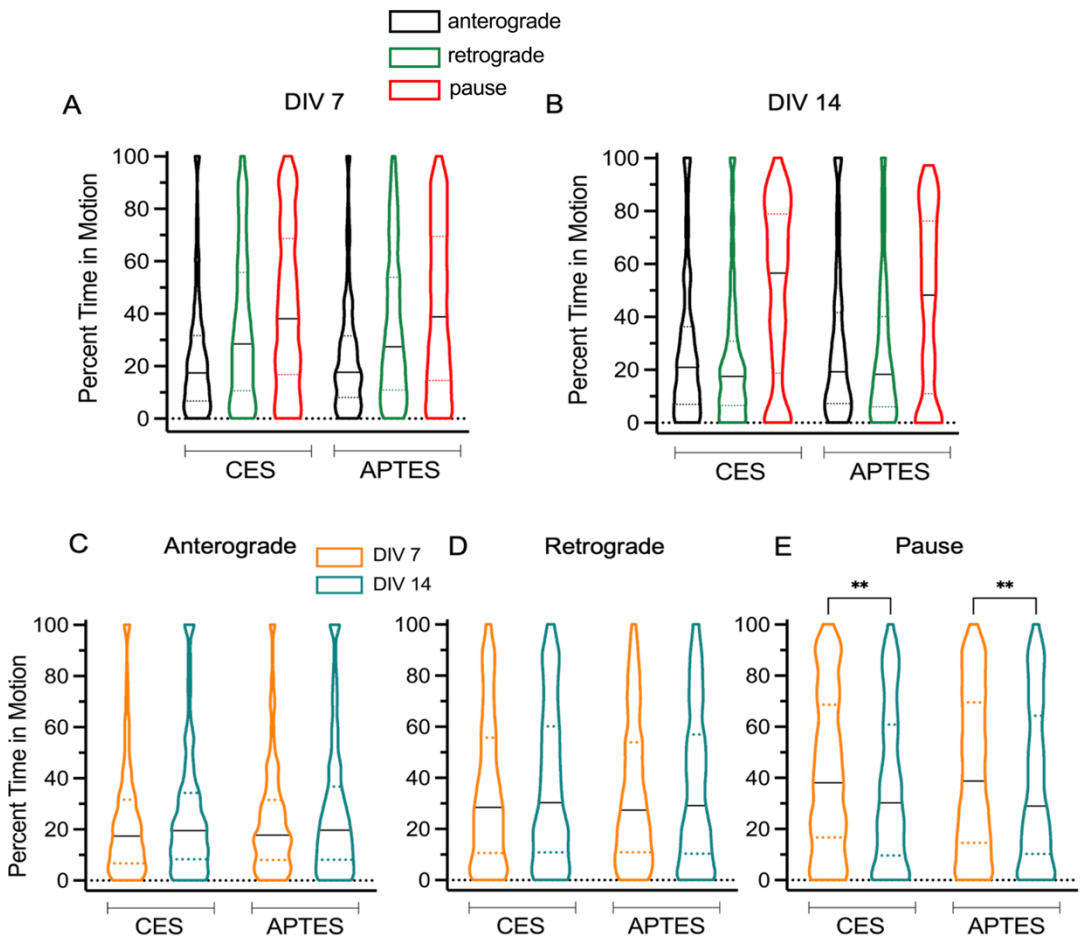

Figure 36. Average percentage of time that mitochondria spent in either anterograde, retrograde or paused motion.

(A) Comparison of the percentage of time mitochondria spent in each type of motion on CES and APTES substrates at DIV 7. (B) Comparison at DIV 14. (C-E) Breakdown of specific motions comparing DIV 7 and DIV 14 for each substrate: (C) anterograde, (D) retrograde, (E) paused. Kruskal-Wallis non-parametric ANOVA with Dunn's post-hoc test. Data shown as violin plots with median values (solid line) and 1.5 x interquartile range (dotted line).

Multiple velocity-related parameters of mitochondrial motion within neurons cultured on CES- and APTES-coated substrates were quantified using KymoAnalyzer. The net velocities of mitochondria measured over the full imaging period at both DIV 7 and DIV 14 (Fig 37A-B) showed no significant differences between the two

substrates at either time point. However, when comparing the velocities of mitochondria travelling in the retrograde direction on CES substrates between DIV 7 and DIV 14, a significant increase was observed. At DIV 14, the median retrograde velocity was 0.15 μm/s (IQR = 0.10–0.21), compared to 0.09 μm/s (IQR = 0.06–0.16) at DIV 7, ($p<0.05$, Fig 36D). No major changes in anterograde velocities were observed between time points (Fig 37C).

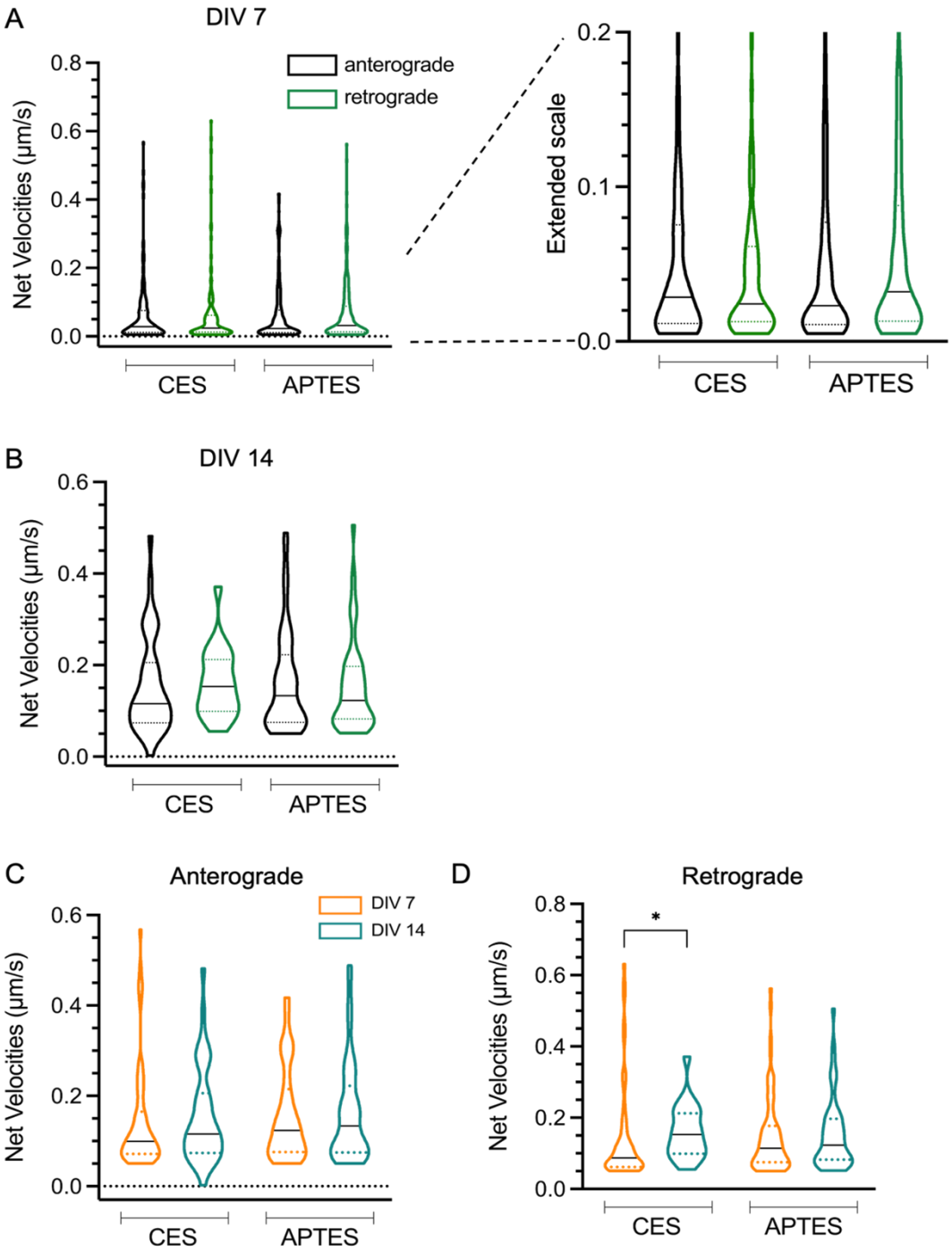

Figure 37. Graphs of mean average velocities of mitochondria moving either net anterograde or net retrograde on CES- or APTES-substrates at DIV 7 and 14.

(A) Velocities of mitochondria moving in either direction between substrates at DIV 7. (B) Velocities at DIV 14. The right panel of (A) shows a zoomed-in scale for better visualization of the median and interquartile range. (C-D) Comparison of mitochondrial velocities within each substrate between DIV 7 and DIV 14. (C)

*anterograde velocities, (D) retrograde velocities. Violin plots indicate the distribution of all data points; solid lines mark medians and dotted lines mark 1.5 x interquartile ranges. Kruskal-Wallis non-parametric ANOVA with Dunn's post-hoc test was applied for group-wise comparisons in (A-B), and unpaired Kolmogorov-Smirnov tests were used for DIV 7 vs DIV 14 comparisons in (C-D). *p<0.05*

Significant differences were observed in the segmental velocities of mitochondrial movements. At DIV 7, the retrograde velocity of mitochondria on APTES substrates (median = 0.11 μm/s, IQR = 0.07–0.18) was significantly higher compared to CES substrates (median = 0.10 μm/s, IQR = 0.07–0.16, $p<0.05$, Fig. 38A). A similar trend was observed at DIV 14, where the retrograde velocity on APTES (median = 0.12 μm/s, IQR = 0.08–0.19) was also greater than that on CES (median = 0.11 μm/s, IQR = 0.08–0.16, $p<0.05$, Fig 38B).

When comparing mitochondrial velocities within each substrate between DIV 7 and DIV 14, retrograde mitochondria on APTES showed a significant increase from DIV 7 (median = 0.11 μm/s, IQR = 0.07–0.18) to DIV 14 (median = 0.12 μm/s, IQR = 0.08–0.19, $p<0.05$, Fig. 38D). However, combined segmental velocities across the two substrates at both DIV 7 and DIV 14 did not show significant differences for anterograde movements (Fig. 38C).

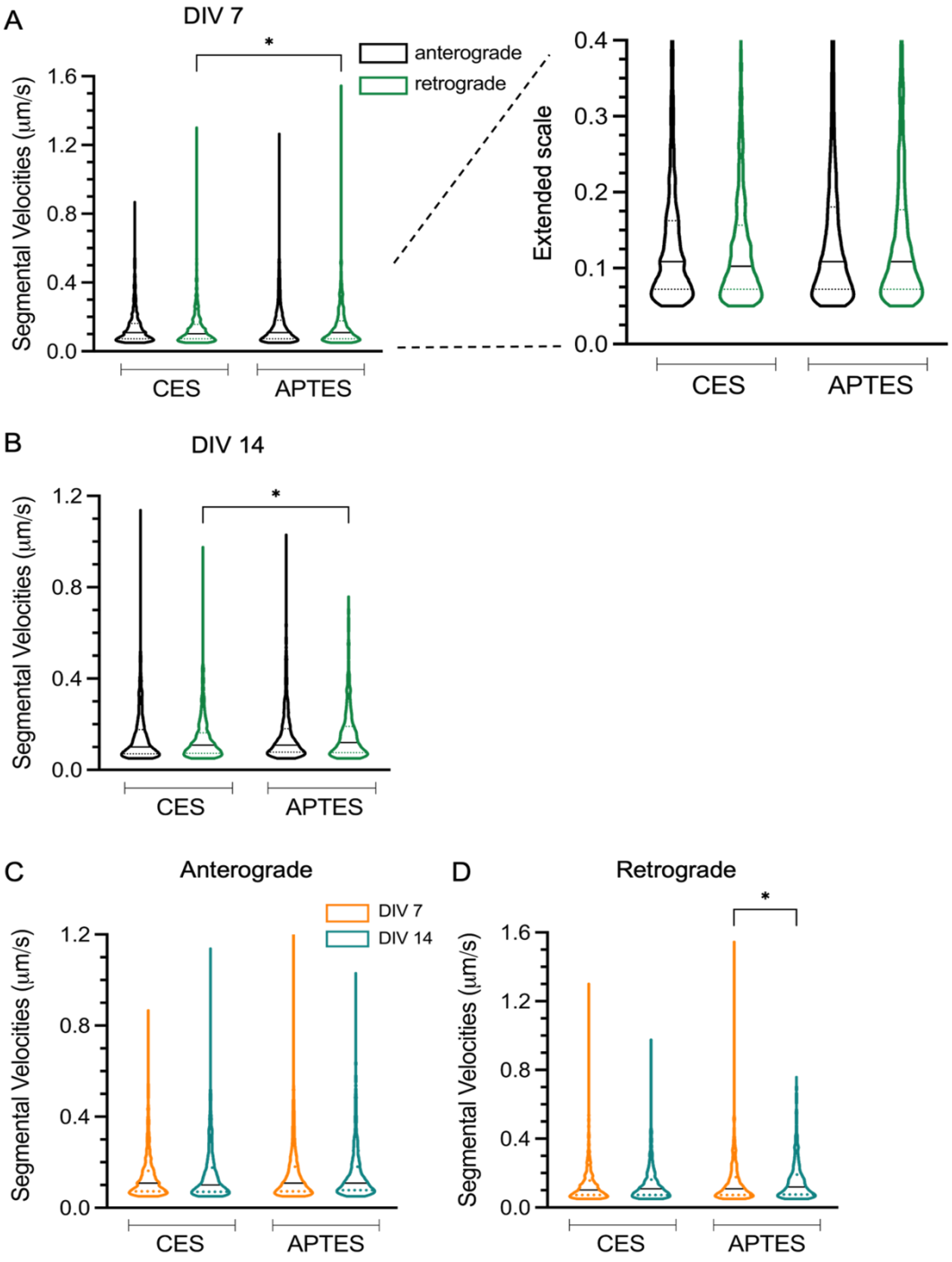

Figure 38. Segmental velocities of mitochondria travelling either anterograde or retrograde.

(A) Segmental velocities of anterograde and retrograde movements between CES and APTES substrates at DIV 7. (B) Segmental velocities at DIV 14. (C-D) Comparison of the velocities of mitochondria within each substrate between DIV 7 and DIV 14:

(C) Anterograde velocities, (D) Retrograde velocities. Violin plots show full data distributions with solid lines indicating medians and dotted lines representing 1.5x interquartile ranges. Kruskal-Wallis non-parametric ANOVA with Dunn's post-hoc test was applied for group-wise comparisons in (A-B), and unpaired Kolmogorov-Smirnov tests were used for DIV7 vs DIV 14. Comparisons in (C-D).

The distance travelled by mitochondria over the imaging period was measured within cell cultures at DIV 7 (Fig 39A). Mitochondria on APTES substrates moving in the retrograde direction travelled longer distances (median = 1.7 μm, IQR = 1.30–2.47) compared to those on CES substrates (median = 1.5 μm, IQR = 1.70–2.15, $p<0.05$). Significant changes were also observed at DIV 14 (Fig 39B), where retrograde-moving mitochondria on APTES substrates travelled a longer median distance (2.47 μm, IQR = 1.89–3.80) compared to those on CES substrates (median = 1.79 μm, IQR = 1.37–2.80, $p<0.05$).

Comparing the distances travelled by mitochondria within each substrate between DIV 7 and DIV 14 revealed that, regardless of the direction of movement or substrate type, mitochondria travelled shorter distances at the earlier timepoint (DIV 7). Anterograde-moving mitochondria at DIV 7 travelled shorter distances on both CES (1.40 μm, IQR = 1.11–1.40) and APTES (1.50 μm, IQR = 1.17–2.15) substrates compared to DIV 14 (CES: 2.08 μm, IQR = 1.63–3.64; APTES: 2.08 μm, IQR = 1.69–2.86, $p<0.001$, Fig 39C). Similarly, retrograde-moving mitochondria travelled shorter distances at DIV 7 (CES: 1.43 μm, IQR = 1.11–2.15; APTES: 1.70 μm, IQR = 1.30–2.47) compared to DIV 14 (CES: 1.79 μm, IQR = 1.37–2.80; APTES: 2.47 μm, IQR = 1.89–3.80, $p<0.001$, Fig 39D).

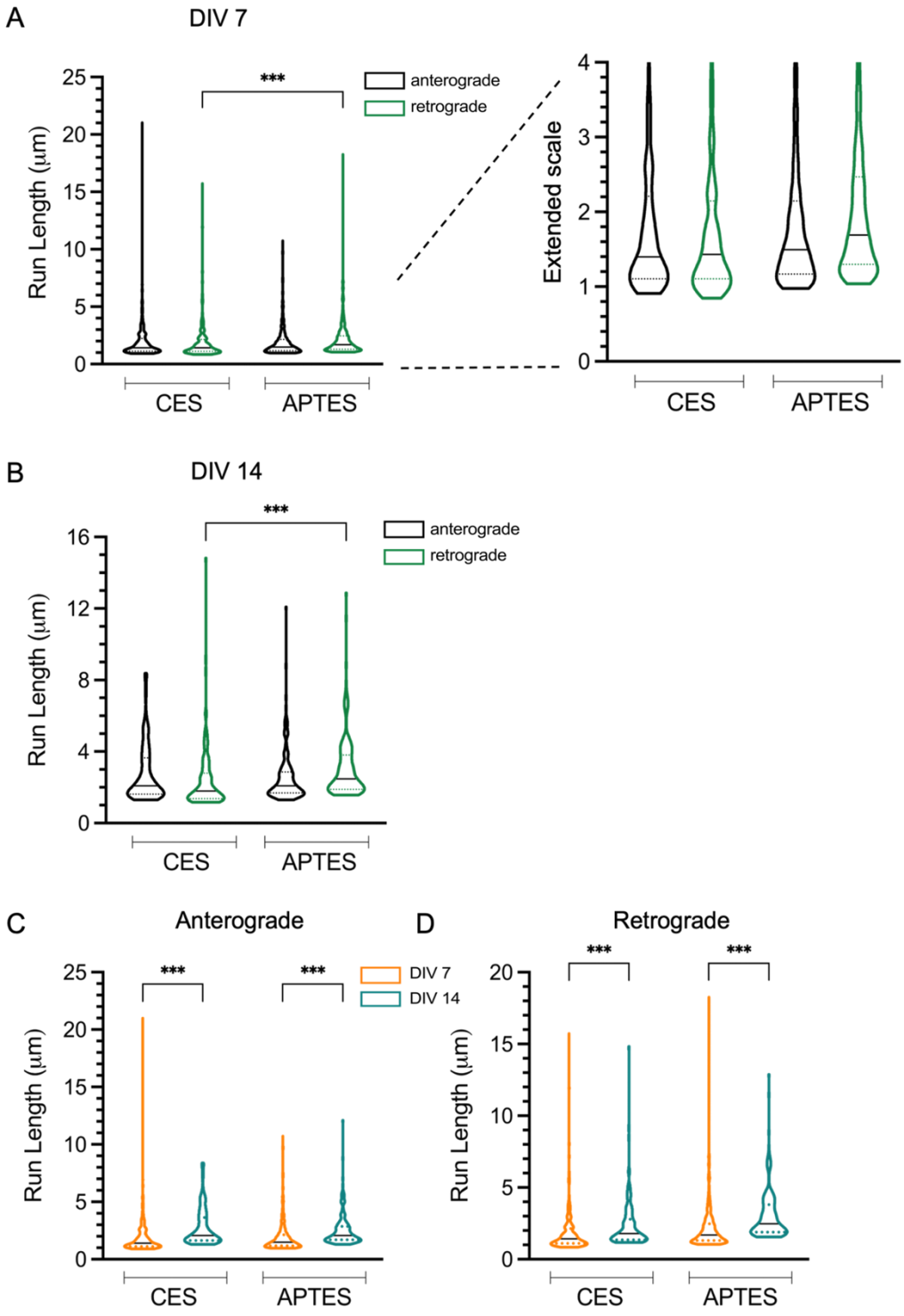

Figure 39. Distance travelled per burst of mitochondrial movement.

The travel distance was measured by tracking mitochondria across a combined segment until they paused or. Hanged direction. (A) Measurement of run lengths for mitochondria moving either anterograde or retrograde on CES and. PTES substrates

at DIV 7. (B) Measurement of run lengths at DIV 14. (C-D) Comparison of mitochondrial travel distances within each. Substrate between DIV 7 and DIV 14: (C) Anterograde movement, (D) Retrograde movement. Violin plots show full data distributions, with solid lines indicating medians and dotted lines representing a.5x interquartile ranges. Kruskal-Wallis non-parametric ANOVA with Dunn's post-hoc test was used for comparisons in (A_B); unpaired Kolmogorov-Smirnov tests were used for (C-D).

The pause duration of mitochondrial movements was measured and compared between CES and APTES substrates (Fig 40). At DIV 14, mitochondria on CES substrates exhibited longer pauses (median = 23.4 s, IQR = 12.0–51.3) compared to those on APTES substrates (median = 19.2 s, IQR = 9.6–40.8, $p<0.05$, Fig 40B). However, at DIV 7, no significant differences in pause duration were observed between the two substrates (Fig. 40A).

When comparing pause duration within each substrate between DIV 7 and DIV 14, both CES and APTES substrates showed longer pause durations at DIV 14 than at DIV 7. Mitochondria at DIV 7 had shorter pause durations on CES (median = 17.4 s, IQR = 9.00–36.0) and APTES (median = 15.6 s, IQR = 8.40–36.0) compared to DIV 14 (CES: 23.4 s, IQR = 12.0–51.3; APTES: 19.2 s, IQR = 9.60–40.8, Fig 40C).
In terms of pause frequency, no significant differences were observed between CES and APTES substrates at either DIV 7 (Fig. 40D) or DIV 14 (Fig 40E). However, when comparing mitochondria between DIV 7 and DIV 14, significant changes were observed on both substrates, with mitochondria at DIV 7 showing higher pause frequencies (CES: 0.02 s^{-1}, IQR = 0.01 – 0.03; APTES: 0.02 s^{-1}, IQR = 0.01–0.03) compared to those at DIV 14 (CES: 0.02 s^{-1}, IQR = 0.01–0.02; APTES: 0.02 s^{-1}, IQR = 0.01–0.02, $p<0.05$, Fig 40F).

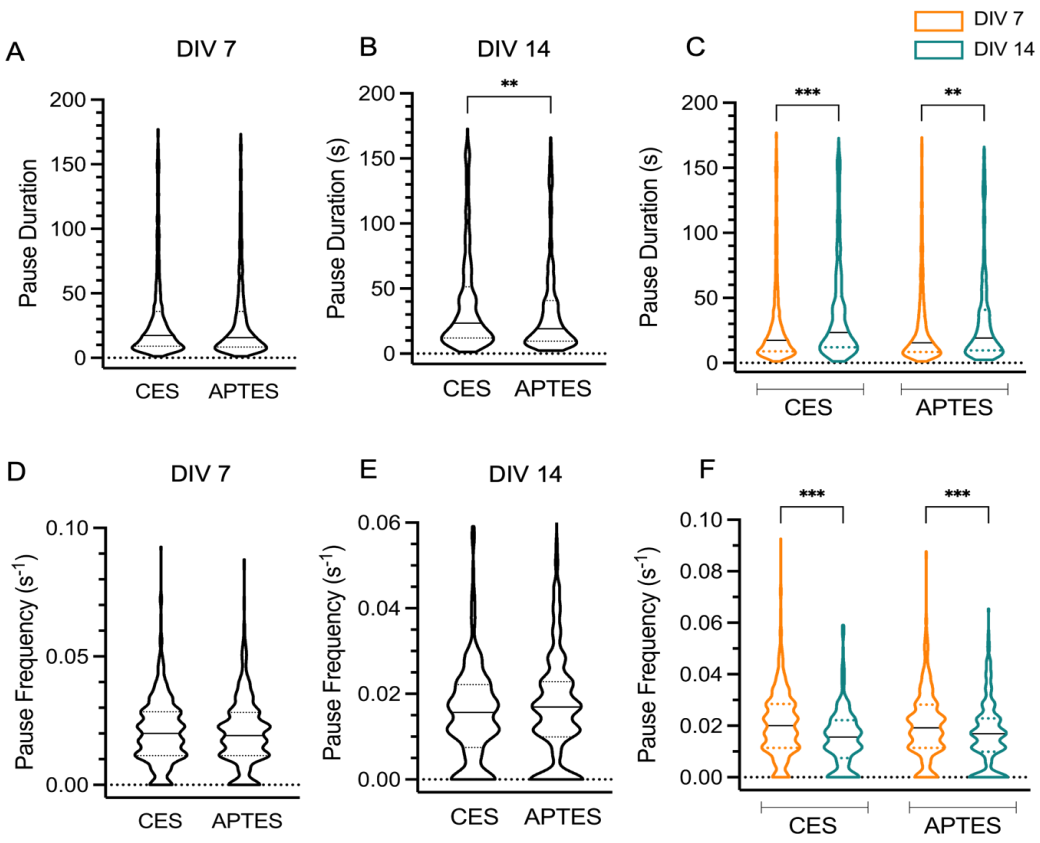

Figure 40. Kymoanalysis of pause-related parameters of mitochondrial movements on CES- and APTES-substrates.

*(A) Comparison of pause duration between CES and APTES at DIV 7. (B) Comparison of pause duration at DIV 14. (C) Pause duration within each substrate between DIV 7 and 14. (D) Number of pauses mitochondria taken during the imaging period at DIV 7, (E) Number of pauses at DIV 14. (F) Pause frequency within each substrate between DIV 7 and 14. Violin plots show full data distributions; solid lines indicate medians and dotted liens represent 1.5x interquartile ranges. Kruskal-Wallis non-parametric ANOVA with Dunn's post-hoc test was applied for (A-B, D-E); unpaired Kolmogorov-Smirnov tests were used for (C, F). **p<0.01, ***p<0.001.*

4.2.5 Overall Comparisons on Hippocampal Cell Behaviours and Mitochondrial Movements Across Traditional and Charged Surface Coated Substrates

So far, various mitochondrial motility-related parameters within primary hippocampal cells cultured on either traditionally coated or charged substrates have been compared. In order to make direct comparisons across all 5 substrates (3 traditional, 2 charged), the data shown above was re-analysed comparing all 5 substrates with DIV 7 cells.

The overall motile fraction of mitochondria on either traditional- or charged-substrates were analysed in Fig 41A. The motile mitochondria on CES-substrates, the negatively charged substrates showed significantly lower fraction of mitochondria – median of 21.4% (IQR = 9.10–37.5) compared to mitochondria on traditional substrates – 36.6% (IQR = 25.0–47.1) on PDL, 33.3% (IQR = 18.4–50.0) on laminin or 41.3% (IQR = 1.25–63.5) on dual substrates. When the fraction of each different motion of mitochondria was measured, cultures on charged substrates showed significantly lower anterograde fraction of mitochondria (Fig 41B) – 0% (IQR = 0.0–7.7) on CES and 0% (IQR = 0.0–8.3) on APTES compared to mitochondria on traditionally substrates – 6.3% (IQR = 0.0–12.6) on PDL, 5.8% (IQR = 0.00–11.8) on laminin or 7.4% (IQR = 0.00–14.1) on dual substrates. Whereas no major differences were observed when retrograde fraction of mitochondria was compared (Fig 41C). Moreover, cultures on charged substrates also showed significantly lower fraction of mitochondria displaying reversing motion – 12.5% on CES (IQR = 0.00–23.1) and 18.2% on APTES (IQR= 10.0–29.0) compared to traditional substrates – 25% on PDL (IQR = 17.2–35.4), 25% on laminin (IQR = 16.7–39.8) and 37% on dual (IQR = 19.2–50.0) (Fig 41D).

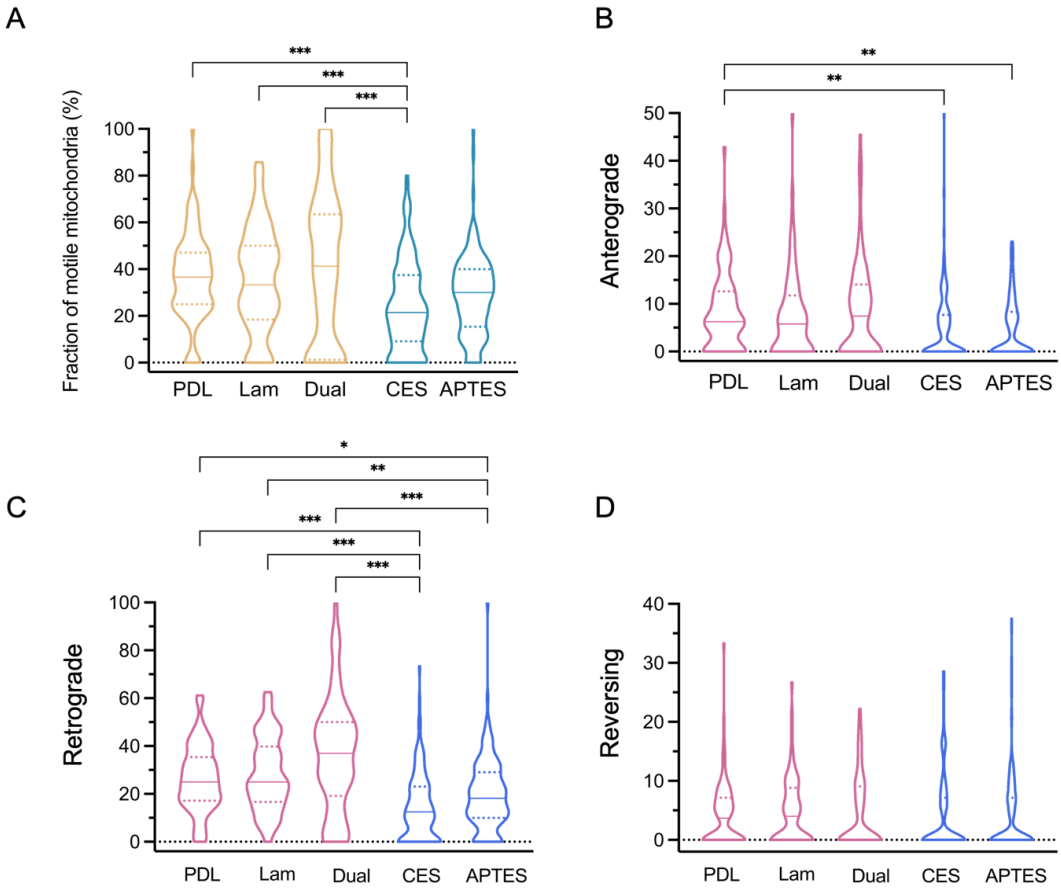

Figure 41. Comparisons of fraction of moving mitochondria within hippocampal cells between traditional- and charged-substrates.

(A) overall fraction of moving mitochondria including any form of motion. Then each motion of mitochondria between traditional and charged substrates were compared; (B) anterograde, (C) retrograde or (D) reversing mitochondria. Statistical analyses between PDL, laminin or dual, and CES or APTES were performed.

When the percent motion time of mitochondria was compared between the two methods of substrates, some major differences were also found (Fig 42). The time mitochondria travelled anterograde direction showed major difference between cells on APTES- and laminin-substrates – median of 17.7% mitochondria (IQR = 7.97–31.5) on APTES-substrates spent more time than on laminin-substrates – with median of 12.8% mitochondria (IQR = 3.75–34.7) in Fig 42A. Percent time mitochondria travelled retrograde showed significant differences between the two main types of substrates too, that mitochondria spent higher time on moving retrograde on two charged substrates – median of 28.4% (IQR = 10.6–55.7) on CES and 27.3% (IQR = 10.8–53.9) on APTES compared to traditional substrates – 10.9% (IQR = 1.72-29.0) on PDL, 16.0% (IQR = 3.77–37.8) on laminin or 12.4% (IQR = 4.08–26.3) on dual substrates (Fig 42B). mitochondria on two charged substrates also show higher time remaining paused – median of 38.0% (IQR = 16.7–68.6) on CES and 38.8% (IQR = 14.5–69.4) on APTES compared to traditional substrates – 61.8% (IQR = 17.5–87.3) on PDL, 56.3% (IQR = 12.7–84.9) on laminin or 64.4% (IQR = 28.3–87.0) on dual substrates (Fig 42C).

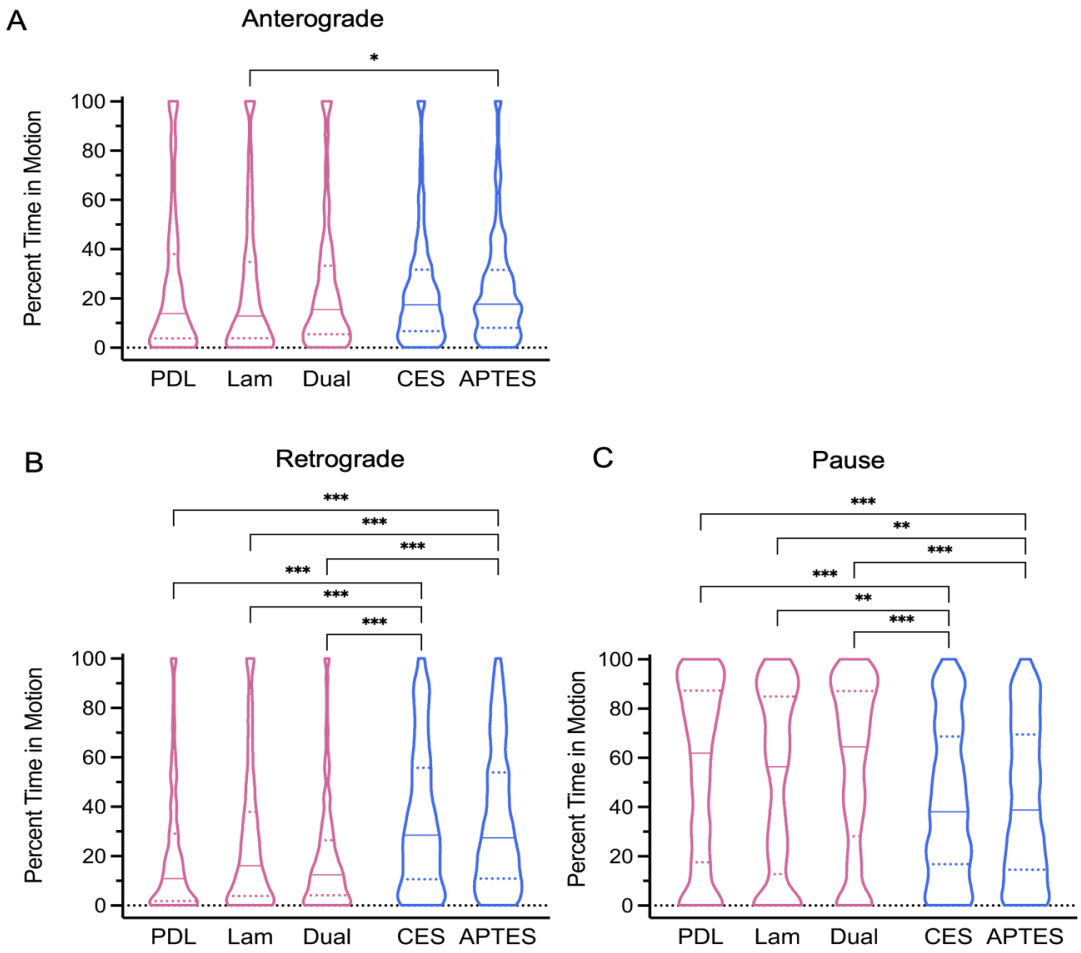

Figure 42. Percent time that mitochondria were in motion, in hippocampal cells on traditional- or charged substrates.

Graphs of the mitochondria that travelled (A) anterograde, (B) retrograde or (C) remained paused are shown.

The velocity-related parameters of mitochondria; net velocities, segmental velocities, combined segmental velocities and run length between traditional and charged substrates were compared to investigate if the types of substrates affect the velocities of mitochondrial movements in Fig 43. As a result, dramatic differences were found between the two types of substrates regardless of directions mitochondria travelled within neuronal processes that mitochondria on charged substrates in general showed significant decreases in velocities and distances of movements. First, the net velocities of mitochondria on charged substrates showed significantly slower velocities than on traditional substrates,

regardless of directions. For anterograde direction in Fig 43A, mitochondria on traditional substrates (0.26 μm/s on PDL; IQR = 0.14 – 0.45, 0.26 μm/s on laminin; IQR = 0.12 – 0.56 or 0.24 μm/s on dual; IQR = 0.11 – 0.44) displayed faster net velocities than charged substrates (0.10 μm/s on CES; IQR = 0.07 – 0.17 or 0.12 μm/s on APTES; IQR = 0.08 – 0.22, $p<0.001$). Retrograde mitochondria in Fig 43B also showed higher velocities of mitochondria on traditional substrates (0.21 μm/s on PDL; IQR = 0.11 – 0.37, 0.21 μm/s on laminin; IQR = 0.11 – 0.37 or 0.18 μm/s on dual; IQR = 0.11 – 0.36) compared to mitochondria on charged substrates (0.09 μm/s on CES; IQR = 0.06 – 0.16 or 0.12 μm/s on APTES; IQR = 0.08 – 0.18, $p<0.01$ and ***$p<0.001$).

Similar results were shown when segmental velocities of mitochondria on 5 different substrates in Fig 43C were measured, that faster velocities of mitochondria travelling anterograde within cells cultured on traditional substrates (0.27/ 0.29/ 0.19 μm/s on PDL-, laminin- or dual-substrates, respectively; IQR = 0.15 – 0.48/ 0.16 – 0.53/ 0.11 – 0.37) were observed compared to mitochondria on charged substrates (0.11 μm/s on CES; IQR = 0.07 – 0.16 or 0.11 μm/s on APTES; IQR = 0.07 – 0.18, $p<0.001$). Similarly, mitochondria moving in the retrograde direction (Fig 43D) exhibited faster segmental velocities on traditional substrates (0.21 μm/s on PDL; IQR = 0.11 – 0.37, 0.1 μm/s on laminin; IQR = 0.11 – 0.37 or 0.18 μm/s on dual; IQR = 0.11 – 0.36) than on charged substrates (0.09 μm/s on CES; IQR = 0.06 – 0.16 or 0.12 μm/s on APTES; IQR = 0.08 – 0.18). Finally, noticeable difference was observed between two types of substrates when the length of distances of mitochondria was measured (Fig 43E-F). Hippocampal cell cultures on traditional substrates showed longer distances of mitochondria travelling anterograde (6.37/ 5.98/ 4.16 μm for anterograde mitochondria on PDL-, laminin- or dual-substrates; IQR = 4.81 – 9.88/ 4.29 – 9.75/ 2.86 – 6.5) compared to cells on charged substrates (1.40/1.50 μm on CES- or APTES-substrates; IQR = 1.11 – 2.21/ 1.17 – 2.15, $p<0.001$) in Fig 43E. Moreover, retrograde mitochondria on traditional substrates travelled longer distances (5.46/ 6.11/ 3.51 μm on PDL-, laminin- or dual-substrates; IQR = 4.29 – 8.32/ 4.55 – 9.23/ 2.47 – 5.72, respectively) than on

charged substrates (1.43/ 1.69 µm on CES- or APTES-substrates; IQR = 1.11 – 2.15/ 1.30 – 2.47, respectively), p<0.001 in Figure 43F.

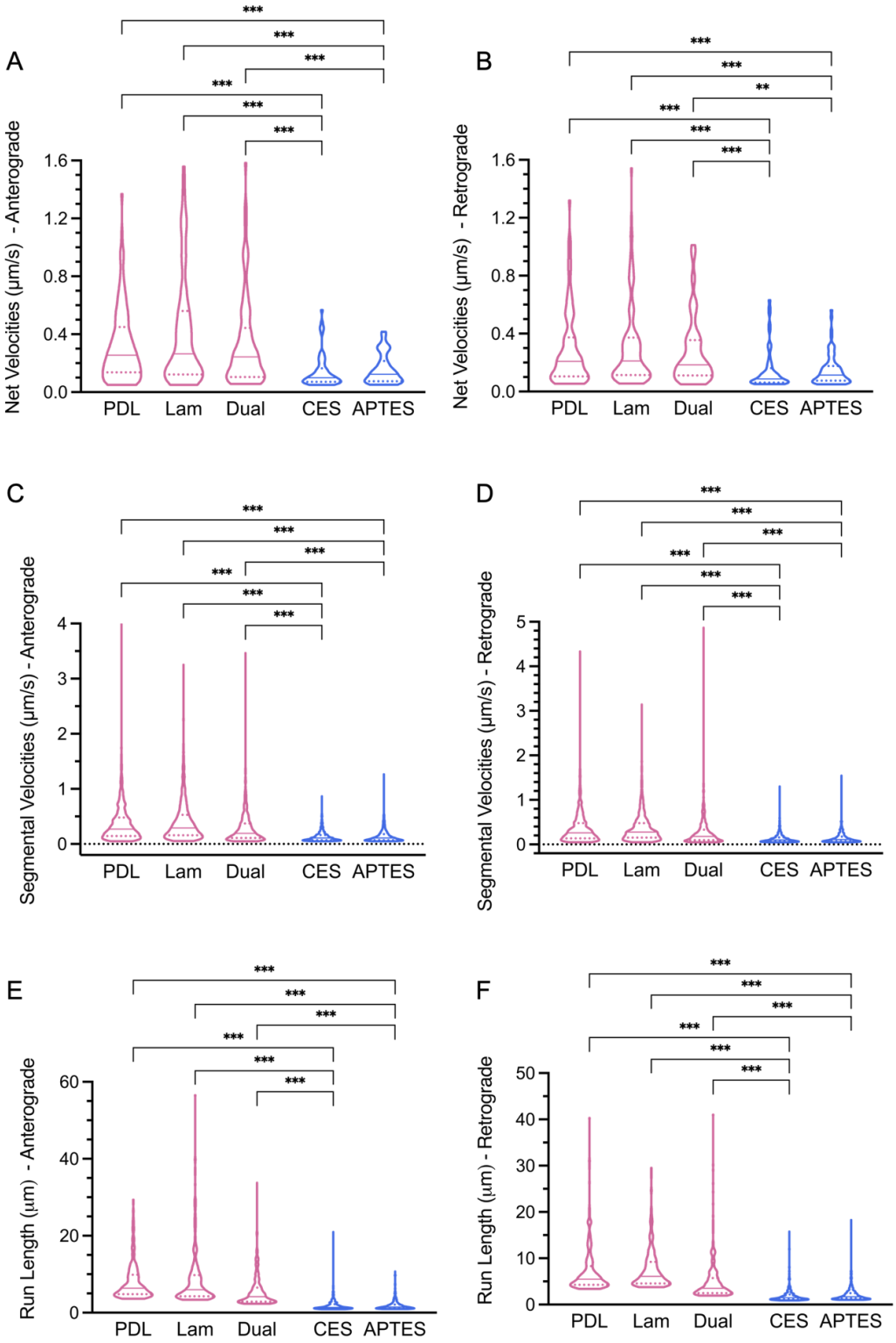

Figure 43. Kymoanalysis of velocity-related parameters of motion of mitochondria between traditional- or charged substrates.

Net velocities of mitochondria moving (A) anterograde or (B) retrograde between substrates were compared. Segmental velocities of mitochondria moving (C) anterograde or (D) retrograde and run lengths of mitochondria either (E) anterograde or (F) retrograde were also compared between substrates.

Mitochondria within cell cultures on traditional substrates additionally presented higher pause duration (32.4/ 34.8/ 28.2 s on PDL-/ laminin-/ dual-substrates; IQR = 14.4–77.1/ 14.4–75.0/ 12.6–64.8, respectively) compared to charged substrates (17.4/ 15.6 s on CES-/ APTES-substrates; IQR = 9.00–36.0/ 8.40–36.0, $p<0.001$) in Fig 44A. On the other hand, mitochondria on each charged substrate in Fig 44B showed significantly higher pause frequency (0.02 s-1 on CES-/ APTES-substrates; IQR = 0.01–0.03) compared to mitochondria on traditional substrates (0.01 s-1 on PDL-/laminin-/dual-substrates; IQR = 0.01–0.02)

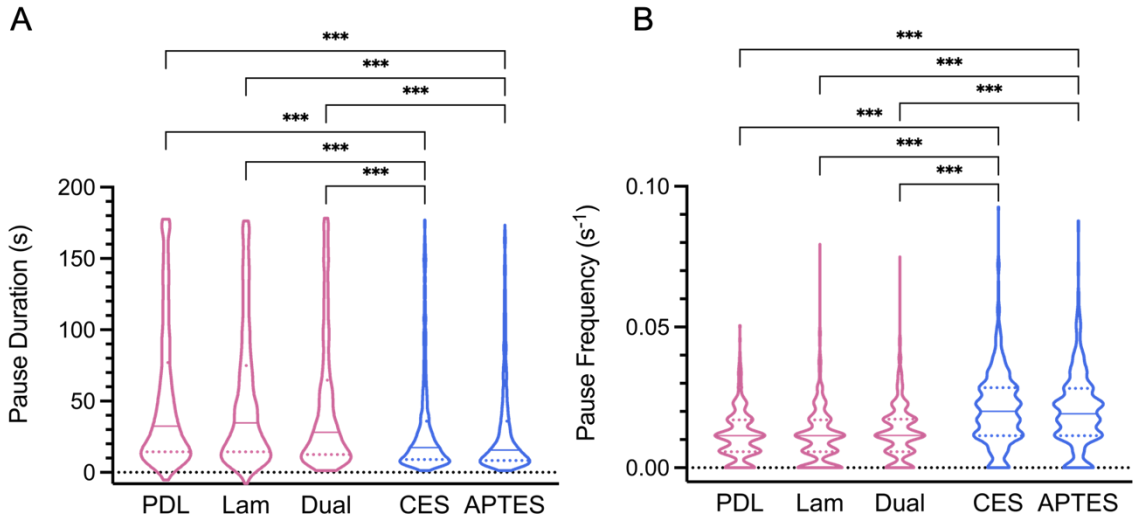

Figure 44. Pause related aspects of mitochondrial motion between traditional- or charged-substrates.

(A) duration of pauses of mitochondria between substrates and (B) frequency of pauses of mitochondria during imaging period between substrates were shown.

4.3 Discussion

This study demonstrates that surface modification for *in vitro* neuronal cultures is critical, as it significantly influences neuronal morphology, adhesion and motion-related mitochondrial dynamics within neuronal processes. The findings from this study highlight the importance of choosing appropriate biomaterials for cell culture substrates, as different coatings can significantly affect the behaviour of neurons and other cell types. Various previous studies have supported the notion that the chemical and physical properties of the substrate influence neuronal attachment, distribution and network formation.

Neuronal cultures on PDL-coated substrates in this study exhibited more even distribution of soma and the formation of thin, elongated neurite networks. This observation aligns with a previous study by Sun's group, which showed that PDL provides a uniform and positively charged substrates, promoting more homogeneous neuronal adhesion compared to laminin or Matrigel, which- while facilitating neurogenesis – also led to soma clustering and neurite fasciculation (Sun *et al.*, 2011). In contrast, laminin- and dual-coated substrates tended to result in soma aggregation and thicker neurite processes, which may affect the synaptic connectivity by forming localised subnetworks rather than integrated neuronal networks (Sun *et al*., 2011). Laminin, while known to promote neurite extension (Lein *et al*., 1992), may also lead to such aggregation due to its interaction with integrin receptors, which promote clustering at cell adhesion points (Liberio *et al*., 2014). Although dual coatings of PDL and laminin are often used to combine the benefits of both cell adhesion and neurite outgrowth promotion (Clark *et al*.,1993; Orlowska *et al*., 2017), the lack of improvement in this study suggests that simple additive approaches may not yield synergistic effects. In this study, the dual-coated condition did not significantly outperform either PDL or laminin alone in terms of cell morphology or apparent cell appearance, and at later timepoints, cell adherence appeared slightly compromised.

At DIV 14, neuronal cultures on PDL substrates showed signs of neurite retraction and partial detachment. This phenomenon has been attributed in

previous studies to the enzymatic degradation of the peptide-based coating over time, as cells secrete proteases that can degrade (Clement *et al*., 2021). In contrast, laminin- and dual-coated cultures maintained better substrate adherence, but the dense clustering and fasciculation of neurites observed on these substrates may hinder synaptic integration, particularly in cultures intended to mimic distributed neural networks.

To address the limitations of traditional substrates, CES and APTES were introduced as chemically defined coatings that present single, covalently bound charge groups – carboxylate, (COO^-) and amine (NH_3^+), respectively. While PDL and laminin also contain charged moieties, they are structurally complex, non-covalently adsorbed molecules that may exhibit batch-to-batch variability and unpredictable surface orientation (due to their size and flexibility). In contrast, CES and APTES provide simpler and more uniform surfaces through silanisation, a covalent process known to result in stable, monolayer coatings when applied following robust literature protocols. In this study, piranha-cleaned coverslips were treated using established silanisation procedures, which are widely used and considered effective for generating reproducible charged surface.

CES introduces carboxylate (COO-) groups, which engage in electrostatic interactions with the positively charged regions of the neuronal membrane. Previous work by Kim's group demonstrated that COO^--rich surfaces enhanced neuronal adhesion, neurite outgrowth, and survival (Kim *et al*., 2017). However, this study did not replicate their findings regarding neurite extension. This discrepancy may be attributed to differences in coating parameters, such as reagent concentration, reaction time, curing conditions, or the base substrate material. The coating procedure in the current study followed a different protocol involving glass coverslips and overnight silanisation.

APTES, which provides a positively charged amine-rich surface, similarly supported early neuronal adhesion and growth. However, clustering of neuronal soma was observed at DIV 14, possibly due to overly adhesive or dense surface charge, which could hinder neurite extension or guidance. These findings suggest

that surface charge alone is not the only determinant of cellular behaviour, and that surface chemistry, functional group density, and molecular architecture all contribute to the biological outcome. This distinction becomes clearer when comparing the chemically defined substrates (CES and APTES) with traditional biological coatings (PDL and laminin). While CES and APTES rely on passive electrostatic interactions through covalently presented single charge groups (COO^- and NH_2, respectively), traditional coatings like laminin and PDL promote adhesion via more complex biological mechanisms, such as integrin-mediated signalling (for laminin) or broad-spectrum electrostatic attraction (for PDL), which may in turn influence downstream cellular responses such as cytoskeletal organisation and mitochondrial transport.

Immunocytochemical analysis revealed that CES and APTES substrates consistently supported a lower proportion of astrocytes compared to traditional coatings at both DIV 7 and DIV 14. This coincided with a relative enrichment of neurons, suggesting that chemically defined charged substrates may selectively favour neuronal survival while inhibiting astrocyte adhesion or proliferation. While negatively charged surfaces (e.g., COO^- or SO_3^-) have previously been shown to suppress astrocyte spreading (Kim et al., 2017), this trend was not clearly observed with laminin or PDL, possibly due to differences in molecular complexity or surface presentation. In this study, astrocyte proportions on CES and APTES were as low as 13.1% and 9.7% at DIV 7, respectively, and remained low at DIV 14. These findings reinforce the concept that precise surface engineering can be used to control neural culture composition.

To further explore how substrate properties affect neuronal physiology at the subcellular level, mitochondrial motility was quantified using KymoAnalyzer. Mitochondria are critical for neuronal function, as they provide ATP and buffer calcium at sites of high metabolic demand, such as synapses. Mitochondrial transport, especially within axons and dendrites, is thus a sensitive readout of neuronal health and intracellular transport capacity. In this study, a broad range of motility-related parameters—including directionality, speed, run length, and pause

characteristics—were measured and compared across the five different substrate types, with data from DIV 7 used for analysis due to the higher motile activity observed at earlier stages of maturation.

The findings clearly showed that traditional substrates (PDL, laminin, and dual) supported significantly greater mitochondrial motility compared to CES and APTES. The overall motile fraction of mitochondria was reduced on charged substrates, with CES and APTES showing median values of ~21%, in contrast to ~33–41% on traditional coatings. When breaking down by movement type, anterograde motion was most dramatically impaired on CES and APTES, where median values dropped to 0%, compared to 5–7% on traditional substrates. Retrograde movement showed less severe differences, but reversing mitochondria also decreased in frequency on charged surfaces.

Further analysis of motion time revealed that mitochondria on CES and APTES spent less time moving in the anterograde direction and more time paused or moving retrogradely. These observations were reinforced by the velocity data: both net and segmental velocities were significantly reduced on CES and APTES for anterograde and retrograde movements alike. For example, anterograde net velocities dropped from ~0.26 µm/s on PDL and laminin substrates to ~0.10–0.12 µm/s on CES and APTES. Segmental velocities followed the same pattern, as did run length. Mitochondria on traditional coatings typically moved 4–6 µm per run, while those on CES and APTES travelled ~1.4–1.5 µm. These data indicate that charged substrates strongly suppress mitochondrial movement, possibly by altering cytoskeletal interactions or increasing adhesion friction, thereby interfering with active transport.

Finally, although the three traditional substrates showed generally similar support for mitochondrial motility, the dual coating condition did not outperform PDL or laminin alone. Across all parameters measured—motile fraction, velocities, run lengths, and pause characteristics—PDL, laminin, and dual substrates performed comparably. This suggests that dual coatings, while widely used, may

not inherently provide superior motility conditions and should be evaluated for consistency and coating integrity when used in long-term cultures.

In conclusion, this study provides a comprehensive comparison of neural cell behaviour and mitochondrial dynamics across traditional and chemically defined culture substrates. CES and APTES surfaces promote neuron-dominant cultures by limiting astrocyte adhesion, but at the expense of intracellular transport efficiency. These findings highlight a trade-off between cellular composition and subcellular functionality, suggesting that optimal substrate selection should consider the specific biological parameters of interest—whether they pertain to cell type enrichment, network architecture, or intracellular dynamics.

CHAPTER FIVE:
Mitochondrial Motility in Micropatterned Neuronal Networks

The previous chapters have been focused on understanding mitochondrial movements in hippocampal cell cultures on bulk-coated substrates *in vitro*. However, even in 2D culture, neurons have extremely varied morphological features, with assemblies of cell bodies intricately connected by elongated axons and dendrites forming complex neural networks. (Bock *et al*., 2011; Fricke *et al*., 2011). As neuronal processes have convoluted geometries and significantly overlap each other, it was challenging to quantify the cellular mechanisms within axonal processes, such as the motion of mitochondria. One technology that could help address this issue is cellular micropatterning: exploiting microfabrication to create micro-scale guidance cues to control the direction of neurite outgrowth. Such an approach also brings the benefit of being able to control the extent of cell-cell connectivity within a network. This chapter will therefore focus on the optimization of a microcontact printing strategy suitable for confining the growth of neurites from primary hippocampal neurons along straight lines segments that facilitate mitochondrial tracking by Kymoanalysis and an analysis of whether micropatterning of neurites influences mitochondrial dynamics.

5.1 Introduction

Microcontact printing is the most common approach to creating micropatterned neural cultures, principally because numerous micropatterned stamps can be created from a single microfabricated master without having to access expensive microfabrication facilities regularly (see Chapter 1). The technique in particular is beneficial for enabling control over network formation, cell-cell interconnectivity and neurite directionality (Branch *et al*., 1998; Yeung *et al*., 2001; Wheeler and Brewer, 2010).

To maintain neuronal cultures in the pattern, as well as to ensure maintenance of the pattern while culturing cells, poly-lysine such as PDL or PLL and ECM molecules such as fibronectin and laminin were commonly used as inks that enable the attachment of neurons to substrates with hydrophobic backgrounds (Hardelauf *et al*., 2014). To visualise patterns printed on a substrate and the

subsequent effect on cell guidance, fluorescently labelled biomolecules can be used, for example FITC-labelled PLL (FITC-PLL) (Chang et al., 2003, Boehler et al., 2012). In addition, neuronal adhesion by poly-lysine molecule can be augmented by additional coating with ECM materials such as laminin or fibronectin during the patterning process (Hardelauf *et al*., 2014).

There are numerous examples of microcontact printing usage for neural cultures (Yeung *et al*., 2001; Offenhausser *et al*., 2007; Frimat *et al*., 2010; Fricke *et al.*, 2011; Boehler, *et al*., 2012; Albers, *et al*., 2015; Albers, *et al*., 2016). For example, Fricke *et al* constructed discontinuous substrate-bound gradients of micropatterns with changes in slope, width and length and engineered defined neural networks to understand mechanism of the axon guidance (Fricke *et al*., 2011). The pattern designs with different levels of discontinuity and use of either laminin/PLL or PLL alone as adhesion molecules were used to discover how neurite growth and axon guidance were affected by each different condition. Notably, the study demonstrated that laminin/PLL coatings were significantly more effective than PLL alone in promoting neuronal adhesion and guiding axonal outgrowth at DIV 3, highlighting the importance of both pattern geometry and the biochemical composition of the adhesive substrate (Fricke *et al*., 2011). Studies with single rat cortical neurons at DIV 3 demonstrated that gradients with laminin/PLL and PLL facilitated neuronal adhesion, controlled neurite growth, and achieved up to 84% axon guidance within the refined micropatterns (Fig 45A-D).

Similarly, Offenhäusser's group developed linked triangular-structured patterns using PLL and laminin on silanised glass substrates. These patterns allowed the growth of primary cortical neurons with constricted gateways, enabling the study of network formation and neuronal information processing in cultures maintained up to DIV 24 (Fig 45E-F) (Albers *et al*., 2015).

Efforts to design systems for controlling and studying cell-cell connectivity have also been explored. West's group introduced a network formation assay (NFA) using a hexagonal array of uniformly spaced nodes with differentiated SH-SY5Y neuroblastoma cells. This pattern-controlled neurite outgrowth length by

maintaining uniform distances between cells, which facilitated the study of neurotoxicity using dose-dependent exposure to acrylamide, a neurotoxic compound that inhibits network formation (Fig 45G-H) (Frimat *et al*., 2010).

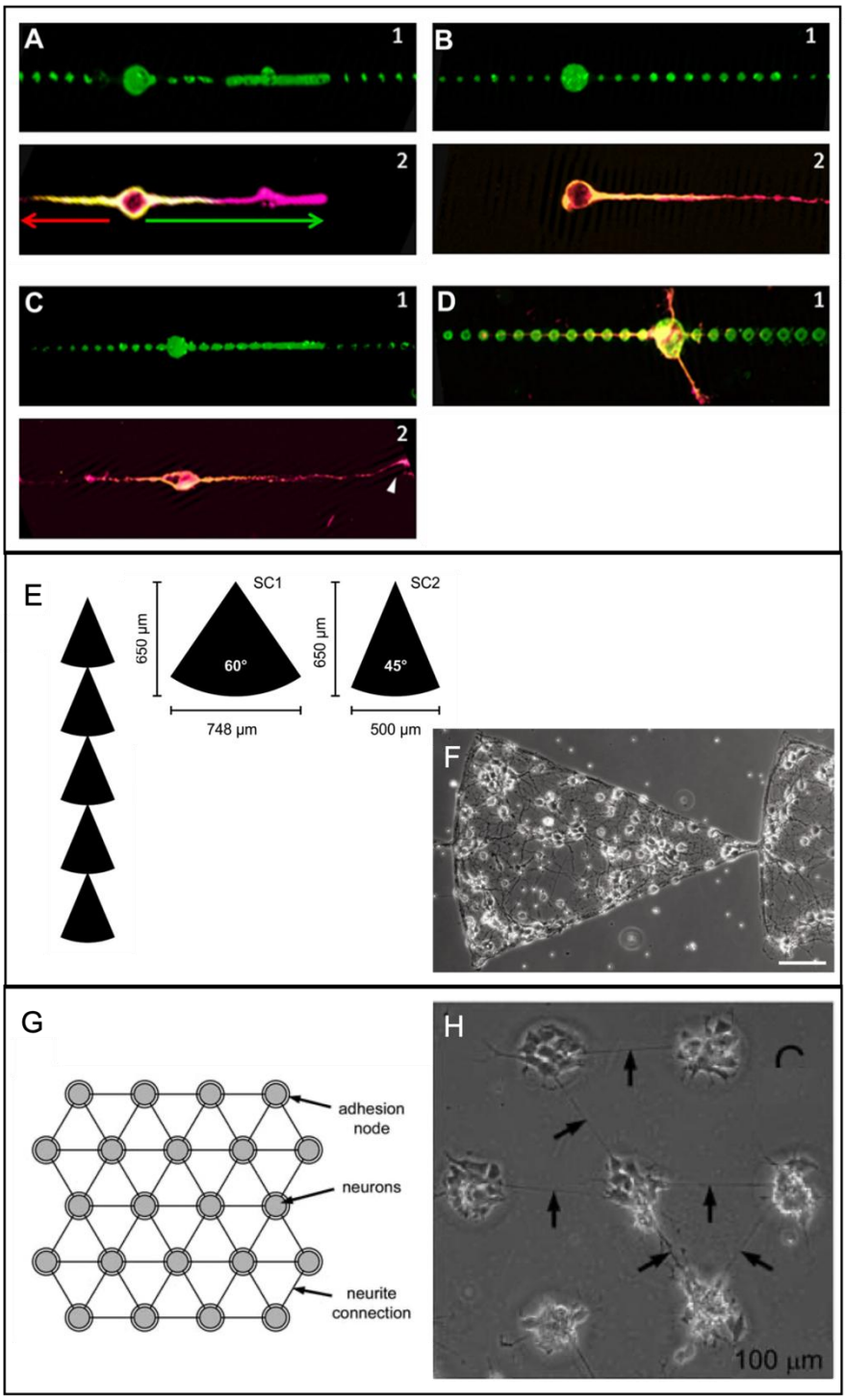

Figure 45. Examples of use of microcontact printing for neuronal cultures.

(A-D) shows culture of a single cortical neurons on discontinuous substrate-bound gradient patterns with different measurements. Fricke et al., 2011: (A) S4-W2-L200 pattern with PLL and neurons stained with MAP2 and Tau-1 showing neurite grown in both directions. (B) S1-W2-L200 pattern with Laminin/PLL. Neurites show growth towards positive side of the gradient (C) S4-W2-L200 pattern with laminin/PLL. Neurites grown in both directions (D) S1-W2-L200 pattern with PLL showing axons grown towards negative side of the gradient. (A/1-C-1) FITC-PLL pattern (A2-C2) MAP2, Tau-1, scale bars 10 um. S= slope; S1 = 0.01 and S4 =0.04/ W= width; W2 = 2um/ L = overall length of structure; L200 = 200 um.
(E-F) example of primary cortical rat neurons cultured on triangular patterns. Albers et al., 2015: (E) Design of triangular patterns and with different angles. (F) Cultured neurons grown within a pattern at DIV 14. Scale bar = 50 µm. (G-H) example of controlled neuronal network and cell-cell connectivity. Frimat et al., 2010: (G) illustration of the hexagonal pattern array (H) microscopic image of neuronal networks of SH-SY5Y cells at 72 h cultured on patterns. Scale bar = 100 µm.

Although a few studies have utilised microengineering methods such as microfluidic devices with ladder-like micropatterned substrates to study mitochondrial dynamics in neuronal cells and neurodegenerative diseases (Kim *et al*., 2012; Kim and Chung, 2015), studies employing microcontact printing for mitochondrial analysis remain very limited.

As tracing mitochondrial movements on conventional unpatterned substrates is known to be challenging, Burbulla *et al* group addressed this by using 10 µm wide line patterns onto gold-coated glass with induced pluripotent stem cells (iPSC) derived neurons. They observed changes in mitochondrial length, interconnectivity and motility in iPSC-derived neurons from DIV 40 to 100, noting a decrease in anterograde movements and an increase in stationary mitochondria over time (Burbulla *et al*., 2017).

This chapter focuses on the application of microcontact printing for studying mitochondrial dynamics within micropatterned neuronal networks, optimising the

use of hydrophobic silane coatings to inhibit off-pattern growth, characterising cell type abundance and mitochondrial motilities on micropatterns, and comparing these findings to bulk-coated substrates analysed in Chapter 4.

5.2 Optimisation of the Microcontact Printing Process for the Creation of Micropatterned Neuronal Networks

There had been many studies on microcontact printing methods that deliver high pattern compliance and long-term stability of cell cultures on patterns. However, the process is highly user-dependent and there are conflicting reports in the literature regarding its optimisation. For example, West's group evaluated a comparison of various aminated adhesion molecules, including poly-lysine/poly-ornithine and amino-silanes, as well as cytophobic coatings such as PEG and methylated silanes. These comparisons were to create refined patterning methods including high pattern compliance and long-term stability for neuronal cultures. They found, for dorsal root ganglion neurons, that PEGylated substrates, specifically PLL grafted with PEG, combined with subsequent poly-lysine patterning, provided superior long-term stability, maintaining patterns for up to 33 days. In contrast, silane-PEG coatings supported cell growth for only 25 days (Hardelauf *et al*., 2014).

Another critical aspect of optimisation involves the geometric design of the patterns. Wheeler and Brewer demonstrated that line thickness and node dimensions significantly impact neuronal behaviour. They observed that lines thinner than 25 μm caused neuronal clumping and reduced electrical activity, whereas optimised designs with 80 μm square nodes and 25 μm wide lines facilitated stable circuit connections and supported neuronal function (Wheeler and Brewer, 2010).

A crucial component of microcontact printing optimisation is the creation of cell-repellent regions (e.g. blocking of non-patterned regions), which ensures the fidelity of micropatterned cultures. This is typically achieved using either PEG-based polymers or silanes, both of which modify the surface chemistry of non-patterned areas to render them cytophobic. PEG-based coatings include compounds such as

PLL-g-PEG, a random graft copolymer consisting of a positively charged PLL backbone and PEG side chains. The PLL backbone adheres electrostatically to negatively charged substrates such as glass or oxidised polymers, while the PEG chains extend outward to form a dense, non-adhesive polymer brush that effectively repels cellular adhesion (Hardelauf *et al*., 2011; Liazoghli *et al*., 2011). Another example is star-PEG, which has been similarly employed to prevent off-pattern cell attachment (Offenhäusser *et al*., 2007). In contrast, hydrophobic silanes act as creating low-energy, non-wettable substrates that inhibit protein and cell adhesion. Examples include dichlorodimethyl silane (DCDMS) (Hardelauf *et al*., 2014) and fluorocarbon-based silanes, including tridecafluoro-1,1,2,2-tetrahydrooctyl)trichlorosilane (FOTCS) (Albers *et al*., 2015; Albers *et al*., 2016). Offenhäusser's group demonstrated that hydrophobic fluorocarbon silanes, such as FOTCS, effectively inhibited off-pattern growth of cortical neurons by leveraging the non-adhesive properties of fluorocarbon groups (see Fig. 45E).

Building on these insights, the current study explored the use of hydrophobic silanes to block off-pattern growth on glass substrates patterned by microcontact printing. Two silanes were selected for testing: trichloro(1H,1H,2H,2H-perfluorooctyl)silane (PFS), which is structurally similar to FOTCS and DCDMS. The structure of PFS, featuring fluorocarbon functional groups, is shown in Fig. 46. This approach aims to balance pattern fidelity with ease of implementation for the creation of stable and reproducible micropatterned neuronal networks.

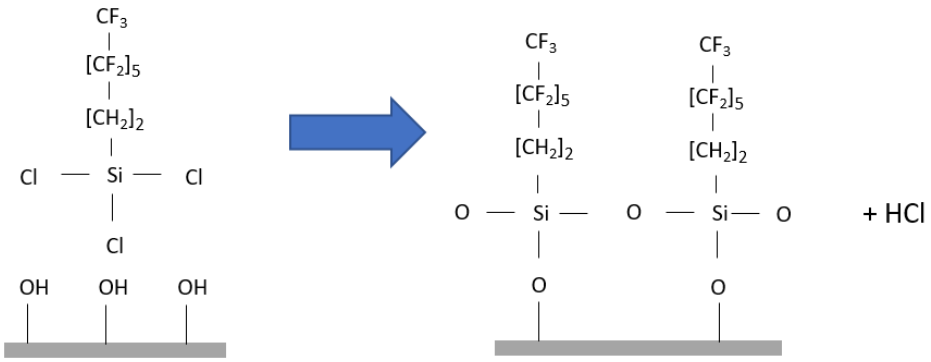

Figure 46. The structure of trichloro(1H,1H,2H,2H-perfluorooctyl) silane and the surface coating resulting from its reaction with silanol groups at the surface of a glass substrate.

Given the diversity of protocols in the literature, several optimisations were required to develop a protocol, specifically tailored for hippocampal cells. First, the relative wettability of stamps to substrates with different surface characteristics were explored to enhance the efficiency of ink transfer (Tan *et al*., 2004). This includes comparisons of different inking and stamping durations. Additionally, the effect of varying blow-drying times for the ink on the stamps prior to stamping was examined, as drying levels have been identified as a critical factor in achieving refined patterning (Bernard *et al*., 2000).

5.2.1 Relative Wettability of Stamps and Substrates: Optimising Ink Transfer to Glass Surfaces by Altering Stamp Wettability

To improve the efficiency and consistency of ink transfer, the transfer of ink onto glass substrates was investigated using a fluorescently labelled-PLL (FITC-PLL) to compare the use of hydrophobic and hydrophilic PDMS stamps along with various inking times (Fig 47). Aggregation of PLL on patterns affected neuronal survival within a week of plating (Boehler et al., 2012). In this optimisation process, two different types of PDMS stamps with different wettability, native PDMS stamps (hydrophobic) and O_2-plasma treated PDMS stamps (hydrophilic), were inked with 0.1 mg/ml FITC-PLL for 30 min and then brought into contact with glass substrates

for 5, 15 or 30 min (Fig 47). Fluorescence imaging (Fig 47A) and subsequent quantification (Fig 47B) showed the presence of FITC-PLL patterns from both types of stamps comparatively, however, O_2-plasma treated PDMS stamps delivered more uniform FITC-PLL transfer onto substrates. In contrast, uneven FITC-PLL transfer with FITC-PLL clustering appeared when transferring from native hydrophobic PDMS stamps. The potential reason is that hydrophobic PDMS stamps repels aqueous biological inks, which leads to inconsistently inked surfaces and irreversible adsorption of the ink, thereby disturbing the transfer of ink to substrates (Kaufmann and Ravoo, 2010). Moreover, the quantitative results show that the different contact times of stamps to substrates affected the intensity of the ink transferred. For further studies, O_2-plasma treated PDMS stamps with a 15 min contact time of ink were selected due to their consistent levels of variance and intensity of micropatterns. It should be noted that a longer contact time of 30 min with ink also yielded consistent micropatterns as well as 15 min, however, the 15 min was chosen to trade-off between consistency and overall protocol time.

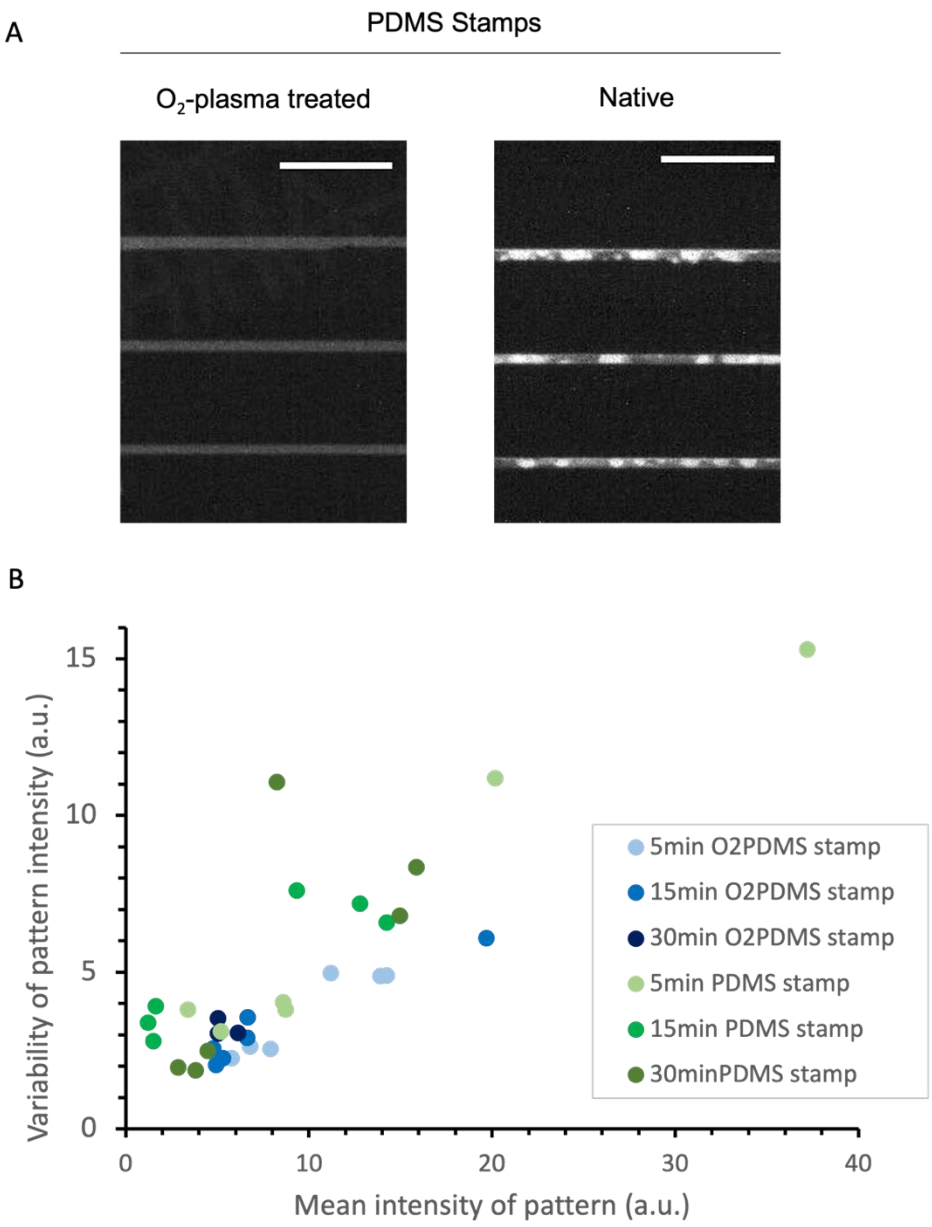

Figure 47. Optimisation of FITC-PLL transfer from stamps to native glass substrates.

The intensity and variance of the fluorescent signal following ink transfer to substrates was investigated for different types of stamps (native or oxygen-plasma treated) with different stamping times (5, 15 or 30 min). A) shows representative fluorescence images of FITC-PLL patterns by stamping with either O_2-plasma treated PDMS (left) or native PDMS (right) stamps. Scale bars = 100 µm. B) Quantification of the mean fluorescence intensity and variance as measured from a rectangular ROI of fixed size drawn within the micropatterned region for each condition. Each dot

represents one image ROI. For all conditions, n=6 images, except 30 min O_2PDMS stamp (n=3). All conditions were tested in a single experimental run

5.2.2 Relative Wettability of Stamps and Hydrophobic Silanised Surface

The intensity and variance of FITC-PLL transfer was also studied on glass substrates pre-treated with PFS and DCDMS, both silanes with demonstrated cell-repellent behaviours (as discussed above).

For the transfer of FITC-PLL from either native or O_2-plasma treated PDMS stamps onto silanised substrates, a 15 min stamping time was used. On both forms of silanised substrates, native PDMS stamps delivered higher intensities of FITC-PLL (Fig 48A, lower panels) compared to O_2-plasma treated PDMS stamps (Fig. 48A upper panels), however ink transfer from native stamps again produced non-uniform patterns. O_2-plasma treated PDMS stamps provided a more uniform, evenly distributed ink transfer onto DCDMS substrates, however with lower overall transfer efficiency. Quantification of intensity and variance of patterned regions showed that hydrophobic stamps resulted in higher intensity signal and higher variance which resulted from inhomogeneous ink transfer (Fig 48B). As hydrophilic stamps provided relatively uniformed ink distribution, they were selected for further studies.

The intensity of FITC-PLL on both silanised substrates tended to show much lower intensities than O_2-plasma treated substrates (no comparative data shown as the two sets required different imaging conditions and cannot be directly compared). This phenomenon is explained by Chen and colleagues, which characterised printing as a function of surface energy and found that as the free energy of the surface decreases, transfer efficacy diminishes and fails completely on low energy, hydrophobic surfaces (Tan *et al*., 2004).

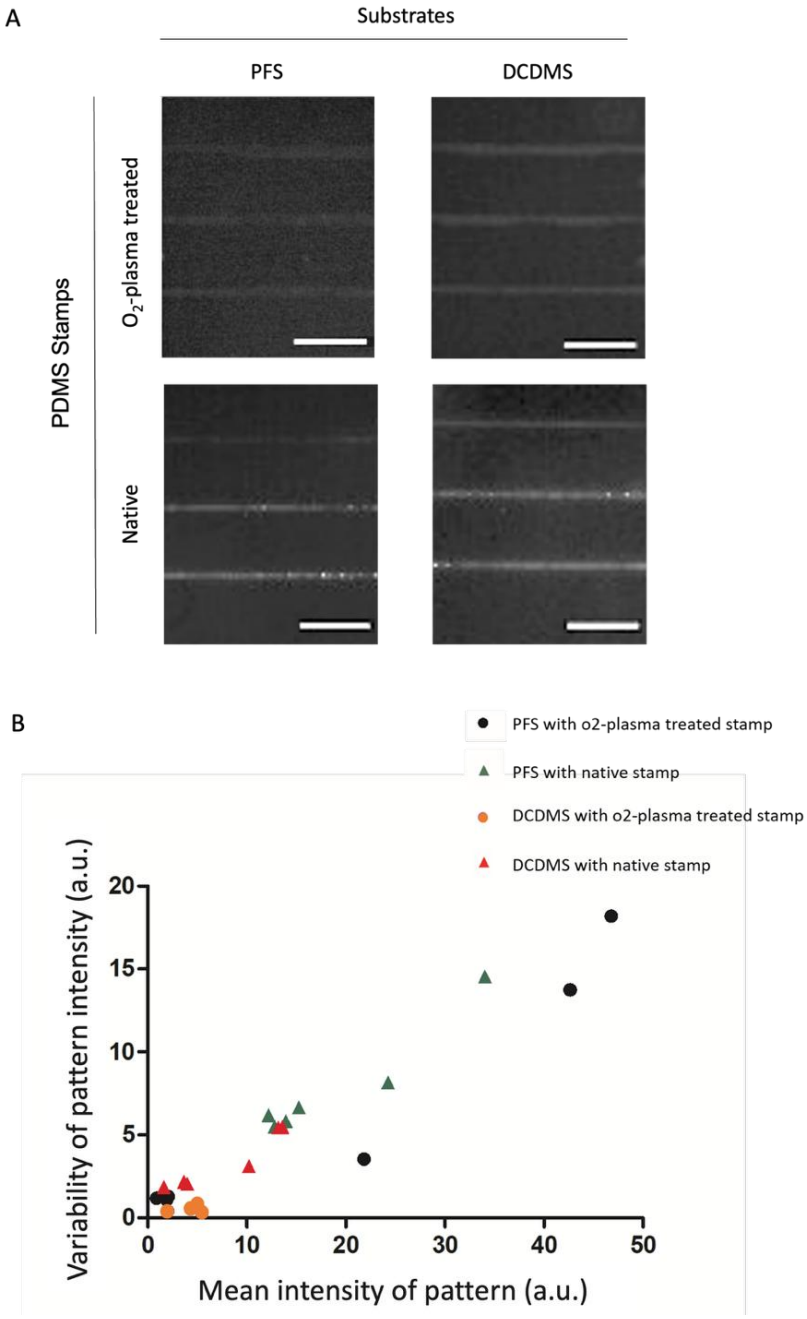

Figure 48. Optimisation of FITC-PLL transfer from different types of stamps onto pre-silanised substrates.

(A) fluorescence images of FITC-PLL micropatterns using either O_2-plasma treated PDMS or native PDMS stamps on silanised substrates; PFS or DCDMS. Scale bar = 100 µm. (B) Quantification of mean intensity of pattern and variance measured from FITC-PLL transferred from either hydrophilic or hydrophobic stamp onto either PFS or DCDMS substrates. Each dot represents one image ROI. For all conditions included 6 images acquired from a single experimental run.

5.2.3 Drying of Inks on the Stamps for Patterning with Nitrogen

The blow-drying step following the removal of excess ink is another critical point in microcontact printing process. Maintaining consistent times and air flow during this step for each stamping is important, as inconsistent timings of these steps can affect amount of ink transferred from stamp to substrates. To optimise these conditions, the effects of different drying durations and waiting times prior to stamping were compared.

For this study, O_2-PDMS stamps were inked with FITC-PLL for 30 min. Excess ink was removed by pipetting and the stamps were blow-dried with nitrogen for 5, 10 or 15 s. Following drying, the stamps were left for 15, 30 or 60 s before being stamped onto substrates (Fig 49). All selected times were kept under one minute, as shorter drying durations are generally recommended to maximise successful ink transfer rates while minimising the risk of protein alteration or denaturation (Bernard *et al*., 2000; Oliva *et al*., 2003).

The results indicate that blow-drying for 10 s followed by a 30s waiting time produced the most consistent and uniform ink transfer. Substrates dried for only 5 s often exhibited smudged patterns, likely due to incomplete drying, while 15 s of drying reduced ink intensity, suggesting over-drying.

A waiting time of 30 s after blow-drying provided the most uniform ink distribution across micropatterned regions. Although a 60 s waiting time also produced acceptable results with 10 s blow drying stamps, the shorter 30 s wait was preferred to reduce overall processing time. In conclusion, the combination of 10 s of blow-drying followed by a 30 s waiting time were identified as optimal for achieving high-quality and reproducible patterns, balancing efficiency with pattern integrity.

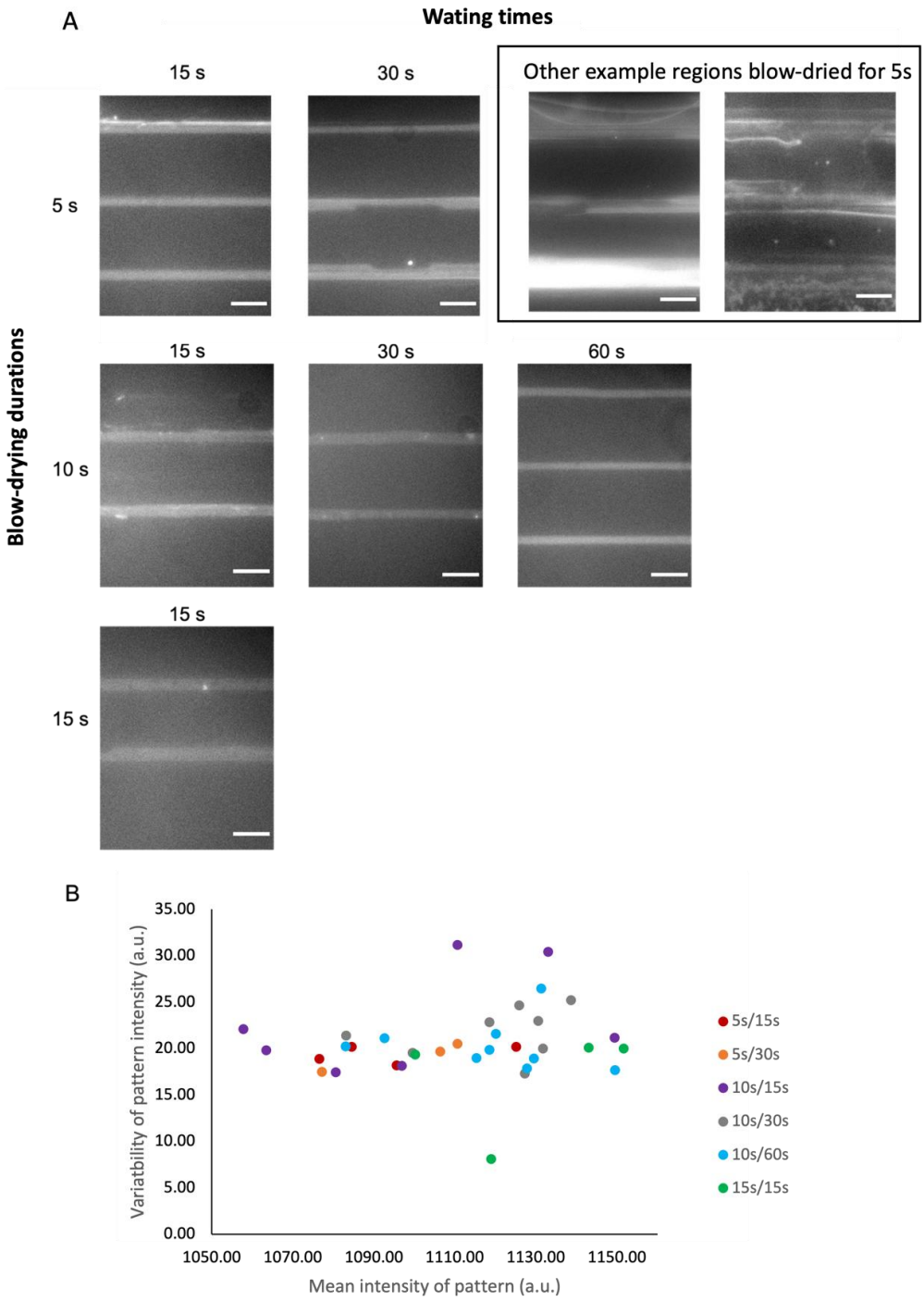

Figure 49. Comparison of different blow-drying and waiting times when stamping onto glass substrates.

(A) Representative images of FITC-PLL micropatterns produced by blow-drying O_2-PDMS stamps for 5, 10 or 15 s after inking for 30 min, followed by waiting times of 15, 30 or 60 s before stamping onto substrates. (B) Quantification of mean fluorescence intensity and signal variance were performed by drawing rectangular regions of interest (ROIs) of fixed size across the patterned regions under each

condition. Each dot represents one image ROI. Sample sizes were n=4 (5s/15s), n=3 (5s/30s), n=7 (10s/15s), n=8 (10s/30s), n=9 (10s/60s) and n=4 (15s/15s).

5.3 Patterning of Hippocampal Cells on Blocked Micropatterned Substrates

5.3.1 Assessing pattern integrity by bright-field imaging

Following the optimised microcontact printing protocol outlined above, hippocampal cells were cultured on micropatterned substrates patterned with a PDL and laminin mixture (referred to as [P+L]), where both components were mixed prior to stamping (to allow for a single-stage inking step), unlike the sequential "dual" coating (PDL followed by laminin) used in Chapter 4. Substrates were blocked with either PFS or DCDMS prior to micropatterning to create a cell repellent background (Fig 50). The patterns included linear tracks as well as crossing lines designed to connect these tracks (Fig 50B). The growth of hippocampal cell cultures on- and off-pattern was evaluated at DIV 7 using bright-field imaging (Fig 50C). Micropatterned substrates with different surface coatings - glass, PFS or DCDMS - all displayed adherence of cells on patterned areas with elongated neurite outgrowths, with varying levels of pattern coverage and pattern integrity. To access the effect of cell-repellent silane coatings on pattern integrity, the average number of on-pattern cells, including cells adhered peripheral to patterns (with peripheral being that all parts of the cell were <7.5 μm from the pattern edge) were calculated per region of images (Fig 50D). The quantitative analysis show that PFS-substrates were more effective in blocking off-pattern cells compared to either DCDMS-substrates or untreated glass substrates. The percentage of on-patterned cells out of total cells on PFS-substrates increased to 48.4±12.3% compared to 36.9±10.1% on plane glass without blockers. In contrast, DCDMS-treated substrates displayed lower levels of cell attachment, with poorer cell-cell connectivity and a similar percentage of on-pattern cells (37.6±11.4%) as observed on non-repellent substrates.

Although cells within micropatterns on PFS exhibited relatively good pattern integrity, clustered somas and thick bundles of neurite processes were frequently

observed. The development of these thick structures remains unclear, but adjustments to line widths and the inclusion of nodes for soma adherence could help control bundle formation. Previous studies have shown that neurons plated on micropattern with circular nodes connected by narrow lines tend to adhere their somas to the nodes and grow its neuronal processes along the lines (Fricke *et al*., 2011). Incorporating design modifications, such as wider separations and the inclusion of nodes, may prevent cells bridging between tracks and reduce cell clustering (see Section 5.6.1).

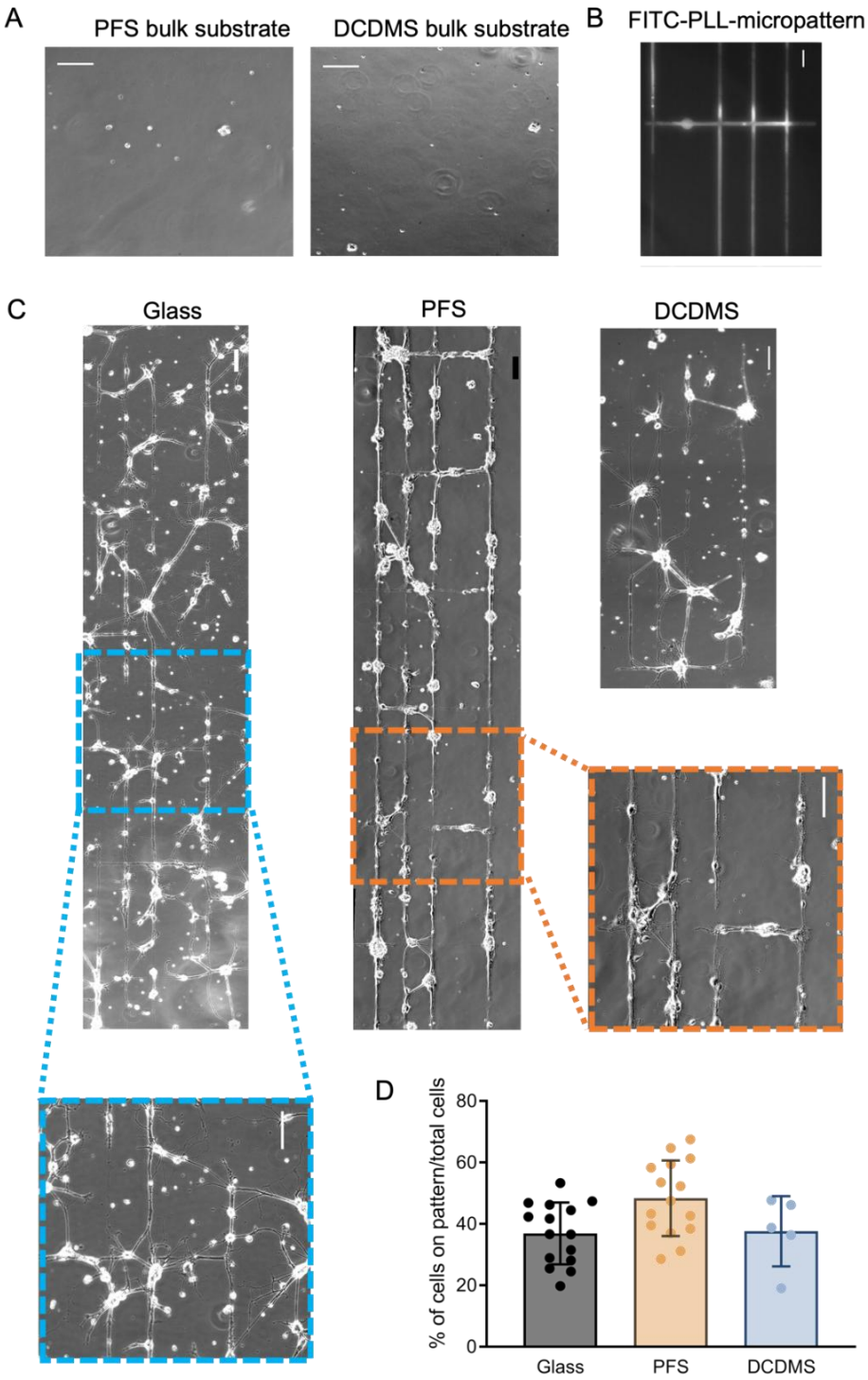

Figure 50. Hippocampal cell cultures at DIV 7 on micropatterns on substrates blocked with either PFS or DCDMS.

(A) Hippocampal cells cultured on bulk substrates blocked with either PFS or DCDMS (B) Pattern design used on substrates. The example image shows the pattern stamped with FITC-PLL. Scale bar = 50 µm (C) Bright-field images of hippocampal

cells on micropatterned substrates with plain glass, PFS or DCDMS coatings. Larger regions were created by stitching multiple images using ImageJ (as described in Chapter 2, section 2.3.2). Representative zoomed-in regions from glass- and PFS-coated substrates illustrate pattern integrity. (D) Percentage of on-pattern cells (including cells peripheral to the patterns, defined as those located <7.5 µm from the pattern edge) out of the total number of cells per image region. The average percentages of on/peripheral pattern cells were 36.4% (n = 15) for plain glass, 48% (n = 15) for PFS, and 37.6% (n = 5) for DCDMS. Experiments were conducted using three hippocampal cell preparations (n=3 animals). For the quantification, the patterns on brightfield images were defined by application of drawn template of patterns with 17.5 µm width of lines and 10 mm and 25 mm spaced apart. Neuronal processes within the template lines were adjusted, and cell counting was performed. Statistical analysis was conducted using one-way ANOVA (mean ± S.D., P < 0.05) and no statistically significant differences were observed between groups.

5.3.2 Immunocytochemistry of Micropatterned Cultures on Blocked Substrates: Staining for Neurons and Astrocytes

The immunostaining revealed MAP2-positive dendrites (red) closely aligned with the linear micropatterns, forming defined networks along the patterned regions (Fig 51). GFAP staining (green) demonstrated that astrocytes also adhered to the patterns, with processes extending alongside neuronal structures, contributing to the overall alignment. Notably, GFAP-positive signals appeared more abundant than MAP2-positive dendrites, suggesting that astrocytes may be more likely to adhere to the micropatterned regions. DAPI staining (blue) highlighted the positions of cell somas, which appeared clustered along the micropatterned tracks.

Despite the clear alignment, the formation of thick bundles of neurite processes in the micropatterned regions posed technical challenges for quantifying the abundance of different cell types.

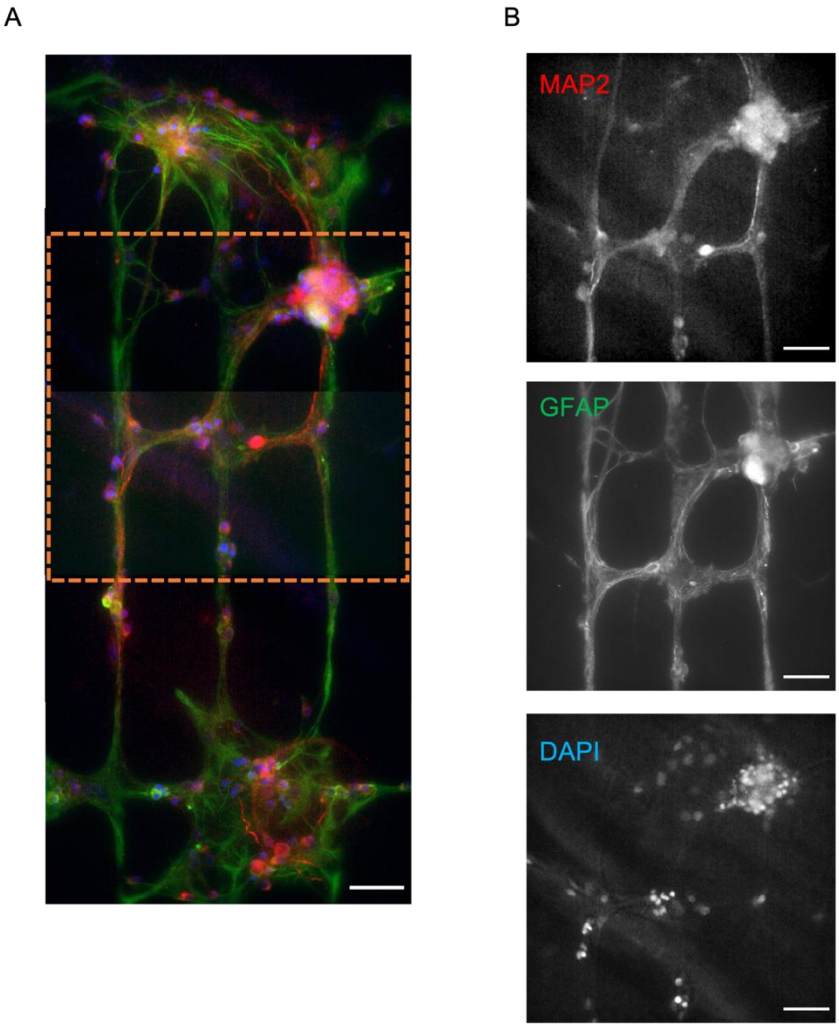

Figure 51. Representative immunocytochemistry of hippocampal cells on micropatterns printed with P+L on PFS-blocked substrates.

Cells were fixed at DIV 7 and stained with GFAP (green; astrocytes) and MAP2 (Red; dendrites) markers. DAPI (blue) was also used to stain nuclei. (A) Merged image with each marker into different colours: GFAP (green), MAPT/tau (red) and DAPI (blue). (B) Individual channels with each marker from region that has been shown in orange box in (A). Scale bar = 50 µm.

5.3.3 Mitochondrial Imaging of Cells on Blocked Micropatterned Substrates

Mitochondrial movements in cells were recorded in hippocampal cells cultured on micropatterned regions on both PFS- and DCMDS- blocked substrates at DIV 7 (Fig 52). Brightfield imaging revealed that cells adhered along the patterns on both substrates. However, the presence of thick bundles, particularly along the micropatterned regions, introduced out-of-focus light, which hindered detailed image analysis (Fig 52A). Mitochondria were visualised using MitoTracker Green, showing that mitochondrial distribution was aligned with the patterned regions.

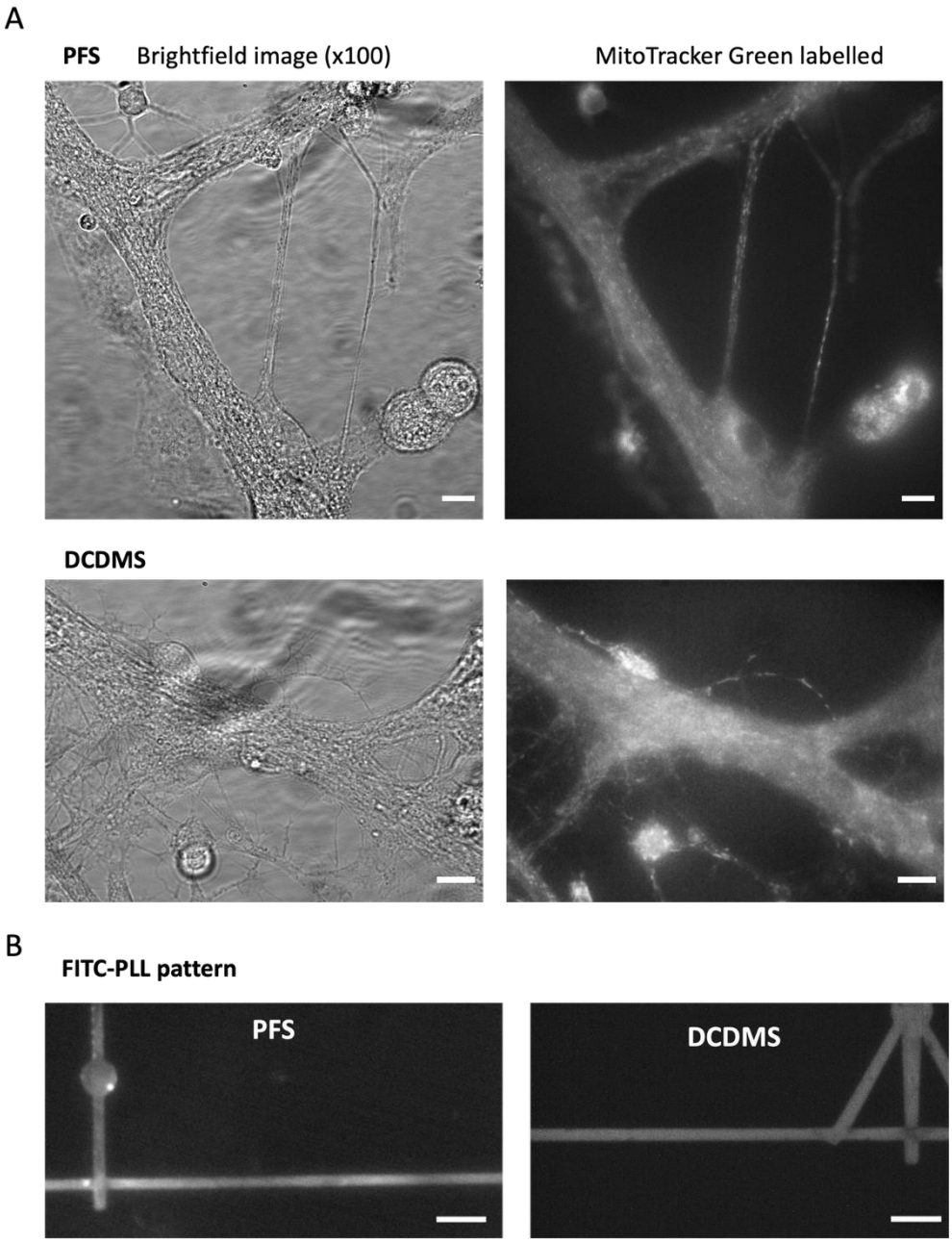

Figure 52. Mitochondrial imaging of hippocampal cells at DIV 7 on P+L micropatterns on substrates blocked with either PFS or DCDMS.

(A) Brightfield images of cells adhered to micropatterned regions on PFS (upper left) or DCDMS (lower left) substrates. Corresponding mitochondrial imaging of cells stained with MitoTracker Green shows mitochondria aligned within the micropatterned regions on PFS (upper right) and DCDMS (lower right) substrates. Scale bar = 10 µm. (B) Representative FITC-PLL micropattern images on PFS- and

DCDMS-coated substrates, illustrating the patterns used for cell culture. Scale bar = 50 µm.

Although PFS-blocked substrates provided improved pattern integrity and reduced off-pattern cell adhesion compared to unblocked substrates, quantifying mitochondrial movements within micropatterned cells remained highly challenging. The dense bundling of neurites made it difficult to isolate individual processes and manually analyse their dynamics using KymoAnalyzer. To address this, subsequent studies returned to unblocked glass substrates, where micropatterned cues guided cell alignment but allowed some off-pattern cell adhesion. For mitochondrial motility analysis, only-cells confined to on-pattern regions were imaged to ensure consistency in the observations.

5.4 Analysis of Hippocampal Cell Populations and Mitochondrial Motilities on Micropatterned Glass Substrates

To enable the tracking of mitochondrial motilities within micropatterned cells, hippocampal cell populations were cultured on micropatterned glass substrates without the use of silane blockers. To facilitate comparisons with bulk substrates discussed in Chapter 4, where various coating materials were employed, micropatterned glass substrates were prepared using PDL, laminin or P+L inks via microcontact printing.

The abundance of different cell types adhering to the micropatterns and the changes in mitochondrial motilities within these patterns were quantified for each bio-ink condition. Finally, mitochondrial movements in cells cultured on bulk substrates were compared to those on micropatterned substrates to investigate whether controlled neurite outgrowth influences mitochondrial motility.

5.4.1 Hippocampal Cells Grown on Micropatterned Glass Substrates

The growth of hippocampal cells cultured on micropatterned glass substrates without blockers was explored. Representative brightfield images in Figure 53 illustrate the progressive formation of neural networks within the micropatterns from DIV 1 to DIV 7. At DIV 1, cells showed selective adherence to the patterned regions, with minimal off-pattern growth. By DIV 7, extensive neurite outgrowth and elongation of processes were observed, aligning along the micropatterns. Neurite extensions began to form organised networks after DIV 5 (data not shown), following the pattern design depicted in Figure 53B.

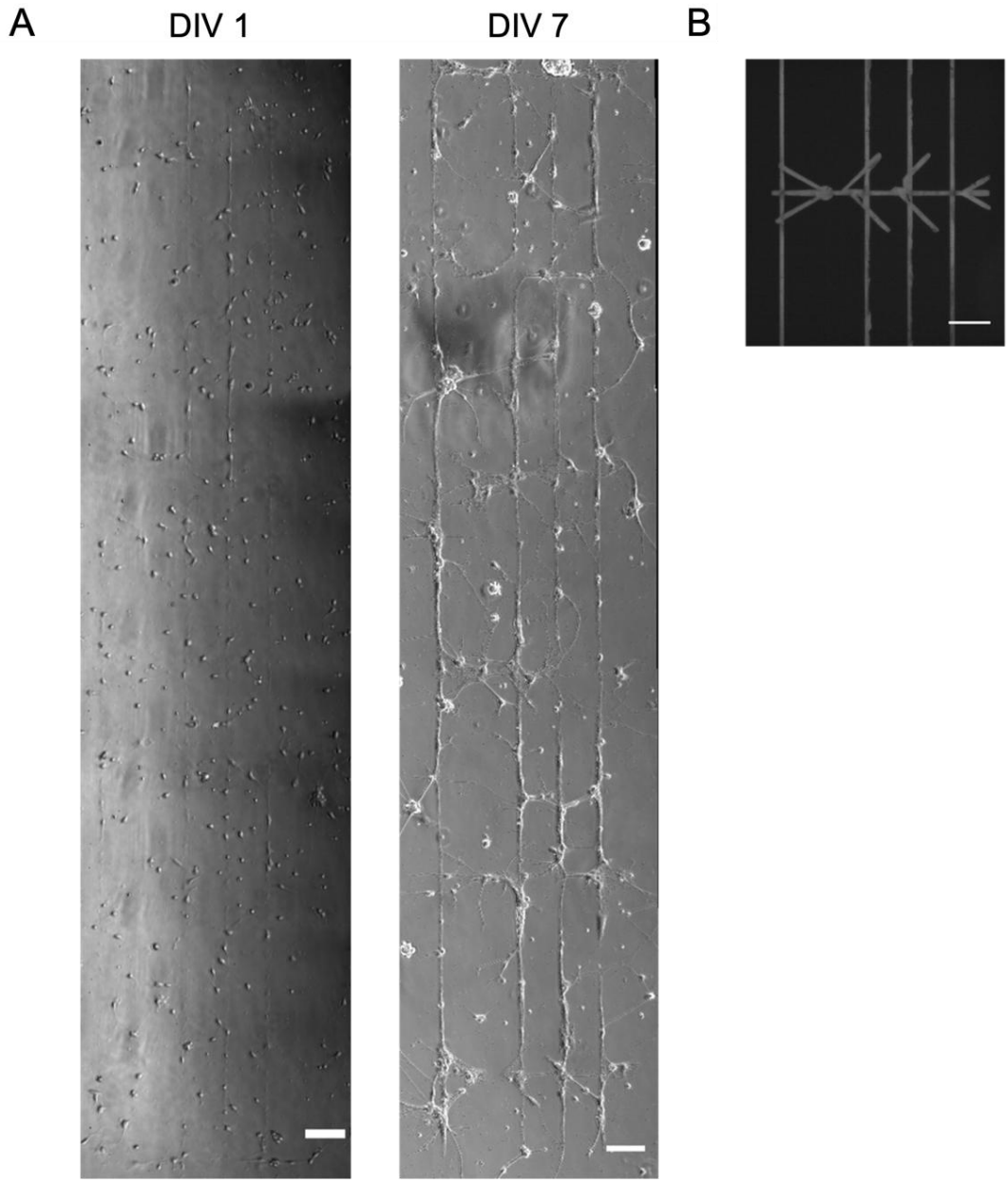

Figure 53. Growth of hippocampal neurons on P+L-micropatterned substrates.
(A) Brightfield images of hippocampal neurons cultured on P+L-micropatterned glass substrates at DIV 1 and DIV 7. Images stitched together as described in previous sections. At DIV 1, neurons adhered selectively to the patterned regions, with neural networks forming by DIV 7. (B) FITC-PLL image illustrating the micropattern design used for the substrates. Scale bar = 100 µm.

5.4.2 Relative abundance of Cell Types Present on the Micropatterned Substrates

The relative abundance of neurons and astrocytes, as well as pattern integrity, was examined by visualising on- and off-pattern cells using immunocytochemistry (Fig 54). Hippocampal cells cultured on laminin- or P+L-stamped micropatterned substrates were stained with antibodies against GFAP (astrocytic marker), MAPT/tau (axonal marker) and MAP2 (dendritic marker) (Fig 54B-D). Quantitative analysis of the percentage of each cell type adhered to on-pattern regions, relative to the total number of cells in the imaged regions, revealed little difference between the two substrates coatings, with laminin substrates supporting 60.6±13.6% neurons and 29.9±19.3% astrocytes, and P+L substrates supporting 59.3±13.9% neurons and 26.4±19.3% astrocytes, respectively (Fig 54E). Regardless of substrate type, neurons were more abundant than astrocytes on patterns.

Additionally, the percentage of each cell type adhered on-pattern was calculated relative to the total number of each cell type (on- and off-pattern) on the substrates (Fig 54F). The analysis showed that astrocytes were more prone to adhere to patterns than neurons, with 72.8±30.7% of astrocytes adhering to patterns on P+L substrates compared to 49.3±18.5% of neurons. Similarly, laminin substrates showed a higher tendency of astrocytes (63.3±37.5%) to adhere to patterns compared to neurons (49.4±22.0%), although no statistically significant differences were observed.

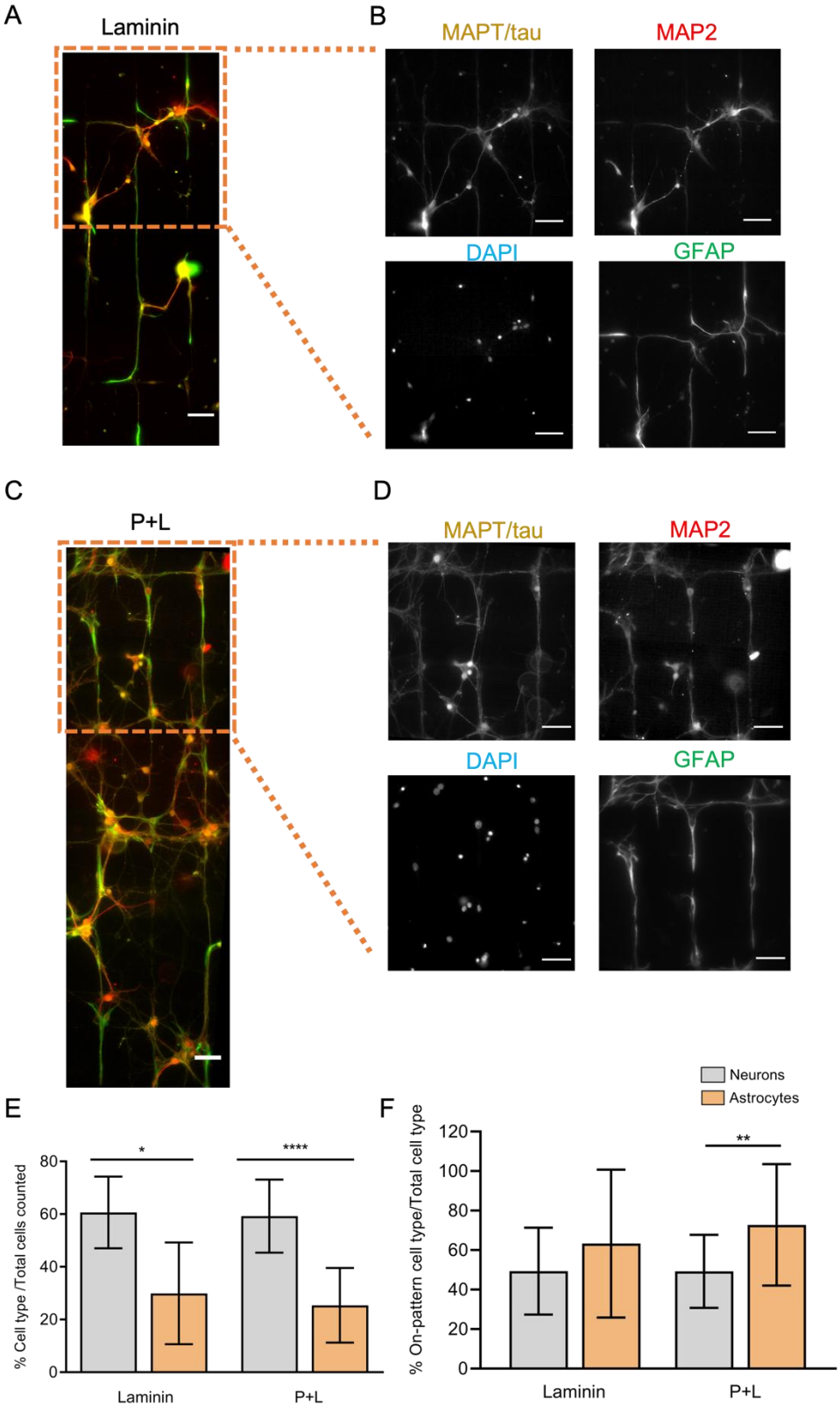

Figure 54. Immunocytochemistry analysis of micropatterned hippocampal cultures using laminin or P+L as bio-inks.

(A, B) Representative images of cells cultured on laminin micropatterns at DIV 7 stained for astrocytes (GFAP, green), axons (MAPT/tau, red), dendrites (MAP2, yellow) and nuclei (DAPI, blue). (A) Merged images of all markers with stitched regions (B) Single-channel images of each marker from the region highlighted by the orange box in (A). (C, D) Corresponding image of cells cultured on P+L micropatterns. (C) Merged images of all markers (D) Single-channel images from the orange boxed region in (C). (E) Percentage of neurons and astrocytes present within on-pattern regions relative to the total number of cells on laminin or P+L micropatterns (F) Percentage of neurons and astrocytes adhered to patterns relative to the total number of each cell type (on- and off-pattern) for each substrate. Quantification was performed on three hippocampal cell preparations (n=3 animals). Statistical significance was assessed using a paired t-test (Wilcoxon test). Scale bar = 50 µm.

5.5 Kymoanalysis of Mitochondrial Motilities within Hippocampal Cells on Micropatterned Glass Substrates

Mitochondrial motilities within hippocampal cells cultured on micropatterned substrates were analysed using live-cell imaging and kymograph-based motion quantification. Substrates stamped with PDL, laminin or P+L bio-inks were utilised to investigate potential differences in mitochondrial motilities associated with these coatings.

As previously mentioned, quantifying mitochondrial movement on bulk-substrates is challenging due to overlapping and convoluted nature of neuronal processes, which form complex and disorganised networks. In contrast, microcontact printing can facilitate the alignment of straight, elongated processes, allowing for more straightforward monitoring of individual mitochondrial dynamics.

Figure 55 illustrates representative still frames of hippocampal cells cultured on patterned regions stamped with PDL, laminin, or P+L bio-inks at DIV 7. The corresponding kymographs display mitochondrial movements, which were categorised as anterograde or retrograde based on their direction of travel relative

to the soma. In these experiments, imaging was performed only on neurites with unambiguous orientation and soma positions clearly identifiable within the field of view, allowing confident assignment of movement direction. These findings highlight the advantage of micropatterning in isolating and analysing mitochondrial motilities within defined neuronal tracks, compared to non-patterned cultures where overlapping, disorganised neurites often obscure individual mitochondrial trajectories and hinder accurate motion quantification.

In addition to facilitating mitochondrial motility analysis, micropatterns influenced neuronal adhesion and neurite alignment. Neurons predominantly adhered to the patterned protein regions, and neurite outgrowth was largely restricted to these coated areas. Notably, neurites reaching the pattern boundaries exhibited directional changes, often following the edges rather than crossing into uncoated regions. This behaviour is likely influenced by variations in protein layer thickness at the pattern edges.

During the inking and stamping process, bio-inks such as PDL and laminin may have accumulated more at the edges compared to uniformly coated areas, as previously observed in microcontact printing studies. Surface plasmon microscopy analyses from prior studies indicate that protein thickness at the edges of stamped structures (~4.9 ± 1.1 nm) was greater than that of uniformly coated regions (~1.1 ± 0.3 nm), which may influence neuronal adhesion and neurite extension (Albers *et al*., 2015). Given the similarities in the stamping technique used in this study, it is plausible that a similar effect contributed to the observed edge-guided neuronal alignment.

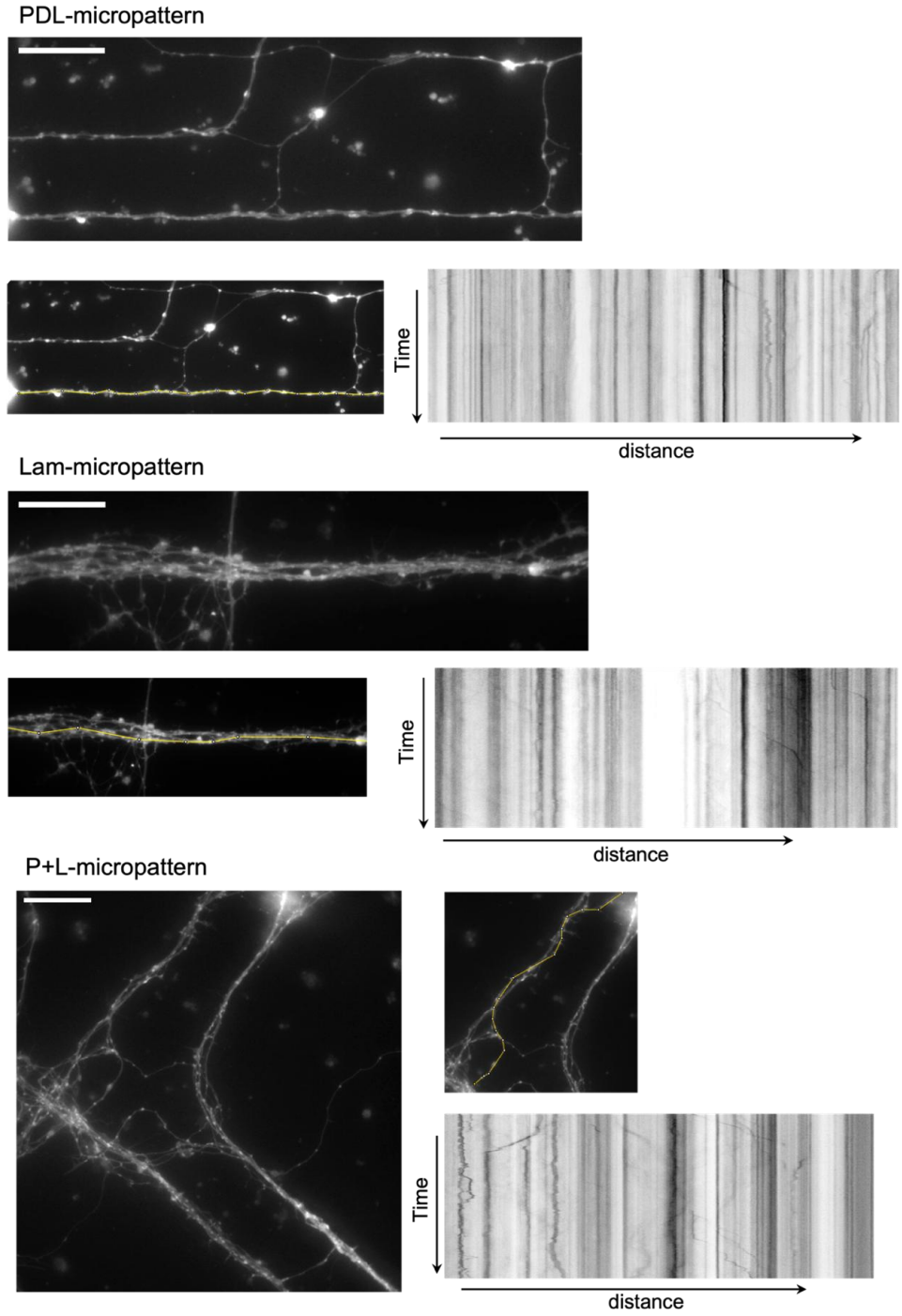

Figure 55. Mitochondrial motility analysis of hippocampal cells on micropatterned substrates stamped with PDL, laminin or P+L.

Representative live-cell imaging still frames of hippocampal cells cultured on micropatterned substrates stamped with each bio-ink are shown alongside their corresponding kymographs. The kymographs illustrate mitochondrial movements, including anterograde, retrograde, and reversing motions. Scale bar = 10 um.

When the fraction of motile mitochondria was calculated, no significant differences were found between micropatterned substrates inked with different biomolecules (PDL, laminin or P+L) (Fig 56A). Among the motile mitochondria, the fractions travelling in different directions (anterograde, retrograde or reversing) were analysed (Fig 56B).

The data revealed that the highest fraction of motile mitochondria on all micropatterns displayed reversing movements, characterised by back-and-forth motion. Specifically, PDL-micropatterned substrates showed a median of 17.9% reversing mitochondria (IQR = 8.80–29.2), which was higher than 0.00% anterograde or 0.00% retrograde mitochondria (both IQR = 0.00–6.19). Similarly, laminin-micropatterned substrates showed a median of 16.2% reversing mitochondria (IQR = 6.61–26.1), compared to 0.00% anterograde (IQR = 0.00–7.53) and 4.35% retrograde mitochondria (IQR = 0.00–7.28). On P+L micropatterns, the median fraction of reversing mitochondria was 20.5% (IQR = 11.8–31.9), higher than 2.08% anterograde (IQR = 0.00–7.85) and 0.00% retrograde mitochondria (IQR = 0.00–7.28).

Additionally, the percentage of time that mitochondria spent being motile on each micropatterned substrate was evaluated. No significant difference in motility time were found between the substrates (Fig 56C).

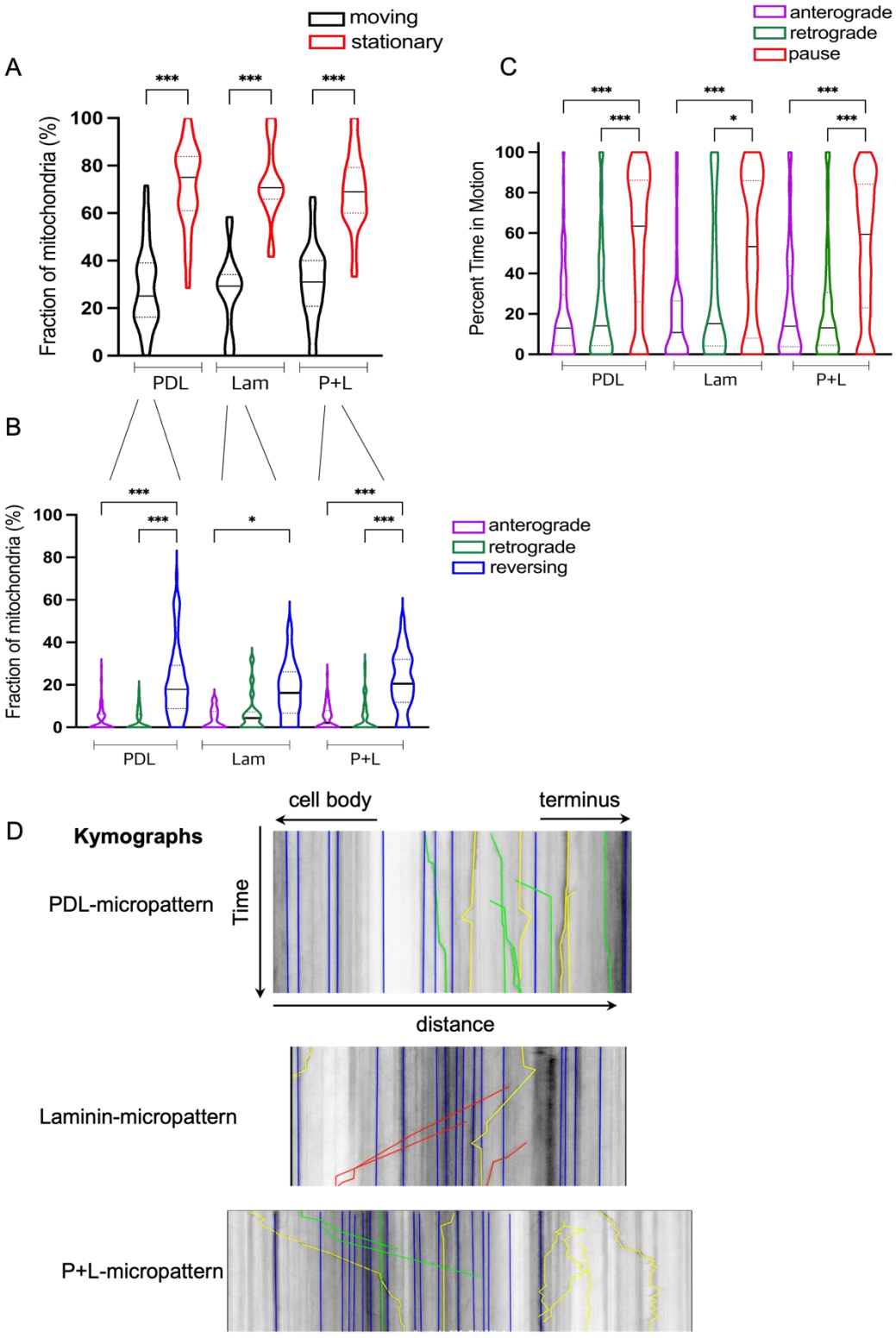

Figure 56. Kymoanalysis quantification of mitochondrial motility and movement dynamics within hippocampal cell cultures on PDL-, laminin- or P+L-patterned substrates at DIV 7.

*(A) The fraction of mitochondria classified as moving or stationary, pooled for each substrate type (B) Moving mitochondria from (A) were further categorised into anterograde, retrograde or reversing motions (C) the percentage of time mitochondria spent either moving or paused across substrates. Statistical significance is indicated (*P<0.01and ***P<0.0001). Violin plots display the data distribution with medians (solid line in black) and 1.5 x interquartile ranges (dotted line). (D) Representative annotated kymographs for each substrate. Tracks are colour-coded to indicate different motion types: anterograde (green), retrograde (red), reversing (yellow) and stationary (blue). Mitochondrial movement was imaged for 180 s using MitoTracker Green dyes. Statistical analyses include one-way ANOVA for (A) and Kruskal-Wallis non-parametric test for (B) and (C), followed by Dunn's post-hoc tests, after performing normality tests.*

Further quantification of distance- and pause-related parameters was performed to gain a deeper understanding of the mitochondrial transport dynamics across the different patterned substrates. When the distances travelled by mitochondria within a combined segment were analysed (Fig 57A), retrograde movements were longer than anterograde on both PDL- and laminin-patterned substrates. On PDL-patterned substrates, retrograde movements had a median distance of 1.82 µm (IQR = 1.17–3.25), compared to 1.56 µm for anterograde (IQR = 1.04–2.60). Similarly, on laminin substrates, retrograde distances had a median of 2.47 µm (IQR = 1.30–4.94), compared to 1.76 µm for anterograde (IQR = 1.01–3.48). In contrast, mitochondria on P+L-patterned substrates showed no significant difference between anterograde (1.30 µm; IQR = 0.91–2.73) and retrograde distances (1.30 µm; IQR = 0.78–2.73). Comparatively, retrograde mitochondria on laminin substrates travelled significantly longer distances than those on PDL or P+L substrates, with the shortest distances observed on P+L micropatterns.
The median pause duration for mitochondria on P+L substrates was significantly shorter than on PDL or laminin substrates (Fig 57B). Specifically, mitochondria on

P+L substrates paused for a median of 28.2 s (IQR = 12.6–61.2), compared to 33.0 s on PDL (IQR = 16.2–81.6) and 38.1 s on laminin (IQR = 17.3–114).

Pause frequency per second was lowest for mitochondria on laminin substrates, significantly lower than on PDL or P+L substrates (Fig 57C). Laminin substrates showed a median pause frequency of 0.007 s^{-1} (IQR = 0.006–0.012), compared to 0.012 s^{-1} on PDL (IQR = 0.006–0.017) and 0.012 s^{-1} on P+L (IQR = 0.006–0.017). Similarly, direction-switch frequency (number of reversals per track per second) was also significantly lower on laminin substrates compared to PDL, though not significantly lower compared to P+L. Laminin substrates exhibited a median switch frequency of 0.006 s^{-1} (IQR = 0.000–0.017), compared to 0.012 s^{-1} on both PDL (IQR = 0.000–0.029) and P+L (IQR = 0.000–0.029).

Overall, laminin micropatterns supported significantly longer retrograde distances and exhibited the lowest pause and switch frequencies among the three substrates tested.

Notably, when net velocities, segmental velocities, and combined segmental velocities were analysed, no significant differences were observed between substrate types or between anterograde and retrograde movements.

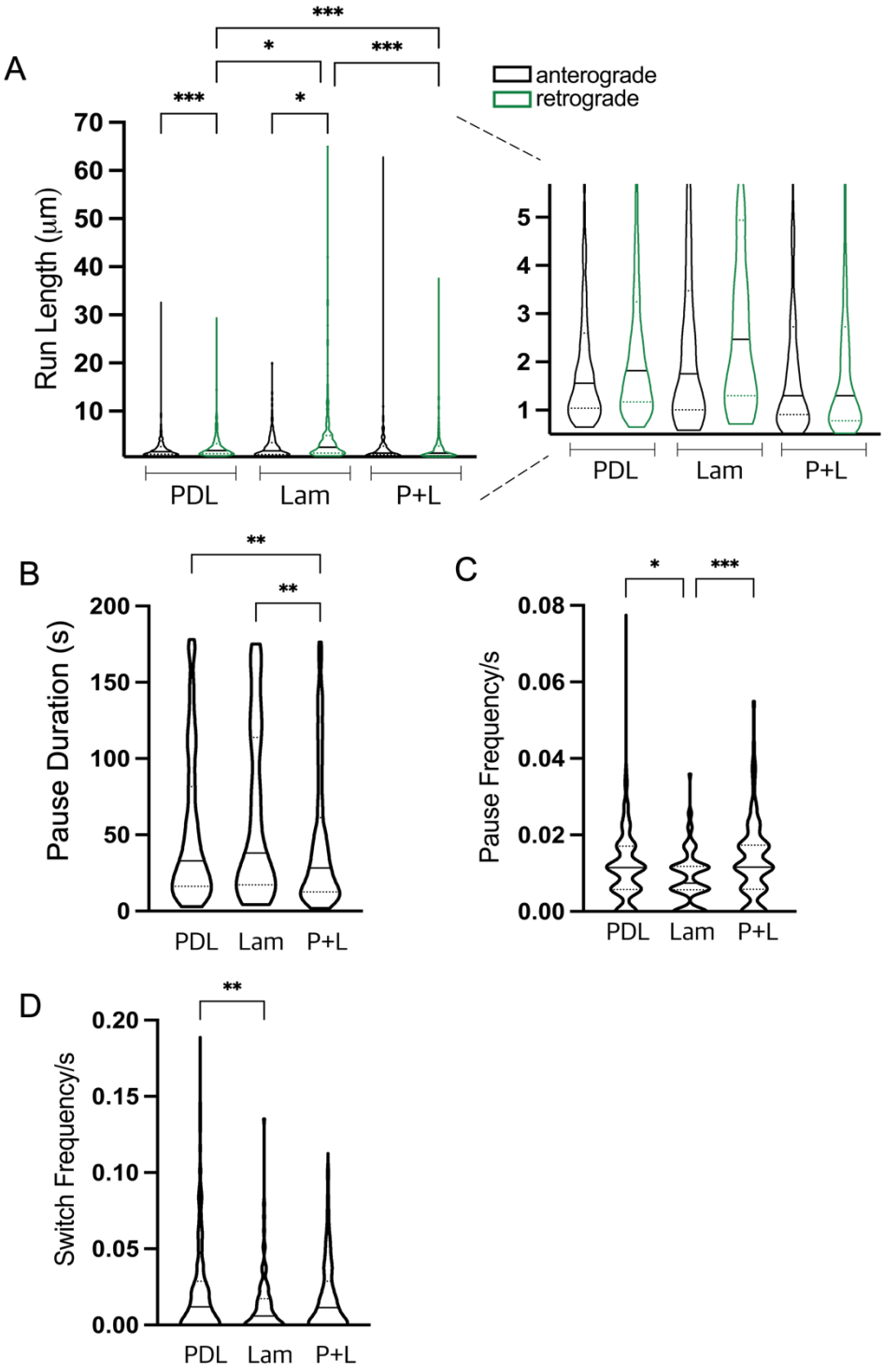

Figure 57. Quantification of mitochondrial transport dynamics: run lengths, pausing and direction reversals.

(A) Mitochondrial run lengths within combined segments on micropatterned substrates. The right panel provides a zoomed-in view to highlight medians and interquartile ranges. (B) Duration of mitochondrial pauses on each substrate. (C)

*Frequency of mitochondrial pauses per track over the imaging period (D) Frequency of direction reversals (switches) per track per unit of time. Statistical significance is indicated as follows: *P<0.01, *P<0.001 and ***P<0.0001 Kolmogorov-Smirnov non-parametric unpaired t-tests were performed for statistical analyses following normality tests.*

5.6 Comparison of Mitochondrial Motility on Micropatterned substrates Versus Bulk-Coated Substrates

The study aimed to determine whether mitochondrial motility in hippocampal cell cultures is influenced by confinement to micropatterns. Comparisons were made between mitochondrial motility on bulk-coated substrates (as described in Chapter 4) and micropatterned substrates. The objective was to evaluate whether culturing cells within defined patterned regions affects mitochondrial movements, including population dynamics, velocities, run lengths and pause durations.

The comparison involved dual-coated bulk substrates (PDL and laminin layers) and P+L micropatterned substrates (a mixture of PDL and laminin) with analyses performed at DIV 7. The results are summarised in Table 3.

General trends indicated a reduction in the overall mitochondrial movement and shorter run lengths across all conditions for micropatterned cells. However, P+L micropatterned substrates exhibited increased segmental and combined segmental velocities compared to the bulk-coated substrates. These differences are explored in more detail in the subsequent table (Table 3), graphs and analyses.

Table 3. A summary of results comparing mitochondrial motions within cells grown on micropatterns as compared to bulk coatings for DIV 7.

		PDL	Lam	P+L
Motile mitochondria population	anterograde	↓	nd (low n-numbers on micropatterns)	nd
	retrograde	Nd	nd	nd
	reversing	↓	↓	↓
	all moving combined	↓	nd	↓
	stationary	↑	↑	↑
Percent time in motion (of those mitos that move)	anterograde	nd	nd	nd
	retrograde	↑	nd	nd
	paused	nd	nd	nd
Net velocities	anterograde	↓	nd	nd
	retrograde	nd	nd	nd
Segmental velocities	anterograde	↓	↓	nd
	retrograde	↓	nd	↑
Combined segmental velocities	anterograde	↓	↓	nd
	retrograde	↓	nd	↑
Run lengths	anterograde	↓	↓	↓
	retrograde	↓	↓	↓
pause / switch parameters	Pause duration	nd	nd	nd
	Pause frequency	nd	nd	nd
	Switch frequency	nd	↓	nd

↓ = decreased on micropatterns compared to bulk-coated substrates; ↑ = increased on micropatterns compared to bulk-coated substrates; nd = no difference.

The fraction of mitochondria within cells cultured on bulk-coated substrates (data from Chapter 4) were compared with those on patterned-substrates for each type of ink (Fig 58A). The motile mitochondrial fraction (i.e., those classified as moving in anterograde, retrograde, or reversing directions) was significantly higher on PDL- and dual-bulk substrates compared to patterned substrates. Specifically, PDL-bulk substrates showed a median mitochondrial fraction of 36.6% (IQR = 25.0–47.1), compared to 25.0% on PDL-patterned substrates (IQR = 16.2–39.0). Similarly, dual-bulk substrates exhibited a median fraction of 41.3% (IQR = 1.25–63.5), which was higher than the 31.0% observed on P+L-patterned substrates (IQR = 20.8–40.0).

The moving mitochondria were further categorized into anterograde, retrograde, or reversing populations (Fig 58B). A significantly greater fraction of anterograde-moving mitochondria was observed on PDL-bulk substrates (median = 6.25%, IQR = 0.00–12.6) compared to PDL-patterned substrates (median = 0.00%, IQR = 0.00–6.16). While no significant changes were found in retrograde-moving mitochondria between bulk- and patterned substrates, a notable difference was observed in reversing mitochondria. Bulk substrates consistently supported a higher fraction of reversing mitochondria compared to patterned substrates. For instance, PDL-bulk substrates had a median reversing fraction of 25.0% (IQR = 17.2–35.4), laminin-bulk substrates had 25.0% (IQR = 16.7–39.8), and dual-bulk substrates had 37.0% (IQR = 19.2–50.0). In contrast, PDL-patterned substrates showed a median reversing fraction of 17.9% (IQR = 8.80–29.2), laminin-patterned substrates had 16.3% (IQR = 6.61–26.1), and P+L-patterned substrates had 20.5% (IQR = 11.8–31.9).

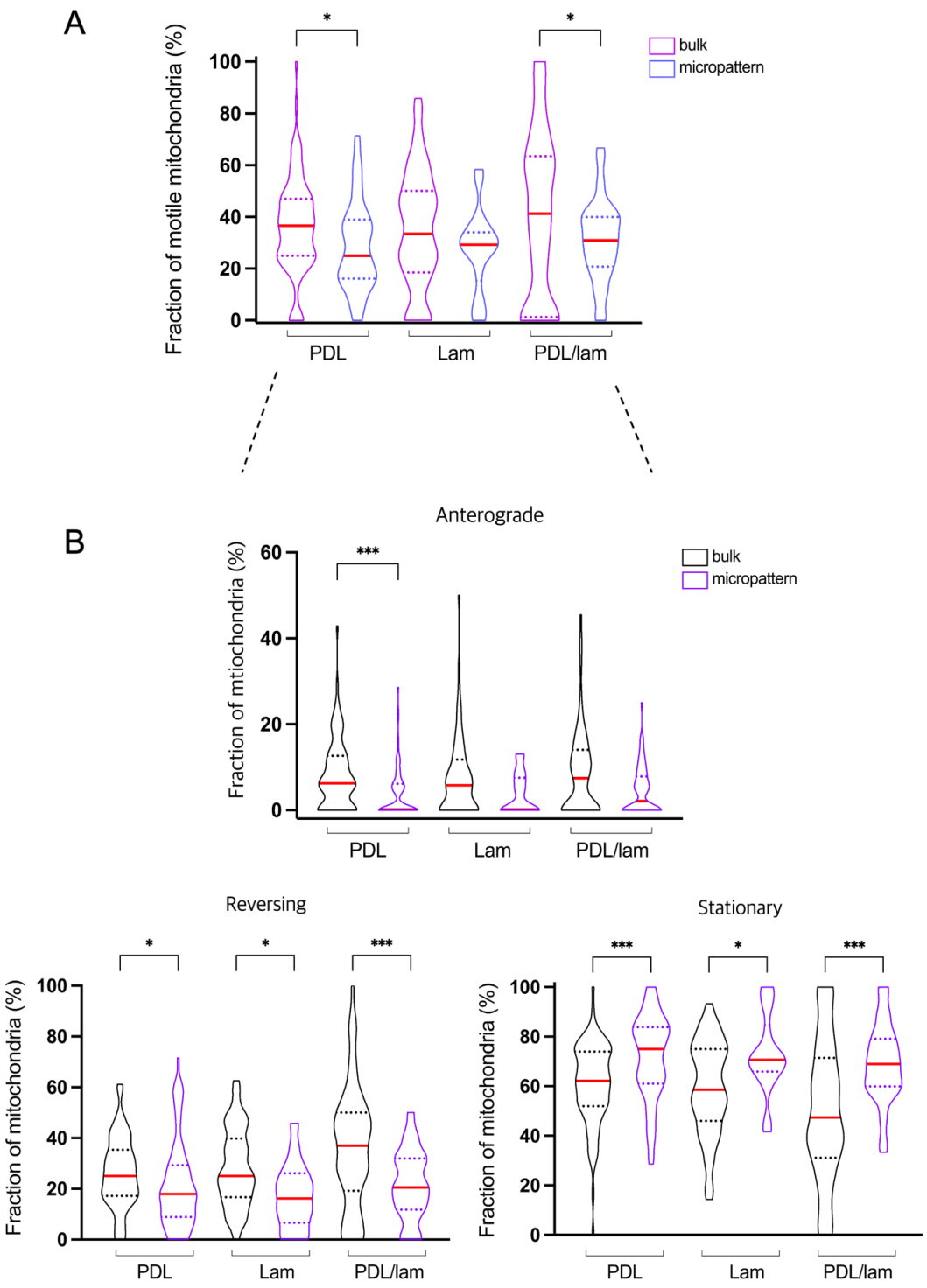

Figure 58. Quantification of mitochondrial fractions in hippocampal cells cultured on bulk-coated and micropatterned substrates.

(A) The relative mitochondrial fraction on bulk-coated substrates (PDL, laminin or dual) compared to micropatterned substrates stamped with PDL, laminin or P+L. (B) The fraction of moving mitochondria, categorised into anterograde, retrograde or

*reversing movements as well as stationary mitochondria. Statistical significance is indicated as follows: *P<0.01and ***P<0.0001. Violin plots display the data distribution, with medians (solid line in red) and 1.5 x interquartile ranges (dotted line). Data were collected from 3 independent culture preparation, with 5 images acquired per culture and per substrate condition. For each image, approximately 10-15 neurites were manually traced to generate kymographs for mitochondrial motility analysis. The number of traces was similar across bulk and patterned substrate conditions. Statistical analyses included Anova for (A) and Kruskal-Wallis non-parametric tests for (B) and (C), followed by Dunn's post-hoc tests after normality tests.*

The overall comparison of mitochondrial net velocities in anterograde and retrograde directions between bulk substrates and patterned substrates revealed significant differences (Fig 59A). On PDL-bulk substrates, anterograde mitochondria displayed faster velocities (median = 0.26 µm/s, IQR = 0.14–0.45) compared to PDL-patterned substrates (median = 0.11 µm/s, IQR = 0.07–0.20).
When segmental velocities were analysed, mitochondria on PDL- and laminin-bulk substrates exhibited higher anterograde velocities compared to their patterned counterparts (Fig 59B). For example, anterograde mitochondria on PDL-bulk substrates travelled at a median velocity of 0.27 µm/s (IQR = 0.15–0.48), compared to 0.19 µm/s on PDL-patterned substrates (IQR = 0.10–0.34). Similarly, anterograde mitochondria on laminin-bulk substrates travelled at a median velocity of 0.29 µm/s (IQR = 0.16–0.53), compared to 0.19 µm/s on laminin-patterned substrates (IQR = 0.11–0.35). Retrograde mitochondria on PDL-bulk substrates also showed faster velocities (median = 0.26 µm/s, IQR = 0.14–0.48) compared to PDL-patterned substrates (median = 0.22 µm/s, IQR = 0.12–0.39). However, on dual-bulk substrates, retrograde velocities (median = 0.18 µm/s, IQR = 0.10–0.33) were slower compared to P+L-patterned substrates (median = 0.20 µm/s, IQR = 0.11–0.40).

Analysis of combined segmental velocities showed similar trends (Fig. 59C). Anterograde mitochondria on PDL-bulk substrates had a median velocity of 0.24 µm/s (IQR = 0.14–0.43), which was faster than on PDL-patterned substrates (median = 0.19 µm/s, IQR = 0.11–0.34). Likewise, anterograde mitochondria on laminin-bulk substrates exhibited faster movements (median = 0.26 µm/s, IQR = 0.15–0.44) compared to laminin-patterned substrates (median = 0.18 µm/s, IQR = 0.10–0.32). Retrograde mitochondria on PDL-bulk substrates showed a median velocity of 0.24 µm/s (IQR = 0.13–0.42), faster than on PDL-patterned substrates (median = 0.22 µm/s, IQR = 0.12–0.37). Conversely, retrograde velocities were higher on P+L-patterned substrates (median = 0.18 µm/s, IQR = 0.11–0.34) compared to dual-bulk substrates (median = 0.17 µm/s, IQR = 0.09–0.29).
When mitochondrial travel distances were measured, significant differences were observed between bulk and patterned substrates (Fig 59D). Regardless of direction, mitochondria on all bulk substrates travelled longer distances than those on patterned substrates. For example, anterograde mitochondria on PDL-bulk substrates travelled a median distance of 6.37 µm (IQR = 4.81–9.88), compared to 1.56 µm on PDL-patterned substrates (IQR = 1.04–2.60). Similarly, laminin-bulk substrates supported longer distances (median = 5.98 µm, IQR = 4.29–9.75) compared to laminin-patterned substrates (median = 1.75 µm, IQR = 1.00–3.48). On dual-bulk substrates, mitochondria travelled a median distance of 4.16 µm (IQR = 2.86–6.50), compared to 1.30 µm on P+L-patterned substrates (IQR = 0.91–2.73).

Finally, pause-related parameters, including pause duration and frequency per track, were analysed but showed no significant differences between bulk and patterned substrates.

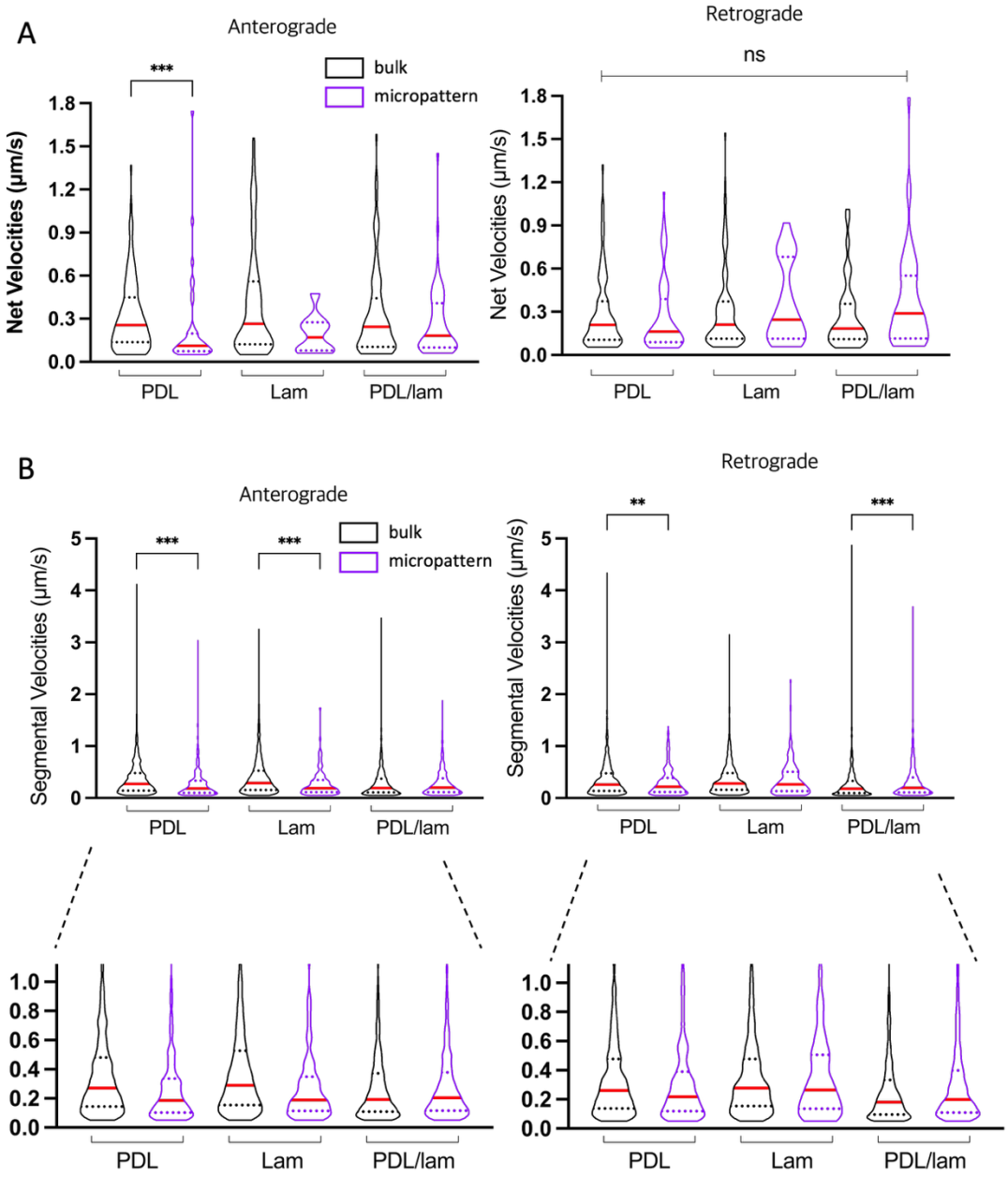
A
Anterograde
Retrograde
bulk
micropattern
***
ns
Net Velocities (µm/s)
1.8
1.5
1.2
0.9
0.6
0.3
0.0
PDL
Lam
PDL/lam
B
Anterograde
Retrograde
bulk
micropattern
***
***
**
***
Segmental Velocities (µm/s)
5
4
3
2
1
0
1.0
0.8
0.6
0.4
0.2
0.0
PDL
Lam
PDL/lam

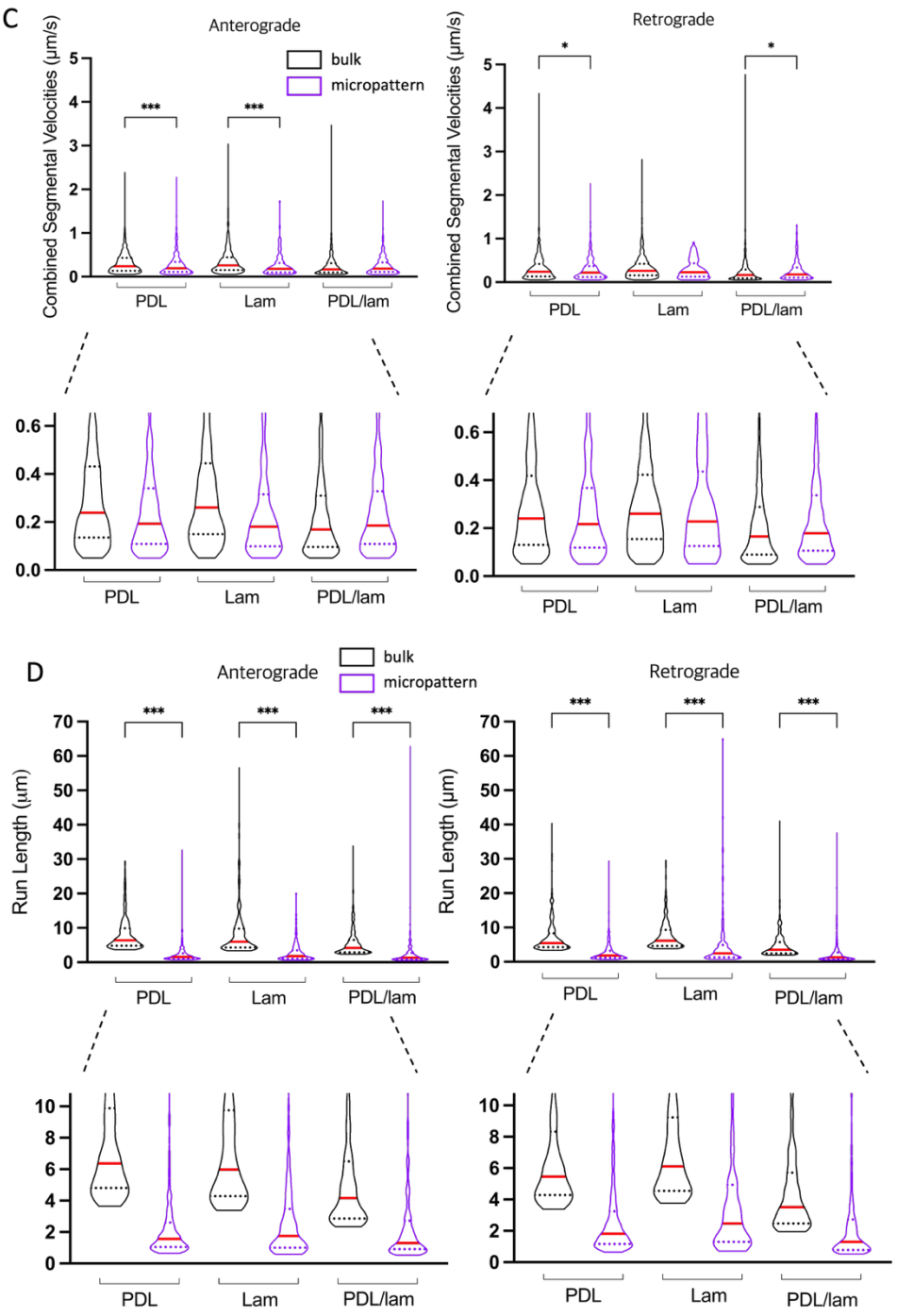

Figure 59. Kymoanalysis of mitochondrial movement velocities and travel distances on bulk-coated and micropatterned substrates.

(A)Net velocities of mitochondrial motility in anterograde or retrograde directions on bulk-coated and micropatterned substrates. (B) Segmental velocities of mitochondria travelling within a single uninterrupted segment (C) Combined segmental velocities of mitochondria moving through multiple segments without

*pausing (D) Distances travelled by mitochondria in one direction within combined segments. Statistical significance is indicated as follows: *P < 0.01, **P < 0.001, ***P < 0.0001. Data were collected from 3 independent culture preparations per substrate condition, with 5 images acquired per culture. For each image, approximately 10-15 neurites were manually traced to generate kymographs for mitochondrial motion analysis. Kruskal-Wallis non-parametric tests with Dunn's post-hoc analyses were used for (B) and (C) following normality tests.*

In summary, the analysis of mitochondrial motions within hippocampal cell cultures revealed distinct differences between traditional bulk substrates and micropatterned substrates. Mitochondria on bulk substrates exhibited higher fractions of motile mitochondria, along with greater velocities (net, segmental, and combined segmental) and longer run lengths compared to those on micropatterned substrates. Notably, PDL-micropatterned substrates demonstrated significant reductions in mitochondrial motile fractions, velocities, and run distances, highlighting the impact of patterning on mitochondrial dynamics. Such substrate-dependent differences suggest that spatial constraints imposed by micropatterns may influence key intracellular transport mechanisms, with potential implications for the validity and physiological relevance of *in vitro* neuronal models.

5.7 Future work: Pilot Data and Suggestions for Future Directions

5.7.1 Limitations and Further Studies

One of the limitations encountered during this study was determination of an appropriate blocking compound to create a strongly-cell repellent background that maximised pattern integrity during microcontact printing, while preserving cell morphology. Based on previous studies with similar compounds (Albers *et al*., 2015; Albers *et al*., 2016), PFS was anticipated to be an effective candidate. For example, the Offenhäusser group successfully cultured primary cortical embryonic rat neurons on 2D triangular micropatterns blocked with FOTCS, another fluorosilane compound. Their results demonstrated restricted neurite growth along the triangular patterns, with neurite bundles forming and aligning along the edges of the patterns (Fig 45).

However, a similar issue was encountered in this study, as neurite bundles formed along the edges of line patterns, eventually merging into large bundles within each line. While PFS acted as a cell repellent (Fig 50), its effects on cell morphology hindered the accuracy and feasibility of mitochondrial measurement.

To address these challenges, future studies should focus on both testing of additional blockers, as well as on optimising micropattern design. For the latter, incorporating nodes of different sizes, reducing line widths, or modifying interconnections within pattern geometries may all help mitigate the formation of large neurite bundles. As it is possible that PFS substrates inherently promote bundle formation, identifying and testing alternative blocking compounds that are more suitable for hippocampal neural cells could provide improved results, ensuring both pattern integrity and cell morphology conducive to mitochondrial measurements. Moreover, the observed differences in mitochondrial dynamics between micropatterned and bulk-coated cultures highlight that geometrical confinement may significantly alter intracellular transport. This suggests that micropatterned culture systems could influence the physiological relevance of *in vitro* neuronal models, especially when studying neurodegenerative mechanisms.

5.7.2 Alternative Blocker: Preliminary Results with Lipidure®-CM

An ideal cell repellent compound should efficiently block non-patterned regions to prevent any cell/neurite attachment without significant changes to the morphology of on-pattern cells. Lipidure®-CM has recently emerged as a highly effective and biocompatible blocker, though its use in microengineering applications remains limited (Eilenberger *et al*., 2021). Lipidure® -CM is a water-soluble polymer composed of a polymer of 2-(methacryloyoxy)ethyl phosphorylcholine (MPC) which mimics the phosphatidylcholine headgroup found in natural cell membrane (Fig 60). The MPC unit involves hydrophobic alkyl methacrylate monomer with a hydrophilic phosphorylcholine group (Iwasaki and Ishihara, 2012). The copolymer also includes a second methacrylate-based co-monomer unit (denoted as R in the figure), which is incorporated to modulate the physical properties of the polymer, such as film stability and mechanical strength.

Several studies have demonstrated the efficacy of phospholipid-mimetic surfaces, like MPC-based coatings, in preventing unwanted biological responses. For instance, Sibarani *et al*. showed that coating microchannel surfaces in microfluidic devices with MPC significantly reduced serum albumin adsorption (Sibarani *et al*., 2007). Similarly, Nakatoh's group used Lipidure for micropatterned substrate fabrication with non-neuronal cell cultures, including Dictyostelium cells (AX2) and Cos-1 (African green monkey kidney cell line) (Nakatoh *et al*., 2022). In their work, Lipidure-coated coverslips or plastic dishes were selectively exposed to air plasma through a mask with holes to create adhesive areas for cells. Alternatively, gold-coated surfaces treated with Lipidure were locally modified using scanning laser ablation to define adhesive regions. Both approaches effectively restricted cells to adhesive areas, allowing for prolonged culture durations and enabling studies on various aspects of cell behaviour. These findings highlight the potential of MPC-based coatings, such as Lipidure®, for applications requiring precise cell patterning with minimal biological interference.

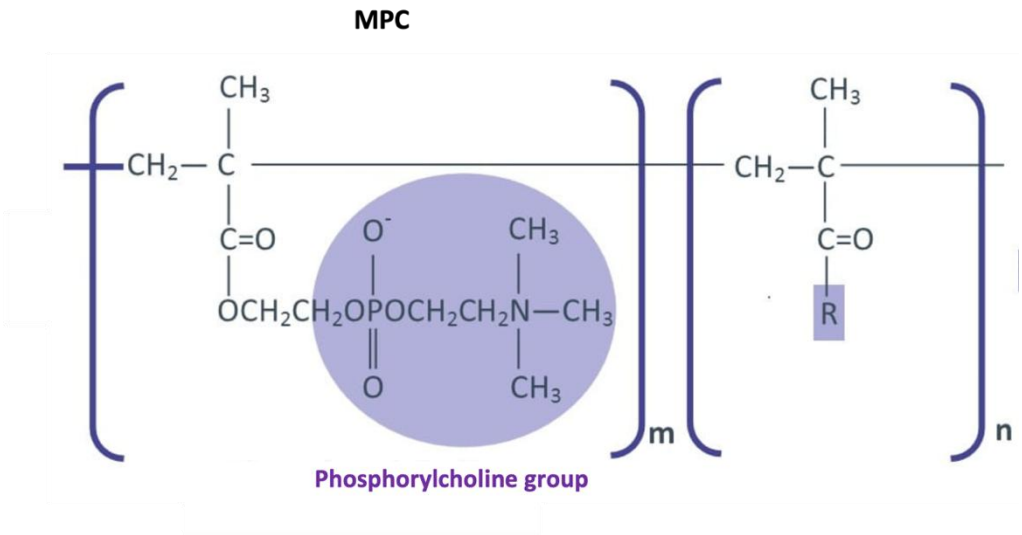

Figure 60. Chemical structure of MPC polymer, the primary building block of Lipidure®-CM.

The molecule consists of a methacrylate group on the left ($CH_2=C(CH_3)$-COO-), which provides a polymerisable site for copolymer formation and a phosphorylcholine group on the right (OCH_2CH_2-PO_4^--$CH_2CH_2N^+(CH_3)_3$), which mimic the hydrophilic head of natural phospholipids found in cell membranes (highlighted in purple). The highly hydrophilic and biocompatible nature of MPC enables the formation of cell-repellent substrates with minimal protein or cell adhesion. The copolymer also contains a second methacrylate-based co-monomer unit ($CH_2=C(CH_3)$-C(=O)-R) which enhances material stability and performance depending on the formulation (Structure adapted from AMSBIO).

In preliminary experiments with hippocampal neural cultures, Lipidure®-CM was evaluated for its efficacy as a cell-repellent compound. Micropatterned substrates were prepared by stamping PDL lines with widths and gaps of either 12 µm or 16 µm onto glass substrates pre-treated with Lipidure. For comparison, the same procedure was performed using PFS as the blocking agent. Hippocampal cells were plated onto these substrates, and neurite growth was monitored at DIV 7 (Fig 61). The data suggest that Lipidure-blocked substrates exhibited superior neuronal alignments along the micropatterns, with reduced off-pattern cell adhesion compared to PFS-blocked substrates. When comparing the two line/gap widths, 16

µm patterns demonstrated clearer cell alignment and patterning than 12 µm patterns. Additionally, PFS-blocked substrates showed more extensive neurite crossing between adjacent lines, while Lipidure-blocked substrates effectively minimized such crossing.

Unfortunately, imaging of mitochondrial movements within these micropatterned cells could not be completed due to the COVID-19 lockdown, resulting in the termination of experiments at DIV 7. Nevertheless, the preliminary findings indicate that Lipidure may serve as an efficient blocker for future neuronal microcontact printing studies. The 12 µm line/gap width patterns with Lipidure demonstrated better pattern integrity and reduced neurite bundling, highlighting its potential for enhancing neuronal patterning and facilitating studies on mitochondrial dynamics.

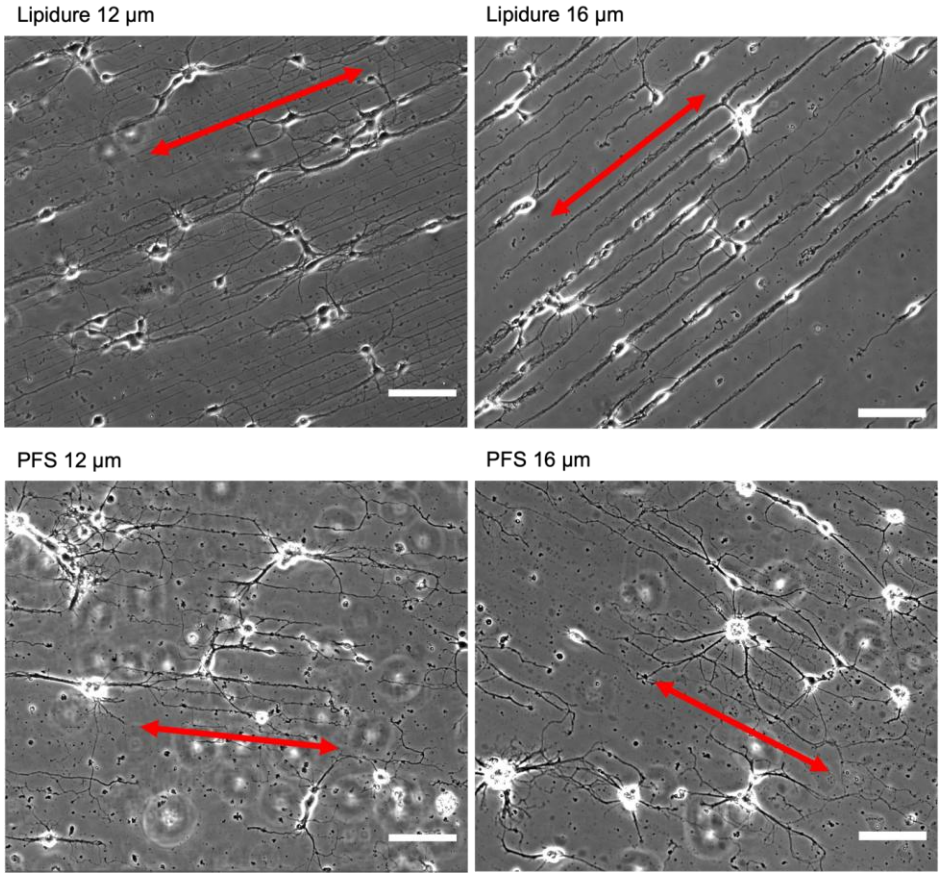

Figure 61. Brightfield images of hippocampal neurite outgrowth on PDL-micropatterned substrates that were blocked by either Lipidure®-CM or PFS at DIV 7.

The micropatterns consists of either 12 µm or 16 µm line widths and gaps. The red arrows indicate the directions of the micropatterned lines. Scale bar = 100 µm.

5.7.3 Design of Micropatterned Substrates for Future Work

Future studies should focus on the development of customized micropattern designs optimized for mitochondrial imaging in hippocampal neurons. The patterns used in this chapter had notable limitations, including the absence of nodes for soma adhesion, which likely contributed to cell clustering on blocked substrates. Additionally, the line-shaped patterns provided limited control over cell-cell connectivity, and the 10 µm line widths were thicker than ideal for guiding neurite processes, potentially contributing to the formation of thick neurite bundles.

Figure 62 illustrates a proposed micropattern design for future hippocampal cell studies. This asymmetric pattern features rectangular repeating units, each with eight connections stemming from a single node. To optimize the design, the nodes are arranged with a gradient in diameter from 10 to 30 µm (left to right), enabling evaluation of the ideal node size for promoting soma adhesion. Suggested line widths for initial testing are 3 µm and 5 µm, with the potential to include a gradient in line widths, such as a horizontal gradient in node diameter and a vertical gradient in line thickness.

These proposed designs would allow a more systematic evaluation of how variations in micropattern geometry affect hippocampal cell behaviour, including soma placement, neurite growth, and cell-cell connectivity. Future studies should focus on plating hippocampal cells onto these improved patterns to assess their efficacy and explore the diversity in pattern designs to enhance imaging and analysis of mitochondrial dynamics.

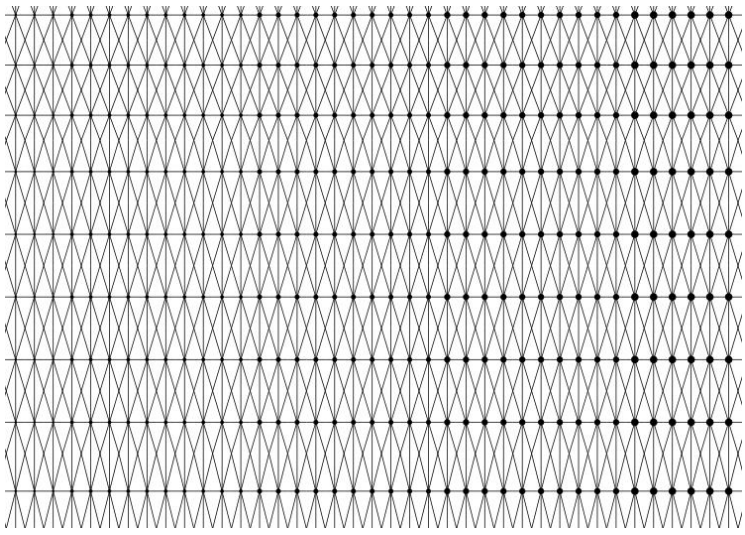

Figure 62. Proposed neuronal micropattern design for mitochondrial studies in hippocampal cells.

Example of an asymmetric micropattern featuring rectangular repeating units, with each node connected by eight lines. The node diameters range from 10 to 30 um (increasing from left to right) to facilitate the evaluation of optimal soma adhesion.

5.8 Overall Conclusion

This study demonstrates that microcontact printing offers an alternative to standard bulk-coated substrates that can enable the establishment of neuronal cultures with controlled cellular geometries, which can potentially facilitate more straightforward quantification of dynamic intracellular cargo, such as mitochondria. Achieving optimal outcomes required several critical optimizations, including evaluating the wettability of different stamps on various substrates and determining the appropriate ink drying and transfer times. The optimized conditions—using hydrophilic stamps with 15 min ink incubation, 10 s blow-drying, and a 30 s wait time—enabled efficient ink transfer to substrates, supporting cell adhesion and growth.

Although PFS, a hydrophobic silane, minimized off-pattern cell adhesion, it also induced clustered soma and thick neurite bundles that hindered mitochondrial analysis. This limitation led to the exploration of micropatterned substrates without blockers, which revealed that neurons were more abundant overall, but astrocytes showed a higher tendency to remain confined within patterns.

Kymoanalysis of mitochondrial motility on substrates patterned with PDL, laminin, or P+L demonstrated key differences. Laminin substrates supported longer retrograde mitochondrial movements, potentially reflecting mitochondrial return to the soma for recycling. These substrates also exhibited longer pause durations and the lowest pause and switch frequencies, suggesting differences in mitochondrial dynamics linked to the extracellular environment. However, when comparing mitochondrial motility on micropatterned substrates with bulk substrates, the former showed significant reductions in motile fractions, velocities, and run lengths, underscoring the potential constraints introduced by micropatterning.

Despite the advantages of microcontact printing, challenges remain in sustaining long-term cultures with healthy neuronal morphologies. As discussed in Section 5.5.2, Lipidure®-CM emerged as a promising alternative blocker, showing better alignment of neuronal growth with reduced off-pattern adhesion in preliminary experiments. Coupling Lipidure with a new geometric pattern design—such as one

incorporating multiple connections per node and gradients in node diameters or line widths—may address existing limitations. This combination has the potential to foster well-structured neuronal cultures that not only support mitochondrial analysis but also maintain pattern integrity and physiological relevance over extended periods.

In summary, this study highlights the potential of microcontact printing for neuronal culture applications while identifying critical areas for further improvement. By integrating biocompatible blockers like Lipidure and optimising micropattern geometries, future studies can advance the development of platforms capable of supporting long-term neuronal health and dynamic analyses of intracellular organelles.

CHAPTER SIX:
General Discussion

6.1 Principal Findings

This thesis aimed to characterise mitochondrial motility in primary hippocampal cells, employing both conventional bulk-coated substrates and micropatterned neuronal cultures to facilitate precise quantification. In Chapter 3, I established an optimised imaging and analytical framework for tracking mitochondrial movement in hippocampal cells cultured on PDL and laminin-coated substrates. Quantitative analysis revealed distinct transport dynamics, with differential motility characteristics depending on substrate composition. Chapter 4 extended this analysis to a broader set of surface coatings, revealing that traditional ECM-based substrates (PDL, laminin, and dual) supported higher mitochondrial motility compared to chemically charged coatings such as CES and APTES. While PDL, laminin, and dual coatings showed similar transport-supportive properties, CES and APTES significantly reduced motile fractions, velocities, and run lengths of mitochondria, indicating a substrate-dependent modulation of intracellular dynamics.

Finally, Chapter 5 introduced a micropatterned neuronal culture system, demonstrating its utility for restricting neurite outgrowth to predefined pathways. This system facilitated mitochondrial tracking within aligned neurite processes and allowed a comparative assessment of mitochondrial motility between micropatterned and bulk-coated substrates. Notably, micropatterned substrates resulted in shorter run lengths and lower mitochondrial motile fractions, suggesting that confined neurite architecture influences mitochondrial transport properties.

Taken together, these findings underscore the significant impact of extracellular microenvironments on mitochondrial dynamics, with implications for studies on neuronal metabolism, synaptic function, and neurodegenerative diseases. The use of micropatterned cultures as a tool for spatially restricting neurite outgrowth provides a novel methodological approach for dissecting intracellular transport mechanisms in neuronal networks.

6.2 Mitochondrial Motility and Neuronal Microenvironments

Mitochondrial transport is crucial for neuronal function, particularly in the maintenance of synaptic activity and energy homeostasis. The results of this study align with previous reports demonstrating that substrate composition modulates neuronal adhesion and cytoskeletal organization, both of which are critical for intracellular transport (Mohan *et al*., 2019; Kaar *et al*., 2020). It is important to distinguish between neuronal attachment (which supports survival) and neurite elongation (which supports mitochondrial transport). Substrate coatings must first promote sufficient cell adhesion to prevent apoptosis and ensure neuronal survival. Although we did not perform direct viability assays in this study, prior research has shown that inadequate adhesion leads to apoptosis (Vroemen *et al*., 2025), and that chemically defined charged surfaces can influence neuronal viability and cell-type composition (Marques-Almeida *et al*., 2023). On the other hand, differences in neurite outgrowth—driven by substrate-induced cytoskeletal changes—can also influence mitochondrial motility. Bulk-coated substrates, particularly those incorporating laminin, promoted increased mitochondrial movement, likely by enhancing neurite elongation and cytoskeletal stability. Laminin is well known to activate integrin-mediated signalling, which influences cytoskeletal remodelling and intracellular trafficking (Franze *et al*., 2013). The increased retrograde movement of mitochondria observed on laminin-coated substrates suggests an active recycling process, whereby mitochondria are transported back to the soma for degradation or replenishment (Sheng & Cai, 2012). Taken together, these findings highlight that different substrate coatings may differentially affect (1) neuronal attachment and survival and (2) cytoskeletal support for motility. The two processes are related but mechanistically distinct and should be evaluated separately when interpreting mitochondrial dynamics.

In contrast, micropatterned substrates resulted in significantly reduced mitochondrial motility, with lower net velocities and shorter run lengths. This finding suggests that the spatial confinement of neurites may impose physical or biochemical constraints on mitochondrial movement. One potential explanation is

that neurites in micropatterned cultures experience increased mechanical resistance due to the structured architecture of growth pathways. Studies have shown that microtubule organisation and actin-myosin interactions play a crucial role in regulating mitochondrial transport, and the confined geometries of micropatterned substrates may limit cytoskeletal rearrangement (Frederick *et al*., 2019). Alternatively, the increased neurite bundling observed in some micropatterned conditions could lead to steric hindrance, restricting the passage of mitochondria through axonal pathways.

These results highlight the importance of considering the physical constraints of the cellular microenvironment when studying mitochondrial dynamics. While micropatterning provides a useful tool for guiding neurite growth, it also introduces potential limitations that must be accounted for in future experimental designs.

6.3 Implications for Neuronal Health and Disease

Mitochondrial dysfunction is a hallmark of numerous neurodegenerative diseases, including Alzheimer's, Parkinson's, and amyotrophic lateral sclerosis (ALS). Impaired mitochondrial motility has been implicated in synaptic dysfunction, axonal degeneration, and neuronal energy deficits (Baloh *et al*., 2007; Devine & Kittler, 2018). The present study provides further evidence that extracellular factors, including substrate composition and geometric confinement, significantly influence mitochondrial transport properties. This has important implications for understanding how changes in the neuronal microenvironment may contribute to disease pathology.

For instance, in Alzheimer's disease, aberrant axonal morphology and cytoskeletal instability have been linked to impaired mitochondrial transport (Calkins & Reddy, 2011). The findings from micropatterned cultures suggest that architectural constraints within the neuronal environment may exacerbate mitochondrial trafficking defects. Similarly, in ALS, disruptions in microtubule-

associated transport proteins such as kinesin and dynein lead to defects in mitochondrial distribution along axons (Bilsland *et al*., 2010).

To address these implications experimentally, future studies could expose neurons *in vitro* to oligomers of amyloid-β, or could employ primary hippocampal neurons harvested from neurodegenerative mouse models, such as the 3xTg-AD mouse, a well-established *in vivo* model of Alzheimer's disease known to exhibit mitochondrial trafficking impairments within hippocampal neurons (Cavendish, *et al*., 2019). Culturing such neurons on micropatterned substrates at early *in vitro* stages (e.g., DIV5-7) would allow comparative kymographic analysis under controlled neurite geometry, enabling precise quantification of motile fraction, velocities, and directional switching. Mitochondrial markers (such as mito-GFP or MitoTracker) could be used for live-cell imaging to assess how disease-associated genetic pathology interacts with geometric constraints to modulate mitochondrial transport dynamics.

6.4 Limitations and Future Directions

While this study provides valuable insights into mitochondrial motility, several limitations must be acknowledged. First, the reliance on 2D culture systems does not fully recapitulate the complex 3D architecture of neuronal networks *in vivo*. Although micropatterned substrates provide better control over neurite outgrowth compared to conventional bulk-coated substrates, they still do not fully mimic the three-dimensional organisation of neurons within brain tissue. Future studies should explore the application of 3D micropatterning techniques or hydrogels that allow for more physiologically relevant neuronal architectures. However, 3D micropatterning on the scale required to control neurite alignment would be extremely technically challenging, due to fabrication constraints, limited optical accessibility, and the mechanical complexity of 3D scaffolds (Kunze *et al*., 2011).

Second, the assessment of mitochondrial motility was based on kymograph analysis, which provides robust tracking of mitochondrial displacement but does not fully capture dynamic interactions with cytoskeletal elements. The use of super-

resolution imaging techniques, such as stimulated emission depletion (STED) microscopy or lattice light-sheet microscopy, could provide a more detailed view of mitochondrial-cytoskeletal interactions within confined neuronal environments (Wang *et al*., 2019).

Additionally, while this study examined mitochondrial dynamics under baseline conditions, future experiments should investigate how neuronal activity, metabolic stress, or neuroinflammatory factors influence mitochondrial motility in both bulk and micropatterned cultures. The introduction of pharmacological agents targeting key regulatory pathways—such as AMPK signalling or mitochondrial fission/fusion proteins—could provide further mechanistic insights into how mitochondrial transport is modulated under different physiological and pathological conditions.

A particularly promising avenue for future research is the integration of Lipidure®-CM as a cell-repellent blocker in micropatterned neuronal cultures. Preliminary results suggest that Lipidure®-CM may offer superior pattern integrity compared to traditional silane-based blockers such as PFS. Further investigations are needed to confirm whether this blocker can improve neuronal alignment while maintaining optimal mitochondrial motility for long-term imaging studies.

6.5 Conclusion

This study underscores the significant impact of extracellular environments on mitochondrial motility in primary hippocampal neurons. Bulk-coated substrates, particularly those incorporating laminin, promote enhanced mitochondrial transport, while micropatterned cultures impose spatial constraints that reduce motile fractions and alter transport dynamics. These findings have important implications for understanding mitochondrial behaviour in both physiological and pathological conditions, particularly in neurodegenerative diseases characterised by transport deficits.

The development of micropatterned neuronal cultures provides a valuable tool for studying intracellular trafficking under controlled conditions. However,

careful consideration must be given to the effects of spatial confinement on neuronal morphology and organelle dynamics. Future studies integrating advanced imaging techniques and refined micropatterning strategies will be crucial for elucidating the precise mechanisms governing mitochondrial transport in complex neuronal networks.

By advancing our understanding of mitochondrial motility in controlled microenvironments, this work lays the foundation for future research exploring how mitochondrial transport defects contribute to neuronal dysfunction and neurodegenerative disease progression.

7. References

Akeson, R. and Warren, S.L. 1986. PC12 adhesion and neurite formation on selected substratum are inhibited by some glycosaminoglycans and a fibronectin-derived tetrapeptide. Exp. Cell Res. 162, 347-362

Akther, F., Yakob, S.B., Nguyen, N-T. and Ta, H.T. 2020. Surface modification techniques for endothelial cell seeding in PDMS microfluidic devices. Biosensors. 10(11), 182

Albers, J., Toma, K. and Offenhäusser, A. 2015. Engineering connectivity by multi scale micro patterning of individual populations of neurone. Biotechnol. J. 10, 332-338

Alzahid, Y.A., Mostaghimi, P., Gerami, A., Singh, A., Privat, K., Amirian, T. and Armstrong, R.T. 2018. Functionalisation of polydimethylsiloxane (PDMS)-microfluidic devices coated with rock minerals. Sci Rep. 8, 1-15

AMSBIO. (n.d.). *Lipidure® Coating for Cell Culture*. Available at: https://www.amsbio.com/3d-cell-culture-extracellular-matrices/lipidure-coating/ (Accessed: 30 March 2025).

Baloh, R.H., Schmidt, R.E., Pestronk, A. And Milbrandt, J. 2007. Altered axonal mitochondrial transport in the pathogenesis of Charcot-Marie-Tooth disease from mitofusin 2 mutations. J Neurosci. 27, 422-430

Barnhart, E.L. 2016. Mechanics of mitochondrial motility in neurons. Curr. Opin. Cell Biol. 38, 90–99

Basarsky, T.A., Parpura, V. and Hayden, P.G. (1994) Hippocampal synaptogenesis in cell culture: developmental time course of synapse formation, calcium influx, and synaptic protein distribution. J Neurosci. 14: 6402-11

Basu, H., Ding, L., Pekkurnaz, G., Cronin, M., & Schwarz, T. L. (2020). Kymolyzer, a semi-autonomous kymography tool to analyze intracellular motility. Current Protocols in Cell Biology, 87, e107

Baxter, K.K., Uittenbogaard, M., Yoon, J., Chiaramello. A. 2009. The neurogenic basic helix–loop–helix transcription factor NeuroD6 concomitantly increases mitochondrial mass and regulates cytoskeletal organization in the early stages of neuronal differentiation. ASN NEURO 1(4), 195-211.

Bayhuber, M., Meins, T., Habeck, M., Becker, S., Giller, K., Villinger, S., Vonrhein, C., Griesinger, C., Zweckstetter, M. and Zeth, K. 2008. Structure of the human voltage-dependent anion channel. Proc Natl Acad Sci. 105 (40), 15370-15375

Belkaid, W., Thostrup, P., Yam, P.T., Juzwik, C.A., Ruthazer, E.S., Dhaunchak, A.S. and Colman, D.R. 2013. Cellular response to micropatterned growth promoting and inhibitory substrates. BMC Biotechnol. 13, 86

Bernard, A., Renault, J.P., Michel, B., Bosshard, H.R. and Delamarche, E. 2000. Microcontact printing of proteins. Adv Master. 12, 1067-1070

Bock D.D., Lee W.C., Kerlin A.M., Andermann M.L., Hood G., Wetzel A.W., Yurgenson S., Soucy E.R., Kim H.S. and Reid R.C. 2011. Network anatomy and in vivo physiology of visual cortical neurons. Nature. 471, 177–182

Boehler, M.D., Leondopulos, S.S., Wheeler, B.C. and Brewer, G.J. 2012. Hippocampal networks on reliable patterned substrates. J Neurosci. Methods. 203, 344-353

Burbulla, L.F., Beaumont, K.G., Mrksich, M. and Krainc, D. 2017. Micropatterning facilitates the long-term growth and analysis of iPSC-derived individual human neurons and neuronal networks. Adv Healthc Mater. 5(15), 1894-1903

Branch DW, Corey JA, Weyhenmeyer GJ, Brewer GJ, Wheeler BC. 1998 Microstamp patterns of biomolecules for high-resolution neuronal networks. Med Biol Eng Comput. 36,135e41

Brickley, K. and Stephenson, F.A. 2011. Trafficking Kinesin Protein (TRAK)-mediated Transport of Mitochondria in Axons of Hippocampal Neurons. J Biol Chem. 286, 18079–18092

Bros, H., Hauser, A., Paul, F., Niesner, R. And Infante-Duarte, C. 2015. Assessing mitochondrial movement within neurons: Manual versus automated tracking methods. Traffic. 16(8), 906-917

Cai, Q., Gerwin, C. and Sheng, Z-H. 2005. Syntabulin-mediated anterograde transport of mitochondria along neuronal processes. J Cell Biol. 170, 959–969

Cavendish, J.Z., Sarkar, S.N., Colantonio, M.A., Quintana, D., Ahmed, N., White, B.A., Engler-Chiurazzi, E.B. and Simpkins, J.W. 2020. Mitochondrial movement and number deficits in embryonic cortical neurons from 3xTG-AD mice. J Alzheimers Dis. 70(1), 139-151

Chang, D.T., Reynolds, I.J., 2006. Differences in mitochondrial movement and morphology in young and mature primary cortical neurons in culture. Neuroscience 141, 727–736.

Chazotte, B. 2009. Labeling mitochondria with fluorescent dyes for imaging. Cold Spring Harb Protoc. (6), pdb prot4948

Chen, Y. and Sheng, Z.-H. 2013. Kinesin-1–syntaphilin coupling mediates activity-dependent regulation of axonal mitochondrial transport. J Cell Biol. 202(2), 351–364

Chen, Y., Guo, S., Tang, Y., Mou, C., Hu, X., Shao, F., Yan, W and Wu, Q. 2020. Mitochondrial Fusion and Fission in Neuronal Death Induced by Cerebral Ischemia-Reperfusion and Its Clinical Application: A Mini-Review. Med Sci Monit. 26, e928651-1-e928651-12.

Chen, Y.-M., Gerwin, C. and Sheng, Z-H. 2009. Dynein Light Chain LC8 Regulates Syntaphilin-Mediated Mitochondrial Docking in Axons. J Neurosci. 29(30), 9429–9438

Chiba, K., Shimada, Y., Sinjo, M., Suzuki, T. And Uchiha, S. 2014. Simple and direct assembly of kymographs from movies using KYMOMAKER. Traffic. 15(1), 1-11

Clark, P., Britland, S., Connolly, P. 1993. Growth cone guidance and neuron morphology on micropatterned laminin surface. J. Cell Sci. 105(Pt 1), 203-212

Clement, J.P., Al-Alwan, L. Glasgow, S.D., Stolow, A., Ding, Y., Melo, T.Q., Khayachi, A., Liu, Y., Hellmund, M., Haag, R., Milnerwood, A.J., Grutter, P. and Kennedy, T.E. 2021. Dendritic polyglycerol amaine: an enhanced substrate to support long-term neural cell culture. ASN Neuro. 14, 1-17

Course, M.M., Hsieh, C-H., Tsai, P-I., Codding-Bui, J.A., Shaltouki, A. and Wang, X. 2017. Live imaging mitochondrial transport in neurons. Neuromethods. 123, 49-66

Cullen, D.K., Gilroy, M.E., Irons, H.R., Laplaca, M.C., 2010. Synapse-to-neuron ratio is

Dai, X. and Xie, H. 2017. New methods of fabricating gratings for deformation measurements: A review. Opt Lasers Eng. 92, 48-56

De Vos, K.J., Chapman, A.L., Tennant, M.E., Manser, C., Tudor, E.L., Lau, K-F., Brownlees, J., Ackerley, S., Shaw, P.J., McLoughlin, D.M., Shaw, C.E., Leigh, N., Miller, C.C.J. and Grierson, A.J. 2007. Familial amyotrophic lateral sclerosis-linked SOD1 mutants perturb fast axonal transport to reduce axonal mitochondria content. Hum Mol Genet. 16(22), 2720-2728

Delamarche, E., Schmid, H., Biehuyck, H.A., Michel, B. 1997. Stability of moulded polydimethylsiloxane microstructures. Adv Mater. 9, 741-746

Delettre, C., Lenaers, G., Griffoin, J.M., Gigarel, N., Lorenzo, C., Belenguer, P., Pelloquin, L., Grosgeorge, J., Turc-Carel, C., Perret, E., Astarie-Dequeker, C., Lasquellec, L., Arnaud, B., Ducommun, B., Kaplan, J. And Hamel, C.P. 2000. Nuclear gene OPA1, encoding a mitochondrial dynamic-related protein, is mutated in dominant optic atrophy. Nat Genet. 26, 207-210

Devine, M.J. and Kittler, J.T. 2018. Mitochondria at the neuronal presynapse in health and disease. Nat Rev Neurosci. 19(2), 63-80

Drabik, K., Piecyk, K., Wolny, A., Szulc-Dabrowska, L., Debska-Vielhaber, G., Vielhaber, S., Duszynski, J., Malinska, D. And Szczepanowska, J. 2020. Adaptation of mitochondrial network dynamics and velocity of mitochondrial movement to chronic stress present in fibroblasts derived from patients with sporadic form of Alzheimer's disease. FASEB J. 35(6), e21586

Edda, T. and Eva-Maria, M. 2007. Missorting of tau in neurons causes degeneration of synapses that can be rescued by the kinase MARK2/Par-1. J Neurosci. 27(11), 2896-2907

Eilenberger, C., Rothbauer, M., Salinger, F., Gerhartl, A., Jordan, C., Harasek, M., Scchadl, B., Grillari, J., Weghuber, J., Neuhaus, W., Kupcu, S. and Ertl, P. 2021. A microfluidic multisize spheroid array for multi parametric screening of anticancer drugs and blood-brain barrier transport properties. Adv Sci. 8, 2004856

Ekanayake, S.B., El-Zawily, A.M., Paszkiewicz, G., Rolland, A. And Logan, D.C. 2015. Imaging and analysis of mitochondrial dynamics in living cells. Methods Mol Biol. 1305, 223-240

Eliceiri, K.W., Berthold, M.R., Goldberg, I.G., Luis, Ibanez., Manjunath, B.S., Martone, M.E., Murphy, R.F., Peng, H., Plant, A.L., Roysam, B., Stuurmann, N., Swedlow, J.R., Tomancak, P. And Carpenter, A.E. 2012. Biological imaging software tools. Nature Methods. 9(7), 697-710

Fransson, S., Ruusala, A. and Aspenström, P. 2006. The atypical Rho GTPases Miro-1 and Miro-2 have essential roles in mitochondrial trafficking. Biochem Biophys Res Commun. 344(2), 500–510.

Frederick, R.L., McCaffery, J.M., Cunningham, K.W., Okamoto, K. and Shaw, J.M. 2004. Yeast Miro GTPase, Gem1p, regulates mitochondrial morphology via a novel pathway. J Cell Biol 167(1), 87–98

Freire, E., Gomes, F.C.A., Linden, R., Neto, V.M and Coelho-Sampaio, T. 2002. Structure of laminin substratum modulates cellular signalling for neuritogenesis. J. Cell Sci. 115, 4867–4876

Fricke, R., Zentis, P.D., Rajappa, L.T., Hofmann, B., Banzet, M., Offenhäusser, A. and Meffert, S.H. 2011. Axon guidance of rat cortical neurone by micro contact printed gradients. Biomaterials. 32(8), 2070-2076

Friedman, J.R., Lackner, L.L., West, M., DiBenedetto, J.R., Nunnery, J. And Voeltz, G.K. 2011. ER tubules mark sites of mitochondrial division. Science. 334, 358-362

Frimat, J-P., Sisnaiske, J., Subbiah, S., Menne, H., Godoy, P., Lampen, P., Leist, M., Franzke, J., Hengstler, J.G., van Thriel, C. and West, J. 2010. The network formation assay: a spatially standardized neurite outgrowth analytical display for neurotoxicity screening. Lab on a chip. 10(6), 701

Ganote, C. E. and Armstrong, S.C. 2003. Effects of CCCP-induced mitochondrial uncoupling and cyclosporin A on cell volume, cell injury and preconditioning protection of isolated rabbit cardiomyocytes. J Mol Cell Cardiol. 35, 749-759

Geissler, M., Chen, J. and Xia, Y. 2004. Comparative study of monolayers self-assembled from alkylisocynadies and alkanethiols on polycrystalline Pt substrates. Langmuir. 20, 6993-6997

George E.B., Schneider, B.F., Lasek, R.J. and Katz, M.J. 1988. Axonal shortening and the mechanisms of axonal motility. Cell motil. Cytoskelet. 9(1), 48-59

Glater, E.E., Megeath, L.J., Stowers, R.S. and Schwarz, T.L. 2006. Axonal transport of mitochondria requires milton to recruit kinesin heavy chain and is light chain independent. J Cell Biol. 173(4), 545–557

Gokaltun, A., Yarmush, M.L., Asatekin, A. and Usta, O.B. 2017. Recent advances in nonbiofouling PDMS surface modification strategies applicable to microfluidic technology. Technology. 5, 1-12

Guckenberger, D.J., Berthier, E., Young, E.W. and Beebe, D.J. 2012. Induced hydrophobic recovery of oxygen plasma-treated surfaces. Lab Chip. 12, 2317-2321

Guo, X., Macleod, G.T., Wellington, A., Hu, F., Panchumarthi, S., Schoenfield, M., Marin, L., Charlton, M.P., Atwood, H.L. and Zinsmaier, K.E. 2005. The GTPase dMiro Is Required for Axonal Transport of Mitochondria to Drosophila Synapses. Neuron. 47(3), 379–393

Hardelauf, H., Sisnaiske, J., Taghipour-Anvari, A.A., Jacob, P., Drabiniok, E., Marggraf, U., Frimat, J-P., Hengstler, J.G., Neyer, A., van Thriel, C. and West, J. 2011. High fidelity neuronal networks formed by plasma masking with a bilayer membrane: analysis of neurodegenerative and neuroprotective processes. Lab Chip, 11, 2763-2771

Hardelauf, H., Waide, S., Sisnaiske, J., Jacob, P., Hausherr, V., Schobel, N., Janasek, D., Van Thriel, C. and West, J. 2014. Micropatterning neuronal networks. Analyst. 139-3256-3264

Higuchi-Sanabria, R., Swayne, T.C., Boldogh, I.R. and Pon, L.A. 2016. Live-cell imaging of mitochondria and the actin cytoskeleton in budding yeast. Methods Mol Biol. 1365, 25-62

Hinckley, T.F., Salvagio, L.A., Fudge, D.H., Verhey, K., Markus, S.M. and Qin, Yan. 2021. Zinc arrests axonal transport and displaces tau, doublecortin, and MAP2C from microtubules. bioRxiv

Hurd, D.D. and Saxton, W.M. 1996. Kinesin mutations cause motor neuron disease phenotypes by disrupting fast axonal transport in Drosophila. Genetics. 144(3), 1075–1085.

Ishihara, K. and Take, M. 2009. Bioinspired interface for nanobiodevices based on phospholipid polymer chemistry. J R Soc Interface. 6, S279-S291

Iwasaki, Y. and Ishihara, K. 2012. Cell membrane-inspired phospholipid polymers for developing medical devices with excellent bio interfaces. Sci Technol Adv Mater. 13(6), 064101

Iyer, S.P.N. and Hart, G.W. 2003. Roles of the Tetratricopeptide Repeat Domain in O -GlcNAc Transferase Targeting and Protein Substrate Specificity. J Biol Chem. 278(27), 24608–24616

Jakobs, M.A., Dimitracopoulos, A. And Franze, K. 2019. KymoButler, a deep learning software for automated kymograph analysis. Elife. 13(8), e42288

Jakobs, M.A.H., Zemel, A. And Franze, K. 2022. Unrestrained growth of correctly oriented microtubules instructs axonal microtubule orientation. eLife. 11, 377608

Kanai, Y., Okada, Y., Tanaka, Y., Harada, A., Terada, S. and Hirokawa, N. 2000. KIF5C, a novel neuronal kinesin enriched in motor neurons. J Neurosci. 20(17), 6374-6384

Kandel, J., Chou, P. And Eckmann, D.M. 2015. Automated detection of whole-cell mitochondrial motility and its dependence on cytoarchitectural integrity. Biotechnol Bioeng. 112(7), 1395-1405

Kang, J-S., Tian, J-H., Pan, P-Y., Zald, P., Li, C., Deng, C. and Sheng, Z-H. 2008. Docking of Axonal Mitochondria by Syntaphilin Controls Their Mobility and Affects Short-Term Facilitation. Cell. 132(1), 137–148

Kann O, Kovács R. 2007. Mitochondria and neuronal activity. Am J Physiol Cell Physiol. 292(2):C641-C657.

Kaufmann, T. and Ravoo, B.J. 2010. Stamps, inks and substrates: polymers in micro contact printing. Polym Chem. 1, 371-387

Kim, H.J., Park, J.W., Byun, J.H., Poon, W.W., Cotman, C.W., Fowlkes, C.C. and Jeon, N.L. 2012. Quantitative analysis of axonal transport by using compartmentalized and surface micropatterned culture of neurons. ACS Chem. Neurosci. 3, 433-438

Kim, N.H. and Chung, Y. 2015. Automated tracking and analysis of axonal transport using combined filtering methods. BioChip J. 9(3), 194-201

Kim, M.H., Park, J.H., Joo, S.H., Hong, D.W., Park, M., Choi, J.Y., Moon, H.W., Kim, Y.G., Kang, K.T and Choi, I.S. 2018. Accelerated development of hippocampal neurons and limited adhesion of astrocytes on negatively charged surfaces. Langmuir. 34, 1767-1774

King, S.J. and Schroer, T.A. 2000. Dynactin increasese the processivity of the cytoplasmic dynein motor. Nat Cell Biol. 2, 20-24.

Kleinfeld, D., Fahler, K.H. and Hockberger, P.E. 1988. Controlled outgrowth of dissociated neurons on patterned substrates. J Neurosci. Res. 8, 4098-4120

Kunze, A., Giugliano, M., Valero, A. and Renaud, P. 2011. Micropatterning neural cell cultures in 3D with a multi-layered scaffold. Biomaterials. 32(8), 2088-2098.

Lee, C.W. and Peng, H.B. 2006. Mitochondrial clustering at the vertebrate neuromuscular junction during presynaptic differentiation. J. Neurobiol. 66(6), 522–536.

Lee, J.N., Park, C and Whitesides, G.M. 2003. Solvent compatibility of poly(dimethylsiloxane)-based microfluidic devices. Anal Chem. 75, 6544

Lee, M.W., Bassiouni, R., Sparrow, N.A., Iketani, A., Booker, R.J., Moskowitz, C., Vishnubhotla, P., Khaled, A.S., Over, J., Copik, A., Fernandez-Valle, C., Perez, J.M. and Khaled, A.R. 2014. The CT20 peptide causes detachment and death of metastatic breast cancer cells by promoting mitochondrial aggregation and cytoskeletal disruption. Cell Death Dis. 5, e1249

Lein, P. J., Banker, G. A. and Higgins, D. 1992. Laminin Selectively Enhances Axonal Growth and Accelerates the Development of Polarity by Hippocampal Neurons in Culture. Dev. Brain Res. 69, 191− 197

Lewis, T.L., Turi, G.F., Kwon, S.K., Losonczy, A. and Polleux, F. 2016. Progressive decrease of mitochondrial motility during maturation of cortical axons in vitro and in vivo. Curr Biol. 26(19), 2602-2608

Li, J. and Yeung, E.S. 2008. Real-time single-molecule kinetics of trypsin proteolysis. Anal. Chem. 80(22), 8509-8513

Li, Z., Okamoto, K., Hayashi, Y. and Sheng, M. 2004. The importance of dendritic mitochondria in the morphogenesis and plasticity of spines and synapses. Cell. 119, 873–87

Liazoghli, D., Roth, A.D., Thostrup, P. and Colamn, D.R. 2011. Substrate micropatterning as a new in vitro cell culture system to study myelination. ACS Chem Neurosci. 3, 90-95

Liberio, M.S., Sadowski, M.C., Soekmadji, C., Davis, R.A. and Nelson, C.C. 2014. Differential effects of tissue culture coating substrates on prostate cancer cell adherence, morphology and behavior. PLoS ONE. 9(11)

Ligon, L. and Steward, O. 2000a. Movement of mitochondria in the axons and dendrites of cultured hippocampal neurons. J Comp Neurol. 427(3), 340–350

Ligon, L.A. and Steward, O. 2000b. Role of microtubules and actin filaments in the movement of mitochondria in the axons and dendrites of cultured hippocampal neurons. J. Comp. Neurol. 427, 351-361

Liu, M., Sun, J. and Chen, Q. 2009. Influences of heating temperature on mechanical properties of polydimethylsiloxane. Sensors Acturators A Phys. 151, 42-45

Liu, W., Sun, M., Han, K., Hu, R., Liu, D. and Wang, J. (2020). Comprehensive evaluation of stable neuronal cell adhesion and culture on one-step modified polydimethylsiloxane using functionalized plu

Liu, Y.J., McInytre, R.L., Janssens, G.E. and Houtkooper, R.H. 2020. Mitochondrial fission and fusion: A dynamic role in aging and potential target for age-related disease. Mech Ageing Dev. 186, 111212

Lopez-Domenech, G., Covill-Cooke, C., Ivankovic, D., Halff, E.F., Sheehan, D.F., Norkett, R., Birsa, N. and Kittler, J. 2018. Miro proteins coordinate microtubule- and actin- dependent mitochondrial transport and distribution. EMBO J. 37, 321–336

Loss, O., Stephenson, F.A. (2017) Developmental changes in trak-mediated mitochondrial transport in neurons. Mol. Cell. 80: 134-147

Lovas, J.R. and Wang, X. 2013. The meaning of mitochondrial movement to a neuron's life. Biochim Biophys Acta. 1833(1), 184–194

Love, J.C., Wolfe, D.B., Chabinyc, M.L., Paul, K.E. and Whitesides, G.M. 2002. Self-assembled monolayers of alkanethiolates on palladium are good etch resists. J Am Chem. 124, 1576-1577

Lu, X., Kim-Han, J.S., O'Malley, K.L., Sakiyama-Elbert, S.E. 2012. A microdevice platform for visualizing mitochondrial transport in aligned dopaminergic axons. J Neurosci Methods. 209:35-39

Ma, W., Tavakoli, T., Derby, E., Serebryakova, Y., Rao, M.S. and Mattson, M.P. 2008. Cell-extracellular matrix interactions regulate neural differentiation of human embryonic stem cells. BMC. 8(90), 1-13

MacAskill, A.F., Brickley, K., Stephenson, F.A. and Kittler, J.T. 2009a. GTPase dependent recruitment of Grif-1 by Miro1 regulates mitochondrial trafficking in hippocampal neurons. Mol Cell Neurosci. 40, 301-312

MacAskill, A.F., Rinholm, J.E., Twelvetrees, A.E., Arancibia-Carcamo, I.L., Muir, J., Fransson, A., Aspenstrom, P., Attwell, D. and Kittler, J.T. 2009b. Miro1 Is a Calcium Sensor for Glutamate Receptor-Dependent Localization of Mitochondria at Synapses. Neuron. 61(4), 541–555

Mahmoud, M.B., Ratkai, A., Bauer, K., Bencsik, N., Szucs, A., Schlett, K. and Tarnok, K. 2025. Multifactorial approach is needed to unravel the maturation phases of human neurons derived from induced pluripotent stem cells. Sci Rep. 2627

Mandal, A. and Drerup, C.M. 2019. Axonal Transport and Mitochondrial Function in Neurons. Front Cell Neurosci. 13, 373

Mangeol, P., Prevo, B., Peterman, E.J. 2016. KymographClear and KymographDirect: two tools for the automated quantitative analysis of molecular and cellular dynamics using kymographs. Mol Biol Cell. 27, 1948-1957

Martinez-Rivas, A., Gonzalez-Quijano, G.K., Proa-Coronado, S., Severac, C. and Dague, E. 2017. Methods of micropatterning and manipulation of cells for biomedical applications. Micromachines. 8, 347

Marques-Almeida, T., Ribeiro, C., Irastorza, I., Miranda-Azpiazu, P., Torres-Alemán, I., Silvan, U. and Lanceros-Méndez, S. 2023. Electroactive Materials Surface Charge Impacts Neuron Viability and Maturation in 2D Cultures. ACS Appl Mater Interfaces. 5;15(26), 31206-31213

Matta, A., Fleischman, A.J. and Roy, S. 2005. Characterization of polydimethylsiloxane (PDMS) properties for biomedical micro/nanosystem.s Biomed Microdevices. 7, 281-293

Mattson, M.P., Gleichmann, M. and Cheng, A. 2008. Mitochondria in neuroplasticity and neurological disorders. Neuron. 60(5), 748-766.

Mazia, G. and Sale, W. 1975. Adhesion of cells to surfaces coated with polylysine. Applications to electron microscopy. J Cell Biol. 66(1), 198-200

McCarron, J.G., Wilson, C., Sandison, M.E., Olson, M.L., Girkin, J.M., Saunter, C. and Chalmers, S. 2013. From structure to function: Mitochodnrial morphology, motion and shaping in vascular smooth muscle. J Vasc Res. 50, 357-371

McDonald, J.C. and Whitesides, G.M. 2002. Poly(dimethylsiloxane) as a material for fabricating microfluidic devices. Acc Chem Res. 35, 491-499

Minckley, T.F., Salvagio, L.A., Fudge, D.H., Verhey, K., Markus, S.M., Qin, Y. 2023. Zn2+ decoration of microtubules arrests axonal transport and displaces tau, doublecortin, and MAP2C. J Cell Biol. 222(8):e202208121.

Miyazono, Y., Hirashima, S., Ishihara, N., Kusukawa, J., Nakamura, K-I. and Ohta, K. 2018. Uncouped mitochondria quickly shorten along their long axis to form indented spheroids, instead of rings, in a fission-independent manner. Sci Rep. 8(350)

Modi, S., Lopez-Domenech, G., Half, E.F., Covill-Cooke, C., Ivanovic, D., Melandri, D., Arancibia-Carcamo, L., Burden, J.J., Lowe, A.R. and Kittler, J.F. 2019. Miro clusters regulate ER-mitochondria contact sites and link Cristal Organization to the mitochondrial transport machinery. Nat Commun. 10, 4399

Morris, R.L. and Hollenbeck, P.J. 1993. The regulation of bidirectional mitochondrial transport is coordinated with axonal outgrowth. J Cell Biol. 104(3), 917-27

Morris, R.L. and Hollenbeck, P.J. 1995. Axonal transport of mitochondria along microtubules and F-actin in living vertebrate neurons. J Cell Biol. 131(5), 1315-26

Nakatoh, T., Osaki, T., Tanimoto, S., Jahan, M. GS., Kawakami, T., Chihara, K., Sakai, N. and Yumura, S. 2022. Cell behaviors within a confined adhesive area fabricated using novel micropatterning methods. PLoS ONE. 17(1)

Neumann, S., Chassefeyre, R., Campbell, G.E. and Encalada, S.E. 2017. KymoAnalyzer: a software tool for the quantitative analysis of intracellular transport in neurons. Traffic. 18(1), 71-88

Ng, J.M., Gitlin, I., Stroock, A.D. and Whitesides, G.M. 2002. Components for integrated poly(dimethylsiloxane) microfluidic systems. Electrophoresis. 23, 3461-3473

Oeding, S. J., Majstrowicz, K., Hu, X-P., Schwarz, V., Freitag, A., Honnert, U., Nikolaus, P. and Bahler, M. 2018. Identification of Miro1 and Miro2 as mitochondrial receptors for myosin XIX. J Cell Sci. 131 (7), jcs219469

Offenhäusser, A., Bocker-Meffert, S., Decker, T., Lehpenstein, R., Gasteier, P., Groll, J., Moller, M., Reska, A., Schafer, S., Schulte, P. and Vogt-Eisele, A. 2007. Microcontact printing of proteins for neuronal cell guideance. Soft Matter. 3, 290-298

Oliva, A.A., James, C.D., Kingman, C.E., Craighead, H.G. and Banker, G.A. 2003. Patterning axonal guidance molecules using a novel strategy for microcontact printing. Neurochem Res. 28, 1639-1648

Perl, A., Reinhoudt, D.N and Huskens, J. 2009. Microcontact Printing: Limitations and Achievements. Adv Mater. 21, 2257-2268

Pigino, G., Morfini, G., Pelsman, A., Mattson, M.P., Brady, S.T. and Busciglio, J. 2003. Alzheimer's Presenilin 1 mutations impair kinesin-based axonal transport. J Neurosci. 23(11), 4499-4508

Pilling, A.D., Horiuchi, D., Lively, C.M. and Saxton, W.M. 2006. Kinesin-1 and Dynein Are the Primary Motors for Fast Transport of Mitochondria in Drosophila Motor Axons. Mol Biol Cell. 17(4), 2057–2068

Qin, D., Xia, A. and Whitesides, G.M. 2010. Soft lithograph for micro-and nanoscale patterning. Nature protocols, 5, 491-502

Rao, S.S. and Winter, J.O. 2009. Adhesion molecule-modified biomaterials for neural tissue engineering. Front. Neuroeng. 2(6).

Rintoul, G.L., Filiano, A.J., Brocard, J.B., Krees, G.J. and Reynolds, I.J. 2003. Glutamate decreases mitochondrial size and movement in primary forebrain neurons. J Neurosci. 23(21), 7881-7888

Roach, P., Parker, T., Gadegaard, N. And Alexander, M.R. 2010. Surface strategies for control of neuronal cell adhesion: A review. Surf Sci Rep. 65, 145-173

Ruiz, S.A. and Chen, C.S. 2007. Microcontact printing: A tool to pattern. Soft Matter. 3, 1-11

Russo, G.J., Louie, K., Wellington, A., Macleod, G.T., Hu, F., Panchumarthi, S. and Zinsmaier, K.E. 2009. Drosophila Miro Is Required for Both Anterograde and Retrograde Axonal Mitochondrial Transport. J Neurosci. 29(17), 5443–5455

Saotome, M., Safiulina, D., Szabadkai, G., Das, S., Fransson, A., Aspenstrom, P., Rizzuto, R. and Hajnóczky, G. 2008. Bidirectional Ca2+-dependent control of mitochondrial dynamics by the Miro GTPase. Proc Natl Acad Sci. 105(52), 20728–20733

Schindelin, J., Arganda-Carreras, I., Frise, E., Kaynig, V., Longair, M., Pietzsch, T., Preibisch, S., Rueden, C., Saalfeld, S., Schmid, B., Tinevez, J-Y., White, D.J., Hartenstein, V., Eliceiri, K., Tomancak, P and Cardona, A. 2012. Fiji: an open-source platform for biological-image analysis. Nat Methods. 9, 676-682

Sebastian, D. And Zorzano, A. 2018. Mitochondrial dynamics and metabolic homeostasis. Curt Opin Physiol. 3, 34-40

Shahen, V.A., Cantrill, L.C., Sangani, N.B., Christodoulou, J., Gold, W.A. 2018. A simple and efficient toolset for analysing mitochondrial trafficking in neuronal cells. Acta Histochem. 120, 797-805.

Sheng, Z-H. 2014. Mitochondrial trafficking and anchoring in neurons: New insight and implications. J Cell Biol. 204(7), 1087–1098

Sibarani, J., Take, M. and Ishihara, K. 2007. Surface modification on micro fluidic devices with 2-methacryloyloxyethyl phosphorylcholine polymers for reducing unfavourable protein adsorption. Colloids Surf. B. 54: 88-93

Smith, G.M. and Gallo, G. 2018. The role of mitochondria in axon development and regeneration. Dev Neurobiol. 78(3), 221-237

Stenger, D. A., Georger, J.H., Dulcey, C.S., Hickman, J.J., Rudolph, A.S., Nielsen, T.B., McCort, S.M. and Calvert, J.M. 1992. Coplanar Molecular Assemblies of Amino- and Perfluorinated Alkylsilanes: Characterization and Geometric Definition of Mammalian Cell Adhesion and Growth. J. Am. Chem. Soc. 114, 8435−8442.

Stowers, R.S., Megeath, L.J., Górska-Andrzejak, J., Meinertzhagen, I.A. and Schwarz, T.L. 2002. Axonal Transport of Mitochondria to Synapses Depends on Milton, a Novel Drosophila Protein. Neuron 36(6), 1063–1077.

Sun, Y., Huang, Z., Liu, W., Yang, K., Sun, K., Xing, S., Wang, D., Zhang, W. and Jiang, W. 2012. Surface coating as a key parameter in engineering neuronal network structures in vitro. Biointerphases. 7, 1-14

Tan, J.L., Liu, W., Nelson, C.M., Raghavan, S. and Chen, C.S. 2004. Simple approach to micropattern cells on common culture substrates by tuning substrate wettability. Tissue Eng. 10(5-6), 865-872

Tan, J.L., Tien, J. and Chen, C.S. 2002. Microcontact printing of proteins on mixed self-assembled monolayers. Langmuir. 18, 519-523

Tanaka, Y., Kanai, Y., Okada, Y., Nonaka, S., Takeda, S., Harada, A. and Hirokawa, N. 1998. Targeted Disruption of Mouse Conventional Kinesin Heavy Chain kif5B, Results in Abnormal Perinuclear Clustering of Mitochondria. Cell 93(7), 1147–1158

Tauchi, H., Sato, T., 1968. Age changes in size and number of mitochondria of human hepatic cells. J. Gerontol. 23, 454–461.

Taylor, C.S., Chen, R., Sa, R.D., Hunt, J.A., Curran, J.M. and Haycock, J.W. 2021. Cost effective optimised synthetic surface modification strategies ofr enhanced control of neuronal cell differentiation and supporting neuronal and Schwann cell viability. J Biomed Mater Res. 109, 1713-1723

Tessier-Lavigne, M. and Goodman, C. S. 1996. The Molecular Biology of Axon Guidance. Science, 274, 1123−1133.

Vogt, A.K., Brewer, G.J. and Offenhäusser, A. 2005. Connectivity patterns in neuronal networks of experimentally defined geometry. Tissue Eng. 11(11/12), 1757-1767

Vogt, A.K., Lauer, L., Knoll, W. nd Offenhäusser, A. 2003. Micropatterned substrates for the growth of functional neuronal networks of defined geometry. Biotechnol. Prog. 19, 1562-1568

Vroemen, P., Seijas-Gamardo, A., Palmen, R., Wieringa, P.A., Webers, C., Moroni, L. and Gorgels, T. 2025. The Importance of Coating Surface and Composition for Attachment and Survival of Neuronal Cells Under Mechanical Stimulation. J Biomed Mater Res A. 113(5), e37919.

Wai, T. And Langer, T. 2016 Mitochondria dynamics and metabolic regulations. Trends Endocrine. Metal. 27, 105-117

Wang, X., Schwarz, T.L., 2009. The Mechanism of Ca2+-Dependent Regulation of Kinesin-Mediated Mitochondrial Motility. Cell. 136(1), 163–174

Wang, X., Winter, D., Ashrafi, G., Schlehe, J., Wong, Y.L., Selkoe, D., Rice, S., Steen, J., Lavoie, M.J. and Schwarz, T.L. 2011. PINK1 and parkin target Miro for phosphorylation and degradation to arrest mitochondrial motility. Cell. 147(4), 893-906

Wheeler, B.C. and Brewer, G.J. 2010. Designing Neural Network in Culture. Proc IEEE Inst Electr Electron Eng. 98(3), 398–406

Widge, A.S., Jeffries-El, M., Cui, X., Lagenaur, C.F. and Matsuoka, Y. 2007. Self-assembled monolayers of polythiophene conductive polymers improve biocompatibility and electricalimpedance of neural electrodes. Biosens Bioelectron. 22, 1723–32

Wu, S., Zhou, F., Zhang, Z. and Xing, D. 2011. Mitochondrial oxidative stress causes mitochondrial fragmentation via differential modulation of mitochondria fission-fusion proteins. FEBS J. 278, 941-954

Wysotzki, P. And Gimsa, J. 2019. Surface coatings modulate the differences in the adhesion forces of eukaryotic and prokaryotic cells as detected by single cell force microscopy. Int. J. Biomater. 1-12

Xia, Y. And Whitesides, G.M. 1998. Soft lithography. Annu Rev Mater Sci. 28, 153-184

Xia, Y., Kim, E., Mrksich, M. and Whitesides, G.M. 1996. Microcontact printing of alkanethiols on copper and its application in microfabrication. Chem Mater. 8, 601-603

Yanfang, R., Priyanka, T., Zuoping, X. and James Q, Z. 2006. Acute impairment of mitochondrial trafficking by β-amyloid peptides in hippocampal neurons. J Neurosci. 26(41), 10480-10487

Yavin, E., and Yavin, Z. 1974. Attachment and culture of dissociated cells from rat embryo cerebral hemispheres on polylysine-coated surface. J. Cell Biol. 62, 540–546

Yeung, C.K., Lauer, L. and Offenhäusser A, Knoll W. 2001. Modulation of the growth and guidance of rat brain stem neurons using patterned extracellular matrix proteins. Neurosci Lett. 301(2), 147-150

Yoshida S., Negishi, M.K. and Takeuchi, S. 2018. Assembly and connection of micro patterned single neurons for neuronal network formation. Micromachines (Basel). 9(5), 235

Zala, D., Hinckelmann, M.V., Yu, H., Lyra da Cunha, M.M., Liot, G., Cordelieres F.P., Marco, S. and Saudou, F. 2013. Vesicular glycolysis provides on-board energy for fast axonal transport. Cell. 152, 479-491

Zhou, B., Yu, P., Lin, M.Y., Sun, T., Chen, Y. and Sheng, Z.H. 2016. Facilitation of axon regeneration by enhancing mitochondrial transport and rescuing energy deficits. J Cell Biol. 214, 103-119ß

van Spronsen, M., Mikhaylova, M., Lipka, J., Schlager, M.A., van den Heuvel, D.J., Kuijpers, M., Wulf, P.S., Keijzer, N., Demmers, J., Kapitein, L.C., Jaarsma, D., Gerritsen, H.C., Akhmanova, A. and Hoogenraad, C.C. 2013. TRAK/Milton Motor-Adaptor Proteins Steer Mitochondrial Trafficking to Axons and Dendrites. Neuron. 77(3), 485–502